Dissertations - ALL                                      SURFACE at Syracuse University

Summer 8-27-2021

# Computational Methodologies for the Simulation and Analysis of Low-frequency Vibrations in Molecular Crystals

Sara Jean Dampf
*Syracuse University*

## Recommended Citation

# Abstract

Quantum mechanical models are used to calculate a host of physical phenomena in molecular solids ranging from mechanical elasticity to the energetic stability ordering of polymorphs. However, with the many software packages and methodologies available, it can be difficult to select the most suitable model for the problem at hand without prior knowledge. A promising approach for evaluating the performance of solid-state models is the comparison of the simulations to experimentally measured low-frequency (sub-200 $cm^{-1}$) vibrational spectra. As this region is dominated by weak intermolecular forces and shallow potential energy surfaces, even slight miscalculations in the solid-state packing arrangements can become readily apparent. In this work, terahertz time-domain spectroscopy and low-frequency Raman spectroscopy are used as benchmark experimental targets to develop computational methodologies for simulating and analyzing the lattice vibrations of molecular crystals such as torsions and translations. The developed computational approaches utilize solid-state density functional theory to account for the periodic nature of a molecular crystal and include careful consideration of the effects that functional choice, basis set composition, and energetic tolerances have on the frequencies and spectral intensities of the sub-200 $cm^{-1}$ vibrations. These computational methodologies serve as standards for accurately modeling low-frequency vibrations across a range of molecular solids from a small molecule that exhibits unusual thermal behavior to the intricacies of an extensively hydrogen bonded oligopeptide.

COMPUTATIONAL METHODOLOGIES FOR THE SIMULATION AND ANALYSIS OF
LOW-FREQUENCY VIBRATIONS IN MOLECULAR CRYSTALS

by

Sara J. Dampf

B.S., University of New Haven, 2015
B.S., University of New Haven, 2015
M.Phil., Syracuse University, 2017

Dissertation

Submitted in partial fulfillment of the requirements for the degree of

Doctor of Philosophy in Chemistry.

Syracuse University

August 2021

# ACKNOWLEDGEMENTS

# Table of Contents

# List of Illustrative Methods

ix

# Chapter 1: Introduction

## 1.1 Motivation

Computational models have been used across a wide range of scientific disciplines, finding uses from physics to food science.[1-7] These models are applicable to all states of matter, but have often been applied to complex solid-state problems such as to help differentiate between the many polymorphs of chocolate, and explain why in the late 1990's the HIV drug Ritonavir started failing dissolution tests and had to be pulled from the shelves.[8-12] Quantum mechanical models are particularly advantageous over classical force fields, as they do not require the use of empirical parameters, however, they do come with a large computational cost that has proven to be overwhelming for large systems.[13-15] This challenge has been addressed through continuous improvements to computers and software codes, increasing the potential applications of quantum mechanical models.[16-18]

Even with improvements to scalability, the difficulty remains in knowing how far a quantum mechanical model can be trusted.[19-21] A target accuracy of 1 kcal/mol (4.2 kJ/mol) is often used, but this has proven to be insufficient when describing small energy changes such as ranking the stability of polymorphs.[22-28] To validate these models, replication of experimental measurements is necessary, with models often focusing first on accurately predicting atomization energies.[29-31] This focus, however, is not an appropriate target for condensed phase systems, as their errors increase with system size.[32-34] A promising benchmark for determining the success of molecular solid simulations is the replication of low-frequency vibrations. These vibrations ($< 200$ cm$^{-1}$) are associated with large-scale, global motions of the molecular species in the solid

and require that the model accounts for not only the covalent forces within a single molecule, but also the intermolecular forces that hold the solid together.[35-38]

Developing methodologies that focus on the low-frequency region of the electromagnetic spectrum provides realistic expectations for the simulation of condensed phase systems. In the past, the combination of quantum models and low-frequency vibrational spectroscopy has worked very well, but improvements to technology and software codes allow even further understanding to be gained.[39-45] These insights can come in the form of observing low-frequency Raman vibrations within 5 cm$^{-1}$ of the Rayleigh line, or through the use of a hybrid density functional in studying biomolecules.[42, 46-49] As the restraints that previously bound quantum mechanical models are relaxed, a new set of methodologies can emerge to model physical phenomena in ways that were once thought to be impractical. These approaches can then be used to draw new physical insight and serve as guides for the development of methodologies to be used to evaluate even larger and more complex systems.

## 1.2 Background

To rationally use quantum models in the investigation of solid-state properties, the theoretical methods that form the foundations of the simulations must be at least minimally understood, including an appreciation for the terms used to solve the Schrödinger equation.[50-52] Once solved, the Schrödinger equation can be used to describe all quantum aspects of a system. While this equation can be easily explained for a single electron case, as the size of the system increases to include multiple electrons, the interactions between these electrons greatly complicates solving the many-body Schrödinger equation.[53, 54]

A commonly applied computational method to describe both the classical electrostatics and the quantum effects of condensed phase matter is solid-state density functional theory (ss-DFT).[55-58] In principle, this approach provides an exact solution as the exchange and correlation energy are included as a function of the electron density; however, without knowing the exact form of the exchange and correlation terms, approximations must be made.[59, 60] When performing ss-DFT based calculations, it is important to note which terms can be solved exactly, versus those that must be approximated. In understanding the formation of the density functional used to approximate the exchange and correlation energy, as well as the formation of the molecular orbitals used to describe the electron density, one can begin to understand how one simulation differs from the next. Since these differences in the construction of the model can lead to large changes in the predicted physical properties, it is imperative that they are chosen with care and with respect to the type of system being evaluated.[61-67] In the case of crystalline systems, this includes the use of periodic boundary conditions and the inclusion of London dispersion forces.[68-73]

Since these models are often used to differentiate solids that differ only in their solid-state packing arrangement, and not molecular identities, the experimental measurements to which they are being compared should be able to do the same. One experimental technique that can monitor these often-subtle differences in packing arrangements is low-frequency vibrational spectroscopy. Low-frequency vibrational spectroscopy is governed by the same foundations of classical infrared and Raman spectroscopies. However, unlike spectroscopies that probe the frequency region $> 1500$ cm$^{-1}$ and can only differentiate between the presence of different functional groups, low-frequency vibrational spectroscopy interacts with $< 200$ cm$^{-1}$ frequency range that can be used to differentiate between slight changes to the intermolecular packing

arrangements of solids.[74-79] It can be advantageous to use a combination of low-frequency vibrational spectroscopies to measure all optically allowed vibrations, regardless of vibrational selection rules, using both terahertz time-domain spectroscopy and Raman spectroscopy.[80-82] Just as it is important to understand the energetic transitions and vibrational selection rules that allow a spectral feature to be observed, it is also important to understand how these spectra can be collected and applied.

Another technique often used to characterize crystalline solids is X-ray diffraction.[83-86] Rooted in the directionality and intensity of the diffracted rays, X-ray diffraction is used to not only identify the dimensions of a crystallographic unit cell, but the location of the atoms within it.[87] Knowledge of the foundations that govern X-ray diffraction leads to more meaningful and efficient data collections that can be used to help validate computational models.

## 1.3 Summary of Chapters

The opening sections of this work focus on the foundations that are used to characterize solids both theoretically (**Chapter 2**) and experimentally (**Chapter 3**), paying special attention to solid-state density functional theory and low-frequency vibrational spectroscopy. These foundations enable the processes and applications described in **Chapter 4** to be used appropriately to gain the new physical insights that are detailed in **Chapters 5-7**. The work closes with a series of reflections on the key products of the work and the potential for future directions (**Chapter 8**).

**Chapter 2** begins by briefly exploring the core equations and principles that govern quantum mechanical models with the discussion progressing to the specifics of density

functional theory (DFT). As opposed to wavefunction-based methods, the crux of DFT lies in solving for the electron density, and while several of the energetic components can be solved exactly, there still exists a group of interactions that must be approximated. These approximated terms cover the quantum contributions to kinetic energy as well as electron-electron repulsion. To model these interactions, a number of density functionals and basis sets have been developed using varying levels of complexity. Finally, the application of these principles to solid-state calculations is explored, emphasizing the need for periodic boundary conditions.

**Chapter 3** begins by broadly describing a number of experimental approaches that can be used to characterize solids. The focus is then narrowed down to two regions of the electromagnetic spectrum that can be used to validate the quality of DFT calculations in the solid-state, the terahertz frequency range, from $3 - 333$ cm$^{-1}$, and the X-ray frequency range, from $10^{-9} - 10^{-7}$ cm$^{-1}$. Two different forms of low-frequency vibrational spectroscopy are used to access vibrations in the terahertz range. Both approaches are governed by the same principles that apply to all types of vibrational spectroscopy, with the difference being the vibrational selection rules that are being investigated. Terahertz time-domain spectroscopy (THz-TDS) uses the generation and detection of terahertz waves to probe the infrared-active vibrations by measuring the transmission of light through a sample. Conversely, low-frequency Raman spectroscopy (LFRS) probes the Raman-active vibrations through precise filtering and analysis of the light scattered off the sample. The same types of large-scale global vibrations are seen regardless of which low-frequency technique is used, but having access to both provides a complete spectral picture for the samples being investigated. The X-ray frequency range is utilized through two different approaches as well, powder X-ray diffraction (PXRD) and single-crystal X-ray diffraction (SC-XRD), but these techniques are based on diffraction rather than

absorption. The first approach provides a representative pattern of the bulk sample, while the second approach focuses on the details of an individual crystal.

**Chapter 4** aims to provide practical applications for the foundations established in the previous chapters, and outline processes that can be followed to achieve reliable and sensible results. Cursory descriptions of a selection of tools available within the solid-state DFT software code, CRYSTAL17 are provided as well as examples of input files to start single point energy, geometry optimization, and harmonic frequency calculations for L-cystine, a proposed molecular standard.[88] Also included, are detailed procedures for the collection and analysis of both THz-TDS and LFRS measurements, with examples of spectra for each approach. This chapter concludes with PXRD and SC-XRD procedures for the use of the instruments in the Department of Chemistry at Syracuse University, including specific details about previously used data collection parameters.

**Chapter 5** is a presentation of the proposed crystalline molecular standards to be used for both forms of low-frequency vibrational spectroscopy and ss-DFT calculations. With researchers currently having the accessibility to such a wide number of commercialized and home-built instruments as well as ss-DFT software codes, the situation necessitates the establishment of benchmark molecular targets. Three crystalline solids are proposed to serve as standards: α-lactose monohydrate, biotin, and L-cystine. Each of these systems forms well-characterized crystalline solids under ambient conditions that are stable, inexpensive, and non-hazardous. All three targets also have a number of well-resolved spectral features at room-temperature obtainable through both THz-TDS and LFRS. The same materials were analyzed computationally using identical levels of theory, and good agreement with experimental results

were achieved for each solid. The ideal candidate to serve as a molecular standard across THz-TDS, LFRS, and ss-DFT was determined to be crystalline biotin.

**Chapter 6** reveals an unusual temperature dependence in a lattice vibration of a well-known neurotransmitter, γ-aminobutyric acid (GABA). Typically, when a sample is cooled, the spectral features will shift to a higher frequency, and this is what was seen for the majority of the low-frequency terahertz and Raman peaks of GABA. However, the lowest frequency lattice vibration in crystalline GABA shifts to lower frequency when cooled. This anomalous shift in response to temperature is unusual, but not unheard of. To explain the origin of the unexpected shift, a series of ss-DFT calculations were run, employing numerous functionals, basis sets, and additional keywords to increase accuracy. Regardless of the approach, the anomalous shift was not reproduced using a harmonic approximation for the vibrational frequencies, and it was only once the quasi-harmonic approximation was utilized that the temperature-dependent shift became reproducible using ss-DFT. The combination of the quasi-harmonic approximation and the investigation into the character of the lowest terahertz mode revealed that the shift was most likely dominated by an unusually anharmonic hydrogen bond.

**Chapter 7** increases the size of the system studied to include an oligopeptide in the form of crystalline β-triglycine. β-triglycine is used as a benchmark system to evaluate the impact that different functional and basis set combinations have on the geometry optimization and harmonic vibrational frequencies of an oligopeptide. Successful modeling of an oligopeptide is one of the first steps necessary to developing a methodology capable of being scaled to include even larger biomolecular systems. It was found that while all functionals and basis sets examined provided general agreement with the experiments, the PBE0-D3 functional in combination with the VTZP basis set proved to be superior. In addition to demonstrating the value of the PBE0 hybrid

functional, this work highlights that the VTZP basis set shows great promise for use with large systems that require a hybrid functional to reach good chemical accuracy.

## 1.4 References

1.    Náray-Szabó, G.;  Oláh, J.; Krámos, B. Quantum Mechanical Modeling: A Tool for the Understanding of Enzyme Reactions. *Biomolecules* **2013,** *3* (3), 662-702.

2.    Liu, H.;  Elstner, M.;  Kaxiras, E.;  Frauenheim, T.;  Hermans, J.; Yang, W. Quantum Mechanics Simulation of Protein Dynamics on Long Timescale. *Proteins: Struct., Funct., Bioinf.* **2001,** *44* (4), 484-489.

3.    Georgescu, I. M.;  Ashhab, S.; Nori, F. Quantum Simulation. *Rev. Mod. Phys.* **2014,** *86* (1), 153.

4.    Pozzo, M.;  Davies, C.;  Gubbins, D.; Alfe, D. Thermal and Electrical Conductivity of Iron at Earth's Core Conditions. *Nature* **2012,** *485* (7398), 355-358.

5.    Orio, M.;  Pantazis, D. A.; Neese, F. Density Functional Theory. *Photosynth. Res.* **2009,** *102* (2), 443-453.

6.    Cirac, J. I.; Zoller, P. Goals and Opportunities in Quantum Simulation. *Nat. Phys.* **2012,** *8* (4), 264-266.

7.    van Mourik, T.;  Bühl, M.; Gaigeot, M.-P. Density Functional Theory Across Chemistry, Physics and Biology. *Philos. Trans. A Math Phys. Eng. Sci.* **2014,** *372* (2011), 20120488-20120488.

8.    Abramov, Y. A. QTAIM Application in Drug Development: Prediction of Relative Stability of Drug Polymorphs from Experimental Crystal Structures. *J. Phys. Chem. A* **2011,** *115* (45), 12809-12817.

9.    Wang, C.;  Rosbottom, I.;  Turner, T. D.;  Laing, S.;  Maloney, A. G. P.;  Sheikh, A. Y.;  Docherty, R.;  Yin, Q.; Roberts, K. J. Molecular, Solid-State and Surface Structures of

the Conformational Polymorphic Forms of Ritonavir in Relation to their Physicochemical Properties. *Pharm. Res.* **2021,** *38* (6), 971-990.

10.    Lewars, E. G. *Computational Chemistry: Introduction to the Theory and Applications of Molecular and Quantum Mechanics*, Springer: 2003.

11.    Ramachandran, K.; Deepa, G.; Namboori, K. *Computational Chemistry and Molecular Modeling: Principles and Applications*, Springer Science & Business Media: 2008.

12.    Aspuru-Guzik, A.; Atahan-Evrenk, S. *Prediction and Calculation of Crystal Structures: Methods and Applications*, Springer International Publishing 2014.

13.    Hofer, T. S.; de Visser, S. P. Editorial: Quantum Mechanical/Molecular Mechanical Approaches for the Investigation of Chemical Systems – Recent Developments and Advanced Applications. *Front. Chem.* **2018,** *6* (357).

14.    Ratcliff, L. E.; Mohr, S.; Huhs, G.; Deutsch, T.; Masella, M.; Genovese, L. Challenges in Large Scale Quantum Mechanical Calculations. *Wiley Interdiscip. Rev.: Comput. Mol. Sci.* **2017,** *7* (1), e1290.

15.    Yang, L.; Hood, R. Q.; Pask, J.; Klepeis, J. Large-scale Quantum Mechanical Simulations of High-Z Metals. *J. Comput.-Aided Mater. Des.* **2007,** *14* (3), 337-347.

16.    Schleder, G. R.; Padilha, A. C.; Acosta, C. M.; Costa, M.; Fazzio, A. From DFT to Machine Learning: Recent Approaches to Materials Science–A Review. *JPhys Mater.* **2019,** *2* (3), 032001.

17.    Prentice, J. C. A.; Aarons, J.; Womack, J. C.; Allen, A. E. A.; Andrinopoulos, L.; Anton, L.; Bell, R. A.; Bhandari, A.; Bramley, G. A.; Charlton, R. J.; et al. The ONETEP Linear-scaling Density Functional Theory Program. *J. Chem. Phys.* **2020,** *152* (17), 174111.

18.  Fox, S. J.;  Pittock, C.;  Fox, T.;  Tautermann, C. S.;  Malcolm, N.; Skylaris, C.-K. Electrostatic Embedding in Large-scale First Principles Quantum Mechanical Calculations on Biomolecules. *J. Chem. Phys.* **2011,** *135* (22), 224107.

19.  Dewar, M. J. S. Applications of Quantum Mechanical Molecular Models to Chemical Problems. Part 70. Quantum Mechanical Molecular Models. *J. Phys. Chem.* **1985,** *89* (11), 2145-2150.

20.  Li, K.;  Khanna, R.;  Zhang, J.;  Li, G.;  Li, H.;  Jiang, C.;  Sun, M.;  Wang, Z.;  Bu, Y.; Bouhadja, M.;  Liu, Z.; Barati, M. Determination of the Accuracy and Reliability of Molecular Dynamics Simulations in Sstimating the Melting Point of Iron: Roles of Interaction Potentials and Initial System Configurations. *J. Mol. Liq.* **2019,** *290*, 111204.

21.  Heo, L.; Feig, M. Experimental Accuracy in Protein Structure Refinement via Molecular Dynamics Simulations. *Proc Natl Acad Sci U S A* **2018,** *115* (52), 13276-13281.

22.  Chmiela, S.;  Sauceda, H. E.;  Müller, K.-R.; Tkatchenko, A. Towards Exact Molecular Dynamics Simulations with Machine-learned Force Fields. *Nat. Commun.* **2018,** *9* (1), 3887.

23.  Bash, P. A.;  Ho, L. L.;  MacKerell, A. D.;  Levine, D.; Hallstrom, P. Progress Toward Chemical Accuracy in the Computer Simulation of Condensed Phase Reactions. *Proc Natl Acad Sci U S A* **1996,** *93* (8), 3698-3703.

24.  Bogojeski, M.;  Vogt-Maranto, L.;  Tuckerman, M. E.;  Müller, K.-R.; Burke, K. Quantum Chemical Accuracy from Density Functional Approximations via Machine Learning. *Nat. Commun.* **2020,** *11* (1), 5223.

25. Aldeghi, M.; Heifetz, A.; Bodkin, M. J.; Knapp, S.; Biggin, P. C. Accurate Calculation of the Absolute Free Energy of Binding for Drug Molecules. *Chem. Sci.* **2016,** *7* (1), 207-218.

26. Cruz-Cabeza, A. J.; Reutzel-Edens, S. M.; Bernstein, J. Facts and Fictions About Polymorphism. *Chem. Soc. Rev.* **2015,** *44* (23), 8619-8635.

27. Stephenson, G. A.; Kendrick, J.; Wolfangel, C.; Leusen, F. J. J. Symmetry Breaking: Polymorphic Form Selection by Enantiomers of the Melatonin Agonist and Its Missing Polymorph. *Cryst. Growth Des.* **2012,** *12* (8), 3964-3976.

28. Wen, S.; Beran, G. J. O. Crystal Polymorphism in Oxalyl Dihydrazide: Is Empirical DFT-D Accurate Enough? *J. Chem. Theory Comput.* **2012,** *8* (8), 2698-2705.

29. Drużbicki, K.; Mielcarek, J.; Kiwilsza, A.; Toupet, L.; Collet, E.; Pajzderska, A.; Wąsicki, J. Computationally Assisted (Solid-State Density Functional Theory) Structural (X-ray) and Vibrational Spectroscopy (FT-IR, FT-RS, TDs-THz) Characterization of the Cardiovascular Drug Lacidipine. *Cryst. Growth Des.* **2015,** *15* (6), 2817-2830.

30. Lauro, G.; Das, P.; Riccio, R.; Reddy, D. S.; Bifulco, G. DFT/NMR Approach for the Configuration Assignment of Groups of Stereoisomers by the Combination and Comparison of Experimental and Predicted Sets of Data. *J. Org. Chem.* **2020,** *85* (5), 3297-3306.

31. Lejaeghere, K.; Van Speybroeck, V.; Van Oost, G.; Cottenier, S. Error Estimates for Solid-state Density-functional Theory Predictions: An Overview by Means of the Ground-state Elemental Crystals. *Crit. Rev. Solid State Mater. Sci.* **2014,** *39* (1), 1-24.

32. Korth, M.; Grimme, S. "Mindless" DFT Benchmarking. *J. Chem. Theory Comput.* **2009,** *5* (4), 993-1003.

33. Brorsen, K. R.; Yang, Y.; Pak, M. V.; Hammes-Schiffer, S. Is the Accuracy of Density Functional Theory for Atomization Energies and Densities in Bonding Regions Correlated? *J. Phys. Chem. Lett.* **2017,** *8* (9), 2076-2081.

34. Perdew, J. P.; Sun, J.; Garza, A. J.; Scuseria, G. E. Intensive Atomization Energy: Re-Thinking a Metric for Electronic Structure Theory Methods. *Z. Phys. Chem.* **2016,** *230* (5-7), 737-742.

35. Larkin, P. J.; Dabros, M.; Sarsfield, B.; Chan, E.; Carriere, J. T.; Smith, B. C. Polymorph Characterization of Active Pharmaceutical Ingredients (APIs) Using Low-Frequency Raman Spectroscopy. *Appl. Spectrosc.* **2014,** *68* (7), 758-776.

36. Parrott, E. P.; Zeitler, J. A. Terahertz Time-domain and Low-frequency Raman Spectroscopy of Organic Materials. *Appl. Spectrosc.* **2015,** *69* (1), 1-25.

37. Zeitler, J.; Taday, P.; Newnham, D.; Pepper, M.; Gordon, K.; Rades, T. Terahertz-Pulsed Spectroscopy and Imaging in Pharmaceutical Setting. *J. Pharm. Pharmacol.* **2007,** *59*, 209-23.

38. Walther, M.; Plochocka, P.; Fischer, B.; Helm, H.; Uhd Jepsen, P. Collective Vibrational Modes in Biological Bolecules Bnvestigated by Terahertz Time-domain Spectroscopy. *Biopolymers* **2002,** *67* (4-5), 310-313.

39. Zhang, W.; Maul, J.; Vulpe, D.; Moghadam, P. Z.; Fairen-Jimenez, D.; Mittleman, D. M.; Zeitler, J. A.; Erba, A.; Ruggiero, M. T. Probing the Mechanochemistry of Metal–Organic Frameworks with Low-Frequency Vibrational Spectroscopy. *J. Phys. Chem. C* **2018,** *122* (48), 27442-27450.

40. Drużbicki, K.; Pajzderska, A.; Chudoba, D.; Jenczyk, J.; Jarek, M.; Mielcarek, J.; Wąsicki, J. Elucidating the Structure of Ranitidine Hydrochloride Form II: Insights from

Solid-State Spectroscopy and Ab Initio Simulations. *Cryst. Growth Des.* **2018,** *18* (8), 4671-4681.

41.    Davis, M. P.;  Mohara, M.;  Shimura, K.;  Korter, T. M. Simulation and Assignment of the Terahertz Vibrational Spectra of Enalapril Maleate Cocrystal Polymorphs. *J. Phys. Chem. A* **2020,** *124* (47), 9793-9800.

42.    Bērziņš, K.;  Fraser-Miller, S. J.;  Gordon, K. C. Recent Advances in Low-Frequency Raman Spectroscopy for Pharmaceutical Applications. *Int. J. Pharm.* **2020**, 120034.

43.    Zhang, M.;  Hong, H.;  Lin, H.;  Shen, L.;  Yu, H.;  Ma, G.;  Chen, J.; Liao, B.-Q. Mechanistic Insights Into Alginate Fouling Caused by Calcium Ions Based on Terahertz Time-domain Spectra Analyses and DFT Calculations. *Water Res.* **2018,** *129*, 337-346.

44.    Lee, D.;  Cheon, H.;  Jeong, S.-Y.; Son, J.-H. Transformation of Terahertz Vibrational Modes of Cytosine Under Hydration. *Sci. Rep.* **2020,** *10* (1), 10271.

45.    Yamamoto, S.;  Morisawa, Y.;  Sato, H.;  Hoshina, H.; Ozaki, Y. Quantum Mechanical Interpretation of Intermolecular Vibrational Modes of Crystalline Poly-(R)-3-Hydroxybutyrate Observed in Low-Frequency Raman and Terahertz Spectra. *J. Phys. Chem. B* **2013,** *117* (7), 2180-2187.

46.    Carriere, J. T.; Havermeyer, F. Ultra-low Frequency Stokes and Anti-Stokes Raman Spectroscopy at 785nm with Volume Volographic Grating Filters. Proceedings of SPIE BiOS, San Francisco, SPIE: San Francisco, 2012.

47.    Rastogi, V.;  Palafox, M. A.;  Mittal, L.;  Peica, N.;  Kiefer, W.;  Lang, K.; Ojha, S. FTIR and FT-Raman Spectra and Density Functional Computations of the Vibrational Spectra, Molecular Geometry and Atomic Charges of the Biomolecule: 5-Bromouracil. *J. Raman Spectrosc.* **2007,** *38* (10), 1227-1241.

48.    Salahub, D. R.;  de la Lande, A.;  Goursot, A.;  Zhang, R.; Zhang, Y. Recent Progress in
       Density Functional Methodology for Biomolecular Modeling. *Applications of Density*
       *Functional Theory to Biological and Bioinorganic Chemistry* **2013**, 1-64.

49.    Lipiäinen, T.;  Fraser-Miller, S. J.;  Gordon, K. C.; Strachan, C. J. Direct Comparison of
       Low- and Mid-frequency Raman Spectroscopy for Quantitative Solid-state
       Pharmaceutical Analysis. *J. Pharm. Biomed. Anal.* **2018,** *149*, 343-350.

50.    Parr, R. G.; Yang, W. Density-Functional Theory of the Electronic Structure of
       Molecules. *Annual Review of Physical Chemistry* **1995,** *46* (1), 701-728.

51.    Szabo, A. S.; Ostlund, N. S. *Modern Quantum Chemistry: Introduction to Advanced*
       *Electronic Structure Theory*, Courier Corporation: 1996.

52.    Helgaker, T.;  Jorgensen, P.; Olsen, J. *Molecular Electronic-Structure Theory*, Wiley:
       2014.

53.    Baseden, K. A.; Tye, J. W. Introduction to Density Functional Theory: Calculations by
       Hand on the Helium Atom. *J. Chem. Educ.* **2014,** *91* (12), 2116-2123.

54.    Langhoff, S. *Quantum Mechanical Electronic Structure Calculations with Chemical*
       *Accuracy*, Springer Netherlands, 2012.

55.    Burke, K. Perspective on Density Functional Theory. *J. Chem. Phys.* **2012,** *136* (15),
       150901.

56.    Hasnip, P. J.;  Refson, K.;  Probert, M. I. J.;  Yates, J. R.;  Clark, S. J.; Pickard, C. J.
       Density Functional Theory in the Solid State. *Philos. Trans. R. Soc., A* **2014,** *372* (2011),
       20130270.

57.    Vener, M. V.;  Levina, E. O.;  Koloskov, O. A.;  Rykounov, A. A.;  Voronin, A. P.;
       Tsirelson, V. G. Evaluation of the Lattice Energy of the Two-Component Molecular

Crystals Using Solid-State Density Functional Theory. *Cryst. Growth Des.* **2014,** *14* (10), 4997-5003.

58. Neu, J.; Schmuttenmaer, C. A. Terahertz Spectroscopy and Density Functional Theory Investigation of the Dipeptide L-Carnosine. *J. Infrared, Millimeter, Terahertz Waves* **2020,** *41* (11), 1366-1377.

59. Verma, P.; Truhlar, D. G. Status and Challenges of Density Functional Theory. *Trends Chem.* **2020,** *2* (4), 302-318.

60. Vuckovic, S.; Levy, M.; Gori-Giorgi, P. Augmented Potential, Energy Densities, and Virial Relations in the Weak- and Strong-interaction Limits of DFT. *J. Chem. Phys.* **2017,** *147* (21), 214107.

61. Karamertzanis, P. G.; Day, G. M.; Welch, G. W. A.; Kendrick, J.; Leusen, F. J. J.; Neumann, M. A.; Price, S. L. Modeling the Interplay of Inter- and Intramolecular Hydrogen Bonding in Conformational Polymorphs. *J. Chem. Phys.* **2008,** *128* (24), 244708.

62. Presti, D.; Pedone, A.; Menziani, M. C.; Civalleri, B.; Maschio, L. Oxalyl Dihydrazide Polymorphism: A Periodic Dispersion-corrected DFT and MP2 Investigation. *CrystEngComm* **2014,** *16* (1), 102-109.

63. Sousa, S. F.; Fernandes, P. A.; Ramos, M. J. General Performance of Density Functionals. *J. Phys. Chem. A* **2007,** *111* (42), 10439-10452.

64. El-Azhary, A.; Suter, H. Comparison Between Optimized Geometries and Vibrational Frequencies Calculated by the DFT Methods. *J. Phys. Chem.* **1996,** *100* (37), 15056-15063.

65.    Plumley, J. A.; Dannenberg, J. A Comparison of the Behavior of Functional/Basis Set Combinations for Hydrogen-bonding in the Water Dimer with Emphasis on Basis Bet Superposition Error. *J. Comput. Chem.* **2011,** *32* (8), 1519-1527.

66.    Taylor, D. E.;  Ángyán, J. G.;  Galli, G.;  Zhang, C.;  Gygi, F.;  Hirao, K.;  Song, J. W.;  Rahul, K.;  Lilienfeld, O. A. v.;  Podeszwa, R.;  et al. Blind Test of Density-functional-based Methods on Intermolecular Interaction Energies. *J. Chem. Phys.* **2016,** *145* (12), 124105.

67.    Medvedev, M. G.;  Bushmarinov, I. S.;  Sun, J.;  Perdew, J. P.; Lyssenko, K. A. Density Functional Theory is Straying from the Path Toward the Exact Functional. *Science* **2017,** *355* (6320), 49.

68.    Banks, P.;  Burgess, L.; Ruggiero, M., The Necessity of Periodic Boundary Conditions for the Accurate Calculation of Crystalline Terahertz Spectra. ChemRxiv: 2020.

69.    Mazurek, A. H.;  Szeleszczuk, Ł.; Pisklak, D. M. Periodic DFT Calculations—Review of Applications in the Pharmaceutical Sciences. *Pharmaceutics* **2020,** *12* (5), 415.

70.    Grimme, S. Accurate Description of Van der Waals Complexes by Density Functional Theory Including Empirical Corrections. *J. Comput. Chem.* **2004,** *25* (12), 1463-1473.

71.    Van Troeye, B.;  Torrent, M.; Gonze, X. Interatomic Force Constants Including the DFT-D dispersion Contribution. *Phys. Rev. B* **2016,** *93* (14), 144304.

72.    Geatches, D.;  Rosbottom, I.;  Marchese Robinson, R. L.;  Byrne, P.;  Hasnip, P.;  Probert, M. I. J.;  Jochym, D.;  Maloney, A.; Roberts, K. J. Off-the-shelf DFT-DISPersion Methods: Are they now "on-trend" for Organic Molecular Crystals? *J. Chem. Phys.* **2019,** *151* (4), 044106.

73.     Ruggiero, M. T. Invited Review: Modern Methods for Accurately Simulating the Terahertz Spectra of Solids. *J. Infrared, Millimeter, Terahertz Waves* **2020**.

74.     Bawuah, P.; Zeitler, J. A. Advances in Terahertz Time-domain Spectroscopy of Pharmaceutical Solids: A Review. *TrAC, Trends Anal. Chem.* **2021,** *139*, 116272.

75.     Dovbeshko, G.; Berezhinsky, L. Low-frequency Vibrational Spectra of Some Amino Acids. *J. Mol. Struct.* **1998,** *450* (1), 121-128.

76.     Colaianni, S. E. M.; Nielsen, O. F. Low-frequency Raman spectroscopy. *J. Mol. Struct.* **1995,** *347*, 267-283.

77.     Zeitler, J. A.; Newnham, D. A.; Taday, P. F.; Threlfall, T. L.; Lancaster, R. W.; Berg, R. W.; Strachan, C. J.; Pepper, M.; Gordon, K. C.; Rades, T. Characterization of Temperature-induced Phase Transitions in Five Polymorphic Forms of Sulfathiazole by Terahertz Pulsed Spectroscopy and Differential Scanning Calorimetry. *J. Pharm. Sci.* **2006,** *95* (11), 2486-2498.

78.     Yang, L.; Guo, T.; Zhang, X.; Cao, S.; Ding, X. Toxic Chemical Compound Detection by Terahertz Spectroscopy: A Review. *Rev. Anal. Chem.* **2018,** *37* (3).

79.     Neu, J.; Stone, E. A.; Spies, J. A.; Storch, G.; Hatano, A. S.; Mercado, B. Q.; Miller, S. J.; Schmuttenmaer, C. A. Terahertz Spectroscopy of Tetrameric Peptides. *J. Phys. Chem. Lett.* **2019,** *10* (10), 2624-2628.

80.     Marlina, D.; Hoshina, H.; Ozaki, Y.; Sato, H. Crystallization and Crystalline Dynamics of Poly(3-hydroxybutyrate) / Poly(4-vinylphenol) Polymer Blends Studied by Low-frequency Vibrational Spectroscopy. *Polymer* **2019,** *181*, 121790.

81. Mori, S. K. T.; Shibata, T.; Shibata, T.; Kobayashi, Y. Broadband Terahertz Time-Domain and Low-Frequency Raman Spectroscopy of Crystalline and Glassy Pharmaceuticals. *Pharm. Anal. Acta* **2015,** *06* (08).

82. Kleist, E. M.; Korter, T. M. Quantitative Analysis of Minium and Vermilion Mixtures Using Low-Frequency Vibrational Spectroscopy. *Anal. Chem.* **2020,** *92*, 1211-1218.

83. Epp, J., X-ray diffraction (XRD) Techniques for Materials Characterization. In *Materials Characterization using Nondestructive Evaluation (NDE) Methods*, Elsevier, 2016; pp 81-124.

84. Zhang, H.; Lv, X.; Li, Y.; Wang, Y.; Li, J. P25-Graphene Composite as a High Performance Photocatalyst. *ACS Nano* **2010,** *4* (1), 380-386.

85. Ma, T.; Kapustin, E. A.; Yin, S. X.; Liang, L.; Zhou, Z.; Niu, J.; Li, L.-H.; Wang, Y.; Su, J.; Li, J.; Wang, X.; Wang, W. D.; Wang, W.; Sun, J.; Yaghi, O. M. Single-crystal X-ray Diffraction Structures of Covalent Organic Frameworks. *Science* **2018,** *361* (6397), 48-52.

86. Jovanovic, T.; Farid, R.; Friesner, R. A.; McDermott, A. E. Thermal Equilibrium of High- and Low-Spin Forms of Cytochrome P450 BM-3: Repositioning of the Substrate? *J. Am. Chem. Soc.* **2005,** *127* (39), 13548-13552.

87. West, A. R. *Solid State Chemistry and its Applications*, Wiley: 2014.

88. Dovesi, R.; Erba, A.; Orlando, R.; Zicovich-Wilson, C. M.; Civalleri, B.; Maschio, L.; Rérat, M.; Casassa, S.; Baima, J.; Salustro, S.; Kirtman, B. Quantum-mechanical Condensed Matter Simulations with CRYSTAL. *Wiley Interdiscip. Rev.: Comput. Mol. Sci.* **2018,** *8* (4), e1360.

# Chapter 2: Theoretical Foundations for the Characterization of Solids

## 2.1 Introduction

Every development that can be applied to a quantum model provides the opportunity for a more accurate chemical description.[1-3] What started as a way to model a single hydrogen atom has grown to predict physical properties and observables for systems as large as biomolecules, with simulations lending themselves to predicting vibrational spectra, electronic band gaps, and thermodynamic stability.[4-7] All the information needed to solve these problems lies in solving the wave function of a chemical system, the mathematical expression that encompasses the probability of a particle's quantum state.[8] In 1926, Erwin Schrödinger devised an equation capable of solving the wave function ($\Psi$) of a system that could be modified to include or exclude time-varying external forces.[9] The time-independent Schrödinger equation takes the succinct form seen in equation (2.1), where the energy ($E$), is an eigenvalue of the Hamiltonian ($H$, energy operator).[10]

$$\hat{H}\Psi = E\Psi \tag{2.1}$$

The above equation (2.1) has been used to solve the exact wave function of a single hydrogen atom, however, systems composed of many nuclei and electrons such as solids require a many-body solution.[11, 12] Solving the many-body problem of the time-independent Schrödinger equation begins with separating the total energy into its kinetic and potential energy components as seen in equation (2.2). This equation expresses the time-independent Schrödinger equation in terms of the electron coordinates, $r$, spanning the indices $i,j$ for the number of electrons ($N$) and

the nuclear coordinates, $R$, spanning the indices $I,J$ for the number of nuclei ($M$). Other variables

included in equation (2.2) include: $\hbar$, the reduced form of Planck's constant, $m_e$, the mass of an

electron, $M_I$ the nuclear mass, $e$, the charge of an electron, $\varepsilon_0$, the permittivity of a vacuum, $Z$, the

atomic number, and $\nabla^2$, the Laplacian operator defined in equation (2.3).

$$\left[ -\sum_i^N \frac{\hbar^2}{2m_e}\nabla_i^2 - \sum_I^M \frac{\hbar^2}{2M_I}\nabla_I^2 + \frac{1}{2}\sum_{i\neq j}^N \frac{e^2}{4\pi\varepsilon_0}\frac{1}{|r_i - r_j|} + \frac{1}{2}\sum_{I\neq J}^M \frac{e^2}{4\pi\varepsilon_0}\frac{Z_I Z_J}{|R_I - R_J|} \right.$$
$$\left. -\sum_{i,I}^{N,M} \frac{e^2}{4\pi\varepsilon_0}\frac{Z_I}{|r_i - R_I|} \right]\Psi = E_{tot}\Psi$$

(2.2)

$$\nabla^2 = \frac{\partial^2}{\partial x^2} + \frac{\partial^2}{\partial y^2} + \frac{\partial^2}{\partial z^2}$$

(2.3)

While equation (2.2) is quite large it is an *ab initio* solution as none of the variables are

empirically derived.[13] The lengthy expression for the Hamiltonian enclosed in the above brackets

can be reduced to a more approachable form seen in equation (2.4) by expressing the first two

terms as $T_e$ and $T_n$, to represent the kinetic energy of the electrons and nuclei, respectively. The

remaining three terms are expressed as $V_{e\text{-}e}$, $V_{n\text{-}n}$, and $V_{e\text{-}n}$, representing the Coulombic

interactions of electron-electron repulsion, nuclei-nuclei repulsion, and electron-nuclei attraction,

respectively.

$$\left[ \widehat{T_e} + \widehat{T_n} + \widehat{V_{e-e}} + \widehat{V_{n-n}} + \widehat{V_{e-n}} \right]\Psi = E_{tot}\Psi$$

(2.4)

It is the Born-Oppenheimer approximation that allows for the electronic and nuclear terms to be separated, as well as the terms $T_n$ and $V_{n\text{-}n}$ to be removed from further consideration due to the overwhelming mass difference between the nuclei and the electrons.[14]

While the exact wave function for the above equation can be solved for a single hydrogen atom, no exact solution has yet been obtained for a system containing more than a single electron, due to the electron-electron interactions causing multiple terms to be dependent upon one another. The most straightforward approximation to solving the multi-electron problem is to invoke the independent electron approximation, where electrons are treated as non-interacting particles, allowing the Hamiltonian to be separable for each electron. With the understanding that electrons do, in fact, interact with one another, the repulsive Coulombic term can begin to be reintroduced. To begin including electron-electron repulsion, the Hartree approximation can be used, applying the average potential felt by each electron to the entire system.[15-17] This decomposes what was once a problem with 3N dimensionality into N three-dimensional equations and replaces the $V_{e\text{-}e}$ term in equation (2.4) with the Hartree potential, $V_H$, and expresses the electron-electron repulsion in terms of electron density, $n(r)$.[18] While the Hartree approximation is a good starting point, it is only able to account for classical electrostatics and fails to include any quantum effects.

To account for the missing energy terms attributed to quantum effects, such as exchange and correlation energy, either wave function or density-based methods can be used with both approaches constructing a many-body wave function ($\Psi$) through a series of one-electron wave functions ($\psi$). Wave function-based methods, such as Hartree Fock, use a Slater determinant to construct the final wave function, while density-based methods, such as density functional theory, rely on the electron density in place of explicitly solving the wave function.[19, 20]

## 2.2 Density Functional Theory

At the heart of all density functional theory (DFT) calculations are the two theorems developed by Hohenberg and Kohn in 1964. The first states that the ground-state energy is a unique functional of the electron density, and the second states the variational principle, that the electron density that corresponds to the solution of the time-independent Schrödinger equation will be the one in which the total energy is minimized.[21] Only a single year after the Hohenberg-Kohn theorems were released, the Kohn-Sham equations were published, expressing the electron density using single-electron wave functions. These equations allowed the theorems established by Hohenberg and Kohn to be applied to chemical systems as seen in equation (2.5), where the first term ($\frac{-\hbar^2}{2m}\nabla^2$) is the electronic kinetic energy, $V(r)$ is the electron-nuclei interaction, $V_H(r)$ is the Hartree potential, and $V_{XC}(r)$ is the exchange-correlation potential for a position, $r$. The Hartree potential can be further defined in terms of electron density as shown in equation (2.6).

$$\left[\frac{-\hbar^2}{2m}\nabla^2 + V(r) + V_H(r) + V_{xc}(r)\right]\psi_i(r) = E_i\psi_i(r) \tag{2.5}$$

$$V_H(r) = e^2 \int \frac{n(r')}{|r-r'|}d^3r' \tag{2.6}$$

The exchange-correlation potential included in equation (2.5) accounts for the missing electron-electron repulsion and kinetic energy terms left out when using only a classical approach.[22, 23] It is this embracement of the quantum terms established by the exchange-correlation potential that differentiates the Kohn-Sham equations from the Hartree-Fock equations established at the end of section 2.1.[24]  While the inclusion of these additional terms makes for a more accurate

solution, the exact form of $V_{XC}$ is not known and must be approximated using an exchange-correlation functional. While the theory behind DFT is exact, without knowing the true form of $V_{XC}$, the equations can only be solved approximately.

## 2.2.1 Exchange-Correlation Functionals

The exchange-correlation potential ($V_{XC}$) is the functional derivative of the exchange-correlation energy, $E_{XC}$, with respect to the electron density, $n(r)$ as seen in equation (2.7).

$$V_{XC}(r) = \frac{\delta E_{XC}(r)}{\delta n(r)} \tag{2.7}$$

The exchange-correlation energy functional in the above equation can be considered as the summation of both the exchange and correlation energies. A series of functionals have been developed to approximate this unknown term using varying levels of complexity. Some of these functionals only include corrections to a single energy component, exchange, or correlation, while others have been built to include both terms. Commonly, two functionals are combined to account for both exchange and correlation energies with a well-known example of this concatenation being the BLYP functional, composed of the B exchange correction, and the LYP correlation correction. When naming functionals, acronyms corresponding to the last name of the authors who developed it has become common practice. For example, the PBE functional was developed by John Perdew, Kieron Burke, and Matthias Ernzerhof while the LYP functional was developed by Chengteh Lee, Weitao Yang, and Robert G. Parr.[25, 26]

Often, the classes of functionals are represented in reference to the Biblical story of Jacob's ladder, as climbing the rungs leads to heaven, or in the case of DFT, the true form of the

exchange-correlation term. The original DFT version of Jacob's ladder has 5 rungs, local spin density approximation (LSDA), generalized gradient approximation (GGA), meta-GGA, exact exchange and compatible correlation, and exact exchange and exact partial correlation.[27] **Figure 2-1** provides a graphical outline of the exchange-correlation rungs, as well as selected examples from each category.
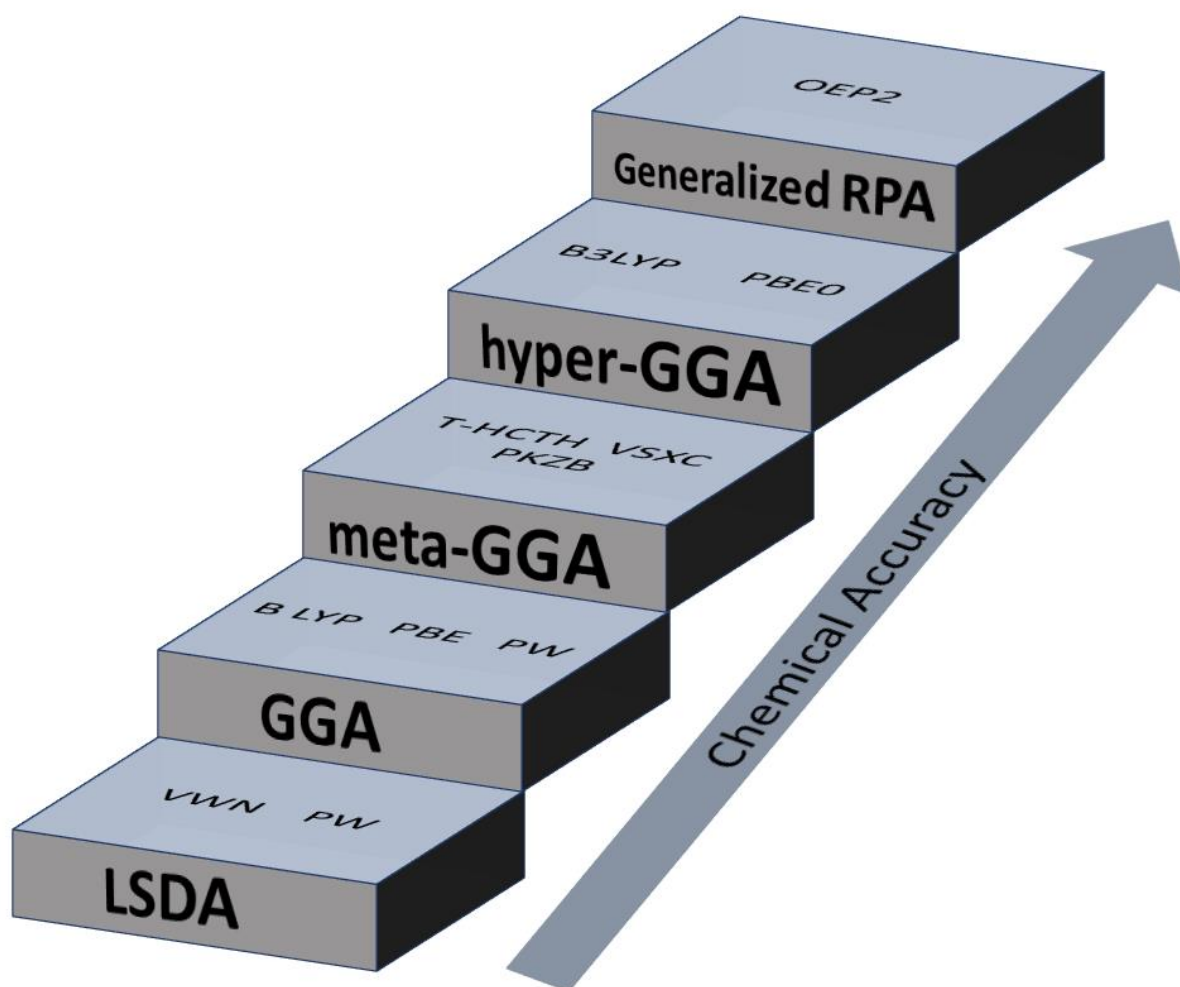
**Figure 2-1.** "Jacob's ladder" of exchange-correlation functionals, with complexity increasing with the height of the ladder.

Starting at the bottom of the ladder is the local density approximation (LDA), where the exchange-correlation energy is equal to that of a uniform electron gas and the contributions from spin density are equal.[28-32] In the case of open-shell systems, the spin-polarized formalism can be incorporated in the form of a local spin density approximation (LSDA).[33] Using the homogenous electron gas, the exact exchange energy can be derived, but approximations must still be used for the correlation energy.[34] While success has been found using this class of functional in systems where the electron density is a slowly varying function, the LDA and LSDA overestimate the

binding energy, and are also prone to underestimating the magnitude of the exchange energy while overestimating the magnitude of the correlation energy.[35]  For solids, this class of functional also often leads to an underestimation of the lattice constants.[36]

The next rung of the ladder is the generalized gradient approximation (GGA) method, adding in the first derivative of the electron density (the gradient, $\nabla$) to the LDA and LSDA methods. This approximation leads to improved internal and external structural components, but has a habit of overcorrecting the overbinding seen in the LDA.[37, 38] The two most popular exchange functionals utilizing a GGA are PBE and B, while PBE and LYP are the two most popular correlation functionals in this category.[39-41] The PBE functional has been modified to better predict the lattice dimensions of solids (PBEsol) however, it fails to replicate experimental atomization energies and has not worked well for the organic molecular crystals studied in this work.[42] Moving to the third rung of the ladder are the meta-GGA class of functionals. The etymology of the word meta means beyond, and so a meta-GGA expands upon the foundations of a GGA by including the kinetic energy density ($\tau$) or the Laplacian for electron density ($\nabla^2$).[43-47]

Hyper-GGAs, also known as hybrid functionals, make up the fourth rung of Jacob's ladder, and include a portion of the exact exchange of Hartree-Fock in the total exchange potential. The additional considerations of this category have led to improvements in modeling solid-state properties and justly have become very popular. Just as with a GGA, hybrid functionals incorporate both an exchange and correlation piece, producing well-represented approximations to the exchange-correlation potential. The B3LYP functional is the most commonly cited, and is a hybrid functional composed of 20% Hartree-Fock exchange, 8% Slater (LSDA) exchange, 72% B (GGA) exchange, 19% VWN1RPA (LSDA) correlation, and 81%

LYP correlation.[48, 49] Other common hybrid functionals include PBE0 (composed of 25 % Hartree-Fock exchange, 75% PBE exchange, and 100% PBE correlation) and HSE.[50, 51] While B3LYP is very popular it is not an *ab initio* approach like PBE0 due to the inclusion of empirically derived parameters. The chemical accuracy of hybrid functionals is quite advantageous, but due to computational expense, functionals in this class and above are often unreasonable for the use on solids.[52-63]

A well-known limitation of the functional classes previously described is the ability to account for the correlation in the form of long-range van der Waals interactions.[64-66] These dispersion interactions have been attempted to be corrected by using a series of methods including nonlocal vdW-DF, parameterized functionals, and semiclassical corrections (DFT-D).[67-70] The iterations of the dispersion correction developed by Grimme have gained traction with condensed phase calculations, with recent versions including the option to include the Becke-Johnson (BJ) damping function and the addition of the Axelrod-Teller-Muto three-body term (ABC).[71-78]

As one moves up the ladder, the complexity of the functional increases and it is often assumed that this leads to more accurate approximations. In fact, the appropriate choice of functional is dictated by the type of system and the properties being studied.[79, 80] Several reviews have been published focusing on the effect that functional choice has on computational calculations for a wide range of systems from gas-phase molecules to crystalline solids.[81-83]

## 2.2.2 Basis Sets

To begin solving the Kohn-Sham equations that include an exchange-correlation functional, an initial guess must be made for the electron density, *n(r)*. This guess begins a circular approach of solving for the electron density known as a self-consistent approach. Here, the initial guess is used to solve for the Hartree potential which is then used to solve the wave function. That wave function is then used to recalculate the electron density using equation (2.8), and the difference between the initial and calculated electron density are compared.[84]

$$n(r) = 2 \sum_i \psi_i^*(r)\psi_i(r) \tag{2.8}$$

The one-electron wave functions that are used to solve for the electron density are constructed using a basis set. Basis sets represent the molecular orbitals ($\psi$) using a sum of basis functions ($\varphi$) and molecular orbital expansion coefficients ($c$) as seen in equation (2.9).

$$\psi_i(r) = \sum_{\alpha=1}^{N} c_{\alpha i}\varphi_\alpha(r) \tag{2.9}$$

While ideally a basis set would utilize an infinite number of functions, finite basis sets have shown excellent results, with the key to a chemically accurate basis set being the flexibility to describe any scenario. These finite basis sets are generally broken down into two groups, plane waves and atomic orbitals, but recently developed real-space methods are showing great promise as well.[85]

Plane-wave basis sets are independent of atomic position, orthogonal, efficient, and inherently periodic, making them ideal for condensed phase calculations and resulting in their implementation in a multitude of DFT software packages.[86-90] The total number of plane waves

used is set through a cutoff value, with larger cutoff values including a larger number of plane waves, leading to increased accuracy, at the cost of computational resources.[91] Unfortunately, using plane waves to describe all the electrons is very computationally demanding as the core electrons require many basis functions for accurate modelling.[92-94]

Atomic orbital basis sets require fewer basis functions than their plane wave counterparts, with even the smallest localized basis sets yielding good results for a single atom. The atomic orbitals are most commonly described as Gaussian-type orbitals, with Slater-type orbitals and numerical atomic orbitals also available.[95-97] Slater-type orbitals do a good job of describing the actual shape of the atomic orbital, but they are computationally difficult. Instead, the Slater-type shape can be mimicked using a linear combination of Gaussian-type orbitals whose integrals can be evaluated analytically, leading to a reduction in computational expense.[98, 99] A single Gaussian function is better known as a primitive Gaussian-type orbital ($g$) and can be defined by equation (2.10), where $N$ is a normalization constant, $\alpha$ is the orbital exponent, $x$, $y$, and $z$ are the Cartesian coordinates of the nucleus, and the exponents $a$, $b$, and $c$ sum to define the angular momentum.

$$g(r) = Ne^{-\alpha r^2}x^a y^b z^c \qquad (2.10)$$

To continue reducing computational cost, a linear combination of primitive Gaussian-type orbitals can be used to describe a single basis function, known as a contraction. The contracted basis set introduces an additional term in the form of a contraction coefficient ($d$) expressing a basis function for an orbital as the summation of the primitive Gaussian-type functions established in equation (2.9) as seen in equation (2.11).

$$\varphi = \sum_n d_n g_n(\alpha, r) \tag{2.11}$$

The simplest form of a contracted basis set is a minimal basis set, containing only a single basis function for each atomic orbital. The most-well known minimal basis sets are the STO-nG family where the n represents the number of primitive gaussians per basis function, keeping in mind that a single basis function can be composed of multiple primitive Gaussians.[100, 101] However, this level of theory, does not always allow for the flexibility necessary, and so basis sets with two or three basis functions (double-$\zeta$ and triple -$\zeta$) per atomic orbital have been constructed.[102-104] In the case that even greater flexibility is necessary, polarization or diffuse functions can be incorporated to allow electrons to occupy orbitals that are not typically occupied in the ground-state.[105-108]

Not only are these larger basis sets typically more computationally accurate, they also tend to have a lower contribution of basis set superposition error (BSSE).[78, 109-111] BSSE is caused by the overlap of basis functions from nearby atoms, artificially increasing the interaction energy between atoms.[112] With the increased size comes computational penalties making large basis sets very expensive.[23] To compromise, the valence electrons (which participate in bonding) can be treated with a larger number of basis functions than their core counterparts, producing split-valence basis sets, which have proven to be very successful.[113-116] Just as with plane wave basis sets, effective core potentials can also be used in conjunction with atomic orbital basis sets to reduce the number of basis functions thereby reducing computational cost.[103, 104]

## 2.3 Solid-state Density Functional Theory

Solid-state density functional theory (ss-DFT) has proven to be particularly useful to pharmaceutical and industrial applications with calculations being used to determine energetic favorability, predict crystal packing arrangements, as well as understand the materials response to external strain.[117-124] While there are a number of computational choices available for performing ss-DFT calculations, they all share one thing in common: the implementation of periodic boundary conditions.[86, 87, 125-130] Crystalline solids are made up of organized, repeating units that extend across three dimensions and for the purposes of computational models, can be viewed as an infinitely repeating arrangement. To model a crystalline solid, the repeating units must first be reduced to a finite number of parameters. This can be done by exploiting the periodicity of a solid as the repeating units can be broken down into a series of crystallographic unit cells, the smallest description necessary to replicate the pattern seen in the bulk. The unit cell can also be further decomposed into a series of asymmetric units, where the symmetry elements inherent to the assigned space group are used to replicate the asymmetric unit throughout each unit cell. A visual representation of a solid from an asymmetric unit to crystalline solid is found in **Figure 2-2**.
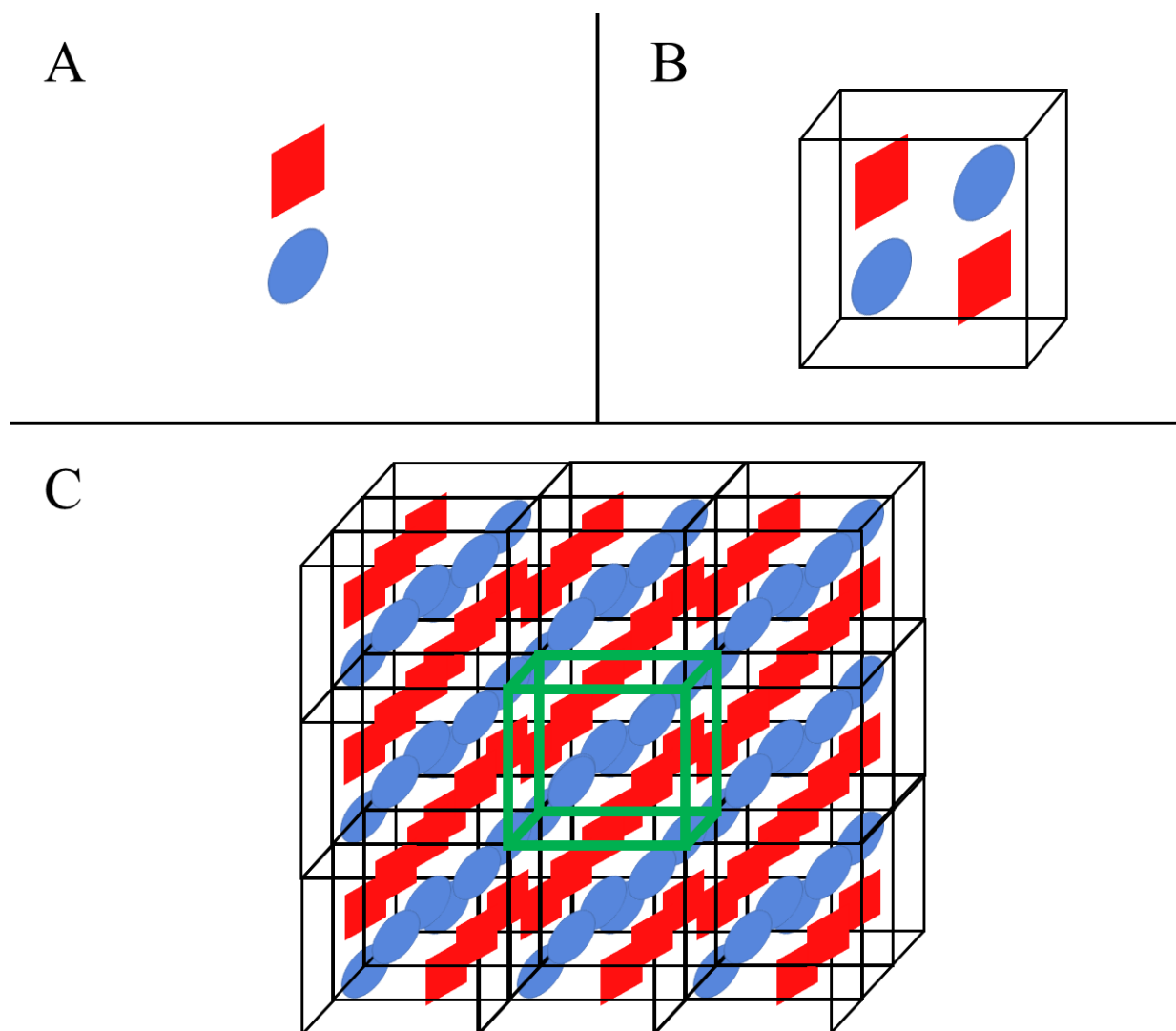
**Figure 2-2.** Visual representation of asymmetric unit (panel A), crystallographic unit cell (panel B), and three-dimensional packing (panel C).

To aid in efficiently modeling periodic solids, the conversion can be made from real to reciprocal space using Bloch's theorem established in equation (2.12), dictating that solutions to the Schrödinger equation for equivalent positions in the lattice will differ by a phase factor. Here, $k$ is the wave vector and $r$ is a position vector given the periodic relationship described in equation (2.13), where R is a lattice vector of the direct lattice.[131, 132]

$$\psi(r + R) = e^{ikR}\psi(r) \tag{2.12}$$

$$U(r + R) = U(r) \tag{2.13}$$

In reciprocal space (**k**-space) a single unit cell is defined as a Brillouin zone, with the smallest space that can be used to represent the bulk solid composing the first Brillouin zone. Considerations of the **k** vector can be restricted to the first Brillouin zone due to the combination of Bloch's theorem and periodic boundary conditions.[133-136] As mentioned in section 2.2.2, plane wave basis sets are inherently periodic, and are often used in reciprocal space calculations as they naturally fulfil the Bloch condition established in equation (2.12). To use the atom-centered basis sets described in section 2.2.2, they must first be transformed into a series of Bloch basis functions to satisfy the Bloch condition. This is done by expanding the Gaussian-type orbitals to include a phase component.[137-140]

A key difference between performing density functional theory calculations on a single molecule versus a crystalline material is in the interaction between neighboring molecules and unit cells.[141-144] This becomes obvious in the calculation of low-frequency ($< 200$ cm$^{-1}$) vibrational spectra, where this frequency range is governed by lattice vibrations, requiring that both intra- and intermolecular forces are accounted for in the model. Calculations performed on only a single molecule, or even a collection of supercells are not able to account for the weak

intermolecular interactions present throughout the crystalline solid and will fail to properly
reproduce the low-frequency region.

When calculating vibrational frequencies for the low-frequency region of solids, one
should always start from an optimized structure, ensuring that the geometry is at a minimum on
the potential energy surface. These optimizations are performed by varying the lattice
dimensions and atomic positions until a set of convergence criteria are met. It is this structure
that is then used to calculate vibrational frequencies by diagonalizing the mass-weighted Hessian
matrix and obtaining a set of eigenvalues. The elements of this matrix, $H$, are seen in equation
(2.12), where $m$ and $q$ represent the reduced mass and cartesian coordinates of atoms $i$ and $j$, with
respect to the energy obtained through a harmonic approximation.

$$H_{ij} = \frac{1}{\sqrt{m_i m_j}} \frac{\partial^2 E}{\partial q_i \partial q_j} \tag{2.12}$$

The second order partial derivatives of energy seen in equation (2.12) with respect to atomic
motion can either be solved analytically or numerically, with the numerical method proving to be
more common.[145] Using the numerical finite difference of the gradient, each atom is displaced by
a given distance ($\Delta$) for each cartesian direction using either a one- or two-point method as seen
in equation (2.13) and (2.14), respectively.[146-148]

$$\frac{\partial^2 E}{\partial q_i \partial q_j} = \frac{\frac{\partial}{\partial q_i} E(q_j + \Delta) - \frac{\partial}{\partial q_i} E(q_j)}{\Delta} \tag{2.13}$$

$$\frac{\partial^2 E}{\partial q_i \partial q_j} = \frac{\frac{\partial}{\partial q_i} E(q_j + \Delta) - \frac{\partial}{\partial q_i} E(q_j - \Delta)}{2\Delta} \tag{2.14}$$

Some ss-DFT software codes have even implemented anharmonic corrections, such as, the quasi-harmonic approximation (QHA), the vibrational self-consistent field theory (VSCF) and the self-consistent *ab initio* lattice dynamics (SCAILD) method to produce more accurate models, however, they come with extensive computational costs.[149-155] To calculate the associated intensity with each vibrational frequency a number of approaches have been developed. For infrared-active vibrations the intensity is related to the derivative of the dipole moment with respect to the atomic coordinates, while the intensity of Raman-active vibrations is solved through the derivative of the polarizability tensor with respect to the atomic coordinates.[156-159] The combination of predicted frequencies and intensities has been used to assign the calculated frequencies to those observed experimentally and from here, those assignments have been used to gain invaluable insight into the intermolecular forces governing crystalline solids.[160, 161]

## 2.4 References

1.     Schleder, G. R.;  Padilha, A. C.;  Acosta, C. M.;  Costa, M.; Fazzio, A. From DFT to Machine Learning: Recent Approaches to Materials Science–A Review. *JPhys Mater.* **2019,** *2* (3), 032001.

2.     Koch, W.; Holthausen, M. C. *A Chemist's Guide to Density Functional Theory*, Wiley: 2015.

3.      Parr, R. G.; Yang, W. Density-Functional Theory of the Electronic Structure of Molecules. *Annu. Rev. Phys. Chem.* **1995,** *46* (1), 701-728.

4.     Ramachandran, K.;  Deepa, G.; Namboori, K. *Computational Chemistry and Molecular Modeling: Principles and Applications*, Springer Science & Business Media: 2008.

5.     Riley, K. E.;  Op't Holt, B. T.; Merz, K. M. Critical Assessment of the Performance of Density Functional Methods for Several Atomic and Molecular Properties. *J. Chem. Theory Comput.* **2007,** *3* (2), 407-433.

6.     Martin, R. M. *Electronic Structure : Basic Theory and Practical Methods*, Cambridge University Press: Cambridge, UK, 2008.

7.     Hasnip, P. J.;  Refson, K.;  Probert, M. I. J.;  Yates, J. R.;  Clark, S. J.; Pickard, C. J. Density Functional Theory in the Solid State. *Philos. Trans. R. Soc., A* **2014,** *372* (2011), 20130270.

8.     Young, D. *Computational Chemistry: A Practical Guide for Applying Techniques to Real World Problems*, John Wiley & Sons: 2004.

9.     Schrödinger, E. Quantisierung als Eigenwertproblem. *Ann. Phys.* **1926,** *384* (4), 361-376.

10.    Thakkar, A. J. *Quantum Chemistry (Second Edition)*, Morgan & Claypool Publishers: 2017.

11.    Schrödinger, E. An Undulatory Theory of the Mechanics of Atoms and Molecules. *Phys. Rev.* **1926,** *28* (6), 1049-1070.

12.    Lewars, E. *Computational Chemistry*, Springer: 2003.

13.    Giustino, F. *Materials Modelling using Density Functional Theory: Properties and Predictions*, 1st ed.; Oxford University Press: Oxford, 2014.

14.    Born, M.; Oppenheimer, R. Zur Quantentheorie der Molekeln. *Ann. Phys.* **1927,** *389* (20), 457-484.

15.    Hartree, D. R. The Wave Mechanics of an Atom with a Non-Coulomb Central Field. I. Theory and Methods. *Proc. Cambridge Philos. Soc.* **1928,** *24*, 89-110.

16.    Hartree, D. R. The Wave Mechanics of an Atom with a Non-Coulomb Central Field. II. Some Results and Discussion. *Proc. Cambridge Philos. Soc.* **1928,** *24*, 111-32.

17.    Hartree, D. R. The Wave Mechanics of an Atom with a Non-Coulomb Central Field. III. Term Values and Intensities in Series in Optical Spectra. *Proc. Cambridge Philos. Soc.* **1928,** *24* (Pt. 3), 426-37.

18.    Seminario, J. M.; Politzer, P. *Modern Density Functional Theory: A Tool for Chemistry*, Elsevier: New York;Amsterdam;, 1995.

19.     Kohanoff, J. *Electronic Structure Calculations for Solids and Molecules: Theory and Computational Methods*, Cambridge University Press: Cambridge, UK;New York;, 2006.

20.     Strinati, G. C., Hartree and Hartree–Fock Methods in Electronic Structure. In *Encyclopedia of Condensed Matter Physics*, Bassani, F.;  Liedl, G. L.; Wyder, P., Eds. Elsevier, Oxford, 2005; pp 311-318.

21.    Hohenberg, P.; Kohn, W. Inhomogeneous electron gas. *Physical review* **1964,** *136* (3B), B864.

22. Kohn, W.; Sham, L. J. Self-consistent Equations Including Exchange and Correlation Effects. *Phys. Rev.* **1965,** *140* (4A), A1133-A1138.

23. Cramer, C. J. *Essentials of Computational Chemistry: Theories and Models*, 2. Aufl. ed.; Wiley: New York, 2005.

24. March, N. H.; Ter Haar, D. *Self-Consistent Fields in Atoms: Hartree and Thomas-Fermi Atoms*, Elsevier Science & Technology: Kent, 2013.

25. Lee, C.; Yang, W.; Parr, R. G. Development of the Colle-Salvetti Correlation-energy Formula into a Functional of the Electron Density. *Phys. Rev. B* **1988,** *37* (2), 785-789.

26. Perdew, J. P.; Burke, K.; Ernzerhof, M. Generalized Gradient Approximation Made Simple. *Phys. Rev. Lett.* **1996,** *77* (18), 3865-3868.

27. Perdew, J. P.; Schmidt, K. Jacob's Ladder of Density Functional Approximations for the Exchange-Correlation Energy. *AIP Conference Proceedings* **2001,** *577* (1), 1-20.

28. Hohenberg, P.; Kohn, W. Inhomogeneous Electron Gas. *Phys. Rev.* **1964,** *136* (3B), B864-B871.

29. Vosko, S. H.; Wilk, L.; Nusair, M. Accurate Spin-dependent Electron Liquid Correlation Energies for Local Spin Density Calculations: A Critical Analysis. *Can. J. Phys.* **1980,** *58* (8), 1200-1211.

30. Perdew, J. P.; Wang, Y. Accurate and Simple Analytic Representation of the Electron-gas Correlation Energy. *Phys. Rev. B* **1992,** *45* (23), 13244-13249.

31. Perdew, J. P.; Zunger, A. Self-interaction Correction to Density-functional Approximations for Many-electron Systems. *Phys. Rev. B* **1981,** *23* (10), 5048-5079.

32. Barth, U. v.; Hedin, L. A Local Exchange-correlation Potential for the Spin Polarized Case. i. *J. Phys. C: Solid State Phys.* **1972,** *5* (13), 1629-1642.

33.     Gunnarsson, O.; Lundqvist, B. I. Exchange and Correlation in Atoms, Molecules, and Solids by the Spin-density-functional Formalism. *Phys. Rev. B* **1976,** *13* (10), 4274-4298.

34.     Dirac, P. A. M. Note on Exchange Phenomena in the Thomas Atom. *Math. Proc. Cambridge Philos. Soc.* **1930,** *26* (3), 376-385.

35.      Zunger, A.;  Perdew, J. P.; Oliver, G. L. A Self-interaction Corrected Approach to Many-electron Systems: Beyond the Local Spin Density Approximation. *Solid State Commun.* **1980,** *34* (12), 933-936.

36.     Haas, P.;  Tran, F.; Blaha, P. Calculation of the Lattice Constant of Solids with Semilocal Functionals. *Phys. Rev. B* **2009,** *79* (8), 085104.

37.     Zupan, A.;  Burke, K.;  Ernzerhof, M.; Perdew, J. P. Distributions and Averages of Electron Density Parameters: Explaining the Effects of Gradient Corrections. *J. Chem. Phys.* **1997,** *106* (24), 10184-10193.

38.     Perdew, J. P.;  Chevary, J. A.;  Vosko, S. H.;  Jackson, K. A.;  Pederson, M. R.;  Singh, D. J.; Fiolhais, C. Atoms, Molecules, Solids, and Surfaces: Applications of the Generalized Gradient Approximation for Exchange and Correlation. *Phys. Rev. B* **1992,** *46* (11), 6671-6687.

39.      Perdew, J. P.;  Burke, K.; Ernzerhof, M. Generalized gradient approximation made simple. *Phys. Rev. Lett.* **1996,** *77* (18), 3865.

40.      Becke, A. D. Density-functional Exchange-energy Approximation with Correct Asymptotic Behavior. *Phys. Rev. A* **1988,** *38* (6), 3098-3100.

41.      Lee, C.;  Yang, W.; Parr, R. G. Development of the Colle-Salvetti correlation-energy formula into a functional of the electron density. *Physical review B* **1988,** *37* (2), 785.

42.    Perdew, J. P.; Ruzsinszky, A.; Csonka, G. I.; Vydrov, O. A.; Scuseria, G. E.; Constantin, L. A.; Zhou, X.; Burke, K. Restoring the Density-Gradient Expansion for Exchange in Solids and Surfaces. *Phys. Rev. Lett.* **2008,** *100* (13), 136406.

43.    Kurth, S.; Perdew, J. P.; Blaha, P. Molecular and Solid-state Tests of Density Functional Approximations: LSD, GGAs, and Meta-GGAs. *Int. J. Quantum Chem.* **1999,** *75* (4-5), 889-909.

44.    Tao, J.; Perdew, J. P.; Staroverov, V. N.; Scuseria, G. E. Climbing the Density Functional Ladder: Nonempirical Meta--Generalized Gradient Approximation Designed for Molecules and Solids. *Phys. Rev. Lett.* **2003,** *91* (14), 146401.

45.    Perdew, J. P.; Kurth, S.; Zupan, A.; Blaha, P. Accurate Density Functional with Correct Formal Properties: A Step Beyond the Generalized Gradient Approximation. *Phys. Rev. Lett.* **1999,** *82* (12), 2544-2547.

46.    Zhao, Y.; Truhlar, D. G. A New Local Density Functional for Main-group Thermochemistry, Transition Metal Bonding, Thermochemical Kinetics, and Noncovalent Interactions. *J. Chem. Phys.* **2006,** *125* (19), 194101.

47.    Sun, J.; Ruzsinszky, A.; Perdew, J. P. Strongly Constrained and Appropriately Normed Semilocal Density Functional. *Phys. Rev. Lett.* **2015,** *115* (3), 036402.

48.    Becke, A. D. A New Mixing of Hartree–Fock and Local Density-functional Theories. *J. Chem. Phys.* **1993,** *98* (2), 1372-1377.

49.    Stephens, P. J.; Devlin, F. J.; Chabalowski, C. F.; Frisch, M. J. Ab initio calculation of vibrational absorption and circular dichroism spectra using density functional force fields. *The Journal of physical chemistry* **1994,** *98* (45), 11623-11627.

50. Adamo, C.; Barone, V. Toward Reliable Density Functional Methods Without Adjustable Parameters: The PBE0 Model. *J. Chem. Phys.* **1999,** *110* (13), 6158-6170.

51. Heyd, J.; Scuseria, G. E.; Ernzerhof, M. Hybrid Functionals Based on a Screened Coulomb Potential. *Journal of Chemical Physics* **2003,** *118* (18), 8207-8215.

52. Simón, L.; Goodman, J. M. How Reliable are DFT Transition Structures? Comparison of GGA, Hybrid-meta-GGA and Meta-GGA functionals. *Org. Biomol. Chem.* **2011,** *9* (3), 689-700.

53. Wang, Y.; Verma, P.; Jin, X.; Truhlar, D. G.; He, X. Revised M06 Density Functional for Main-group and Transition-metal Chemistry. *Proc Natl Acad Sci U S A* **2018,** *115* (41), 10257-10262.

54. Zhao, Y.; Schultz, N. E.; Truhlar, D. G. Exchange-correlation Functional with Broad Accuracy for Metallic and Nonmetallic Compounds, Kinetics, and Noncovalent Interactions. *J. Chem. Phys.* **2005,** *123* (16), 161103.

55. Yanai, T.; Tew, D. P.; Handy, N. C. A New Hybrid Exchange–correlation Functional using the Coulomb-attenuating Method (CAM-B3LYP). *Chem. Phys. Lett.* **2004,** *393* (1), 51-57.

56. Brémond, É.; Pérez-Jiménez, Á. J.; Sancho-García, J. C.; Adamo, C. Range-separated Hybrid Density Functionals Made Simple. *J. Chem. Phys.* **2019,** *150* (20), 201102.

57. Chai, J.-D.; Head-Gordon, M. Systematic Pptimization of Long-range Corrected Hybrid Density Functionals. *J. Chem. Phys.* **2008,** *128* (8), 084106.

58. Leininger, T.; Stoll, H.; Werner, H.-J.; Savin, A. Combining Long-range Configuration Interaction with Short-range Density Functionals. *Chem. Phys. Lett.* **1997,** *275* (3), 151-160.

59. Yan, Z.; Perdew, J. P.; Kurth, S. Density Functional for Short-range Correlation: Accuracy of the Random-phase Approximation for Isoelectronic Energy Changes. *Phys. Rev. B* **2000,** *61* (24), 16430-16439.

60. Ren, X.; Rinke, P.; Joas, C.; Scheffler, M. Random-phase Approximation and its Applications in Computational Chemistry and Materials Science. *J. Mater. Sci.* **2012,** *47* (21), 7447-7471.

61. Grabowski, I.; Hirata, S.; Ivanov, S.; Bartlett, R. J. Ab initio Density Functional Theory: OEP-MBPT(2). A New Orbital-dependent Correlation Functional. *J. Chem. Phys.* **2002,** *116* (11), 4415-4425.

62. Bartlett, R. J.; Grabowski, I.; Hirata, S.; Ivanov, S. The Exchange-correlation Potential in ab initio Density Functional Theory. *J. Chem. Phys.* **2005,** *122* (3), 034104.

63. Dobson, J. F.; Wang, J. Successful Test of a Seamless van der Waals Density Functional. *Phys. Rev. Lett.* **1999,** *82* (10), 2123-2126.

64. Kristyán, S.; Pulay, P. Can (Semi)Local Density Functional Theory Account for the London Dispersion Forces? *Chem. Phys. Lett.* **1994,** *229* (3), 175-180.

65. Hobza, P.; šponer, J.; Reschel, T. Density Functional Theory and Molecular Clusters. *J. Comput. Chem.* **1995,** *16* (11), 1315-1325.

66. Burke, K. Perspective on Density Functional Theory. *J. Chem. Phys.* **2012,** *136* (15), 150901.

67. Dion, M.; Rydberg, H.; Schröder, E.; Langreth, D. C.; Lundqvist, B. I. Van der Waals Density Functional for General Geometries. *Phys. Rev. Lett.* **2004,** *92* (24), 246401.

68. Zhao, Y.; Truhlar, D. G. Density Functionals with Broad Applicability in Chemistry. *Acc. Chem. Res.* **2008,** *41* (2), 157-167.

69.    Grimme, S. Accurate Description of Van der Waals Complexes by Density Functional Theory Including Empirical Corrections. *J. Comput. Chem.* **2004,** *25* (12), 1463-1473.

70.    Grimme, S. Density Functional Theory with London Dispersion Corrections. *Wiley Interdiscip. Rev.: Comput. Mol. Sci.* **2011,** *1* (2), 211-228.

71.    Axilrod, B. M.; Teller, E. Interaction of the Van der Waals Type Between Three Atoms. *J. Chem. Phys.* **1943,** *11* (6), 299-300.

72    . Johnson, E. R.; Becke, A. D. A Post-Hartree-Fock Model of Intermolecular Interactions: Inclusion of Higher-order Corrections. *J. Chem. Phys.* **2006,** *124* (17), 174104.

73.    Grimme, S.; Ehrlich, S.; Goerigk, L. Effect of the Damping Function in Dispersion Corrected Density Functional Theory. *J. Comput. Chem.* **2011,** *32* (7), 1456-1465.

74.    Moellmann, J.; Grimme, S. DFT-D3 Study of Some Molecular Crystals. *J. Phys. Chem. C* **2014,** *118* (14), 7615-7621.

75.    Caldeweyher, E.; Bannwarth, C.; Grimme, S. Extension of the D3 Dispersion Coefficient Model. *J. Chem. Phys.* **2017,** *147* (3), 034112.

76.    Caldeweyher, E.; Ehlert, S.; Hansen, A.; Neugebauer, H.; Spicher, S.; Bannwarth, C.; Grimme, S. A Generally Applicable Atomic-charge Dependent London Dispersion Correction. *J. Chem. Phys.* **2019,** *150* (15), 154122.

77.    Caldeweyher, E.; Mewes, J.-M.; Ehlert, S.; Grimme, S. Extension and Evaluation of the D4 London-dispersion Model for Periodic Systems. *Phys. Chem. Chem. Phys.* **2020,** *22* (16), 8499-8512.

78.    Sancho-García, J. C.; Pérez-Jiménez, A. J.; Olivier, Y. Determining the Cohesive Energy of Coronene by Dispersion-corrected DFT Methods: Periodic Boundary Conditions vs. Molecular Pairs. *J. Chem. Phys.* **2015,** *142* (5), 054702.

79.     Jensen, F. *Introduction to Computational Chemistry*, 2nd ed.; John Wiley & Sons: Chichester, England;Hoboken, NJ;, 2007.

80.     Hait, D.;  Liang, Y. H.; Head-Gordon, M. Too big, Too Small, or Just Right? A Benchmark Assessment of Density Functional Theory for Predicting the Spatial Extent of the Electron Density of Small Chemical Systems. *J. Chem. Phys.* **2021,** *154* (7), 074109.

81.     Sousa, S. F.;  Fernandes, P. A.; Ramos, M. J. General Performance of Density Functionals. *J. Phys. Chem. A* **2007,** *111* (42), 10439-10452.

82.     Vega, L.;  Ruvireta, J.;  Viñes, F.; Illas, F. Jacob's Ladder as Sketched by Escher: Assessing the Performance of Broadly Used Density Functionals on Transition Metal Surface Properties. *J. Chem. Theory Comput.* **2018,** *14* (1), 395-403.

83.     Mardirossian, N.; Head-Gordon, M. Thirty Years of Density Functional Theory in Computational Chemistry: An Overview and Extensive Assessment of 200 Density Functionals. *Mol. Phys.* **2017,** *115* (19), 2315-2372.

84.     Sholl, D.; Steckel, J. A. *Density Functional Theory: A Practical Introduction*, 1. Aufl. ed.; Wiley-Interscience: Hoboken, 2009.

85.     Beck, T. L. Real-space Mesh Techniques in Density-functional Theory. *Rev. Mod. Phys.* **2000,** *72* (4), 1041-1080.

86.     Clark, S. J.;  Segall, M. D.;  Pickard, C. J.;  Hasnip, P. J.;  Probert, M. J.;  Refson, K.; Payne, M. C. First principles Methods using CASTEP. *Z. Krystallog.* **2005,** *220* (5-6), 567-570.

87.     Gonze, X.;  Amadon, B.;  Antonius, G.;  Arnardi, F.;  Baguet, L.;  Beuken, J.-M.; Bieder, J.;  Bottin, F.;  Bouchet, J.;  Bousquet, E.; et al. The Abinitproject: Impact, Environment and Recent developments. *Comput. Phys. Commun.* **2020,** *248*, 107042.

88. Kresse, G.; Furthmüller, J. Efficient Iterative Schemes for ab initio Total-energy Calculations using a Plane-wave Basis Set. *Phys. Rev. B* **1996,** *54* (16), 11169-11186.

89. Valiev, M.; Bylaska, E. J.; Govind, N.; Kowalski, K.; Straatsma, T. P.; Van Dam, H. J. J.; Wang, D.; Nieplocha, J.; Apra, E.; Windus, T. L.; de Jong, W. A. NWChem: A Comprehensive and Scalable Open-source Solution for Large Scale Molecular Simulations. *Comput. Phys. Commun.* **2010,** *181* (9), 1477-1489.

90. Marx, D.; Hutter, J. *Ab Initio Molecular Dynamics: Basic Theory and Advanced Methods* Cambridge University Press: New York, NY, 2009.

91 Payne, M. C.; Teter, M. P.; Allan, D. C.; Arias, T. A.; Joannopoulos, J. D. Iterative Minimization Techniques for ab initio Total-energy Calculations: Molecular Dynamics and Conjugate Gradients. *Rev. Mod. Phys.* **1992,** *64* (4), 1045-1097.

92. von Barth, U.; Gelatt, C. D. Validity of the Frozen-core Approximation and Pseudopotential Theory for Cohesive Energy Calculations. *Phys. Rev. B* **1980,** *21* (6), 2222-2228.

93. Hamann, D. R. Semiconductor Charge Densities with Hard-Core and Soft-Core Pseudopotentials. *Phys. Rev. Lett.* **1979,** *42* (10), 662-665.

94. Vanderbilt, D. Soft Self-consistent Pseudopotentials in a Generalized Eigenvalue Formalism. *Phys. Rev. B* **1990,** *41* (11), 7892-7895.

95. Slater, J. C. Atomic Shielding Constants. *Phys. Rev.* **1930,** *36* (1), 57-64.

96. Delley, B. An All-electron Numerical Method for Solving the Local Density Functional for Polyatomic Molecules. *J. Chem. Phys.* **1990,** *92* (1), 508-517.

97. Huzinaga, S. Basis Sets for Molecular Calculations. *Comput. Phys. Rep.* **1985,** *2* (6), 281-339.

98.    Boys, S. F.; Egerton, A. C. Electronic Wave Functions - I. A General Method of Calculation for the Stationary States of any Molecular System. *Proceedings of the Royal Society of London. Series A. Mathematical and Physical Sciences* **1950,** *200* (1063), 542-554.

99.    Huzinaga, S. Gaussian-Type Functions for Polyatomic Systems. I. *J. Chem. Phys.* **1965,** *42* (4), 1293-1302.

100.    Hehre, W. J.;  Stewart, R. F.; Pople, J. A. Self-Consistent Molecular-Orbital Methods. I. Use of Gaussian Expansions of Slater-Type Atomic Orbitals. *Journal of Chemical Physics* **1969,** *51* (6), 2657-2664.

101.    Hehre, W. J.;  Ditchfield, R.;  Stewart, R. F.; Pople, J. A. Self-Consistent Molecular Orbital Methods. IV. Use of Gaussian Expansions of Slater-Type Orbitals. Extension to Second-Row Molecules. *J. Chem. Phys.* **1970,** *52* (5), 2769-2773.

102.    McLean, A. D.; Chandler, G. S. Contracted Gaussian Basis Sets for Molecular Calculations. I. Second Row Atoms, Z=11–18. *J. Chem. Phys.* **1980,** *72* (10), 5639-5648.

103.    Pacios, L. F.; Christiansen, P. A. Ab initio Relativistic Effective Potentials with Spin-orbit Operators. I. Li through Ar. *J. Chem. Phys.* **1985,** *82* (6), 2664-2671.

104.    Hay, P. J.; Wadt, W. R. Ab initio Effective Core Potentials for Molecular Calculations. Potentials for the Transition Metal Atoms Sc to Hg. *J. Chem. Phys.* **1985,** *82* (1), 270-283.

105.    Francl, M. M.;  Pietro, W. J.;  Hehre, W. J.;  Binkley, J. S.;  Gordon, M. S.;  DeFrees, D. J.; Pople, J. A. Self-consistent Molecular Orbital Methods. XXIII. A Polarization-type Basis Set for Second-row Elements. *J. Chem. Phys.* **1982,** *77* (7), 3654-3665.

106. Hariharan, P. C.; Pople, J. A. The Influence of Polarization Functions on Molecular Orbital Hydrogenation Energies. *Theoretica chimica acta* **1973,** *28* (3), 213-222.

107. Spitznagel, G. W.; Clark, T.; Chandrasekhar, J.; Schleyer, P. V. R. Stabilization of Methyl Anions by First-row Substituents. The Superiority of Diffuse Function-augmented Basis Sets for Anion Calculations. *J. Comput. Chem.* **1982,** *3* (3), 363-371.

108. Jr., T. H. D. Gaussian Basis Sets for use in Correlated Molecular Calculations. I. The Atoms Boron through Neon and Hydrogen. *J. Chem. Phys.* **1989,** *90* (2), 1007-1023.

109. Schwenke, D. W.; Truhlar, D. G. Systematic Study of Basis Set Superposition Errors in the Calculated Interaction Energy of Two HF Molecules. *J. Chem. Phys.* **1985,** *82* (5), 2418-2426.

110. Sancho-García, J. C.; Pérez-Jiménez, A. J.; Olivier, Y. Determining the Cohesive Energy of Coronene by Dispersion-corrected DFT Methods: Periodic Boundary Conditions vs. Molecular Pairs. *J. Chem. Phys.* **2015,** *142* (5), 054702.

111. Boys, S. F.; Bernardi, F. The Calculation of Small Molecular Interactions by the Differences of Separate Total Energies. Some Procedures with Reduced Errors. *Mol. Phys.* **1970,** *19* (4), 553-566.

112. van Duijneveldt, F. B.; van Duijneveldt-van de Rijdt, J. G. C. M.; van Lenthe, J. H. State of the Art in Counterpoise Theory. *Chem. Rev.* **1994,** *94* (7), 1873-1885.

113. Mayer, I.; Turi, L. An Analytical Investigation into the BSSE Problem. *J. Mol. Struct.: THEOCHEM* **1991,** *227*, 43-65.

114. Binkley, J. S.; Pople, J. A.; Hehre, W. J. Self-consistent Molecular Orbital Methods. 21. Small Split-valence Basis Sets for First-row Elements. *J. Am. Chem. Soc.* **1980,** *102* (3), 939-947.

115.   Gordon, M. S.;  Binkley, J. S.;  Pople, J. A.;  Pietro, W. J.; Hehre, W. J. Self-consistent Molecular-orbital Methods. 22. Small Split-valence Basis Sets for Second-row Elements. *J. Am. Chem. Soc.* **1982,** *104* (10), 2797-2803.

116.   Ditchfield, R.;  Hehre, W. J.; Pople, J. A. Self-Consistent Molecular-Orbital Methods. IX. An Extended Gaussian-Type Basis for Molecular-Orbital Studies of Organic Molecules. *J. Chem. Phys.* **1971,** *54* (2), 724-728.

117.   Hehre, W. J.;  Ditchfield, R.; Pople, J. A. Self—Consistent Molecular Orbital Methods. XII. Further Extensions of Gaussian—Type Basis Sets for Use in Molecular Orbital Studies of Organic Molecules. *J. Chem. Phys.* **1972,** *56* (5), 2257-2261.

118.   Mazurek, A. H.;  Szeleszczuk, Ł.; Pisklak, D. M. Periodic DFT Calculations—Review of Applications in the Pharmaceutical Sciences. *Pharmaceutics* **2020,** *12* (5), 415.

119.   Gruber, T.;  Liao, K.;  Tsatsoulis, T.;  Hummel, F.; Grüneis, A. Applying the Coupled-Cluster Ansatz to Solids and Surfaces in the Thermodynamic Limit. *Phys. Rev. X* **2018,** *8* (2), 021043.

120.   El-Kelany, K. E.;  Ravoux, C.;  Desmarais, J.;  Cortona, P.;  Pan, Y.;  Tse, J.; Erba, A. Spin Localization, Magnetic Ordering, and Electronic Properties of Strongly Correlated $Ln_2O_3$ Sesquioxides (Ln= La, Ce, Pr, Nd). *Phys. Rev. B* **2018,** *97* (24), 245118.

121.   Genoni, A.;  Bučinský, L.;  Claiser, N.;  Contreras-García, J.;  Dittrich, B.;  Dominiak, P. M.;  Espinosa, E.;  Gatti, C.;  Giannozzi, P.; Gillet, J. M. Quantum Crystallography: Current Developments and Future Perspectives. *Chem. Eur. J* **2018,** *24* (43), 10881-10905.

122. Lejaeghere, K.; Van Speybroeck, V.; Van Oost, G.; Cottenier, S. Error Estimates for Solid-state Density-functional Theory Predictions: An Overview by Means of the Ground-state Elemental Crystals. *Crit. Rev. Solid State Mater. Sci.* **2014,** *39* (1), 1-24.

123. Vener, M. V.; Levina, E. O.; Koloskov, O. A.; Rykounov, A. A.; Voronin, A. P.; Tsirelson, V. G. Evaluation of the Lattice Energy of the Two-Component Molecular Crystals Using Solid-State Density Functional Theory. *Cryst. Growth Des.* **2014,** *14* (10), 4997-5003.

124. Vener, M. V.; Egorova, A.; Churakov, A.; Tsirelson, V. Intermolecular Hydrogen Bond Energies in Crystals Evaluated using Electron Density Properties: DFT Computations with Periodic Boundary Conditions. *J. Comput. Chem.* **2012,** *33* (29), 2303-2309.

125. Erba, A.; Maul, J.; De La Pierre, M.; Dovesi, R. Structural and Elastic Anisotropy of Crystals at High Pressures and Temperatures from Quantum Mechanical Methods: The Case of $Mg_2SiO_4$ Forsterite. *J. Chem. Phys.* **2015,** *142* (20), 204502/1-204502/11.

126. Dovesi, R.; Pascale, F.; Civalleri, B.; Doll, K.; Harrison, N. M.; Bush, I.; D'Arco, P.; Noël, Y.; Rérat, M.; Carbonnière, P.; et al. The CRYSTAL code, 1976–2020 and beyond, a long story. *J. Chem. Phys.* **2020,** *152* (20), 204111.

127. Dovesi, R.; Erba, A.; Orlando, R.; Zicovich-Wilson, C. M.; Civalleri, B.; Maschio, L.; Rérat, M.; Casassa, S.; Baima, J.; Salustro, S.; Kirtman, B. Quantum-mechanical Condensed Matter Simulations with CRYSTAL. *Wiley Interdiscip. Rev.: Comput. Mol. Sci.* **2018,** *8* (4), e1360.

128. Kresse, G.; Furthmüller, J. Efficiency of ab-initio Total Energy Calculations for Metals and Semiconductors using a Plane-wave Basis Set. *Comput. Mater. Sci.* **1996,** *6* (1), 15-50.

129. Soler, J. M.; Artacho, E.; Gale, J. D.; García, A.; Junquera, J.; Ordejón, P.; Sánchez-Portal, D. The SIESTA Method for ab initio Order-N materials Simulation. *J. Phys.: Condens. Matter* **2002,** *14* (11), 2745.

130. Kühne, T. D.; Iannuzzi, M.; Del Ben, M.; Rybkin, V. V.; Seewald, P.; Stein, F.; Laino, T.; Khaliullin, R. Z.; Schütt, O.; Schiffmann, F.; et al. CP2K: An Electronic Structure and Molecular Dynamics Software Package - Quickstep: Efficient and Accurate Electronic Structure Calculations. *J. Chem. Phys.* **2020,** *152* (19), 194103.

131. Kratzer, P.; Neugebauer, J. The Basics of Electronic Structure Theory for Periodic Systems. *Front. Chem.* **2019,** *7* (106).

132. Martyna, G. J.; Tuckerman, M. E. A Reciprocal Space Based Method for Treating Long Range Interactions in ab initio and Force-field-based Calculations in Clusters. *J. Chem. Phys.* **1999,** *110* (6), 2810-2821.

133. Monkhorst, H. J.; Pack, J. D. Special Points for Brillouin-zone Integrations. *Phys. Rev. B* **1976,** *13* (12), 5188-5192.

134. Ashcroft, N. W.; Mermin, N. D. *Solid State Physics*, Holt, Rinehart and Winston: 1976.

135. Chadi, D. J.; Cohen, M. L. Special Points in the Brillouin Zone. *Phys. Rev. B* **1973,** *8* (12), 5747-5753.

136. Simon, S. H. *The Oxford Solid State Basics*, OUP Oxford: 2013.

137. Zicovich-Wilson, C. M.; Dovesi, R. On the use of Symmetry-adapted Crystalline Orbitals in SCF-LCAO Periodic Calculations. I. The Construction of the Symmetrized Orbitals. *Int. J. Quantum Chem.* **1998,** *67* (5), 299-309.

138. Zicovich-Wilson, C. M.; Dovesi, R. On the use of Symmetry-adapted Crystalline Orbitals in SCF-LCAO Periodic Calculations. II. Implementation of the Self-consistent-field Scheme and Examples. *Int. J. Quantum Chem.* **1998,** *67* (5), 311-320.

139. Kudin, K. N.; Scuseria, G. E. Linear-scaling Density-functional Theory with Gaussian Orbitals and Periodic Boundary Conditions: Efficient Evaluation of Energy and Forces via the Fast Multipole Method. *Phys. Rev. B* **2000,** *61* (24), 16440-16453.

140. Towler, M. D.;  Zupan, A.; Causà, M. Density Functional Theory in Periodic Systems using Local Gaussian Basis Sets. *Comput. Phys. Commun.* **1996,** *98* (1), 181-205.

141. Makov, G.; Payne, M. Periodic Boundary Conditions in ab initio Calculations. *Phys. Rev. B* **1995,** *51* (7), 4014.

142. Caldeweyher, E.; Brandenburg, J. G. Simplified DFT Methods for Consistent Structures and Energies of Large Systems. *J. Phys.: Condens. Matter* **2018,** *30* (21), 213001.

143. Vener, M. V.;  Egorova, A.;  Churakov, A. V.; Tsirelson, V. G. Intermolecular Hydrogen Bond Energies in Crystals Evaluated using Electron Density properties: DFT Computations with Periodic Boundary Conditions. *J. Comput. Chem.* **2012,** *33* (29), 2303-2309.

144. Schahl, A.;  Gerber, I. C.;  Réat, V.; Jolibois, F. Diversity of the Hydrogen Bond Network and Its Impact on NMR Parameters of Amylose B Polymorph: A Study Using Molecular Dynamics and DFT Calculations Within Periodic Boundary Conditions. *J. Phys. Chem. B* **2021,** *125* (1), 158-168.

145. Kubicki, J. D.; Watts, H. D. Quantum Mechanical Modeling of the Vibrational Spectra of Minerals with a Focus on Clays. *Minerals* **2019,** *9* (3), 141.

146.    Liu, K.-Y.;  Liu, J.; Herbert, J. M. Accuracy of Finite-difference Harmonic Frequencies in Density Functional Theory. *J. Comput. Chem.* **2017,** *38* (19), 1678-1684.

147.    Pascale, F.;  Zicovich-Wilson, C. M.;  López Gejo, F.;  Civalleri, B.;  Orlando, R.; Dovesi, R. The Calculation of the Vibrational Frequencies of Crystalline Compounds and its Implementation in the CRYSTAL Code. *J. Comput. Chem.* **2004,** *25* (6), 888-897.

148.    Zicovich-Wilson, C. M.;  Pascale, F.;  Roetti, C.;  Saunders, V. R.;  Orlando, R.; Dovesi, R. Calculation of the Vibration Frequencies of Alpha-quartz: The Effect of Hamiltonian and Basis Set. *J. Comput. Chem.* **2004,** *25* (15), 1873-81.

149.    Erba, A.;  Maul, J.; Civalleri, B. Thermal Properties of Molecular Crystals through Dispersion-corrected Quasi-harmonic ab initio Calculations: The Case of Urea. *Chem. Commun.* **2016,** *52* (9), 1820-1823.

150.    Erba, A.;  Shahrokhi, M.;  Moradian, R.; Dovesi, R. On How Differently the Quasi-harmonic Approximation Works for Two Isostructural Crystals: Thermal Properties of Periclase and Lime. *J. Chem. Phys.* **2015,** *142* (4), 044114.

151.    Bowman, J. M. The Self-consistent-field Approach to Polyatomic Vibrations. *Acc. Chem. Res.* **1986,** *19* (7), 202-208.

152.    Souvatzis, P.;  Eriksson, O.;  Katsnelson, M.; Rudin, S. Entropy Driven Stabilization of Energetically Unstable Crystal Structures Explained From First Principles Theory. *Phys. Rev. Lett.* **2008,** *100* (9), 095901.

153.    Erba, A.;  Maul, J.;  Ferrabone, M.;  Carbonnière, P.;  Rérat, M.; Dovesi, R. Anharmonic Vibrational States of Solids from DFT Calculations. Part I: Description of the Potential Energy Surface. *J. Chem. Theory Comput.* **2019,** *15* (6), 3755-3765.

154. Hanson-Heine, M. W. D. Intermediate Vibrational Coordinate Localization with Harmonic Coupling Constraints. *J. Chem. Phys.* **2016,** *144* (20), 204116.

155. Panek, P. T.; Jacob, C. R. On the Benefits of Localized Modes in Anharmonic Vibrational Calculations for Small Molecules. *J. Chem. Phys.* **2016,** *144* (16), 164111.

156. Yamaguchi, Y.; Frisch, M.; Gaw, J.; Schaefer, H. F.; Binkley, J. S. Analytic Evaluation and Basis Set Dependence of Intensities of Infrared Spectra. *J. Chem. Phys.* **1986,** *84* (4), 2262-2278.

157. Porezag, D.; Pederson, M. R. Infrared Intensities and Raman-scattering Activities within Density-functional Theory. *Phys. Rev. B* **1996,** *54* (11), 7830-7836.

158. Zvereva, E. E.; Shagidullin, A. R.; Katsyuba, S. A. Ab Initio and DFT Predictions of Infrared Intensities and Raman Activities. *J. Phys. Chem. A* **2011,** *115* (1), 63-69.

159. Dovesi, R.; Kirtman, B.; Maschio, L.; Maul, J.; Pascale, F.; Rérat, M. Calculation of the Infrared Intensity of Crystalline Systems. A Comparison of Three Strategies Based on Berry Phase, Wannier Function, and Coupled-Perturbed Kohn–Sham Methods. *J. Phys. Chem. C* **2019,** *123* (13), 8336-8346.

160. Allis, D. G.; Fedor, A. M.; Korter, T. M.; Bjarnason, J. E.; Brown, E. R. Assignment of the Lowest-lying THz Absorption Signatures in Biotin and Lactose Monohydrate by Solid-state Density Functional Theory. *Chem. Phys. Lett.* **2007,** *440* (4), 203-209.

161. Li, R.; Zeitler, J. A.; Tomerini, D.; Parrott, E. P. J.; Gladden, L. F.; Day, G. M. A Study into the Effect of Subtle Structural Details and Disorder on the Terahertz Spectrum of Crystalline Benzoic Acid. *Phys. Chem. Chem. Phys.* **2010,** *12* (20), 5329-5340.

# Chapter 3: Experimental Foundations for the Characterization of Solids

## 3.1 Introduction

Matter in the solid state can be characterized using a wide array of analytical methods, with the most powerful analyses utilizing a collection of techniques.[1, 2] One way in which these methods can be combined is by using complementary regions of the electromagnetic spectrum.[3, 4] The electromagnetic spectrum spans the entire range of electromagnetic radiation frequencies and is typically described as bands grouped by common characteristics such as source or the way in which they interact with matter.[5] The terahertz (THz) frequency range, $0.1 - 10$ THz ($1 \times 10^{11}$ $- 1 \times 10^{12}$ Hz, $3$ -$333$ cm$^{-1}$, $\lambda = 3 \times 10^{-3}- 3 \times 10^{-5}$ m) has proven to be particularly useful for characterizing solids and bridges the gap between the infrared and microwave regions.[6] Accessing this region through low-frequency vibrational spectroscopy allows weak, noncovalent interactions to be explored, and it is due to the unique nature of these vibrations that solids can be characterized in this region. Another region commonly used to characterize solids is the X-ray region ($\lambda = 0.1 - 10$ nm), which is capable of providing details into atomic and molecular structures through X-ray crystallography.[7]

Both frequency regions, the THz, and the X-ray, can be used to differentiate between different molecular identities, as well as different solid-state packing arrangements. These often-subtle changes can have large consequences on the physical properties, and so the ability to detect the presence of a salt, hydrate, or different polymorphic form is critical to categorizing and understanding the chemical species.[8-10] It is by combining low-frequency vibrational spectroscopy with X-ray crystallography that both a static and dynamic picture can be captured.[11]

## 3.2 Vibrational Spectroscopy

Before delving into the intricacies of low-frequency vibrational spectroscopy, it is best to understand the foundations that govern vibrational spectroscopy as a whole. Vibrational spectroscopy refers to instances when the interaction of energy with a medium is sufficient to promote molecules from one discrete vibrational energy level to another, in turn causing the molecule to vibrate.[12] The number of unique ways in which the molecule can vibrate is dictated by its vibrational degrees of freedom. The vibrational degrees of freedom for a linear system are given by 3N-5, where N is the number of nuclei present, whereas a non-linear system possess 3N-6 vibrational degrees of freedom. Each vibrational degree of freedom gives rise to a fundamental motion in the form of a normal mode of vibration, and so for the simple case of a diatomic molecule (N=2), only a single normal mode of vibration would be expected (3(2)-6). Moving from a simple diatomic to a solid will increase the number of normal modes of vibration, as now the contents of the entire unit cell must be accounted for. Focusing on crystalline solids, these normal modes of vibration can be further decomposed into internal (molecular) and external (lattice) modes where the number of internal modes can be determined by using the formula 3N-6M, and external modes by the formula 6M-3, with M being the number of molecules, each with N atoms within a single unit cell.[13, 14] To observe these normal modes of vibration, they must first meet a set of criteria established by their energetics and interaction with incident radiation.[15]

The first criteria pertains to the transition between energy levels. For a diatomic molecule, each discrete energy level, $E_n$, can be expressed by the quantum harmonic oscillator as seen in equation (3.1), where $n$ is a positive integer value that defines the energy state, $\hbar$ is the reduced form of Planck's constant, $c$ is the speed of light, and $\bar{v}$ is the frequency.

$$E_n = \left(n + \frac{1}{2}\right)\hbar c\bar{v}$$
(3.1)

The frequency, $\bar{v}$, can be further defined by equation (3.2) through the force constant, $k$, and the

reduced mass, $\mu$.

$$\bar{v} = \frac{1}{2\pi c}\sqrt{\frac{k}{\mu}}$$
(3.2)

Using the quantum harmonic oscillator, the energy for the lowest energy level ($n = 0$) would not

be equal to 0, but to $\frac{1}{2}\hbar c\bar{v}$. This is known as the zero-point energy and gives the important

implication that a molecule can never be completely at rest. The inclusion of the zero-point

energy is one facet that differentiates the quantum harmonic oscillator seen above from the

classical harmonic oscillator. If the energy supplied by the incident radiation is exactly equal to

the difference in energy between discrete energy levels, the first criteria for observing a normal

mode of vibration is met.

Using the quantum harmonic oscillator described, the potential energy, $V$, can be

determined by the force constant, $k$, as a function of internuclear separation using equation (3.3)

with the change in interatomic distance ($r$) from the equilibrium position ($r_e$) represented as,

$r - r_e$.

$$V = \frac{1}{2}k(r - r_e)^2$$
(3.3)

Using equation (3.3), the energy levels will be evenly spaced due to the quadratic nature of the

harmonic oscillator. However, in reality, the energy levels are not all evenly spaced, and there

comes an energy limit where the bond will dissociate. These deviations from harmonic behavior

are known as mechanical anharmonicity, and result in the true potential energy curve being asymmetric, with unevenly spaced energy levels. To account for the real-life deviations from the quantum harmonic oscillator model described in equation (3.3), higher ordered terms can be included, and while these additional terms would improve the approximation, the quantum harmonic oscillator is still a fair assumption when the displacement from the equilibrium position is small.[16, 17]

An alternative route to accounting for anharmonicity is to approximate the potential energy using a Morse potential as seen in equation (3.4) accounting for the dissociation energy, $D_e$, and the 'width' of the potential, $\beta$.

$$V = D_e(1 - e^{-\beta(r-r_e)})^2$$

$$(3.4)$$

This approach leads to the potential energy curve becoming flatter as the dissociation energy is approached and the force constant is reduced as seen in **Figure 3-1**.[18]
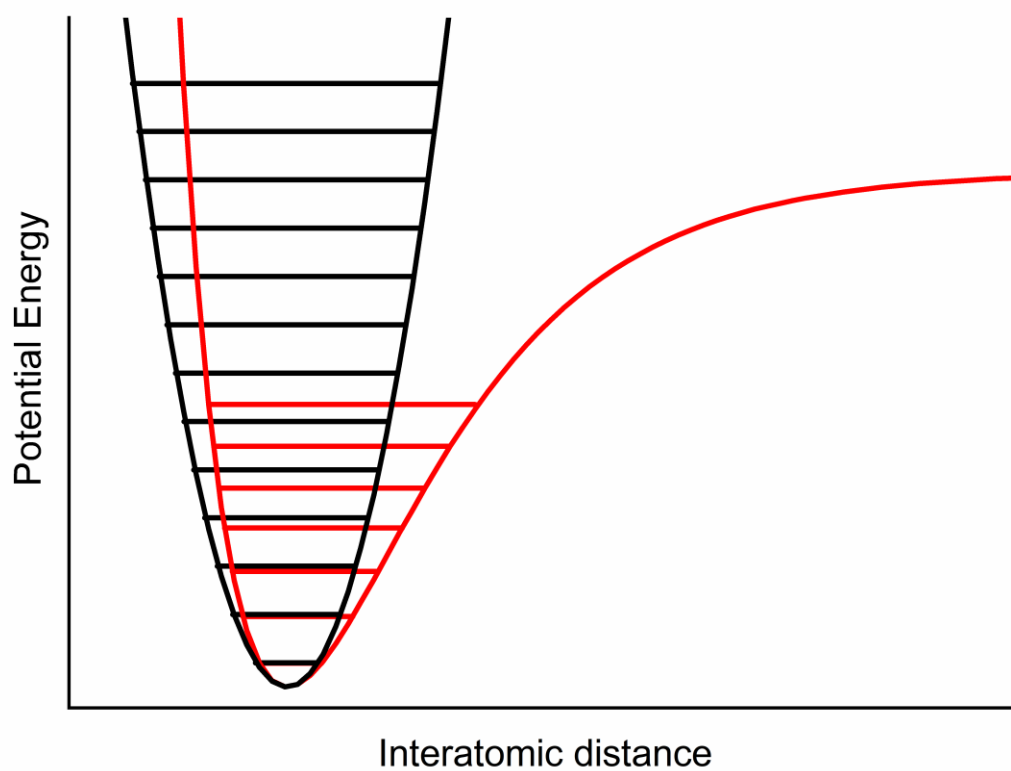
**Figure 3-1.** Deviation of an anharmonic Morse potential (red) from a quantum harmonic oscillator (black) as adapted from Herzberg, Spectra of Diatomic Molecules.[19]

The second criteria that must be met for a transition to be observed is based on vibrational selection rules. Transitions that meet the energy criteria and experience a change in the dipole-moment ($\mu$) with respect to the vibrational coordinates ($q$) will be infrared-active (equation (3.5)) while changes to polarizability ($\alpha$) with respect to the vibrational coordinates ($q$) will be Raman-active (equation (3.6)).[20, 21] The symmetry associated with each normal mode can also be used to determine if it will be infrared-active, Raman-active, both, or, potentially, neither.[22] It is possible for a normal mode to be both infrared- and Raman-active but their intensities will be inversely related.

$$\frac{\partial \mu}{\partial q} \neq 0$$

(3.5)

$$\frac{\partial \alpha}{\partial q} \neq 0$$

(3.6)

Each of the normal modes that satisfy the above two criteria have the potential to yield an observable band in the vibrational spectrum.[23] To observe these allowed vibrational transitions, infrared and Raman spectroscopy can be used. The core difference between the two spectroscopic methods beyond their differing selection rules described above is that in infrared spectroscopy, the light that is absorbed is measured, while in Raman spectroscopy the light that is scattered is measured.[24]

To generalize basic infrared spectroscopy, a sample sits between a light source and a detector, and while the light source contains many different infrared wavelengths, only those that match the intrinsic vibrational frequencies of the system being studied are absorbed.[25] The transmitted light is then sent to the detector where it is separated by wavelength, and the resultant

intensity of each wavelength is detected. One of the most common applications of infrared spectroscopy is the identification of functional groups in the 1500 – 3700 cm^{-1} range for characterizing organic compounds, however, it has also led to a better understanding of proteins, biological imaging, and the monitoring of produce quality to name only a few of the countless applications.[26-34]

Conversely, Raman spectroscopy uses a monochromatic light source to raise photons to a virtual energy state and detects the resultant scattering of emitted photons. These scattered photons fall into two categories, elastic scattering, where the final frequency matches that of the incident beam (Rayleigh scattering), and inelastic scattering, where it does not (Raman scattering). Only 1 in 10[8] of the scattered photons falls into the latter category, with the remainder of the scattered light manifesting as an intense Rayleigh peak, making filtering out the inelastically scattered light more difficult as proximity to the Rayleigh line increases.[35, 36] Of the inelastically scattered photons, the majority will shift to higher wavelengths as a result of losing energy, and are known as Stokes peaks. Alternatively, photons who gain energy will shift to lower wavelengths (anti-Stokes peaks). These shifts from the Rayleigh line are referred to as Raman shifts, $\Delta\bar{v}$ (cm^{-1}), and can be calculated using equation (3.6), where $\lambda_0$ is the laser excitation wavelength in nm, and $\lambda_1$ is the scattered wavelength in nm.

$$\Delta\bar{v} = 10^7 (\frac{1}{\lambda_0} - \frac{1}{\lambda_1})$$

(3.6)

The Raman shift between Stokes and anti-Stokes peaks will be symmetrical on either side of the Rayleigh line, differing only in intensity, as the anti-Stokes peaks are generated from molecules that are already in an excited state prior to the incident radiation (usually from thermal excitation), and are considerably weaker than their Stokes counterpart. This is due to the

population of molecules that start in an excited vibrational state being much lower than those which start at the ground state.[37, 38]

## 3.3 Low-frequency Vibrational Spectroscopy

Typically, when discussing vibrational spectroscopy, it refers to either infrared or Raman spectroscopy probing the frequency range between 200 and 4000 $cm^{-1}$.[39] At the higher end of this region, $> 1500$ $cm^{-1}$, the position of the frequency correlates with specific functional groups, while the lower end has been deemed the fingerprint region.[40, 41] The collection of spectra obtained below 200 $cm^{-1}$ is considered low-frequency vibrational spectroscopy, and even though it is governed by the same foundational principles as higher frequencies, the types of vibrations seen in this region are quite different than those typically considered as infrared or Raman vibrations.[42, 43]

This becomes apparent when attempting to differentiate between solid polymorphs of the same chemical species.[44, 45] The difference between polymorphs is in the packing arrangement within the unit cell, causing a change to the intermolecular forces that hold the distinct solids together. Two polymorphs of the same chemical species would have similar (and often indistinguishable) features above the $> 1500$ $cm^{-1}$ frequency region, where the frequency region below 200 $cm^{-1}$ would be unique. These differences in low-frequency spectra are due to the fact that the low-frequency region represents the intermolecular vibrations related to the crystal lattice, whereas the higher frequency range is dominated by intramolecular vibrations that apply to a single molecule.[46-48] While low-frequency spectra can be easily used to differentiate between crystal structures, interpreting the spectra becomes very complicated as the nature of these

vibrations is unique to each crystalline solid. These complex vibrations in the low-frequency region often consist of a mixture of internal and external modes, making the collective vibrations difficult to classify, but it is these complexities that give low-frequency spectroscopy its power to differentiate even subtle differences in crystalline solids.[49-51]

### 3.3.1 Terahertz Time-Domain Spectroscopy

Accessing the frequencies between the infrared and microwave regions has previously been restricted by the physical limits of the instrumentation, but advancements to the generation and detection of terahertz pulses, has made this region much more approachable.[52, 53] The technology to access this region is now commercially available, leading to decreases in costs, as well as increases in the standardization of measurements. The popularity of terahertz spectroscopy continues to grow, as it can be used in either imaging or spectroscopic configurations.[54-56] Terahertz time-domain spectroscopy (THz-TDS) is both a chemically specific and penetrative technique, all while being non-invasive and non-destructive. However, due to the strong absorption of water vapor in the terahertz region, its applicability is often limited to laboratory settings.[57-62]

The Toptica (Graefelfing, Germany) TeraFlash is an example of a commercial instrument that can achieve a bandwidth capability of more than 6 THz (**Figure 3-2**).[63] This instrument includes a $\lambda = 1.5$ µm pulsed femtosecond laser, a THz emitter in the form of a InGaAs 25 µm strip-line photoconductive antenna, and a THz detector in the form of a InGaAs 25 µm dipole photoconductive antenna. The femtosecond laser pulse is split into two branches, with one sent to the emitter, while the other travels to the detector along a delay line. The branch that is sent to the emitter generates terahertz radiation, which is then guided to the sample. Once the terahertz

radiation has interacted with the sample, the modified wave travels to the detector where it meets

the pulse that was initially diverted to the detector branch. Together, this allows for the electric

field of the broadband THz pulse to be measured as a function of time producing a terahertz

waveform that contains information on both the phase and amplitude components.



**Figure 3-2.** Toptica TeraFlash Time-domain Terahertz Platform.

### 3.3.2 Low-Frequency Raman Spectroscopy

Since the proposal of a "secondary radiation" in 1928, Raman spectroscopy has continued to grow in its capabilities and applications.[64, 65] The availability of more advanced optical filters has led to spectral features close to the Rayleigh line being quickly resolved, since if not properly rejected, the intense Raleigh line can overshadow vibrations below 200 cm$^{-1}$.[66, 67] Despite the fact that terahertz waves are not generated or detected, using Raman spectroscopy to probe the frequency range below 200 cm$^{-1}$ is often referred to as terahertz-Raman spectroscopy, while more appropriately, it can be referred to as low-frequency Raman spectroscopy (LFRS). Just like THz-TDS, LFRS is also material specific and non-invasive, leading to similar applications, including monitoring the solubility and crystallinity of drugs, as well as polymorph identification.[68-71] An advantage of LFRS over THz-TDS is that LFRS is not impacted by the presence of moisture in the air; however, it can be destructive under certain laser conditions, and due to its scattering nature is generally not a penetrative technique.[72]

The Ondax (Coherent, Santa Clara, CA, USA) SureBlock XLF-CLM THz-Raman system can resolve spectral features as low as 5 cm$^{-1}$ with the use of a SureBlock ultra-narrow-band volume holographic grating (VGH). This instrument utilizes a SureLock 785 nm laser source fiber coupled to an Andor Shamrock 750 spectrograph with an iDus 416 CCD, providing a resultant spectral resolution of 0.65 cm$^{-1}$. The small, portable unit allows data to be collected with little sample preparation due to the equipped vial holder and has low risk of damaging the sample due to the sliding power adjustment (**Figure 3-3**).
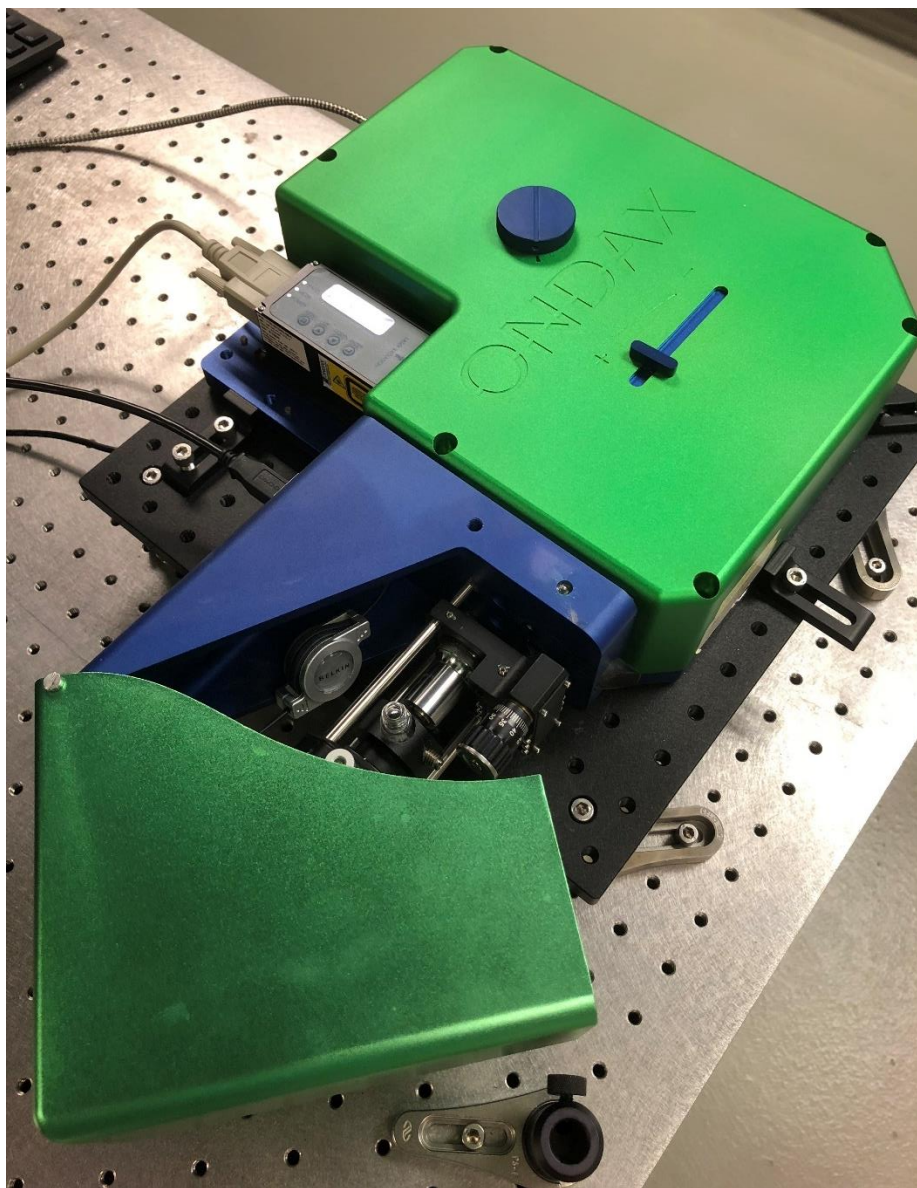
**Figure 3-3.** Benchtop Ondax (Coherent) SureBlock XLF-CLM THz-Raman system with vial holder attachment.

## 3.4 X-ray Crystallography

Since the discovery of X-ray diffraction in 1912, over a dozen Nobel prizes have been awarded in relation to X-ray crystallography, and the technique continues to assert itself at the core of characterizing crystalline solids for use in fingerprint identification and structure determination.[73, 74] As an X-ray wave passes through a crystalline material, diffracted rays (reflections) are generated, and the direction and intensity of the reflections are measured. These measurements can be used to garner information about the three-dimensional electron density of the unit cell, which in turn can be used to produce an atomic model.[75-77] Dependent upon the goals of the experiment, X-ray crystallography can be performed on either a single crystal or a polycrystalline material.[78]

Instruments used to perform X-ray crystallography are known as diffractometers, minimally consisting of a source to generate an incident X-ray beam, a sample stage, and a detector to collect the resulting reflections.[79] A common source for generating X-rays are X-ray tubes, where X-ray tubes use electrical power to accelerate electrons from the negatively charged cathode to strike the positively charged anode.[80] This process generates two types of spectra, a continuous spectrum known as bremsstrahlung or white radiation, and a characteristic spectrum.[81] The characteristic spectrum is a set of discrete peaks produced when an inner shell electron is ejected from the metal of the anode. The most radiation seen is the K$\alpha$ peak which comes from a 2p $\rightarrow$ 1s transition while the weaker K$\beta$ radiation if produced from a 3p $\rightarrow$ 1s transition. The wavelength of the K$\alpha$ radiation is determined by the target material, with common materials typically being high in atomic number and melting point.  Copper (Cu) and molybdenum (Mo) are common choices for X-ray diffraction, while tungsten (W) is a common choice of target material for medical applications.[82] The size and composition of the crystal

should be considered when choosing a target metal as Cu Kα radiation is typically used for large unit cells and small crystals, while Mo Kα radiation is more desirable when dealing with smaller unit cells or materials that contain heavy atoms.

When the generated X-ray beam strikes a sample, the X-ray waves are scattered. If the scattered waves interfere constructively, Bragg's law (3.7) is satisfied, and a Bragg reflection is generated. Bragg's law is defined by *n,* the order of diffraction (an integer), $\lambda$, the wavelength of the incident X-ray, *d*, the spacing of the crystal layers, and $\theta$, the incident angle.[83]

$$n\lambda = 2d\sin(\theta)$$

(3.7)

It is by rotating the sample and/or the X-ray beam, that all possible reflections can be collected. These reflections are then measured using a detector, where the diffracted rays are converted into electrical signals that are counted.[84] The collection of all possible reflections will yield a diffraction pattern that is used to help characterize the material.

From the scattering angle of the reflections collected, the lattice parameters can be determined, while the intensity of the reflections can be used to determine the atomic positions. These lattice parameters (*a, b, c, α, β, and γ*) allow the unit cell to be classified into a series of seven crystal systems and represent the external dimensions of each unit cell.[80, 85] The internal parameters of each unit cell can be described through a set of asymmetric units, or the smallest group of atoms representative to the crystal. These asymmetric units are replicated through a series of symmetry operations inherent to the unit cell, and it is these same symmetry operations that are extended outside the unit cell to describe the three-dimensional solid. Together, the

symmetry of the lattice parameters and the internal coordinates of the unit cell can be described by one of the 230 space groups.

### 3.4.1 Powder X-ray Diffraction

Powder X-ray diffraction (PXRD) has been used to characterize both organic and inorganic materials ranging from pharmaceutical polymorphs to quantum dots.[86-92] The random arrangement of a polycrystalline sample assumes that all crystalline orientations are accounted for, making PXRD patterns representative of the bulk material. Each crystal orientation will have an associated $\theta$ value that satisfies Bragg's law (3.7) creating a cone of diffracted rays (**Figure 3-4**), and as these cones are counted by the detector, they appear as Debye-Scherrer rings as seen in **Figure 3-5**. While PXRD in theory can be used to discern unit cell dimensions and atomic positions, the feasibility of these tasks is limited by the symmetry of the crystal, but thankfully advancements to software have increased the applicability of indexing powder patterns.[93-96]

One commercial option for the collection of PXRD data is the Bruker (Billerica, MA, USA) D2 Phaser. This benchtop instrument is equipped with a copper X-ray tube ($\lambda = 1.54184$ Å) and a 1D LYNXEYE detector in a Bragg-Brentano geometry producing high quality diffraction patterns in a timely manner. The strip detector allows for much faster data collection than typical point detectors, as a point detector only records a single position in time, while the strip detector can record more than 150 2θ positions simultaneously. This specific instrument can hold up to six samples at a time, requires little to no sample preparation, and can also rotate the sample as data is collected to ensure that all possible crystalline orientations are sampled. The included software, DIFFRAC.EVA, allows for analysis of powder diffraction patterns, as well as sample identification through reference databases.[97]
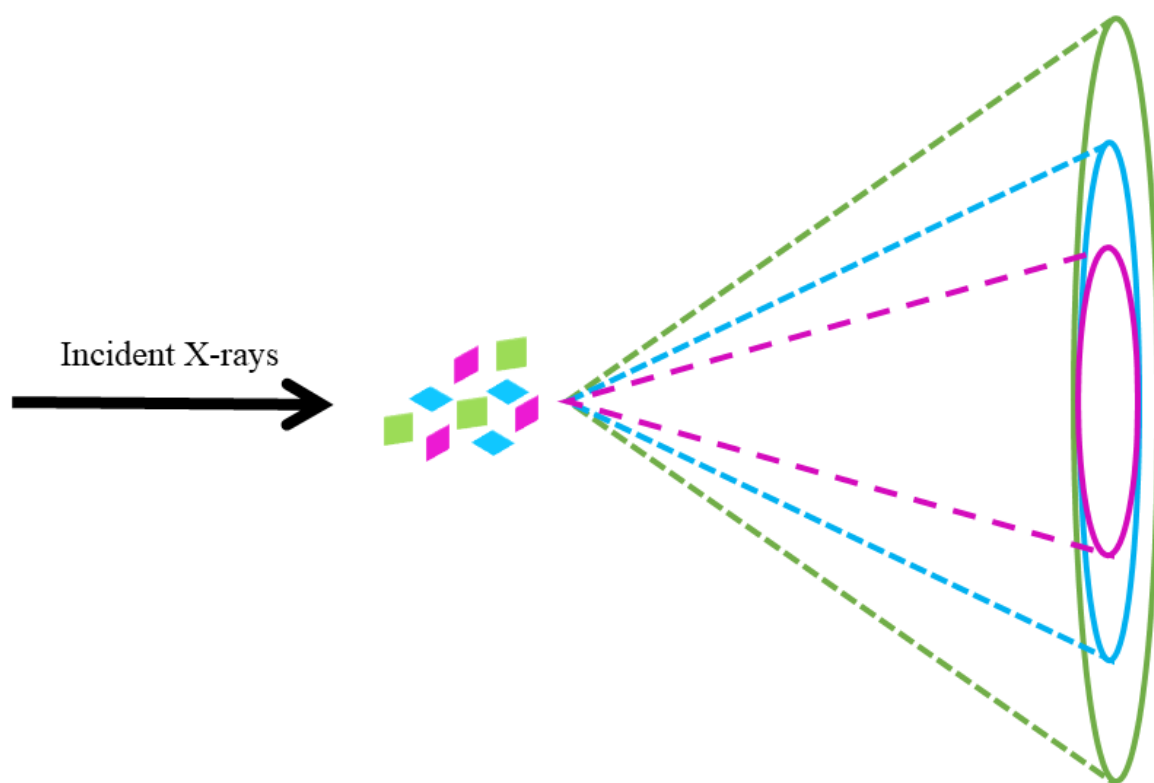
**Figure 3-4.** Debye-Scherrer rings (solid lines) formed from a cone of diffracted rays (dashed lines) for a randomly oriented polycrystalline sample.
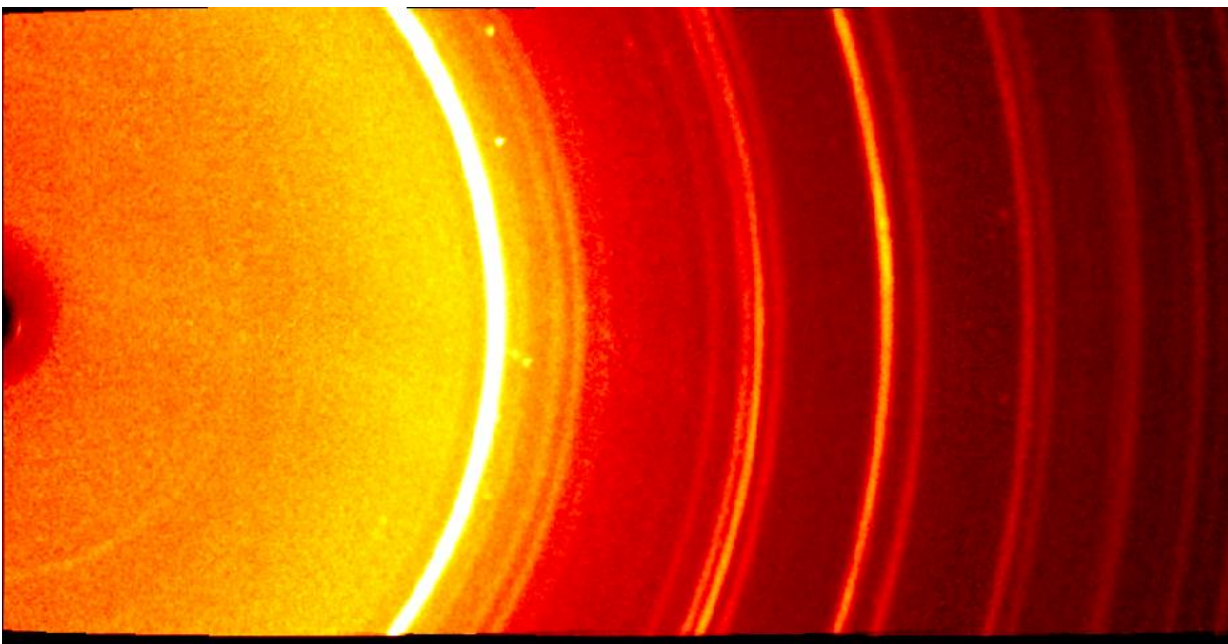
**Figure 3-5.** Debye rings generated from a polycrystalline sample of L-cystine.

### 3.4.2 Single Crystal X-ray Diffraction

Unlike PXRD, single crystal X-ray diffraction (SC-XRD) requires careful selection of a single crystal, and when examined, should produce a number of discrete, bright reflections. If the crystal selected is not of high enough quality or size, the reflections collected will be difficult to impossible to use for further data interpretation. Preparing and choosing a suitable crystal is not a trivial task, and it requires skill and patience. If the crystals grown are not sufficient for SC-XRD measurements, changes to the recrystallization process can aid in producing more desirable crystals.[98, 99] Obtaining a suitable crystal of large proteins and other biomolecules remains a challenge, but advancements to instrumentation have allowed for some structures to be elucidated.[100-102]

Most SC-XRD measurements begin with a partial data collection that is used for a dual purpose. First, to determine if the crystal is of suitable quality for a full data collection, and secondly, to determine the crystal system based off the systematic absences of reflections. This partial collection determines the parameters that should be used in a full data collection to collect as many reflections as possible set by the limitations of the instrument and potentially the time allowed. From a full data collection, the integrated raw intensities are reduced to relative structure factors to begin creating an electron density map. A number of functions can then be applied to solve the phase problem, and compute a full electron density map which is used to decipher the positions of the atoms in the unit cell, with the most common method being the Patterson method which takes the Fourier transform of the square of the structure factor amplitudes .[103-105] Other common methods to solve the phase problem include reciprocal space (direct methods) and dual space methods.[106, 107] Finally, the structure is refined to best fit the calculated structure factors to those observed experimentally.[108, 109] While individual software

programs have unique graphical user interfaces and tools available to streamline the process of

collecting and analyzing X-ray data, they all follow the same general methodologies and steps

outlined above.[110, 111]

## 3.5 References

1. Law, D.; Zhou, D., Chapter 3 - Solid-State Characterization and Techniques. In *Developing Solid Oral Dosage Forms (Second Edition)*, Qiu, Y.; Chen, Y.; Zhang, G. G. Z.; Yu, L.; Mantri, R. V., Eds. Academic Press, Boston, 2017; pp 59-84.

2. Storey, R. A.; Ymeacute; n, I. *Solid State Characterization of Pharmaceuticals*, 1. Aufl. ed.; Wiley-Blackwell: Hoboken, 2011.

3. Munson, E. J., Chapter 3 - Analytical Techniques in Solid-state Characterization. In *Developing Solid Oral Dosage Forms*, Qiu, Y.; Chen, Y.; Zhang, G. G. Z.; Liu, L.; Porter, W. R., Eds. Academic Press, San Diego, 2009; pp 61-74.

4. Krimm, S.; Bandekar, J., Vibrational Spectroscopy and Conformation of Peptides, Polypeptides, and Proteins. In *Advances in Protein Chemistry*, Anfinsen, C. B.; Edsall, J. T.; Richards, F. M., Eds. Academic Press, 1986; Vol. 38, pp 181-364.

5. Butcher, G.; Mottar, J.; United States. National, A.; Space, A. *Tour of the Electromagnetic Spectrum*, National Aeronautics and Space Administration: Washington, D.C. , 2010.

6. Chamberlain, J. Where Optics Meets Electronics: Recent Progress in Decreasing the Terahertz Gap. *Philos. Trans. R. Soc., A* **2004,** *362* (1815), 199-213.

7. Shih, K. *X-ray Diffraction: Structure, Principles, and Applications*, Nova Publishers: Hauppauge, New York, 2013.

8. Heinz, A.; Strachan, C. J.; Gordon, K. C.; Rades, T. Analysis of Solid-state Transformations of Pharmaceutical Compounds using Vibrational Spectroscopy. *J. Pharm. Pharmacol.* **2009,** *61* (8), 971-988.

9. Stephenson, G. A.; Forbes, R. A.; Reutzel-Edens, S. M. Characterization of the Solid State: Quantitative Issues. *Adv. Drug Delivery Rev.* **2001,** *48* (1), 67-90.

10.     Lipiäinen, T.;  Fraser-Miller, S. J.;  Gordon, K. C.; Strachan, C. J. Direct Comparison of Low- and Mid-frequency Raman Spectroscopy for Quantitative Solid-state Pharmaceutical Analysis. *J. Pharm. Biomed. Anal.* **2018,** *149*, 343-350.

11.     Sathyanarayana, D. N. *Vibrational Spectroscopy: Theory and Applications*,

12.     Harris, D. C.; Bertolucci, M. D. *Symmetry and Spectroscopy* Dover Publications Inc.: New York, NY, 1989.

13.     Sherwood, P. M. A.; Sherwood, P. M. A. *Vibrational Spectroscopy of Solids*, Cambridge University Press: 1972.

14.     Wilson, E. B.;  Decius, J. C.; Cross, P. C. *Molecular Vibrations: The Theory of Infrared and Raman Vibrational Spectra*, Dover Publications: 1980.

15.     Painter, P. C.;  Coleman, M. M.; Koenig, J. L. *The Theory of Vibrational Spectroscopy and Its Application to Polymeric Materials*, Wiley: 1982.

16.     Decius, J. C.; Hexter, R. M. *Molecular Vibrations in Crystals* McGraw-Hill Inc. : United States of America, 1977.

17.     Kaufman, E. D. *Advanced Concepts in Physical Chemistry*, McGraw-Hill: 1966.

18.     Morse, P. M. Diatomic Molecules According to the Wave Mechanics. II. Vibrational Levels. *Phys. Rev.* **1929,** *34* (1), 57-64.

19.     Herzberg, G. *Molecular Spectra and Molecular Structure I. Spectra of Diatomic Molecules*, Krieger Pub Co.: 1989.

20.     Colaianni, S. E. M.; Nielsen, O. F. Low-frequency Raman Spectroscopy. *J. Mol. Struct.* **1995,** *347*, 267-283.

21.     McHale, J. L. *Molecular Spectroscopy*, CRC Press: 2017.

22. Cid, M. a.-M.; Bravo, J. *Structure Elucidation in Organic Chemistry: The Search for the Right Tools*, Wiley-VCH: Weinheim, Germany, 2015.

23. Hollas, J. M. *High Resolution Spectroscopy*, 2nd ed.; John Wiley & Sons Ltd.: West Sussex, England, 1998.

24. Siesler, H. W., Vibrational Spectroscopy. In *Reference Module in Materials Science and Materials Engineering*, Elsevier, 2016.

25. Fredericks, P.;  Rintoul, L.; Coates, J., Vibrational Spectroscopy: Instrumentation for Infrared and Raman Spectroscopy. 4 ed.; CRC Press, 2019; pp 165-232.

26. Moye, A. L.; Cochran, T. A. Simplified Infrared Functional Group Correlation Chart. *J. Chem. Educ.* **1972,** *49* (2), 129.

27. Socrates, G. *Infrared Characteristic Group Frequencies: Tables and Charts*, 2nd ed.; Wiley: New York;Chichester;, 1994.

28. Lin-Vien, D.;  Colthup, N. B.;  Fateley, W. G.; Grasselli, J. G. *The Handbook of Infrared and Raman Characteristic Frequencies of Organic Molecules*, Elsevier: 1991.

29. Barth, A. Infrared Spectroscopy of Proteins. *Biochim. Biophys. Acta, Bioenerg.* **2007,** *1767* (9), 1073-1101.

30. Fabian, H.; Mäntele, W. Infrared Spectroscopy of Proteins. *Handbook of vibrational spectroscopy* **2006**.

31. Yang, K.;  Zhang, S.;  Zhang, G.;  Sun, X.;  Lee, S.-T.; Liu, Z. Graphene in Mice: Ultrahigh In Vivo Tumor Uptake and Efficient Photothermal Therapy. *Nano Lett.* **2010,** *10* (9), 3318-3323.

32.    Nicolaï, B. M.;  Beullens, K.;  Bobelyn, E.;  Peirs, A.;  Saeys, W.;  Theron, K. I.;  Lammertyn, J. Nondestructive Measurement of Fruit and Vegetable Quality by Means of NIR Spectroscopy: A Review. *Postharvest Biol. Technol.* **2007,** *46* (2), 99-118.

33.    Wang, W.; Paliwal, J. Near-infrared Spectroscopy and Imaging in Food Quality and Safety. *Sens. Instrum. Food Qual. Saf.* **2007,** *1* (4), 193-207.

34.    Bureau, S.;  Ruiz, D.;  Reich, M.;  Gouble, B.;  Bertrand, D.;  Audergon, J.-M.; Renard, C. M. Rapid and Non-destructive Analysis of Apricot Fruit Quality using FT-near-infrared Spectroscopy. *Food Chem.* **2009,** *113* (4), 1323-1328.

35.    Hoffmann, G. *Raman Spectroscopy, Volume I : Principles and Applications in Chemistry, Physics, Materials Science, and Biology*, Momentum Press: New York, 2019.

36.    Graves, P. R.; Gardiner, D. J. *Practical Raman Spectroscopy*, 1989.

37.    Vandenabeele, P. *Practical Raman Spectroscopy: An Introduction*, John Wiley & Sons: 2013.

38.    Colthup, N. *Introduction to Infrared and Raman Spectroscopy*, Elsevier: 2012.

39.    Siebert, F.; Hildebrandt, P. *Vibrational Spectroscopy in Life Science*, Wiley: 2008.

40.    Thompson, J. M. *Infrared Spectroscopy*, Jenny Stanford Publishing: 2018.

41.    Schliesser, A.;  Picqué, N.; Hänsch, T. W. Mid-infrared Frequency Combs. *Nat. Photonics* **2012,** *6* (7), 440-449.

42.    Go, N.;  Noguti, T.; Nishikawa, T. Dynamics of a Small Globular Protein in Terms of Low-frequency Vibrational Modes. *Proc Natl Acad Sci U S A* **1983,** *80* (12), 3696-3700.

43.    Teeters, D.; Frech, R. Temperature Dependence of the Low-frequency Vibrational Modes in LiNaSO$_4$ and LiKSO$_4$. *Phys. Rev. B* **1982,** *26* (10), 5897.

44.     Larkin, P. J.;  Dabros, M.;  Sarsfield, B.;  Chan, E.;  Carriere, J. T.; Smith, B. C. Polymorph Characterization of Active Pharmaceutical Ingredients (APIs) Using Low-Frequency Raman Spectroscopy. *Appl. Spectrosc.* **2014,** *68* (7), 758-776.

45.     Strachan, C. J.;  Taday, P. F.;  Newnham, D. A.;  Gordon, K. C.;  Zeitler, J. A.;  Pepper, M.; Rades, T. Using Terahertz Pulsed Spectroscopy to Quantify Pharmaceutical Polymorphism and Crystallinity. *J. Pharm. Sci.* **2005,** *94* (4), 837-846.

46.     Yamamoto, S.;  Morisawa, Y.;  Sato, H.;  Hoshina, H.; Ozaki, Y. Quantum Mechanical Interpretation of Intermolecular Vibrational Modes of Crystalline Poly-(R)-3-Hydroxybutyrate Observed in Low-Frequency Raman and Terahertz Spectra. *J. Phys. Chem. B* **2013,** *117* (7), 2180-2187.

47.     Fumino, K.;  Reichert, E.;  Wittler, K.;  Hempelmann, R.; Ludwig, R. Low-Frequency Vibrational Modes of Protic Molten Salts and Ionic Liquids: Detecting and Quantifying Hydrogen Bonds. *Angew. Chem.* **2012,** *51* (25), 6236-6240.

48.     Damari, R.;  Weinberg, O.;  Krotkov, D.;  Demina, N.;  Akulov, K.;  Golombek, A.;  Schwartz, T.; Fleischer, S. Strong Coupling of Collective Intermolecular Vibrations in Organic Materials at Terahertz Frequencies. *Nat. Commun.* **2019,** *10* (1), 1-8.

49.     Parrott, E. P.; Zeitler, J. A. Terahertz Time-domain and Low-frequency Raman Spectroscopy of Organic Materials. *Appl. Spectrosc.* **2015,** *69* (1), 1-25.

50.     Zeitler, J.;  Taday, P.;  Newnham, D.;  Pepper, M.;  Gordon, K.; Rades, T. Terahertz-Pulsed Spectroscopy and Imaging in Pharmaceutical Setting. *J. Pharm. Pharmacol.* **2007,** *59*, 209-23.

51. Williams, M. R.; Aschaffenburg, D. J.; Ofori-Okai, B. K.; Schmuttenmaer, C. A. Intermolecular Vibrations in Hydrophobic Amino Acid Crystals: Experiments and Calculations. *J. Phys. Chem. B* **2013,** *117* (36), 10444-10461.

52. Dexheimer, S. L. *Terahertz Spectroscopy: Principles and Applications*, CRC Press: 2017.

53. Rettich, F.; Vieweg, N.; Cojocari, O.; Deninger, A. Field Intensity Detection of Individual Terahertz Pulses at 80 MHz Repetition Rate. *J. Infrared, Millimeter, Terahertz Waves* **2015,** *36* (7), 607-612.

54. Liu, G. Visualization of Patents and Papers in Terahertz Technology: A Comparative Study. *Scientometrics* **2013,** *94* (3), 1037-1056.

55. Schmuttenmaer, C. A. Exploring Dynamics in the Far-Infrared with Terahertz Spectroscopy. *Chem. Rev.* **2004,** *104* (4), 1759-1780.

56. Jepsen, P. U.; Cooke, D. G.; Koch, M. Terahertz Spectroscopy and Imaging – Modern Techniques and Applications. *Laser Photonics Rev.* **2011,** *5* (1), 124-166.

57. Wilke, I., Terahertz Spectroscopy Applications. In *Encyclopedia of Spectroscopy and Spectrometry (Third Edition)*, Lindon, J. C.; Tranter, G. E.; Koppenaal, D. W., Eds. Academic Press, Oxford, 2017; pp 427-431.

58. Prabhu, S. S., Terahertz Spectroscopy: Advances and Applications. 2017.

59. Neu, J.; Schmuttenmaer, C. A. Tutorial: An Introduction to Terahertz Time Domain Spectroscopy (THz-TDS). *J. Appl. Phys.* **2018,** *124* (23), 231101.

60. Naftaly, M.; Vieweg, N.; Deninger, A. Industrial Applications of Terahertz Sensing: State of Play. *Sensors (Basel)* **2019,** *19* (19), 4203.

61. Zhang, X. C.; Xu, J. *Introduction to THz Wave Photonics*, Springer US: 2009.

62. Withayachumnankul, W.; Fischer, B. M.; Abbott, D. Numerical Removal of Water Vapour Effects from Terahertz Time-domain Spectroscopy Measurements. *Proc. R. Soc. A* **2008,** *464* (2097), 2435-2456.

63. Vieweg, N.; Rettich, F.; Deninger, A.; Roehle, H.; Dietz, R.; Göbel, T.; Schell, M. Terahertz-time Domain Spectrometer with 90 dB Peak Dynamic Range. *J. Infrared, Millimeter, Terahertz Waves* **2014,** *35* (10), 823-832.

64. Raman, C. V.; Krishnan, K. S. A New Type of Secondary Radiation. *Nature* **1928,** *121* (3048), 501-502.

65. Kudelski, A. Analytical Applications of Raman Spectroscopy. *Talanta* **2008,** *76* (1), 1-8.

66. Mah, P. T.; Fraser, S. J.; Reish, M. E.; Rades, T.; Gordon, K. C.; Strachan, C. J. Use of Low-frequency Raman Spectroscopy and Chemometrics for the Quantification of Crystallinity in Amorphous Griseofulvin Tablets. *Vib. Spectrosc.* **2015,** *77*, 10-16.

67. Moser, C.; Havermeyer, F. Ultra-narrow-band Tunable Laserline Notch Filter. *Appl. Phys. B: Lasers Opt.* **2009,** *95* (3), 597-601.

68. Salim, M.; Fraser-Miller, S. J.; Bērziņš, K. r.; Sutton, J. J.; Ramirez, G.; Clulow, A. J.; Hawley, A.; Beilles, S. p.; Gordon, K. C.; Boyd, B. J. Low-Frequency Raman Scattering Spectroscopy as an Accessible Approach to Understand Drug Solubilization in Milk-Based Formulations during Digestion. *Mol. Pharmaceutics* **2020,** *17* (3), 885-899.

69. Hédoux, A.; Paccou, L.; Guinet, Y.; Willart, J. F.; Descamps, M. Using the Low-frequency Raman Spectroscopy to Analyze the Crystallization of Amorphous Indomethacin. *Eur. J. Pharm. Sci.* **2009,** *38* (2), 156-64.

70. Larkin, P. J.; Dabros, M.; Sarsfield, B.; Chan, E.; Carriere, J. T.; Smith, B. C. Polymorph characterization of active pharmaceutical ingredients (APIs) using low-frequency Raman spectroscopy. *Appl Spectrosc* **2014,** *68* (7), 758-76.

71. Bērziņš, K.; Fraser-Miller, S. J.; Gordon, K. C. Recent Advances in Low-Frequency Raman Spectroscopy for Pharmaceutical Applications. *Int. J. Pharm.* **2020**, 120034.

72. Bertoldo Menezes, D.; Reyer, A.; Yüksel, A.; Bertoldo Oliveira, B.; Musso, M. Introduction to Terahertz Raman spectroscopy. *Spectrosc. Lett.* **2018,** *51* (8), 438-445.

73. West, A. R. *Solid State Chemistry and its Applications*, Wiley: 2014.

74. Spiller, E. *Soft X-ray Optics*, SPIE Optical Engineering Press: Bellingham, Wash., USA, 1994.

75. Cole, R. H.; Coles, J. S. *Physical Principles of Chemistry* W.H. Freeman: 1965.

76. Kittel, C. *Introduction to Solid State Physics*, John Wiley & Sons: 1962.

77. Hammond, C. *The Basics of Crystallography and Diffraction*, Fourth ed.; Oxford University Press: Oxford, 2015.

78. Seeck, O. H.; Murphy, B. M. *X-ray Diffraction: Modern Experimental Techniques*, CRC Press: Boca Raton, Florida, 2014.

79. Bunaciu, A. A.; Udriştioiu, E. g.; Aboul-Enein, H. Y. X-Ray Diffraction: I nstrumentation and Applications. *Crit. Rev. Anal. Chem.* **2015,** *45* (4), 289-299.

80. Girolami, G. S. *X-Ray Crystallography*, University Science Books: 2015.

81. Lee, M. *X-ray Diffraction for Materials Research: From Fundamentals to Applications*, 1 ed.; Apple Academic Press: Oakville, ON, Canada;Waretown, NJ, USA;, 2016.

82.  Martz, H. E.;  Logan, C. M.;  Schneberk, D. J.; Shull, P. J. *X-ray Imaging: Fundamentals, Industrial Techniques, and Applications*, Taylor & Francis, CRC Press: Boca Raton, 2017.

83.  Moore, E. A.; Smart, L. *Solid State Chemistry: An Introduction*, CRC Press: 2020.

84.  Datta, A.;  Zhong, Z.; Motakef, S. A New Generation of Direct X-ray Detectors for Medical and Synchrotron Imaging Applications. *Sci. Rep.* **2020,** *10* (1), 20097.

85.  Hokkaido, M.; Nagano, E. *Crystallography: Research, Technology and Applications*, Nova Science Publishers: Hauppauge, N.Y, 2012.

86.  Hofman, E.;  Robinson, R. J.;  Li, Z.-J.;  Dzikovski, B.; Zheng, W. Controlled Dopant Migration in CdS/ZnS Core/Shell Quantum Dots. *J. Am. Chem. Soc.* **2017,** *139* (26), 8878-8885.

87.  Harris, K. D. M.;  Tremayne, M.; Kariuki, B. M. Contemporary Advances in the Use of Powder X-Ray Diffraction for Structure Determination. *Angew. Chem.* **2001,** *40* (9), 1626-1651.

88.  Souza, M. M.;  Maza, A.; Tuza, P. V. X-ray Powder Diffraction Data of $LaNi_{0.5}Ti_{0.45}Co_{0.05}O_3$, $LaNi_{0.45}Co_{0.05}Ti_{0.5}O_3$, and $LaNi_{0.5}Ti_{0.5}O_3$ Perovskites. *Powder Diffr.* **2021**, 1-6.

89.  Goloveshkin, A. S.;  Korlyukov, A. A.; Vologzhanina, A. V. Novel Polymorph of Favipiravir—An Antiviral Medication. *Pharmaceutics* **2021,** *13* (2), 139.

90.  Scrivens, G.;  Ticehurst, M.; Swanson, J. T., Chapter 7 - Strategies for Improving the Reliability of Accelerated Predictive Stability (APS) Studies. In *Accelerated Predictive Stability*, Qiu, F.; Scrivens, G., Eds. Academic Press, Boston, 2018; pp 175-206.

91.  Chauhan, A.; Chauhan, P. Powder XRD Technique and its Applications in Science and Technology. *J. Anal. Bioanal. Tech* **2014,** *5* (5), 1-5.

92.   Karki, S.;  Fábián, L.;  Friščić, T.; Jones, W. Powder X-ray Diffraction as an Emerging Method to Structurally Characterize Organic Solids. *Org. Lett.* **2007,** *9* (16), 3133-3136.

93.   Simon, S. H. *The Oxford Solid State Basics*, OUP Oxford: 2013.

94.   Dinnebier, R. E.;  Billinge, S. J. L.;  Chemistry, R. S. o.;  Bail, A. L.;  Cranswick, L. M. D.; Madsen, I. *Powder Diffraction: Theory and Practice*, Royal Society of Chemistry: 2008.

95.   Louër, D.; Boultif, A. Some Further Considerations in Powder Diffraction Pattern Indexing with the Dichotomy Method. *Powder Diffr.* **2014,** *29* (S2), S7-S12.

96.   Coelho, A. A. An Indexing Algorithm Independent of Peak Position Extraction for X-ray Powder Diffraction Patterns. *J. Appl. Crystallogr.* **2017,** *50* (5), 1323-1330.

97.   Gates-Rector, S.; Blanton, T. The Powder Diffraction File: A Quality Materials Characterization Database. *Powder Diffr.* **2019,** *34* (4), 352-360.

98.   Paul, E. L.;  Tung, H.-H.; Midler, M. Organic Crystallization Processes. *Powder Technol.* **2005,** *150* (2), 133-143.

99.   Tung, H. H.;  Paul, E. L.;  Midler, M.; McCauley, J. A. *Crystallization of Organic Compounds: An Industrial Perspective*, Wiley: 2009.

100.   Beis, K.; Evans, G. *Protein Crystallography: Challenges and Practical Solutions*, Royal Society of Chemistry: London, UK, 2018.

101.   Sherwood, D.; Cooper, J. *Crystals, X-rays, and Proteins: Comprehensive Protein Crystallography*, Oxford University Press: New York, 2011.

102.   Weber, P. C., Overview of Protein Crystallization Methods. In *Methods in Enzymology*, Academic Press, 1997; Vol. 276, pp 13-22.

103.    Glusker, J. P.; Trueblood, K. N. *Crystal Structure Analysis: A Primer*, 3rd ed.; Oxford University Press: New York;Oxford;, 2010.

104.    Sheldrick, G. A Short History of SHELX. *Acta Crystallogr., Sect. A: Found. Adv.* **2008,** *64* (1), 112-122.

105.    Patterson, A. L. A Fourier Series Method for the Determination of the Components of Interatomic Distances in Crystals. *Phys. Rev.* **1934,** *46* (5), 372-376.

106.    Monaco, H. L.;  Artioli, G.;  Viterbo, D.;  Ferraris, G.;  Gilli, G.;  Zanotti, G.; Catti, M. *Fundamentals of Crystallography*, Oxford university press, USA: 2002.

107.    Giacovazzo, C.;  Siliqi, D.;  Gonzalez Platas, J.;  Hecht, H. J.;  Zanotti, G.; York, B. The ab initio Crystal Structure Solution of Proteins by Direct Methods. VI. Complete Phasing up to Derivative Resolution. *Acta Crystallographica, Section D: Biological Crystallography* **1996,** *52* (Pt 4), 813-25.

108.    Müller, P.;  Herbst-Irmer, R.;  Spek, A. L.;  Schneider, T. R.; Sawaya, M. R. *Crystal Structure Refinement: A Crystallographer's Guide to SHELXL*, Oxford University Press: Oxford, 2006.

109.    Li, J.;  Abramov, Y. A.; Doherty, M. F. New Tricks of the Trade for Crystal Structure Refinement. *ACS Cent. Sci.* **2017,** *3* (7), 726-733.

110.    Powell, H. R. X-ray data processing. *Biosci. Rep.* **2017,** *37* (5), BSR20170227.

111.    Luger, P. *Modern X-ray Analysis on Single Crystals: A Practical Guide*, 2nd fully revis and extend ed.; De Gruyter: Berlin;Boston;, 2014.

# Chapter 4: Procedure for Experimental and Theoretical Characterization of Solids

## 4.1. Introduction

The following chapter outlines various procedures used to apply the foundations established by Chapters 2 and 3. These procedures can be modified to better suit the user's exact needs, with the hope that each section can serve as a user-friendly guide. Critical aspects of each procedure are outlined as well as some of the more subtle intricacies.  The first section is devoted to solid-state density functional theory calculations using the CRYSTAL17 software package detailing a few of the common applications used in this work. The remaining sections focus on sample preparation, data collection, and data processing for a series of experimental methods including: terahertz time-domain spectroscopy, low-frequency Raman spectroscopy, powder X-ray diffraction, and single-crystal X-ray diffraction.

## 4.2 Solid-state Density Functional Theory

Solid-state density functional theory (ss-DFT) calculations were performed using the *ab initio* periodic software package, CRYSTAL. Since its initial release in 1988, subsequent versions have been released implementing new features and algorithms, with the calculations in this work performed using CRYSTAL17.[1, 2] CRYSTAL17 has many keywords and parameters that can be used to fine-tune each calculation to the needs of the user. The following discussion is intended to serve as a guide to understanding the 'typical' process of running a geometry optimization and harmonic vibrational frequency calculation and is in no way intended to be

exhaustive as to the potential applications and keywords implemented in the software. Additional help on preparing CRYSTAL input files and understanding CRYSTAL output files can be found in the CRYSTAL user's manual and through an online set of tutorials provided by the software developers.[3]

When defining block 1 of the input file (the section dedicated to the geometry input), the user must first define the dimensionality of the system. In the case of modeling crystalline solids, the appropriate keyword to come after the title is **CRYSTAL**, indicating that the system being studied is in three dimensions. The next line is composed of three integers, the first, to set whether the space group is being defined by space group number or by the Hermann-Mauguin alphanumeric code, the second, to set the type of cell (refers to rhombohedral groups), and the third, to set the origin of the unit cell. Example 1 in **Figure 4-1** uses the space group number, and so a is the first digit on the third line of the input file, with the number 14 on the following line indicating that the space group to use is $P2_1/c$. To explicitly define the space group by name instead of number, example 2 in **Figure 4-1** can be used with the first digit on the third line of the input file being a 1, indicating that the alphanumeric code will come on the following line. This is the method that must be used when using a non-standard space group setting, as seen in example 3 in **Figure 4-1** such as using the space group $P2_1/n$. The next two lines list the minimal set of lattice parameters necessary, as defined by the Bravais lattice, and the number of atoms in the asymmetric unit, respectively. The proceeding lines then describe the relative positions of each atom in the asymmetric unit cell, listing the conventional atomic number followed by the fractional coordinates (x/a, y/b, z/c), with starting lattice dimensions and atomic positions often obtained through X-ray diffraction studies. For previously published crystal structures, the Cambridge Crystallographic Data Centre (CCDC) is an excellent resource that can be accessed

through the ConQuest application or the online repository.[4, 5] The geometry input block must then be closed with the keyword **END**.

| 1. TITLE | 2. TITLE | 3. TITLE |
|---|---|---|
| CRYSTAL | CRYSTAL | CRYSTAL |
| 0 0 0 | 1 0 0 | 1 0 0 |
| 14 | P 21/c | P 21/n |

**Figure 4-1.** Different ways to enter space group symmetry into a CRYSTAL input file.

The second block of the input file is dedicated to defining the basis set and setting the initial electron configuration. To construct the one-electron wavefunctions, CRYSTAL expresses the crystalline orbitals through a series of Gaussian-type atomic orbitals with the option to include an effective core potential. CRYSTAL17 has a number of internally stored basis sets, but it also allows the option for manual input. To use an internally stored basis set, the **END** keyword used to close block 1 must be removed and block 2 must be opened using the keyword **BASISSET** followed by the keyword for the desired basis set on the next line. There are no additional keywords necessary to close block 2 when using an internally stored basis set. If the desired basis set is not internally stored, the Basis Set or Basis Sets Library on the CRYSTAL webpage can be used.[6-8] While there is currently no option to download basis sets in the CRYSTAL format from the Basis Set Exchange, the conversion can be easily done manually starting from the Gaussian format. The Gaussian basis sets downloaded from the Basis Set Exchange are expressed using a series of shells and primitives as seen in **Figure 4-2**. To convert from a Gaussian to a CRYSTAL format, the first line will be composed of the conventional

atomic number followed by the total number of shells for the element. The next line introduces

the first shell by listing the basis set type, type of shell, number of primitives, number of

electrons, and a scale factor. Below that line, the primitives for the specified shell are described

using the exponent and a contraction coefficient from the Gaussian format. These same steps are

repeated for each shell of the element being described, and then for each element present. An

example of converting from a Gaussian formatted basis set to a CRYSTAL formatted basis set is

given in **Figure 4-3** for carbon using the 6-311G(d,p) basis set (listed in the Basis Set Exchange

as 6-311G**).[9] To close block 2 for a manually input basis set, the section should be closed with

the 2-line sequence of **99 0** followed by **END**.

```
C   0
S   6  1.00
    0.3047524880D+04    0.1834737132D-02        Primitive 1
    0.4573695180D+03    0.1403732281D-01        Primitive 2
    0.1039486850D+03    0.6884262226D-01        Primitive 3        Shell 1
    0.2921015530D+02    0.2321844432D+00        Primitive 4
    0.9286662960D+01    0.4679413484D+00        Primitive 5
    0.3163926960D+01    0.3623119853D+00        Primitive 6
SP  3  1.00
    0.7868272350D+01   -0.1193324198D+00    0.6899906659D-01        Primitive 1
    0.1881288540D+01   -0.1608541517D+00    0.3164239610D+00        Primitive 2    Shell 2
    0.5442492580D+00    0.1143456438D+01    0.7443082909D+00        Primitive 3
SP  1  1.00
    0.1687144782D+00    0.1000000000D+01    0.1000000000D+01        Primitive 1    Shell 3
```

**Figure 4-2.** Difference between shells and primitives in the Gaussian format of the 6-31G(d,p) basis set for carbon.

| Gaussian | | | CRYSTAL | | |
|---|---|---|---|---|---|
| | | | 6 5 | | |
| | | | 0 0 6 2.0 1.0 | | |
| C  S | | | | | |
| 4563.240 | 0.00196665 | | 4563.240 | 0.00196665 | |
| 682.0240 | 0.0152306 | | 682.0240 | 0.0152306 | |
| 154.9730 | 0.0761269 | | 154.9730 | 0.0761269 | |
| 44.45530 | 0.2608010 | | 44.45530 | 0.2608010 | |
| 13.02900 | 0.6164620 | | 13.02900 | 0.6164620 | |
| 1.827730 | 0.2210060 | | 1.827730 | 0.2210060 | |
| C  SP | | | 0 1 3 4.0 1.0 | | |
| 20.96420 | 0.114660 | 0.0402487 | 20.96420 | 0.114660 | 0.0402487 |
| 4.803310 | 0.919999 | 0.237594 | 4.803310 | 0.919999 | 0.237594 |
| 1.459330 | -0.00303068 | 0.815854 | 1.459330 | -0.00303068 | 0.815854 |
| C  SP | | | 0 1 1 0.0 1.0 | | |
| 0.4834560 | 1.000000 | 1.000000 | 0.4834560 | 1.000000 | 1.000000 |
| C  SP | | | 0 1 1 0.0 1.0 | | |
| 0.1455850 | 1.000000 | 1.000000 | 0.1455850 | 1.000000 | 1.000000 |
| C  D | | | 0 3 1 0.0 1.0 | | |
| 0.626 | 1.000000 | | 0.626 | 1.000000 | |

**Figure 4-3.** Conversion of the 6-311G(d,p) basis set for carbon from Gaussian to CRYSTAL format.

The final block of the input file is devoted to specifying the Hamiltonian and choosing the parameters for the self-consistent field (SCF). The only required input to this section is to set the shrinking parameters through the keyword **SHRINK**. This is done by listing the desired Pack-Monkhorst shrinking factor and Gilat shrinking factor on the following line.[10-12] The section must then be closed with the keyword **END**. A minimal input file for crystalline L-cystine is presented in **Figure 4-4** using the published SC-XRD structure obtained at 110 K.[13] While the presented input file is quite short, a number of additional parameters are included in

the calculation using their designated default values including: the choice of Hamiltonian, the coulomb and exchange sums truncation criteria (modified using the keyword **TOLINTEG**), and the energy difference necessary between SCF cycles for convergence (modified using the keyword **TOLDEE**).[14-16]

```
BASIC INPUT FILE FOR L-CYSTINE FROM CSD CODE LCYSTI14
CRYSTAL
0 0 0
178
5.412 55.956
13
1          -0.31048          0.42059          0.06023
1          -0.44231          0.65857          0.06635
1          -0.40397          0.57561          0.0241
1          0.01816           0.52107          0.02503
1          0.22427           0.86655          0.03052
1          0.04481           0.75936          0.00508
6          -0.172            1.0311           0.02913
6          -0.2129           0.732            0.03332
6          -0.2656           0.6395           0.05941
7          0.032             0.7173           0.02317
8          0.0738            1.225            0.02275
8          -0.383            1.0614           0.0323
16         0.03234           0.8306           0.0798
BASISSET
def2-SVP
SHRINK
4 1
END
```

**Figure 4-4.** Minimal set of input parameters necessary to run a CRYSTAL calculation.

To begin the process of evaluating a crystalline system, the basic input file seen in **Figure 4-4** needs to be modified. First, to use a density functional theory (DFT) Hamiltonian, block 3 should contain the keyword **DFT**, followed by the desired exchange and correlation functionals to be used and closed with the keyword **END**. A range of functionals are included in the CRYSTAL software package ranging from simplistic local-density approximations to complex double-hybrids. If a dispersion correction is desired, the **-D3** prefix can be added to parameterized functionals or the D3 input block can be opened using the keyword **DFTD3**.[17-20] Within this input block, different versions of Grimme's dispersion correction can be selected using varying damping functions as well as the inclusion of the three-body dispersion term (**ABC**).[21] The choice of functional has large implications on the remainder of the calculation, influencing computational time, necessary parameter thresholds, and, most importantly, calculation accuracy.

The first set of calculations that should be run when evaluating a solid are focused on determining the appropriate shrinking parameters with the same value typically used for both the Pack-Monkhorst shrinking factor and the Gilat shrinking factor. To determine an appropriate shrinking factor, a series of single point energy calculations can be run at varying shrinking factors using a **TOLDEE** of 10. Once the total energy has converged, the shrinking factors can be set. However, they should be checked periodically throughout the process of studying a system, as changes to lattice dimension and functional choice can impact the appropriate shrinking values. If the calculation does not finish using the default number of allowed SCF cycles, this number can be increased by inserting the **MAXCYCLE** keyword in block 3 of the input file, followed on the next line by the desired limit of SCF cycles allowed. The convergence of the total energy for the L-cystine structure given in **Figure 4-4** using the PBE-D3 functional

with the built in def2-SVP basis set is given in **Figure 4-5**, indicating the appropriate shrinking value is 10.
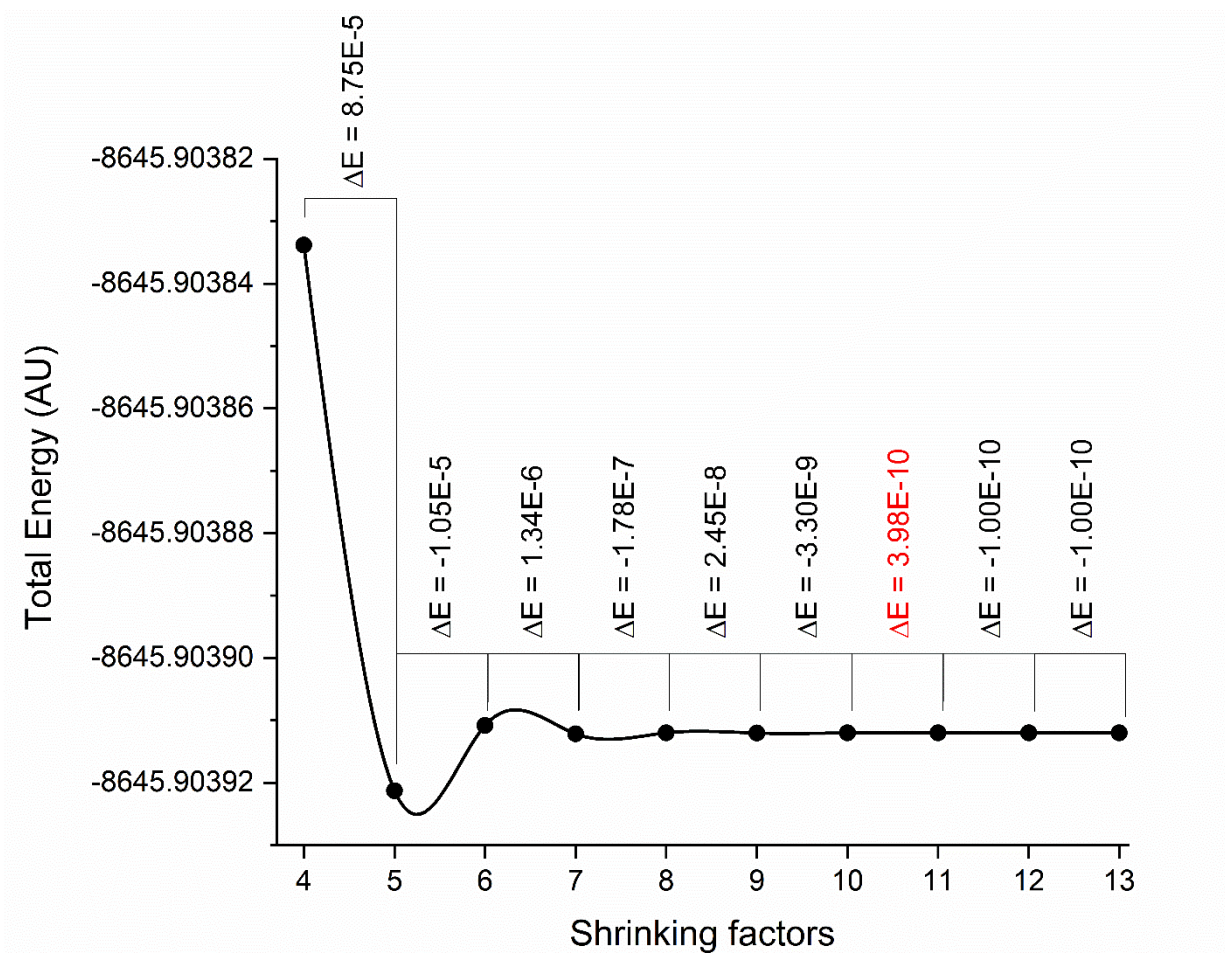


**Figure 4-5.** Determination of appropriate shrinking factors for L-cystine.

To calculate the equilibrium structure, the keyword **OPTGEOM** should be added to block 1 to optimize both the lattice parameters and the atomic coordinates. [22] The value for **TOLDEE** should also be changed to 8 to ensure acceptable levels of convergence are reached for a geometry optimization. By default, the geometry optimization restarts until the single-point energy and gradient convergence criteria are satisfied. For more stringent gradient criteria, the keywords **TOLDEG** and **TOLDEX** are often set to 0.000010 and 0.000040, respectively. If the optimization ends before convergence is achieved, the number of allowed optimization steps can be increased using the **MAXCYCLE** keyword in the geometry optimization block. When an optimization struggles to converge, it may indicate a problem with the set space group symmetry, or the arrangement of the atoms within the unit cell. If this is not the case, changing to a different functional/ basis set may relieve the problems as well as increasing the **TOLINTEG** and **FMIXING** values. A common problem encountered when using a hybrid functional or a large basis set with diffuse functions is that the SCF cycles indicate a possible conduction state for what is a well-known insulator. To address this problem, either the size of the basis set can be reduced, or the values assigned to the **TOLINTEG** keyword can be increased. The geometry optimization input section must then be closed with the keyword **END**. A sample geometry optimization calculation is included in **Figure 4-6**, based off the L-cystine shrink calculations performed in **Figure 4-5**. A geometry optimization can be restarted from a previous unfinished calculation, given the proper restart files are included in the restart directory, and the keyword **RESTART** is added to the **OPTGEOM** block.

```
BASIC INPUT FILE FOR L-CYSTINE FROM CSD CODE LCYSTI14
CRYSTAL
0 0 0
178
5.412 55.956
13
1               -0.31048              0.42059              0.06023
1               -0.44231              0.65857              0.06635
1               -0.40397              0.57561              0.0241
1               0.01816               0.52107              0.02503
1               0.22427               0.86655              0.03052
1               0.04481               0.75936              0.00508
6               -0.172                1.0311               0.02913
6               -0.2129               0.732                0.03332
6               -0.2656               0.6395               0.05941
7               0.032                 0.7173               0.02317
8               0.0738                1.225                0.02275
8               -0.383                1.0614               0.0323
16              0.03234               0.8306               0.0798
OPTGEOM
TOLDEG
0.000010
TOLDEX
0.000040
END OPTGEOM
BASISSET
def2-SVP
DFT
PBE-D3
END DFT
SHRINK
10 10
TOLDEE
8
END
```

**Figure 4-6.** Sample geometry input for L-cystine using PBE-D3 with the def2-SVP basis set.

The optimized geometry should then be converted into a crystallographic information file (.cif), so that the external and internal structure can be compared to experimental measurements. Keep in mind that the output file will print the fractional coordinates for all atoms in the unit cell, but only the atoms that belong to the asymmetric unit (demarked with a T in the listing of the atoms) are needed. The symmetry operations associated with the given space group will replicate the asymmetric unit to produce a representative unit cell. To view each step along the geometry optimization, the output file can be loaded into the Jmol software, or the steps can be transformed into a .cif, and visualized using the CCDC software, Mercury.[5, 23-25] The lattice dimensions of the optimized structure obtained from the above input file (**Figure 4-6**) are compared to published SC-XRD data in **Table 4-1**. It has been found that errors less than 1% in the external lattice dimensions are usually necessary to produce quality vibrational frequency calculations. Additional keywords can be included in the geometry optimization block to fix elements of the external and internal structure, such as fixing the lattice dimensions or atomic positions.

**Table 4-1.** Percent error in the lattice dimensions of L-cystine after full geometry optimization.

|                | Experiment (100 K) | Theory | Percent Error |
|----------------|--------------------|--------|---------------|
| a (Å)          | 5.412              | 5.347  | -1.20 %       |
| b (Å)          | 5.412              | -      | -             |
| c (Å)          | 55.956             | 55.806 | -0.27 %       |
| α (°)          | 90                 | -      | -             |
| β (°)          | 90                 | -      | -             |
| γ (°)          | 120                | -      | -             |

To perform a harmonic frequency calculation, the input file should be updated to include the lattice dimensions and fractional atomic positions from the geometry optimization and the **TOLDEE** should be set to 10. Block 1 is then modified to remove all keywords from the **OPTGEOM** block and replace them with the keyword **FREQCALC** for a harmonic frequency calculation. Ultimately, this block needs to be closed with the keyword **END**. Similar to a geometry optimization, a frequency calculation can be restarted from a previous unfinished calculation, if the proper restart files are included, and the keyword **RESTART** is added to the **FREQCALC** block. To more accurately compute the numerical first derivative of the gradient, the keyword **NUMDERIV** can be included in the **FREQCALC** block followed by the number 2 on the next line to calculate two displacements for each atom along each cartesian direction using the central-difference formula.[26] This keyword has proven useful for removing small negative calculated vibrational frequencies.

Within the **FREQCALC** block, keywords can be included to calculate IR and Raman intensities. IR intensities can be calculated through the inclusion of the **INTENS** keyword through the default Berry phase approach, but, if the goal is to additionally calculate Raman intensities, the keyword **INTRAMAN** should follow **INTENS** to open the Raman intensities block followed by the keyword **INTCPHF** to use the Coupled-Perturbed Hartree-Fock/Kohn-Sham approach.[27-31] This results in the Raman tensor being calculated through applying an electric field along each cartesian direction until the CPHF process has converged to the limits set by the keyword **TOLALPHA**. The tensor is then stored in the file TENS_RAMAN.DAT. Inserting the keywords **ANDERSON** and **ANDERSON2** in the INTCPHF block can be helpful in accelerating convergence.[26] An example input file based upon the previous geometry

optimization to calculate both IR and Raman harmonic vibrational frequencies and intensities is

given in **Figure 4-7**.

```
BASIC FREQUENCY CALCULATION (IR & RAMAN) FOR L-CYSTINE FROM CSD CODE LCYSTI14
CRYSTAL
0 0 0
178
5.34721122          55.80635068
13
1          -0.320513766712700 0.403231391143200   0.060419208441340
1          -0.458352995396400 -0.358889441562000  0.066412035206960
1          -0.421345290124100 -0.433829858767800  0.023882018775660
1          0.011566190372010  -0.491875763918000  0.023344546662740
1          0.228312366055000  -0.135063894969100  0.029327996895500
1          0.021363958546940  -0.239886984822200  0.003947206930281
6          -0.188318494831000 0.025794541671070   0.029272367942300
6          -0.221974719802700 -0.274525346329200  0.033229405649550
6          -0.269613996028200 -0.368574053355300  0.059412761889200
7          0.023938896459790  -0.285496992580600  0.022198516883090
8          0.060027126985300  0.227809604721700   0.022538316630630
8          -0.402899382904400 0.056512287540840   0.032895055101660
16         0.036544269579770  -0.173981051594400  0.079725062714360
FREQCALC
INTENS
INTRAMAN
INTCPHF
END INTCPHF
END FREQCALC
BASISSET
def2-SVP
DFT
PBE-D3
END DFT
SHRINK
10 10
TOLDEE
10
END
```

**Figure 4-7.** Sample input file for L-cystine using PBE-D3 with the def2-SVP basis set to calculate harmonic frequency positions, IR intensities and Raman intensities.

The calculated frequency, positions, and intensities can then be convolved for comparison to experiment using the relationship described in Eq. 4.4. Here, a normalized Lorentzian line shape ($L$) is applied to the calculated frequencies ($v_0^i$, cm$^{-1}$) and intensities ($A$, km/mol) to produce spectra in terms of the molar attenuation coefficient ($\varepsilon$, M$^{-1}$cm$^{-1}$) for a given frequency ($v$).[32] The 100/ln(10) seen in equation (4.1) serves as a conversion factor to ultimately produce a spectra of intensity vs. frequency in the desired units. The normalized Lorentzian line shape can be further defined in equation (4.2) with the addition of the full width at half maximum (FWHM) ($\Gamma$, cm$^{-1}$). The value used for FWHM is dependent on the sample and temperature, with broad, room temperature peaks typically having a larger FWHM value. To determine the FWHM that should be used to convolve predicted vibrational frequencies, the experimental peaks should be fit using a peak fitting software. In the case of L-cystine, a FWHM of 4.0 cm$^{-1}$ is appropriate for the terahertz peak widths seen while 2.5 cm$^{-1}$ is appropriate for the Raman peak widths seen in cryogenic experiments.

$$\varepsilon(v) = \frac{100}{\ln(10)} \sum \left[ L\left(v, v_0^i, \Gamma\right) * A(i, v_0^i) \right]$$

$$(4.1)$$

$$L\left(v, v_0^i, \Gamma\right) = \frac{1}{\pi} \frac{\frac{1}{2}\Gamma}{(v - v_0^i)^2 + (\frac{1}{2}\Gamma^2)}$$

$$(4.2)$$

Both the low-frequency IR-active and Raman-active vibrational modes predicted using the PBE-D3/6-311G(d,p) level of theory show strong agreement with the experiment (**Figure 4-8** and **Figure 4-9**). When making comparisons between structures calculated using a full geometry optimization and experiment, lower experimental temperatures are preferred as the calculations are performed at 0 K. The calculated terahertz spectrum predicts the correct number of peaks with mostly appropriate intensities as seen in **Figure 4-8**. The predicted low-frequency Raman spectrum from the results of the input file described in **Figure 4-7** do a good job as well of predicting the position of the vibrational frequency, but do not properly capture the intensities (**Figure 4-9**). To account for experimental conditions, the keyword **RAMEXP** can be inserted below **INTRAMAN** with the following line listing the sample temperature (K) and the wavelength of the incident beam (nm).[33] Inserting a temperature of 78.0 and a wavelength of $\lambda =$ 784.7 nm provides much better intensities as shown in **Figure 4-9**. Volume dependent frequencies can be calculated using the Quasi-Harmonic Approximation through entering the keyword **QHA** within the **FREQCALC** block.[34-37] This keyword automatically performs a series of fixed volume geometry optimizations and subsequent frequency calculations. Take note that this keyword changes the default criteria to compute all bielectronic integrals exactly, just as the keyword **NOBIPOLA** does.
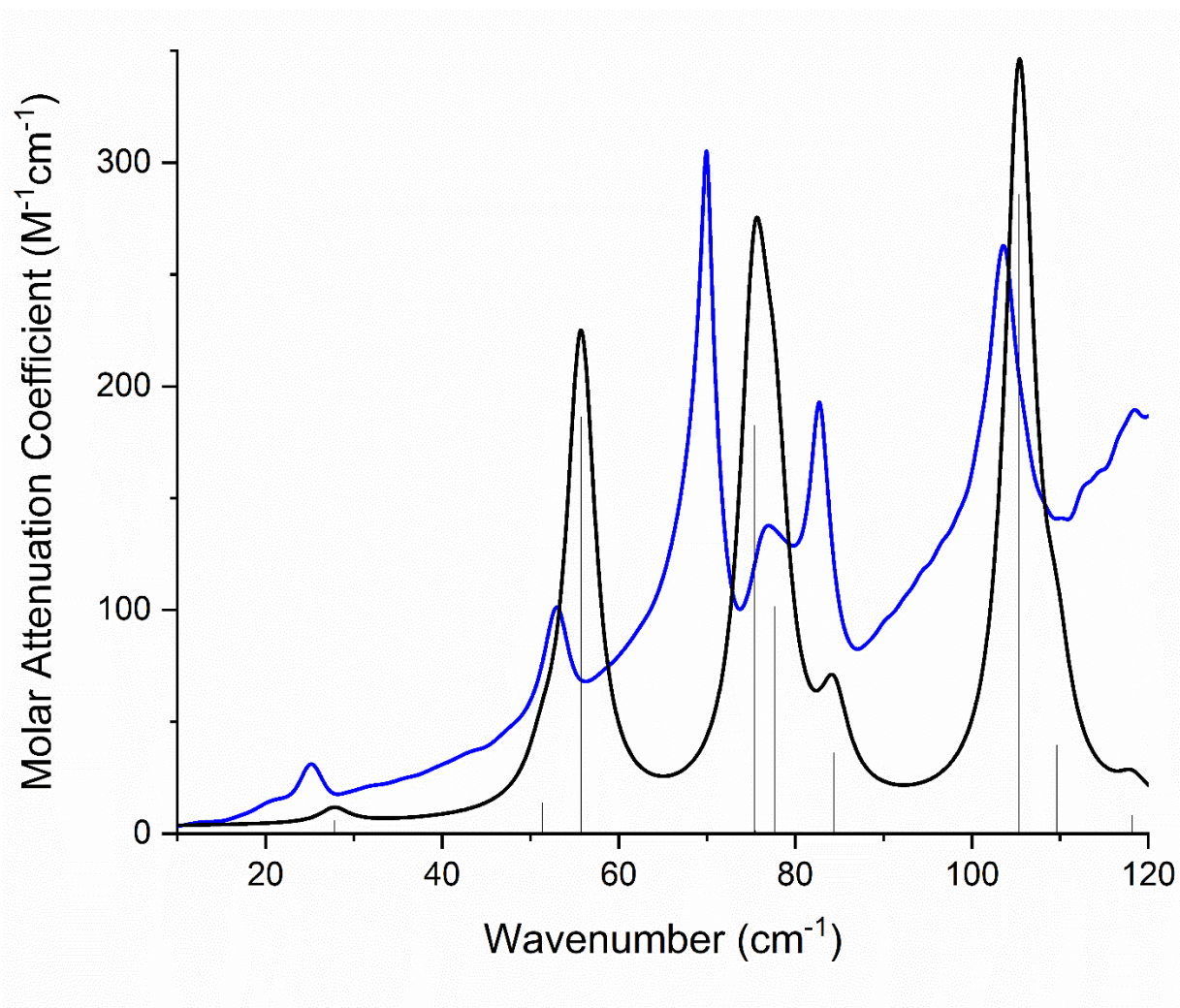
**Figure 4-8.** Overlay of convolved terahertz spectrum for L-cystine using a FWHM of 4.0 cm$^{-1}$ (black) with peak positions denoted as scaled sticks and 50 K experiment (blue) from 10 – 120 cm$^{-1}$.
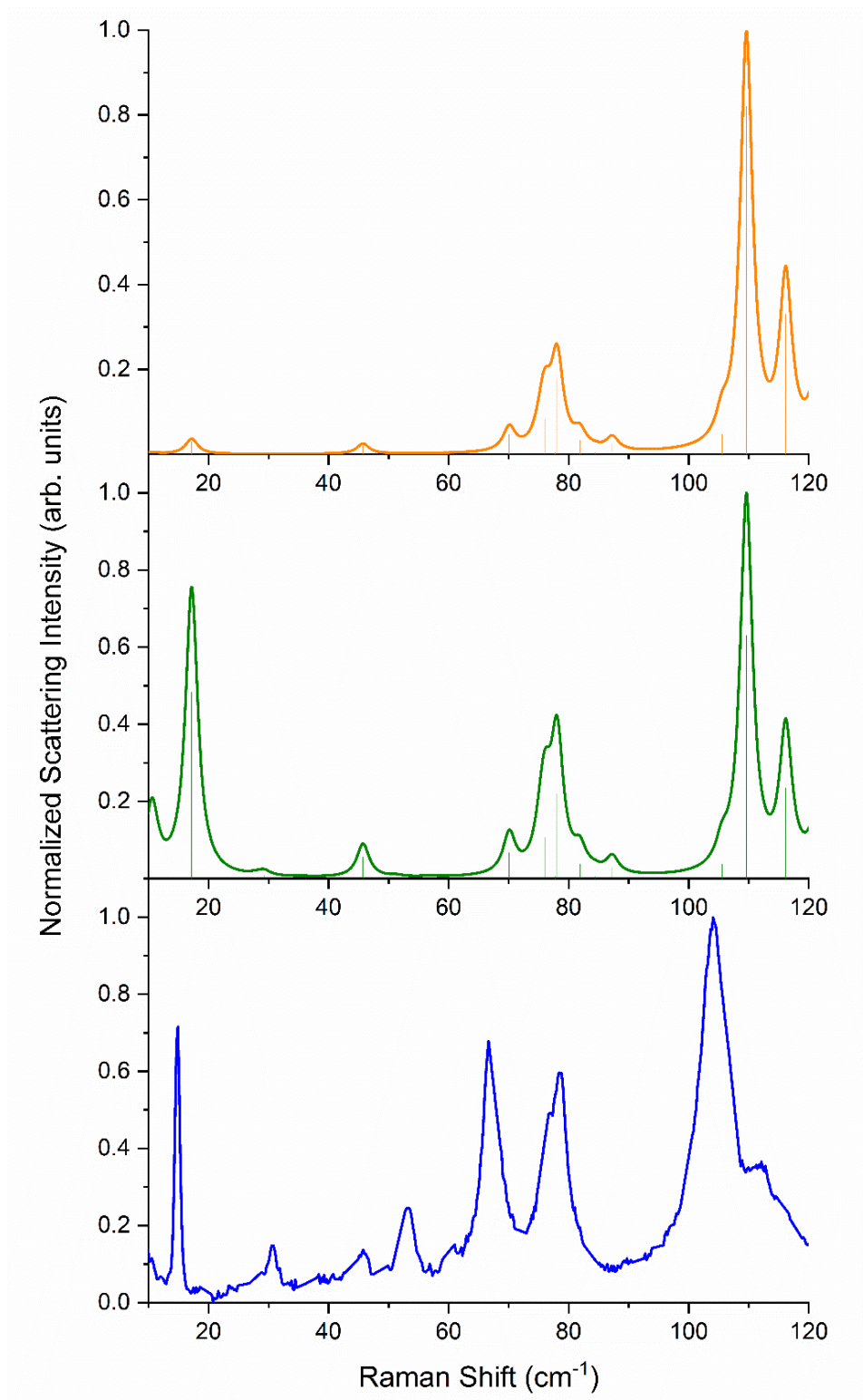
**Figure 4-9.** Comparison of 78 K LFRS (blue) of L-cystine and the predicted vibrational frequencies and intensities using a FWHM of 2.5 cm$^{-1}$ with (green) and without (orange) the INTRARAMAN keyword.

While the predicted vibrational frequency positions and intensities allow mode assignments to be made, they do not provide any detail into the character of the individual modes. Just as with the geometry optimization steps, each normal mode can be visualized by opening the CRYSTAL17 output file in Jmol.[23] This qualitative approach is useful for describing the motions of the molecules within the unit cell, but in the past, has struggled to visualize multiple unit cells using the shortcut buttons. This problem has been addressed by using the script editor and manually defining the packing of the cell. For example, to load the 4$^{th}$ normal mode for a file titled output.out, 'load output.out -4 packed 0.5' would be entered into the script editor. The final number, 0.5 in the example, can be modified to change the number of molecules displayed. The script editor can also be used to turn vibrations on and off, scale the amplitude of the vibration, change the colors displayed, and print a series of images that can ultimately be strung together to create a .gif. To create a .gif of a desired vibration, the command 'write VIBRATION n "filename"' should be entered, where n is the number of vibration cycles. A minimum of four vibration cycles has been needed to create quality .gifs. This command produces a series of JPG files that can be strung together using VideoMach 5.15.1 to produce a .gif.[38] This software has the added benefit of being able to crop the frames, add filters, and remove the background to leave a transparent image.

For a more quantitative approach, the eigenvectors for each eigenvalue can be analyzed. The eigenvectors can be found under the heading 'NORMAL MODES NORMALIZED TO CLASSICAL AMPLITUDES (IN BOHR)' after the printing of the frequency positions and intensities. These eigenvectors can be used for each normal mode to sum the total motion along each crystallographic axes as well as total motion attributed to an atom or group of atoms, and the transpose function in Microsoft Excel is helpful to organizing the list of eigenvectors into a

format that can be easily read and analyzed. The eigenvectors can also be used to create a .cif to visualize the displacement coordinates that can then be used to compare changes in packing arrangement, bond length, bond angle, etc. To obtain a .cif representative of the eigenvector displacements, the general steps can be followed:

1. Obtain the original cartesian coordinates for either the asymmetric unit or the full unit cell in Ångstrom.

2. Convert the cartesian coordinates from Ångstrom to Bohr Radius (1 Å = 1.8897 Bohr radius).

3. Obtain the eigenvectors for the mode of interest; these will be given in Bohr radius from the output file.

4. Choose a scalar to apply to the eigenvector displacements and apply that scalar to the eigenvectors from step 3. Keep in mind, these vibrations are quite small displacements of the unit cell, and the scalar is applied to better visualize the changes from the equilibrium structure.

5. Add the scaled eigenvectors to the equilibrium positions; this will be in units of Bohr radius.

6. Convert the coordinates from step 5 to units of Ångstrom.

7. The converted cartesian coordinates must then be transformed back to fractional coordinates. This is done using the transformation matrix, or the inverse of the direct lattice vectors that is printed in the CRYSTAL output file.

8. The coordinates from step 7 are now in fractional coordinates for the lattice dimensions of the equilibrium structure and can be placed into a $P1$ .cif.

Keep in mind, the .cif should not be used to assign quantitative values to changes in internal structure but as a comparison of the percent changes across the unit cell.

## 4.3 Terahertz Time-Domain Spectroscopy

To prepare a crystalline solid for evaluation using terahertz time-domain spectroscopy (THz-TDS), the sample was first pressed into a free-standing pellet conducive to the sample holder being used. In the Korter research lab at Syracuse University, the pellets were designed to be 13 mm in diameter with an ideal thickness of 3 mm. Pellets made of pure sample often absorb terahertz radiation above the dynamic range of the instrument, so they were diluted with a transparent matrix material.[39] Polytetrafluoroethylene (PTFE) is an excellent choice to serve as a matrix material when making terahertz pellets, with polyethylene and adamantane being common choices as well.[40-49] The majority of pellets analyzed fell within the range of $1 - 3\%$ w/w, while weakly absorbing samples required concentrations of up to 20% w/w.[50] Once the sample and matrix material were weighed out in the correct proportions, the mixture was pulverized in a ball mill to minimizes particle size and produce a homogeneous distribution of the sample and matrix material.[51, 52] The thoroughly mixed material was then pressed into a 13 x 3 mm pellet under 2000 psig of pressure. The final weight of these pellets was typically around 900 mg depending on the compressibility of the sample. A second pellet was then made of pure matrix material to serve as a reference measurement and was made to be of similar thickness to the pellet that contained the sample.

Measurements for this work were taken using the Toptica TeraFlash spectrometer described in **Chapter 3** at Syracuse University in Dr. Timothy Korter's research lab (**Figure 4-**

**10**) and at the University of Vermont in Dr. Michael Ruggiero's research lab. At Syracuse University, a Janis ST-100 optical cryostat was used to hold the samples, while at the University of Vermont, a closed-cycle helium cryostat from Cryocool Industries was used. Both cryostats were equipped with polymethylpentene (TPX) windows to allow terahertz radiation to pass through holding up to three free-standing pellets at a time.[53] The use of a mechanical stage allowed the pellet of interest to be placed in the path of the THz beam. After the sample and reference pellets were loaded into the cryostat, the sample chamber was evacuated, and the area surrounding the photoconductive antennas was purged with dry air. These steps helped to reduce the presence of strongly absorbing water vapor. At the time of the experiments, data collected at Syracuse University had a bandwidth of $10 - 133$ cm$^{-1}$ ($0.3 - 4.0$ THz) while University of Vermont data had a bandwidth of $5 - 167$ cm$^{-1}$ ($0.15 - 5.0$ THz). Differences in the bandwidth between the two research labs was most likely attributed to the optimization of the off-axis parabolic mirrors used to focus the THz beam, and the efficiency at which water vapor was removed from the beam path.
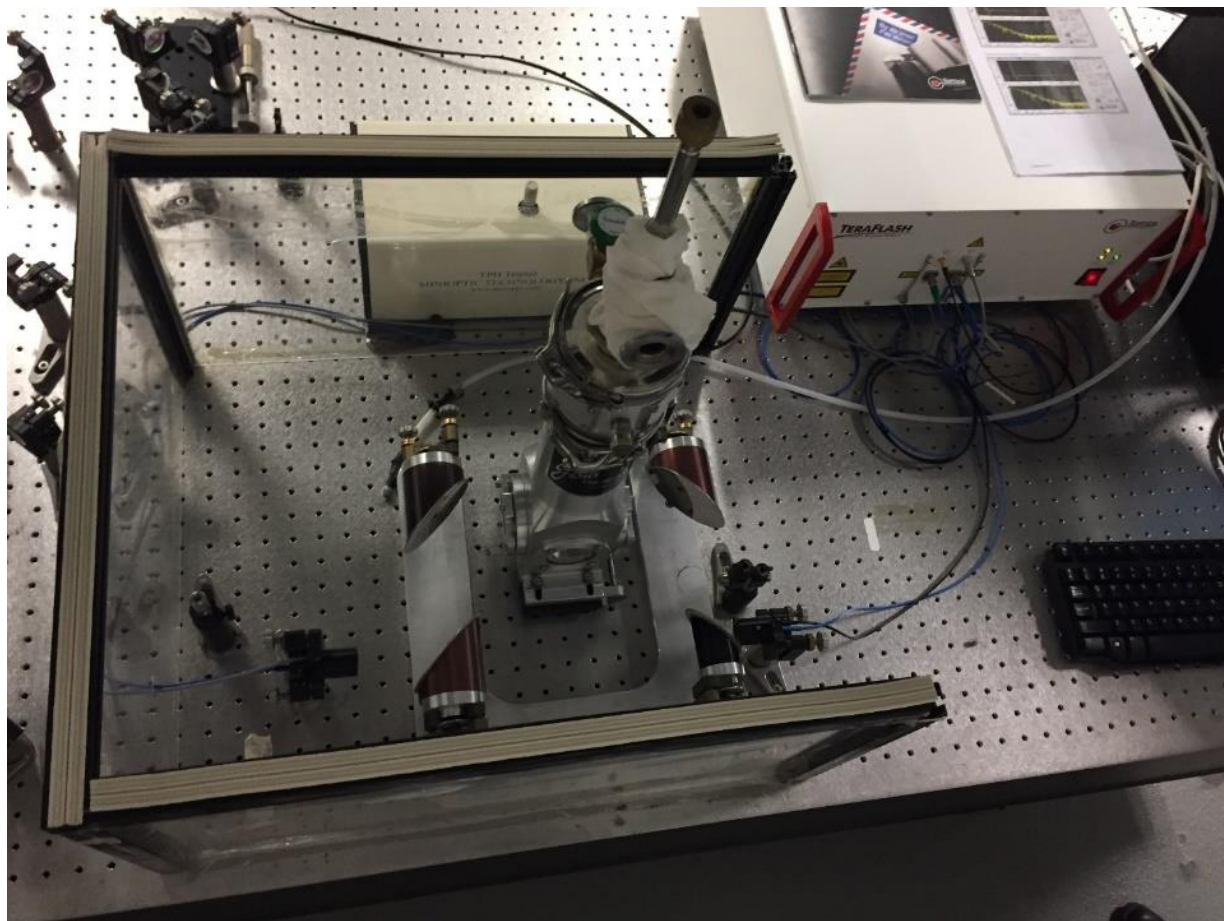
**Figure 4-10.** Toptica TeraFlash set up at Syracuse University using off-axis parabolic mirrors and a Janis ST-100 optical cryostat.

For each measurement, a waveform was collected using a 50 ps time window that averaged over 20,000 scans. Measurements were taken of both the sample and reference pellet under identical conditions. To avoid the first Fabry-Perot etalon reflection generated from the surface of the pellet, each waveform was truncated at 28 ps past the pulse center for 3 mm thick pellets.[54] The thicker the pellet is, the farther out in time the reflection is seen and the more data that can be used.[55] The reflection seen in a pellet of PTFE occurred at approximately 18 ps for a 2 mm thick pellet, 28 ps for a 3 mm thick pellet, and 38 ps for a 4 mm thick pellet as seen in **Figure 4-11.** Increasing the usable time window leads to improved spectral resolution, with a 3 mm thick pellet truncated at 28 ps yielding a spectral resolution of approximately 1.2 cm$^{-1}$.
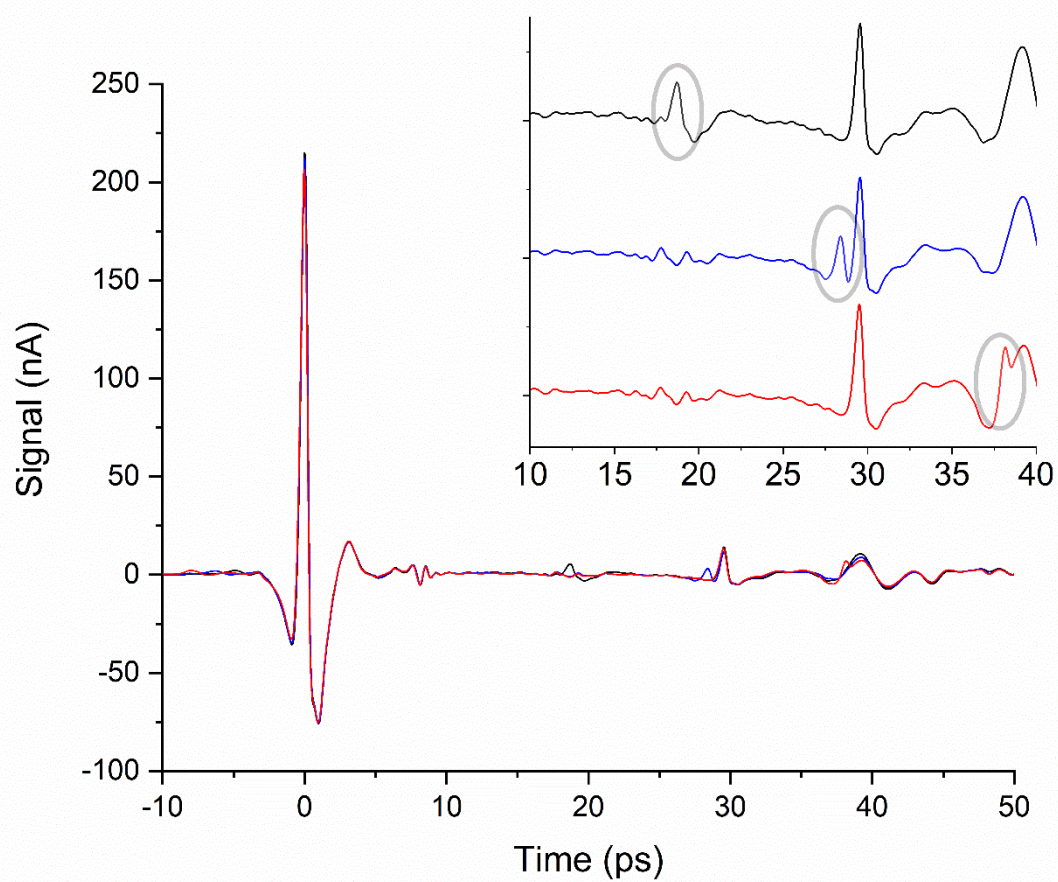
**Figure 4-11.** Terahertz waveform of different PTFE pellet thicknesses, 2 mm (black), 3 mm (blue), 4 mm (red). The reflection for each pellet thickness is highlighted in the inset graph.

Each waveform was then zero-padded to include an equal number of data points before and after the pulse center with the number of data points set to $2^N$ for the purpose of future Fourier-transforms. Care was taken to ensure that the zeroes were added at a point as close to a signal amplitude of 0 as the experimental data points allowed, as to not create artificial pulses. Zero padding does not increase the spectral resolution, as no actual data is added, but instead acts to smooth the resulting spectral features.[56] Zero-padded waveforms were then fast Fourier-transformed (FFT) using the Blackman window in Origin 2020 yielding frequency-domain data.[57]

To arrive at a spectrum in terms of absorbance for only the sample components, a ratio of the magnitude of the FFT between the sample ($I$) and reference ($I_0$) was changed from transmission to absorbance in units of optical density (equation (4.3)). The factor of 2 is necessary in equation (4.3) to properly represent the absorbance as a function of the electric field.[58, 59]

$$A = 2\log\left(\frac{I_0}{I}\right) \tag{4.3}$$

Ultimately, the final units desired for absorbance were in molar attenuation coefficient ($\varepsilon$, $M^{-1}cm^{-1}$) and conversion from optical density was performed using the Beer-Lambert law (equation (4.4)) taking the crystallographic unit cell into consideration. The Beer-Lamber Law relates the absorbance, $A$, to the molar attenuation coefficient, $\varepsilon$, through the thickness of the pellet, $l$, and the concentration of the sample in the pellet in terms of crystallographic unit cells, $c$.

$$A = \varepsilon l c \tag{4.4}$$

For the free-standing pellets, the concentration was solved using the mass of sample in the pellet ($m$, g), the molecular weight of the molecule ($MW$, g/mol), the number of molecules per unit cell ($Z$), the radius of the pellet ($r$, cm), and the thickness of the pellet ($l$, cm) using equation (4.5). Previously, the molar attenuation coefficient was referred to as extinction coefficient, but that terminology has been deemed obsolete by IUPAC.[60]

$$c = \frac{1}{1000} \frac{m/(MW x Z)}{\pi r^2 l} \qquad (4.5)$$

An example of a processed terahertz spectra of L-cystine (3% w/w) collected at both 290 and 50 K is found in **Figure 4-12**. Notice that as the sample was cooled, the peaks shifted to higher frequencies. This is most likely due to a contraction of the unit cell and a decrease in intermolecular separation leading to steeper intermolecular potential energy surfaces and thus force constants.[61, 62]
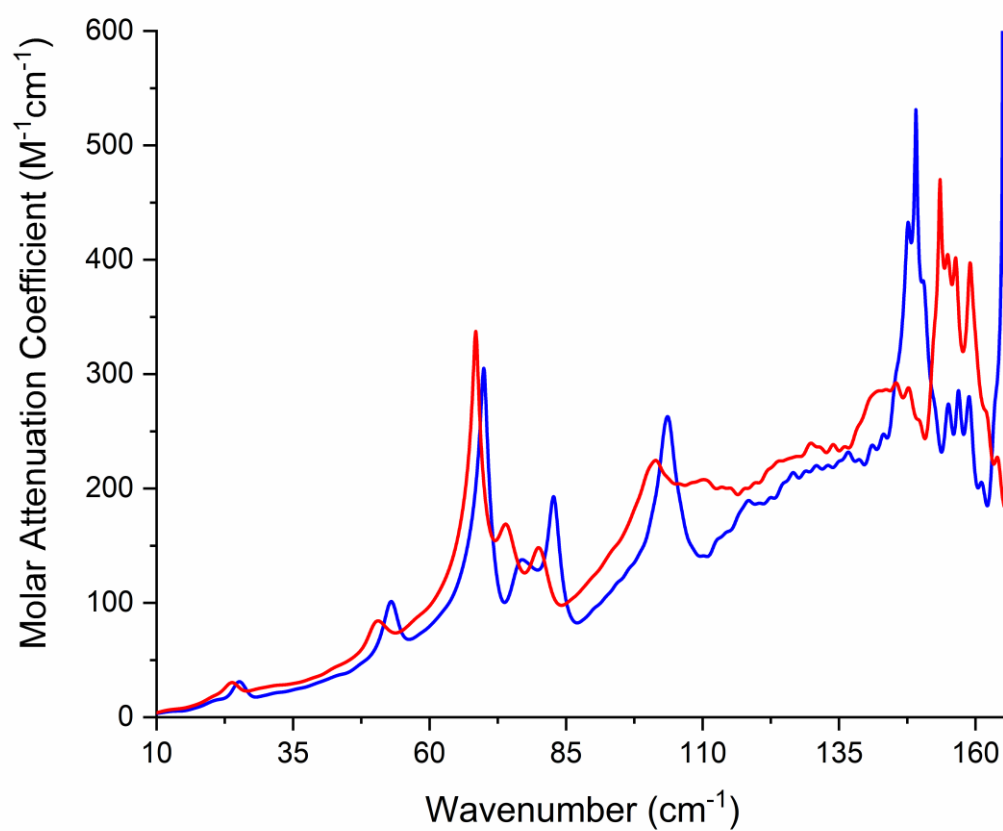
**Figure 4-12.** Terahertz spectra of L-cystine at 290 K (red) and 50 K (blue) from $10 - 120$ cm$^{-1}$.

## 4.4 Low-Frequency Raman Spectroscopy

All low-frequency Raman Spectroscopy (LFRS) data was collected using an Ondax (Coherent) SureBlock XLF-CLM THz-Raman system as described in **Chapter 3**. Two different sample configurations were used depending on the goal of the experiment. The first configuration had the vial holder attachment in place as was commercially intended. In this set-up, the sample was ground using a mortar and pestle and placed in a 10 mm glass vial. This vial was then securely held within the sample vial holder. In the second configuration, the vial holder attachment was removed, and an optical lens and Janis ST-100 optical cryostat with glass windows was set in its place (**Figure 4-13**).  To hold the ground powdered samples within the cryostat, a custom-built brass chamber was designed, sandwiching the sample between 2 glass plates (**Figure 4-14**).
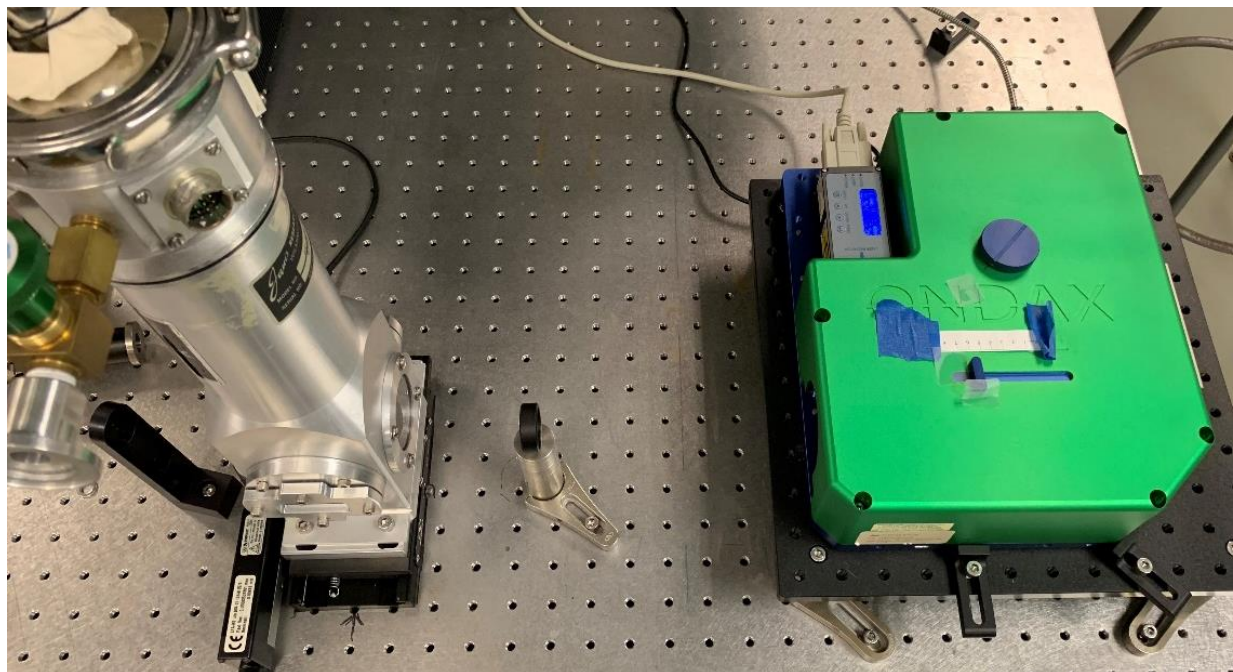
**Figure 4-13.** Ondax THz-Raman XLF-CLM with the sample holder removed and the Janis ST-100 optical cryostat in place.

**Figure 4-14.** Custom-built sample holder for temperature dependent LFRS measurements.

The first configuration provided the highest signal-to-noise ratio and was preferred for room temperature measurements, while the second configuration provided access to temperature-dependent measurements. The second configuration, with the cryostat in place, required additional considerations to account for the change in optical path length between the laser and the sample. This was addressed by placing a lens an appropriate distance between the laser and the sample. Without the vial holder in place, the scattering collection was subjected to interference from the fluorescent room lines, and so all measurements were taken with the room lights turned off. Additional interference was also seen from the atmospheric peaks (specifically the pure rotational Raman spectra of $N_2$ and $O_2$), appearing as narrow spectral features (**Figure 4-15**) that were ultimately subtracted. To verify which features were to be attributed to the

atmosphere of the room, high quality spectra was collected on pure atmosphere alone (**Figure 4-16**). The atmospheric peaks were fit using the peak fitting feature in Origin 2020 (**Table 4-2**) and then subtracted from the sample data set using the Spectragryph software for optical spectroscopy version 1.2.14 (**Figure 4-17**).[57]
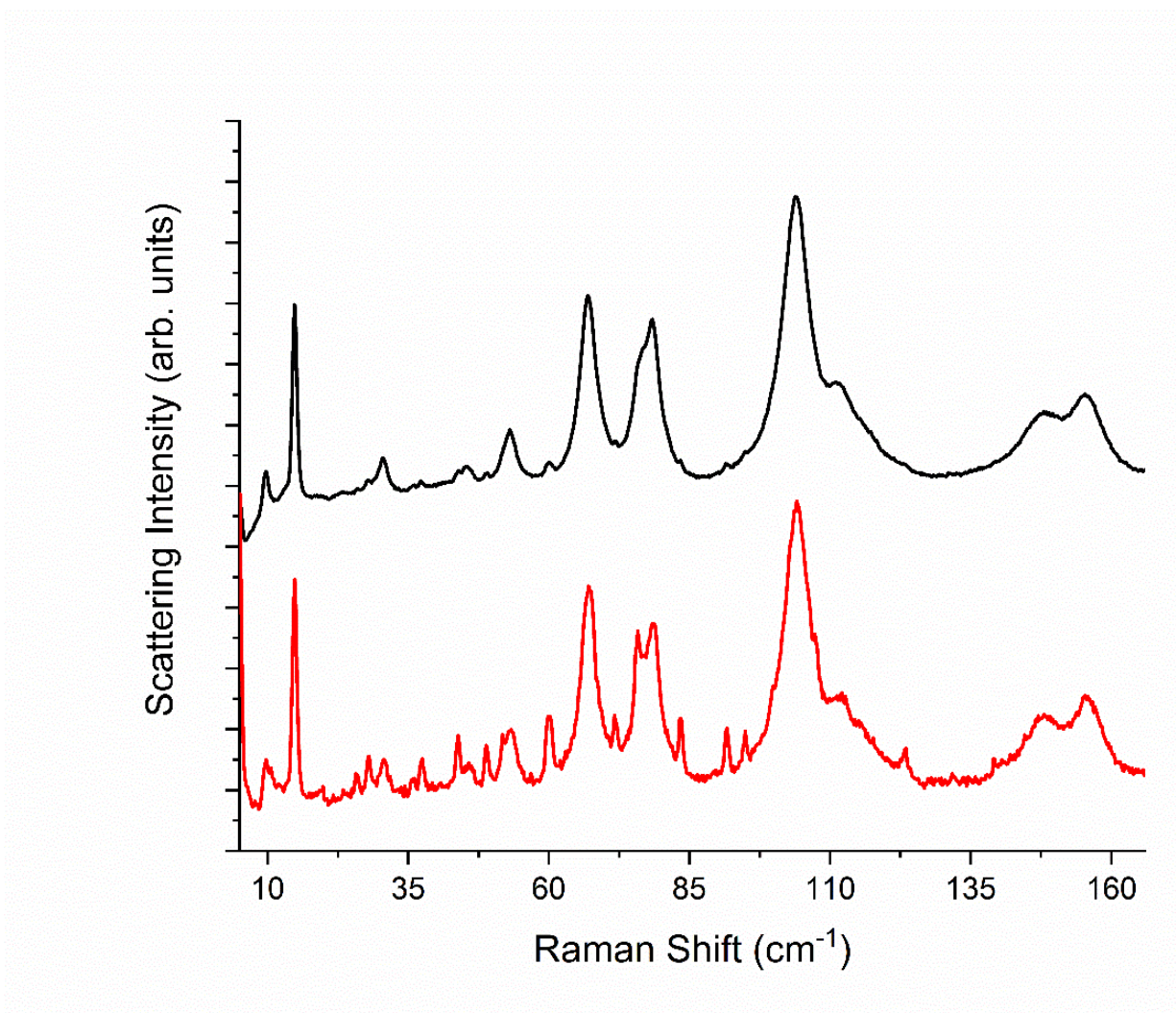
**Figure 4-15.** LFRS data for L-cystine collected using the vial holder (top, black) and cryostat (bottom, red) from 0 – 166 cm$^{-1}$.
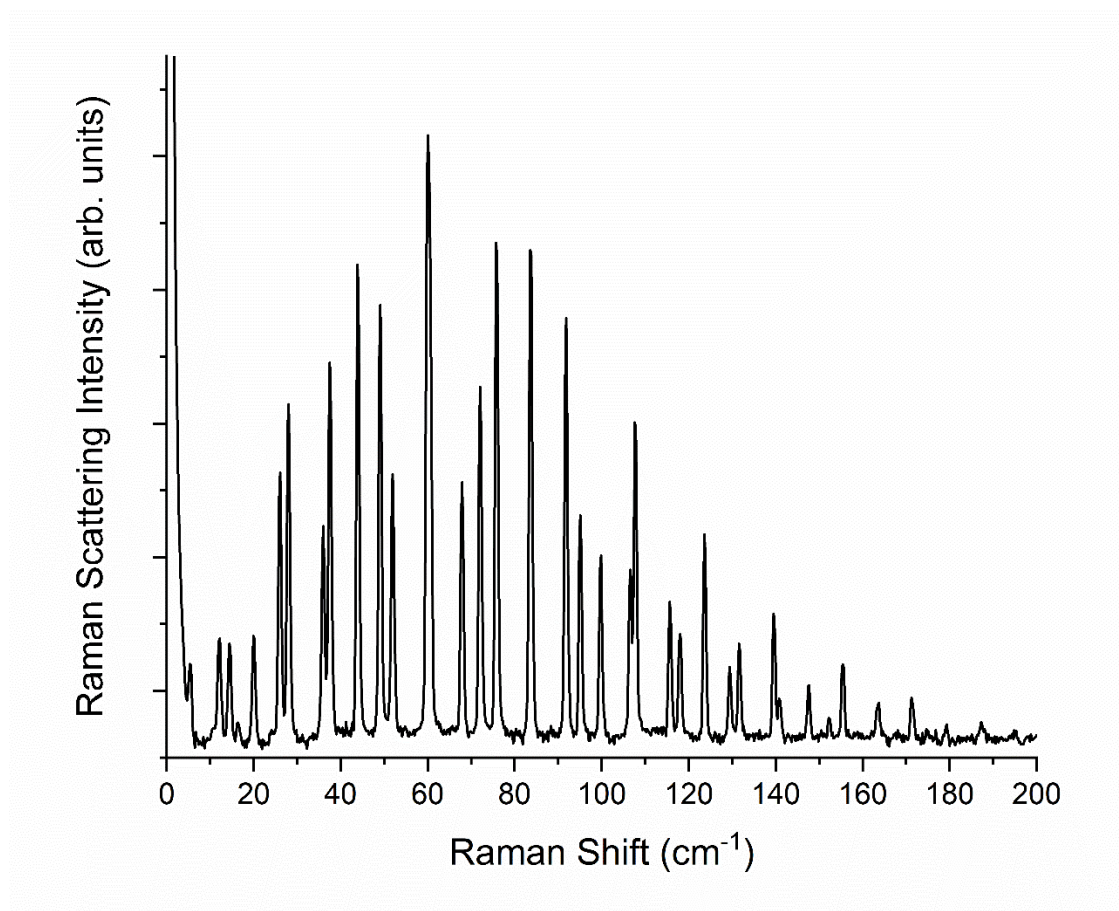
**Figure 4-16.** Raman spectrum of atmosphere from $10 - 200$ cm$^{-1}$ collected at 295 K with an exposure time of 6 seconds and 225 acquisitions.

**Table 4-2.** List of atmospheric rotational peak positions (cm$^{-1}$) peaks subtracted after solid data collection between $5- 200$ cm$^{-1}$.

| 5.4 | 12.2 | 14.4 | 19.9 | 26.1 | 28.1 |
|---|---|---|---|---|---|
| 36.0 | 37.5 | 43.9 | 49.1 | 52.0 | 60.0 |
| 67.9 | 72.0 | 75.7 | 83.6 | 91.8 | 95.1 |
| 99.8 | 106.6 | 107.6 | 115.6 | 118.0 | 123.6 |
| 129.4 | 131.6 | 139.5 | 140.8 | 147.7 | 155.4 |
| 171.2 | | | | | |
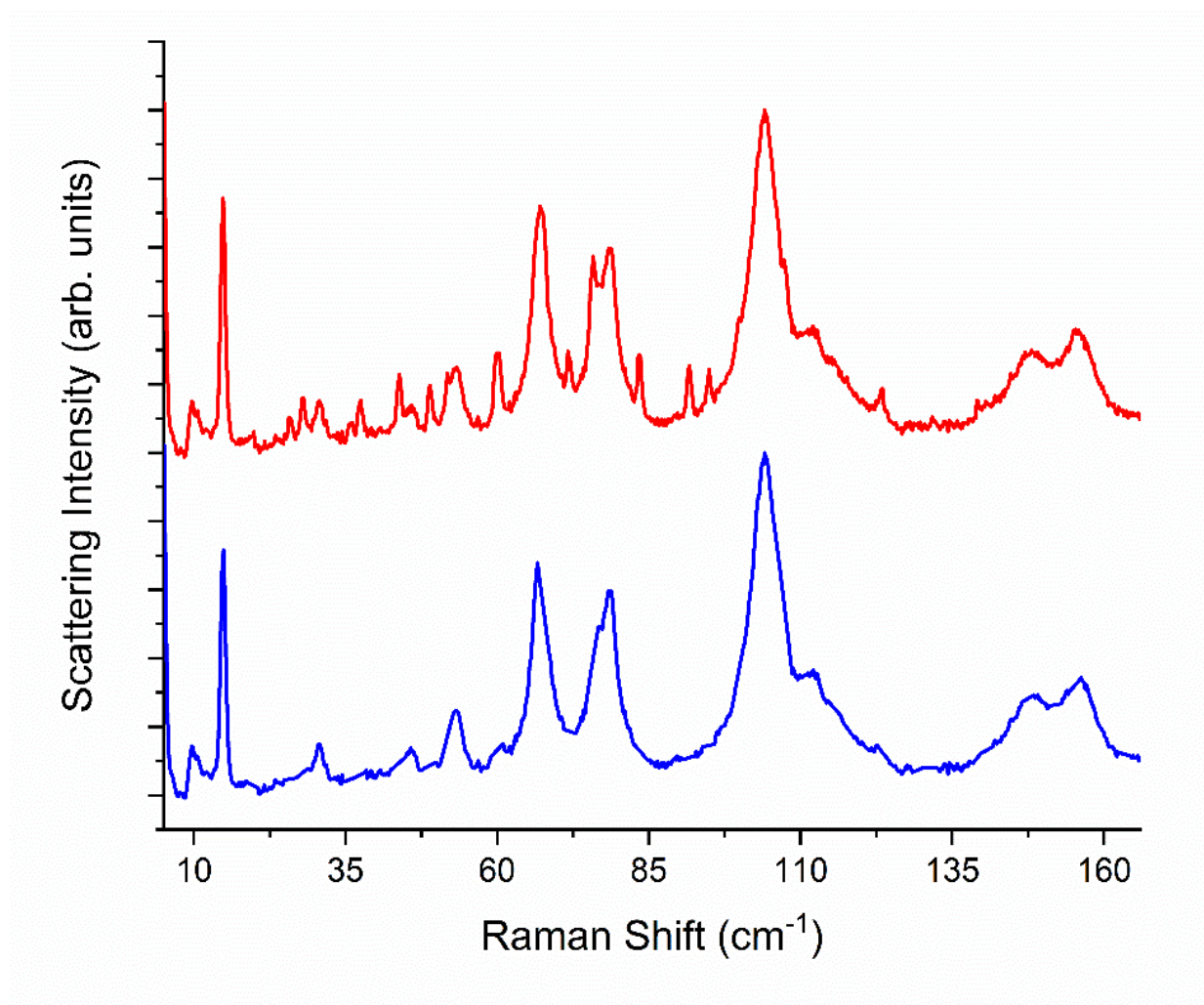
**Figure 4-17.** LFRS of L-cystine collected using the cryostat (top, red) and with the atmospheric peaks removed (bottom, blue) from $0 - 166$ cm$^{-1}$.

Before collecting sample measurements under either configuration, the Rayleigh line was verified to be located at a Raman shift of 0 cm$^{-1}$ using the Andor SOLIS software program (version 4.30.30024.0). If the Rayleigh line was not being properly reported, the spectrograph was recalibrated using the standard procedure in the manual provided.[63] If the vial holder was in use, the laser was also temperature tuned to ensure maximum power with power fluctuations commonly seen after changes to the laboratory's temperature and humidity. All information pertaining to previous temperature tunings can be found in the 'ppfinder' text document stored on the computer attached to the instrument.

Appropriate acquisition settings are linked to the scattering strength of the sample, but it was found that most samples studied produced good signal-to-noise spectra using an exposure time of 3 seconds collected over 225 acquisitions time (**Figure 4-18**). These parameters corresponded to approximately 12 minutes of wait time. To ease comparison between different sample and theoretical predictions, the entire spectrum was normalized using the maximum scattering signal collected past 10 cm$^{-1}$.
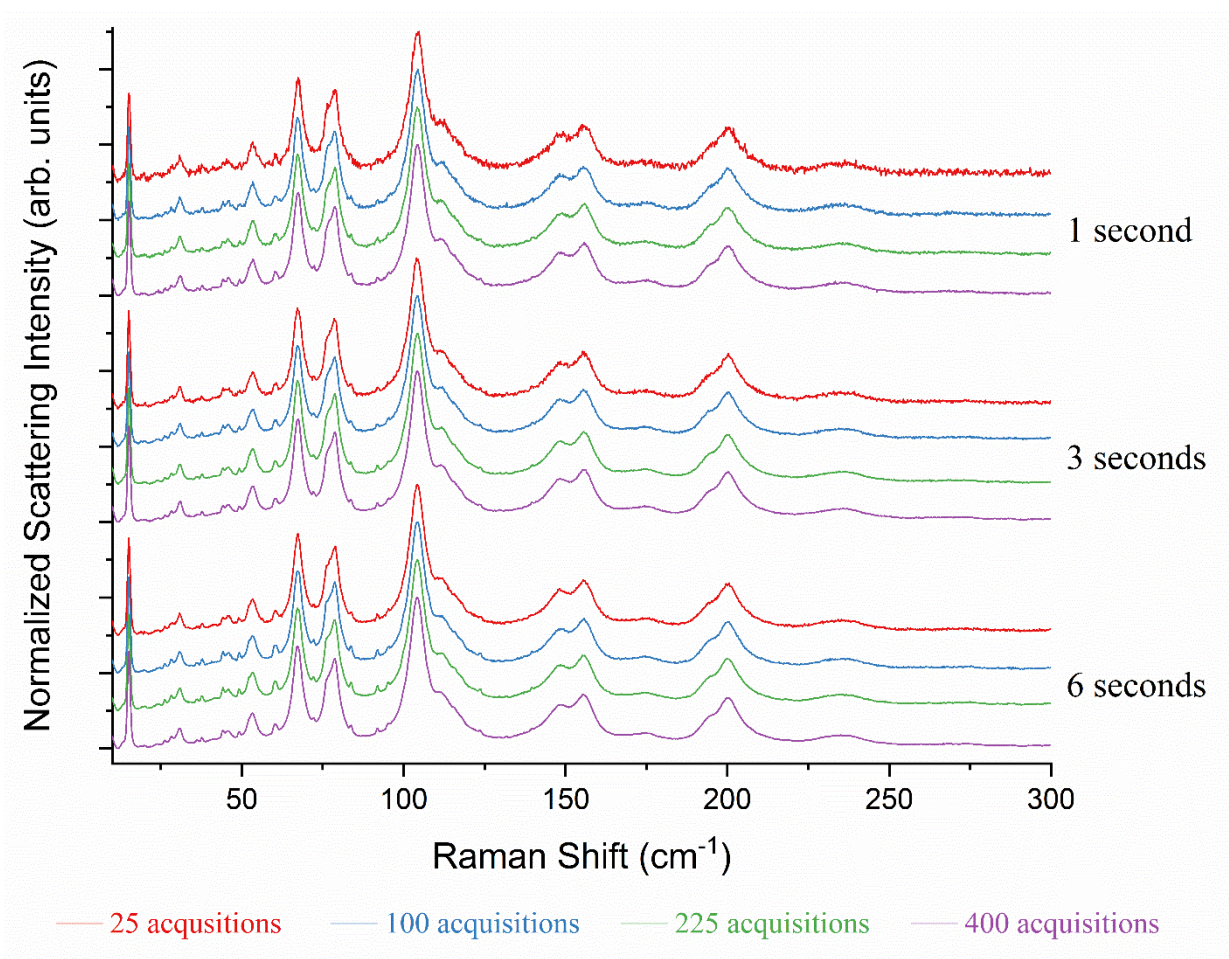
**Figure 4-18.** LFRS of L-cystine collected with the vial holder configuration using varying exposure times and number of acquisitions.

## 4.5 Powder X-ray Diffraction

The majority of powder X-ray diffraction (PXRD) measurements were taken using a Bruker D2 Phaser equipped with a copper X-ray tube as described in Chapter 3 (**Figure 4-19**). Prior to collection, all samples were ground using a mortar and pestle to promote random orientation of the crystals' faces in the path of the incident X-ray beam, and then the sample holder was then filled completely and leveled off to make sure the height of the sample was even with the top ring of the sample holder. This promoted the best data collection and ensured that the airscatter screen did not come in contact with the sample. The sample holder was then raised into position and the scan parameters were set to a scan range of $5 - 70°$ with an increment of $0.02°$ taking 0.5 seconds a step and variable rotation set to 15/min. These collection parameters produced high quality PXRD patterns in under 30 minutes with real-time monitoring of the experiment through the DIFFRAC.SUITE software.[64] A completed job with the desired scan parameters was used to create a job template for future runs, guaranteeing the collection settings were identical between runs. The job template was modified to automatically save the data collected in the desired file format, ensuring that data was not accidentally lost when a new experiment was started. If a measurement was run without a job template, the user had to save the data before a new measurement was started. While the job template was used to follow the same scan parameters, the user had to physically set and verify the position of the airscatter screen, and the divergence slit. Standard measurements had the airscatter screen set to 3 mm to reduce background noise, and used a divergence slit with a slit width of 0.6 mm.
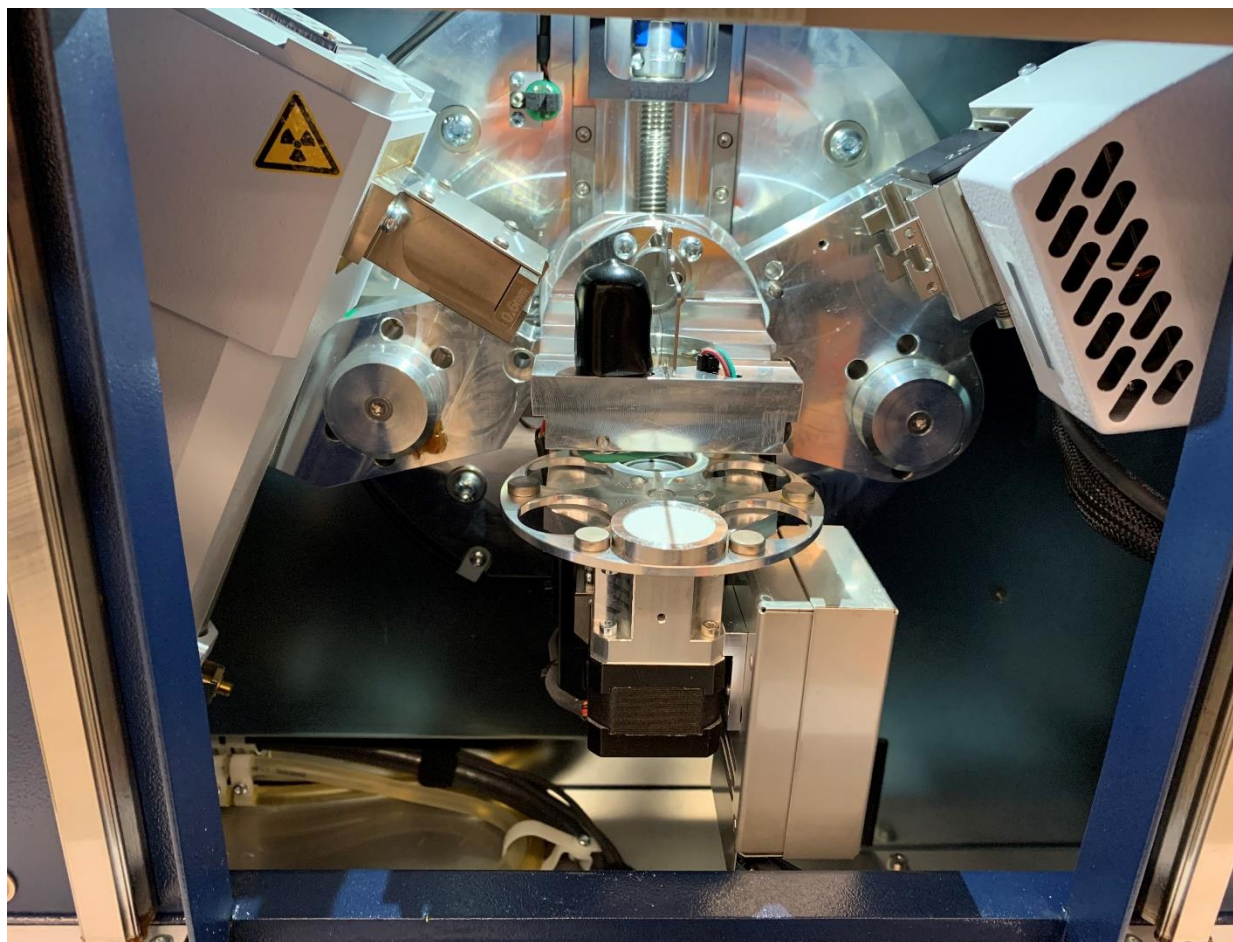
**Figure 4-19.** Bruker D2 Phaser holding a single sample with the divergence slit and airscatter screen in place.

For severely limited sample quantities and temperature dependent measurements, a Bruker Kappa APEX Duo was used to obtain powder patterns. This procedure involved grinding the sample in the same fashion as for collection using the Bruker D2 Phaser, but instead of filling the sample holder, the sample was pressed onto the surface of a MiTeGen mount with a small amount of paratone oil to adhere the sample to the mount. The sample was centered in the X-ray beam and the experimental scan parameters were set. Four phi scans of 180° with an exposure time of 360 seconds were collected using Cu Kα ($\lambda$ = 1.5418 Å) radiation with a detector distance of 150.0 mm. The phi scans covered a 2θ range from -10 to -48° and an omega range from 156 to 174° with a chi angle fixed at 54.720°. If the option to unwarp images was not selected as part of the experimental set-up, they were unwrapped using the 'Unwarp and Convert Images' option in the Apex3 software package.[65] The 'Integrate Debye Rings' option was then used to merge the 4 images together, and the slice tool was used to select the region to be integrated. By right clicking on the region generated by the slice tool, the Debye rings were integrated, and a resultant powder pattern was produced. This powder pattern was then saved as a .raw file. To visualize the powder pattern from the .raw file, a converter was used such as PowDLL or the Bruker EVA program.[64, 66] The powder patterns obtained using this method suffered from a higher signal-to-noise ratio and lower resolution than the previously discussed method using the Bruker D2 Phaser.

## 4.6 Single Crystal X-ray Diffraction

A dual source Bruker Kappa APEX Duo diffractometer system with an APEX II CCD detector was used for all single crystal X-ray diffraction (SC-XRD) measurements (**Figure 4-20**). The molybdenum source was a fine focus Siemens ceramic X-ray tube producing Mo Kα radiation ($\lambda = 0.71073$ Å), while the copper source was an Incoatec microfocus source, IμS, with Cu Kα radiation ($\lambda = 1.54184$ Å). For instrument maintenance and longevity, it was important that the detector and X-ray sources are appropriately cooled. The detector was cooled using a Julabo recirculating cooler set to -3.0°C, filled with a set ratio of water and ethylene glycol. The molybdenum source was cooled using a Haskris R100 chiller that accesses house water set to 73°F. The chiller required routine cleaning to remove the remnants that had built up from the house water, as well as regular monitoring of the water filter. No additional cooling apparatus was required for the copper X-ray source, as it was air-cooled.
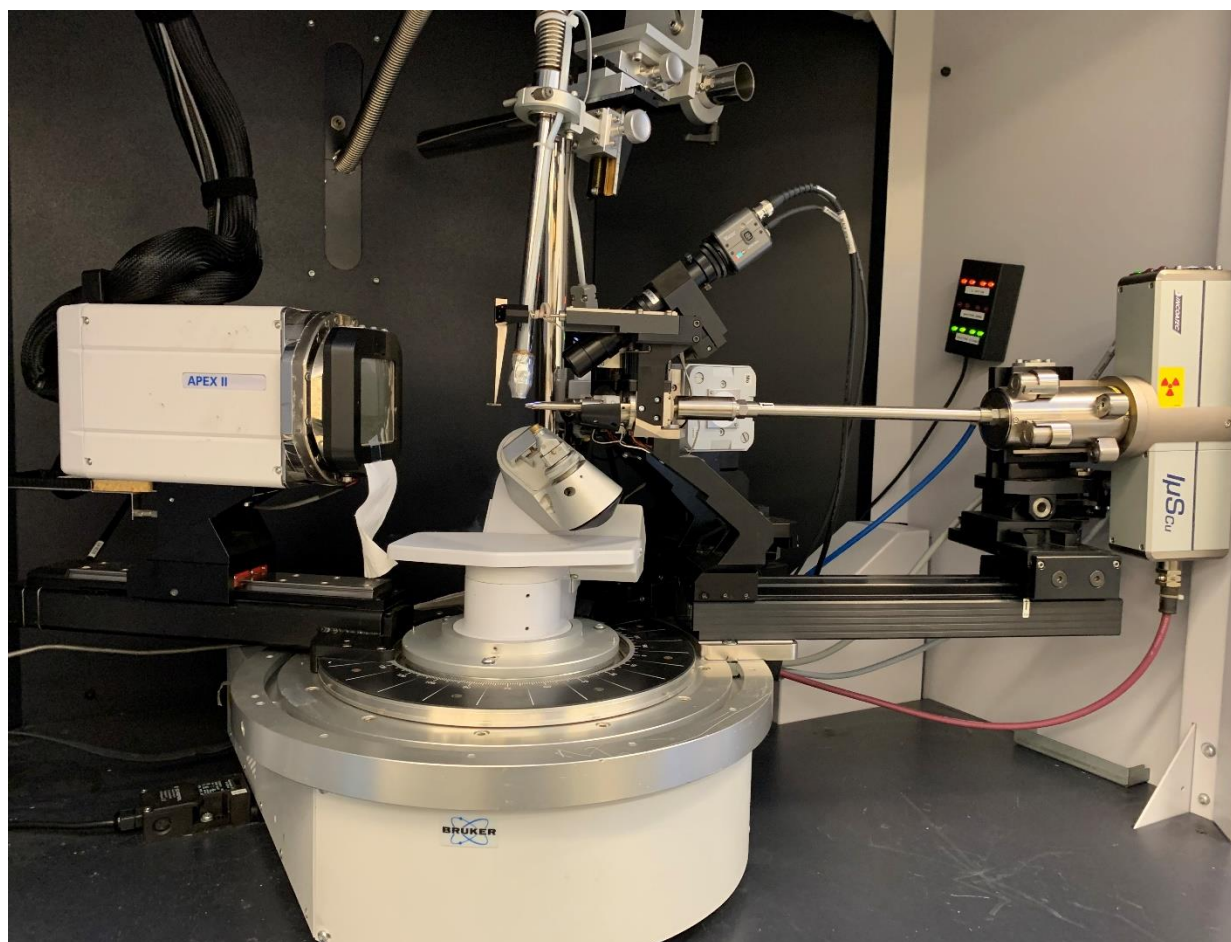
**Figure 4-20.** Dual source Bruker Kappa Apex Duo with low-temperature capability.

The diffractometer was modified for low-temperature measurements using liquid nitrogen as a cooling agent. Cooling the sample allowed for more accurate determination of atomic positions, as thermal motion was reduced. Liquid nitrogen was held in a storage dewar from CRYO Industries that was refilled from a cylinder supplied by Airgas. The desired fill levels for the dewar were set using a LM-500 liquid cryogen level monitor from Cryomagnetics Inc. The liquid nitrogen was then fed from the dewar into a nozzle that blew directly over the crystal sample. The desired sample temperature was set suing a cryogenic temperature controller from Cryogenic Control Systems Inc. (Cryo Con) with a GW Instek GSP-3030D power supply to control the gas flow. Typically, the voltage on the power supply was set to 12.4 V, but in the case of liquid nitrogen dripping from the nozzle, the voltage was raised to a maximum of 18.1 V. During the summer months of high humidity, the sample and MiTeGen mount were prone to icing, an issue that was addressed by making sure the flow of nitrogen was directly over the sample and by checking the orientation of the goniometer.

Before attempting to collect any X-ray measurements, the X-rays were verified to be on, and the shutter closed. This was done using the Bruker Instrument Server (BIS) software, and by physical inspection of the LED lights housed within the enclosure of the diffractometer. Only after BIS was opened could APEX3 be connected to the instrument. The Apex3 software package was used for the collection and analysis of all X-ray measurements, with a step-by-step guide to data collection and software options found in the user's manual, available online, and in the X-ray laboratory.[65, 67-70]

Apex3 is a relatively user-friendly software that begins with describing and centering the crystal. If, when attempting to center the crystal, the crystal and its mount were not moving smoothly as the axes were rotated, the MiTeGen mount was checked to confirm that it was

securely held in place within the goniometer base. Taking extra care to ensure the crystal was properly centered led to a higher quality of data and faster collection times. Once the crystal was screened to determine if it was a good candidate, the unit cell was determined from a collection of 36 frames. A quality crystal had a good number (20 – 50) of strong, discrete reflections when the spots were harvested and it was helpful to view the reciprocal lattice to visualize the reflections before moving forward.[71] To complete the empty fields of the crystal dimensions in the 'Describe Sample' plug-in, a video of the crystal rotating to capture all faces was saved using the 'Index Crystal Faces' plug-in once the unit cell was determined. Next, a data collection strategy was calculated, keeping in mind the desired resolution, completeness, average multiplicity, and total run time. The images were then integrated into a single .raw-file with an updated cell orientation, saved as a .p4p-file. The .raw-file was then scaled and refined to yield a .hkl-file containing all measured reflections. The .p4p-file and .hkl-file were then used to determine the space group and produce an instruction file (.ins). Together, these 3 files were needed to solve the structure and produce a .res-file. From this point, the structure was refined until a quality solution was determined, and then ultimately saved as a crystallographic information file (.cif).[72, 73] The integrity and quality of the crystal structure was checked using checkCIF (checkcif.iucr.org), a service provided by the International Union of Crystallography (IUCr). Crystallographic information files were then published and/or uploaded to an appropriate database.[4, 74-76]

## 4.7 References

1.      Dovesi, R.; Pascale, F.; Civalleri, B.; Doll, K.; Harrison, N. M.; Bush, I.; D'Arco, P.; Noël, Y.; Rérat, M.; Carbonnière, P.; et al. The CRYSTAL Code, 1976–2020 and Beyond, a Long Story. *J. Chem. Phys.* **2020,** *152* (20), 204111.

2.      Dovesi, R.; Erba, A.; Orlando, R.; Zicovich-Wilson, C. M.; Civalleri, B.; Maschio, L.; Rérat, M.; Casassa, S.; Baima, J.; Salustro, S.; Kirtman, B. Quantum-mechanical Condensed Matter Simulations with CRYSTAL. *Wiley Interdiscip. Rev.: Comput. Mol. Sci. 0* (0), e1360.

3.      Dovesi, R.;Saunders, V. R.;Roetti, C.;Orlando, R.;Zicovich-Wilson, C. M.;Pascale, F.;Civalleri, B.;Doll, K.;Harrison, N. M.;Bush, I. J.;et al.. CRYSTAL17 User's Manual. University of Torino: Torino, 2017.

4.      Groom, C. R.; Bruno, I. J.; Lightfoot, M. P.; Ward, S. C. The Cambridge Structural Database. *Acta Crystallographica Section B* **2016,** *72* (2), 171-179.

5.      Bruno, I. J.; Cole, J. C.; Edgington, P. R.; Kessler, M.; Macrae, C. F.; McCabe, P.; Pearson, J.; Taylor, R. New Software for Searching the Cambridge Structural Database and Visualizing Crystal Structures. *Acta Crystallographica Section B* **2002,** *58* (3 Part 1), 389-397.

6.      Schuchardt, K. L.; Didier, B. T.; Elsethagen, T.; Sun, L.; Gurumoorthi, V.; Chase, J.; Li, J.; Windus, T. L. Basis Set Exchange: A Community Database for Computational Sciences. *J. Chem. Inf. Model.* **2007,** *47* (3), 1045-1052.

7.      Pritchard, B. P.; Altarawy, D.; Didier, B.; Gibson, T. D.; Windus, T. L. New Basis Set Exchange: An Open, Up-to-Date Resource for the Molecular Sciences Community. *J. Chem. Inf. Model.* **2019,** *59* (11), 4814-4820.

8.    Feller, D. The Role of Databases in Support of Computational Chemistry Calculations. *J. Comput. Chem.* **1996,** *17* (13), 1571-1586.

9.    Krishnan, R.;  Binkley, J. S.;  Seeger, R.; Pople, J. A. Self-consistent Molecular Orbital Methods. XX. A Basis Set for Correlated Wave Functions. *J. Chem. Phys.* **1980,** *72* (1), 650-4.

10.   Monkhorst, H. J.; Pack, J. D. Special Points for Brillouin-zone Integrations. *Phys. Rev. B* **1976,** *13* (12), 5188-5192.

11.   Gilat, G.; Raubenheimer, L. J. Accurate Numerical Method for Calculating Frequency-Distribution Functions in Solids. *Phys. Rev.* **1966,** *144* (2), 390-395.

12.   Gilat, G. Analysis of Methods for Calculating Spectral Properties in Solids. *J. Comput. Phys.* **1972,** *10* (3), 432-465.

13.   Dahaoui, S.;  Pichon-Pesme, V.;  Howard, J. A. K.; Lecomte, C. CCD Charge Density Study on Crystals with Large Unit Cell Parameters: The Case of Hexagonal l-Cystine. *J. Phys. Chem. A* **1999,** *103* (31), 6240-6250.

14.   Dovesi, R.;  Pisani, C.;  Roetti, C.; Saunders, V. R. Treatment of Coulomb Interactions in Hartree-Fock Calculations of Periodic Systems. *Phys. Rev. B* **1983,** *28* (10), 5781-5792.

15.   Causa, M.;  Dovesi, R.;  Orlando, R.;  Pisani, C.; Saunders, V. R. Treatment of the Exchange Interactions in Hartree-Fock LCAO Calculations of Periodic Systems. *J. Phys. Chem.* **1988,** *92* (4), 909-913.

16.   Saunders, V. R.;  Freyria-Fava, C.;  Dovesi, R.;  Salasco, L.; Roetti, C. On the Electrostatic Potential in Crystalline Systems where the Charge Density is Expanded in Gaussian Functions. *Mol. Phys.* **1992,** *77* (4), 629-665.

17.    Grimme, S.;  Antony, J.;  Ehrlich, S.; Krieg, H. A Consistent and Accurate ab initio Parametrization of Density Functional Dispersion Correction (DFT-D) for the 94 Elements H-Pu. *J. Chem. Phys.* **2010,** *132* (15), 154104/1-154104/19.

18.    Grimme, S.;  Ehrlich, S.; Goerigk, L. Effect of the damping function in dispersion corrected density functional theory. *J. Comput. Chem.* **2011,** *32* (7), 1456-1465.

19.    Grimme, S. Density Functional Theory with London Dispersion Corrections. *Wiley Interdiscip. Rev.: Comput. Mol. Sci.* **2011,** *1* (2), 211-228.

20.    Grimme, S.;  Hansen, A.;  Brandenburg, J. G.; Bannwarth, C. Dispersion-Corrected Mean-Field Electronic Structure Methods. *Chem. Rev.* **2016,** *116* (9), 5105-5154.

21.    Axilrod, B. M.; Teller, E. Interaction of the Van der Waals Type Between Three Atoms. *J. Chem. Phys.* **1943,** *11* (6), 299-300.

22.    Turrell, G. *Infrared and Raman Spectra of Crystals*, Academic Press: 1972.

23.    Jmol: an open-source Java viewer for chemical structures in 3D. http://www.jmol.org/.

24.    Macrae, C. F.;  Edgington, P. R.;  McCabe, P.;  Pidcock, E.;  Shields, G. P.;  Taylor, R.; Towler, M.; van de Streek, J. Mercury: Visualization and Analysis of Crystal Structures. *J. Appl. Crystallogr.* **2006,** *39* (3), 453-457.

25.    Macrae, C. F.;  Sovago, I.;  Cottrell, S. J.;  Galek, P. T. A.;  McCabe, P.;  Pidcock, E.;  Platings, M.;  Shields, G. P.;  Stevens, J. S.;  Towler, M.; Wood, P. A. Mercury 4.0: From Visualization to Analysis, Design and Prediction. *J. Appl. Crystallogr.* **2020,** *53* (1), 226-235.

26.    Anderson, D. G. Iterative Procedures for Nonlinear Integral Equations. *J. ACM* **1965,** *12* (4), 547–560.

27. Zicovich-Wilson, C. M.;  Pascale, F.;  Roetti, C.;  Saunders, V. R.;  Orlando, R.; Dovesi, R. Calculation of the Vibration Frequencies of α-quartz: The Effect of Hamiltonian and Basis Set. *J. Comput. Chem.* **2004,** *25* (15), 1873-1881.

28. Pascale, F.;  Zicovich-Wilson, C. M.;  López Gejo, F.;  Civalleri, B.;  Orlando, R.; Dovesi, R. The Calculation of the Vibrational Frequencies of Crystalline Compounds and its Implementation in the CRYSTAL Code. *J. Comput. Chem.* **2004,** *25* (6), 888-897.

29. Maschio, L.;  Kirtman, B.;  Orlando, R.; Rèrat, M. Ab initio Analytical Infrared Intensities for Periodic Systems through a Coupled Perturbed Hartree-Fock/Kohn-Sham Method. *J. Chem. Phys.* **2012,** *137* (20), 204113.

30. Maschio, L.;  Kirtman, B.;  Rerat, M.;  Orlando, R.; Dovesi, R. Ab initio Analytical Raman Intensities for Periodic Systems through a Coupled Perturbed Hartree-Fock/Kohn-Sham Method in an Atomic Orbital Basis. I. Theory. *J. Chem. Phys.* **2013,** *139* (16), 164101/1-164101/13.

31. Maschio, L.;  Kirtman, B.;  Rèrat, M.;  Orlando, R.; Dovesi, R. Ab initio Analytical Raman Intensities for Periodic Systems through a Coupled Perturbed Hartree-Fock/Kohn-Sham Method in an Atomic Orbital Basis. II. Validation and Comparison with Experiments. *J. Chem. Phys.* **2013,** *139* (16), 164102/1-164102/9.

32. Ewelina, W. Investigation of Explosives and Related Compounds Using Terahertz Spectroscopy and Solid-State Density Functional Theory. Dissertation, Syracuse University, 2012.

33. Veithen, M.;  Gonze, X.; Ghosez, P. Nonlinear Optical Susceptibilities, Raman Efficiencies, and Electro-optic Tensors from First-principles Density Functional Perturbation Theory. *Phys. Rev. B* **2005,** *71* (12), 125107.

34. Erba, A. On Combining Temperature and Pressure Effects on Structural Properties of Crystals with Standard ab initio Techniques. *J. Chem. Phys.* **2014,** *141* (12), 124115/1-124115/9.

35. Erba, A.; Maul, J.; De La Pierre, M.; Dovesi, R. Structural and Elastic Anisotropy of Crystals at High Pressures and Temperatures from Quantum Mechanical Methods: The Case of $Mg_2SiO_4$ Forsterite. *J. Chem. Phys.* **2015,** *142* (20), 204502/1-204502/11.

36. Erba, A.; Maul, J.; Itou, M.; Dovesi, R.; Sakurai, Y. Anharmonic Thermal Oscillations of the Electron Momentum Distribution in Lithium Fluoride. *Phys. Rev. Lett.* **2015,** *115* (11), 117402/1-117402/5.

37. Erba, A.; Shahrokhi, M.; Moradian, R.; Dovesi, R. On How Differently the Quasi-harmonic Approximation Works for Two Isostructural Crystals: Thermal Properties of Periclase and Lime. *J. Chem. Phys.* **2015,** *142* (4), 044114.

38. Gromada , VideoMach software, http://www.gromada.com/index.html.

39. Jepsen, P. U.; Fischer, B. M. Dynamic Range in Terahertz Time-domain Transmission and Reflection Spectroscopy. *Opt. Lett.* **2005,** *30* (1), 29-31.

40. Philip, F. T. Applications of Terahertz Spectroscopy to Pharmaceutical Sciences. *Philosophical Transactions: Mathematical, Physical and Engineering Sciences* **2004,** *362* (1815), 351-364.

41. Tanabe, T.; Watanabe, K.; Oyama, Y.; Seo, K. Polarization Sensitive THz Absorption Spectroscopy for the Evaluation of Uniaxially Deformed Ultra-high Molecular Weight Polyethylene. *NDT&E Int.* **2010,** *43* (4), 329-333.

42. Pensenstadler, D. F.;  Carlson, G. L.;  Fateley, W. G.; Bentley, F. F. The Use of Adamantane as a Pelleting Material for Rar Infrared Spectroscopy of Solids. *Spectrochim. Acta, Part A* **1972,** *28* (1), 183-185.

43. Fan, W. H.;  Burnett, A.;  Upadhya, P. C.;  Cunningham, J.;  Linfield, E. H.; Davies, A. G. Far-Infrared Spectroscopic Characterization of Explosives for Security Applications Using Broadband Terahertz Time-Domain Spectroscopy. *Appl. Spectrosc.* **2007,** *61* (6), 638-643.

44. Burnett, A. D.;  Fan, W.;  Upadhya, P. C.;  Cunningham, J. E.;  Hargreaves, M. D.;  Munshi, T.;  Edwards, H. G.;  Linfield, E. H.; Davies, A. G. Broadband Terahertz Time-domain Spectroscopy of Drugs-of-abuse and the use of Principal Component Analysis. *Analyst* **2009,** *134* (8), 1658-1668.

45. Davis, M. P.;  Mohara, M.;  Shimura, K.; Korter, T. M. Simulation and Assignment of the Terahertz Vibrational Spectra of Enalapril Maleate Cocrystal Polymorphs. *J. Phys. Chem. A* **2020,** *124* (47), 9793-9800.

46. Dampf, S. J.; Korter, T. M. Crystalline Molecular Standards for Low-Frequency Vibrational Spectroscopies. *J. Infrared, Millimeter, Terahertz Waves* **2020,** *41* (11), 1284-1300.

47. Ruggiero, M. T.;  Sibik, J.;  Zeitler, J. A.; Korter, T. M. Examination of l-Glutamic Acid Polymorphs by Solid-State Density Functional Theory and Terahertz Spectroscopy. *J. Phys. Chem. A* **2016,** *120* (38), 7490-7495.

48. Delaney, S. P.; Korter, T. M. Terahertz Spectroscopy and Computational Investigation of the Flufenamic Acid/Nicotinamide Cocrystal. *J. Phys. Chem. A* **2015,** *119* (13), 3269-3276.

49.    King, M. D.;  Buchanan, W. D.; Korter, T. M. Understanding the Terahertz Spectra of Crystalline Pharmaceuticals: Terahertz Spectroscopy and Solid-state Density Functional Theory Study of (S)-(+)-Ibuprofen and (RS)-Ibuprofen. *J. Pharm. Sci.* **2011,** *100* (3), 1116-1129.

50.    Kleist, E. M.;  Koch Dandolo, C. L.;  Guillet, J.-P.;  Mounaix, P.; Korter, T. M. Terahertz Spectroscopy and Quantum Mechanical Simulations of Crystalline Copper-Containing Historical Pigments. *J. Phys. Chem. A* **2019,** *123* (6), 1225-1232.

51.    Shen, Y. C.;  Taday, P. F.; Pepper, M. Elimination of Scattering Effects in Spectral Measurement of Granulated Materials using Terahertz Pulsed Spectroscopy. *Appl. Phys. Lett.* **2008,** *92* (5), 051103.

52.    Franz, M.;  Fischer, B. M.; Walther, M. The Christiansen Effect in Terahertz Time-domain Spectra of Coarse-grained Powders. *Appl. Phys. Lett.* **2008,** *92* (2), 021107.

53.    Podzorov, A.; Gallot, G. Low-loss Polymers for Terahertz Applications. *Appl. Opt.* **2008,** *47* (18), 3254-3257.

54.    Kniffin, G. P.; Zurk, L. M. Model-Based Material Parameter Estimation for Terahertz Reflection Spectroscopy. *IEEE Transactions on Terahertz Science and Technology* **2012,** *2* (2), 231-241.

55.    Namkung, H.;  Kim, J.;  Chung, H.; Arnold, M. A. Impact of Pellet Thickness on Quantitative Terahertz Spectroscopy of Solid Samples in a Polyethylene Matrix. *Anal. Chem.* **2013,** *85* (7), 3674-3681.

56.    Smith, R. M.; Arnold, M. A. Terahertz Time-Domain Spectroscopy of Solid Samples: Principles, Applications, and Challenges. *Appl. Spectrosc. Rev.* **2011,** *46* (8), 636-679.

57. Vázquez Cabo, J.; Chamorro-Posada, P.; Fraile-Pelaez, J.; Rubinos-Lopez, O.; López-Santos, J. M.; Martin-Ramos, P. Windowing of THz Time-domain Spectroscopy Signals: A Study Based on Lactose. *Opt. Commun.* **2016,** *366*, 386-396.

58. Bennett, J. W.; Raglione, M. E.; Oburn, S. M.; MacGillivray, L. R.; Arnold, M. A.; Mason, S. E. DFT Computed Dielectric Response and THz Spectra of Organic Co-Crystals and Their Constituent Components. *Molecules* **2019,** *24* (5), 959.

59. Sun, J.; Lucyszyn, S. Extracting Complex Dielectric Properties From Reflection-Transmission Mode Spectroscopy. *IEEE Access* **2018,** *6*, 8302-8321.

60. Verhoeven, J. W. Glossary of Terms used in Photochemistry (IUPAC Recommendations 1996). *Pure Appl. Chem.* **1996,** *68* (12), 2223-2286.

61. Lucazeau, G. Effect of Pressure and Temperature on Raman Spectra of Solids: Anharmonicity. *J. Raman Spectrosc.* **2003,** *34* (7-8), 478-496.

62. Song, Q.; Han, P.; Zhang, X. C.; Zhang, C.; Zhao, Y. Temperature Dependent Terahertz Spectroscopy of Allopurinol. *J. Infrared, Millimeter, Terahertz Waves* **2009,** *30* (5), 461-467.

63. Prendergast, R. A Solid-State Theoretical and Experimental Analysis of Nitroguanidine and Gunshot Residues. Syracuse University, 2018.

64. *DIFFRAC.SUITE*, Bruker.

65. *Apex3*, Bruker.

66. PowDLL, a reusable .NET component for interconverting powder diffraction data: Recent developments, N. Kourkoumelis, ICDD Annual Spring Meetings (ed. Lisa O'Neil), Powder Diffraction, 28 (2013) 127-48.

67.	Sheldrick, G. Crystal Structure Refinement with SHELXL. *Acta Crystallographica Section C* **2015,** *71* (1), 3-8.

68.	Sheldrick, G. SHELXT - Integrated Space-group and rCystal-structure Determination. *Acta Crystallogr., Sect. A: Found. Adv.* **2015,** *71* (1), 3-8.

69.	Parsons, S.;  Flack, H. D.; Wagner, T. Use of Intensity Quotients and Differences in Absolute Structure Refinement. *Acta Crystallogr., Sect. B: Struct. Sci., Cryst. Eng. Mater.* **2013,** *69* (3), 249-259.

70.	Krause, L.;  Herbst-Irmer, R.;  Sheldrick, G. M.; Stalke, D. Comparison of Silver and Molybdenum Microfocus X-ray Sources for Single-crystal Structure Determination. *J. Appl. Crystallogr.* **2015,** *48* (1), 3-10.

71.	Luger, P. *Modern X-ray Analysis on Single Crystals: A Practical Guide*, 2nd fully revis and extend ed.; De Gruyter: Berlin;Boston;, 2014.

72.	Hall, S. R.; McMahon, B. *International Tables for Crystallography, Definition and Exchange of Crystallographic Data*, Springer Netherlands: 2005.

73.	Hall, S. R.;  Allen, F. H.; Brown, I. D. The Crystallographic Information File (CIF): A New Standard Archive File for Crystallography. *Acta Crystallogr., Sect. A: Found. Adv.* **1991,** *47* (6), 655-685.

74.	Azzarelli, N.;  Ponnala, S.;  Aguirre, A.;  Dampf, S. J.;  Davis, M. P.;  Ruggiero, M. T.;  Lopez Diaz, V.;  Babich, J. W.;  Coogan, M.;  Korter, T.;  Doyle, R. P.; Zubieta, J. Defining the Origins of Multiple Emission/Excitation in Rhenium-bisthiazole Complexes. *Inorganica Chimica Acta* **2019,** *489*, 301-309.

75. Millimaci, A. M.; Meador, R. I. L.; Dampf, S. J.; Chisholm, J. D. Metal Free Amino-Oxidation of Electron Rich Alkenes Mediated by an Oxoammonium Salt. *Israel Journal of Chemistry n/a* (n/a).

76. Case, D. R.; Spear, A.; Henwood, A. F.; Nanao, M.; Dampf, S.; Korter, T. M.; Gunnlaugsson, T.; Zubieta, J.; Doyle, R. P. [Re(CO)$_3$(5-PAN)Cl], a Rhenium(i) Naphthalimide Complex for the Visible Light Photocatalytic Reduction of CO2. *Dalton Transactions* **2021**.

# Chapter 5: Crystalline Molecular Standards for Low-Frequency Vibrational Spectroscopies

The material contained within this chapter is published in the Journal of Infrared, Millimeter, and Terahertz Waves and has been reproduced with permission of Springer Science + Business Media.

## Abstract

The sub-200 cm$^{-1}$ (sub-6 THz) vibrations of molecular crystals provide identifying features that are characteristic of each solid sample under study. These distinctive vibrational spectra have driven the development of new techniques and instrumentation in analytical spectroscopy. As terahertz time-domain spectroscopy and low-frequency Raman spectroscopy become increasingly prevalent in non-specialist laboratories, the need for a common set of spectral standards for use across these techniques becomes imperative. To meet this need, α-lactose monohydrate, biotin, and L-cystine are proposed here as molecular standards to evaluate instrument performance with both terahertz and Raman spectroscopies, as well serve as benchmarks for quantum mechanical simulations and analyses of these spectra. These substances all reveal a series of readily discernable peaks across the low-frequency region and over a range of temperatures (295 K – 50 K) making them even more useful. The often-overlooked aspect of detailed spectral interpretation and assignment is directly addressed with rigorous solid-state density functional theory simulations of the three compounds based on a standard computational

framework. By investigating these proposed molecular crystal standards with commonly available experimental and theoretical approaches, a set of realistic performance expectations can be achieved for both commercial instrumentation and software being used in low-frequency vibrational spectroscopy.

## 5.1 Introduction

Vibrational spectroscopy has long been used to detect, identify, and characterize chemical samples of all types. These studies generally involve infrared absorption and Raman scattering, with spectroscopic selection rules based on dipole moment and polarizability changes, respectively. The measurements typically cover a spectral range of approximately 400 - 4000 $cm^{-1}$, encompassing what is often referred to as the functional group and fingerprint regions. The vibrational frequencies of representative species are tabulated in extensive correlation lists that can be consulted and used to interpret measured vibrational spectra of new or unknown components.[1, 2] Low-frequency ($\leq 200$ $cm^{-1}$) vibrational spectroscopies are far less explored but show great potential for augmenting traditional techniques by extending their spectral coverage to include large-amplitude torsions and lattice vibrations in solids. Vibrational spectroscopy at low frequencies provides additional information about aspects of chemical samples beyond molecular identity alone through the great sensitivity of low-frequency vibrations to molecular conformation, local chemical environment, and solid-state packing.[3] Given these exceptional capabilities, a great deal of interest in the $\leq 200$ $cm^{-1}$ range has been generated over the last two decades, with numerous studies and applications of terahertz-frequency infrared (THz, 1 THz $\approx 33.33$ $cm^{-1}$) and low-frequency Raman spectroscopies appearing, with the majority focused on characterizing solid-state materials.[4-10]

The development of ultrafast laser technology in the 1980s is largely credited with easing access to the terahertz (or far-infrared) region of the electromagnetic spectrum.[3] The primary approach to collecting low-frequency infrared spectra, particularly $\leq 100$ $cm^{-1}$, is terahertz time-domain spectroscopy (THz-TDS) which is based on inducing transient electric fields in antenna structures or semiconductor crystals to function as both terahertz generators and detectors in

spectrometers.[11] The THz-TDS method yields amplitude and phase details of the spectral frequency components within the pulse through Fourier transformation of the time-domain data.[3] Low-frequency Raman spectroscopy (LFRS) provides complimentary vibrational energy data for substances in a similar spectral range. However, the experiment does not depend on generation or detection of terahertz radiation, rather it is based on inelastic scattering of photons from samples (the Raman effect). The key to successful LFRS measurements is the ability of the instrument to prevent elastically scattered (Rayleigh) photons from being detected but allowing those very close to the laser excitation wavelength (within ~5 cm$^{-1}$) to still be observed. Recent advancements in optical filter technology have made LFRS a readily accessible technique with immediate pharmaceutical applications.[9, 12, 13]

As the usage of low-frequency vibrational spectroscopies continues to increase, so does the necessity for a set of well-defined solid-state molecular standards that can be used to evaluate aspects of instrument performance such as bandwidth, resolution, signal-to-noise ratio, and reproducibility. In choosing a set of spectral standards to best represent low-frequency region benchmarks, the experimental properties of the samples being considered are important for both terahertz and Raman measurements. An ideal standard should be inexpensive, non-hazardous, easily obtainable, stable, and only exist as a single crystalline polymorph under ambient conditions. Furthermore, to be of practical use as vibrational spectral references, the criteria must also include clearly identifiable peaks with varying intensities that are discernable over a range of temperatures (including room temperature) since low-frequency spectra can be very sensitive to thermal effects.[14, 15] While a few databases of low-frequency vibrational spectra have been constructed (e.g. http://www.thzdb.org), limited work has appeared on establishing reference spectra.[16] The realization of the need for such spectral standards is not new, as Naftaly has

reported work assembling a database of spectra at room temperature with a variety of terahertz spectroscopy instruments and research has also been done to address calibration and metrology issues.[17-19] In this work, focus is placed specifically on molecular crystals that can be used as low-frequency standards for both terahertz and Raman spectroscopic measurements at ambient temperature and below.

A generally recognized challenge in low-frequency vibrational spectroscopy is the interpretation and assignment of the spectral features observed for solid-state samples. Low-frequency vibrational spectra can be difficult to analyze since each crystalline substance (and even each polymorph of a substance) has a unique fingerprint-like pattern of features arising from lattice interactions.[20, 21] This is unlike conventional vibrational spectroscopy at higher frequencies, where observed band positions are readily attributed to discrete component parts (e.g. carbonyl group) within the molecules.[22] Computational chemistry simulations can facilitate the analysis of experimental spectra by enabling clear spectral assignments and detailed descriptions of mode characters to be reached. The specific computational approach chosen must be reflective of the system being studied, and therefore solid-state density functional theory (ss-DFT) utilizing periodic boundary conditions is an appropriate choice for crystalline samples.[23] Solid-state computational analyses focus on reproducing various experimental aspects including molecular and crystal packing structures, vibrational frequency positions, and spectral intensities.[24-28] It is important to note that while the theory-based assignment of measured spectra is the primary goal in this work, the experimental spectra and crystallographic data also serve to gauge computational accuracy and guide development of new computational methodologies. Rigorous simulations play an essential role in establishing reliable molecular standards that can

be used with both THz-TDS and LFRS, but this research also tests the limits of the available computational tools.

Three organic crystalline solids have been chosen for this work: α-lactose monohydrate ($C_{12}H_{22}O_{11} \cdot H_2O$, CAS: 5989-81-1), biotin ($C_{10}H_{16}N_2O_3S$, CAS: 58-85-5), and L-cystine ($C_6H_{12}N_2O_4S_2$, CAS: 56-89-3). All of these solids have the potential to meet the required experimental and spectral criteria set forth in this work to serve as useful spectral standards and provide the low-frequency spectroscopy community with consistent benchmarks. The materials have well-characterized crystal structures with limited sample variations to complicate their identifying spectra. There are currently no other reported solid-state forms (polymorphs or solvates) of biotin beyond the commonly found pure orthorhombic form. However, the same is not true for L-cystine and α-lactose monohydrate, and therefore complications could exist in the samples. L-cystine crystallizes as both hexagonal plates (space group: $P6_122$) and tetragonal prisms (space group: $P4_1$) at room temperature, but with the hexagonal form dominating and thus the target of the current investigation.[29, 30] In maintaining the choice of using the most common crystallographic forms of these substances as standards, the monohydrated crystal of α-lactose (α-lactose monohydrate) has been selected because it has little propensity for dehydration and is the only form that is commercially available in high purity.[31]

Some low-frequency spectra of the proposed standards have been previously published, including temperature-dependent THz spectra of α-lactose monohydrate and biotin[32, 33], room-temperature THz spectra of L-cystine[34], and room-temperature low-frequency Raman spectra of α-lactose monohydrate and L-cystine[34, 35]. There have also been computational studies reported of the THz spectra of all three standards, including solid-state simulations and more limited

studies using single molecules.[36-39] No simulations of the LFRS of the three solids have appeared in the literature.

To assess the standards, a variety of experimental and computational approaches were taken to carefully evaluate the advantages and disadvantages of each solid to serve as a standard across THz-TDS and LFRS. It is important to note that the spectra obtained using commercial instruments are accompanied by solid-state simulations using commercially available software, making this work approachable and reproducible by all interested. All samples were examined using powder X-ray diffraction (PXRD) to determine bulk crystallinity, as well as by single-crystal X-ray diffraction for unit cell parameters. THz-TDS and LFRS were performed on all samples at laboratory and cryogenic temperatures to test the impact on the low-frequency spectra. Finally, ss-DFT calculations using a widely implemented density functional and a chemically accurate basis set were done to model the low-frequency spectral region and were based on previously published crystal structures for α-lactose monohydrate (CCDC 282535), biotin (CCDC 925753), and L-cystine (CCDC 1204445).[30, 40, 41] This study provides the first combined collection of experimental and computational work on molecular crystal standards covering the low-frequency range up to 5 THz (167 cm$^{-1}$), across different selection rules, and multiple temperatures.

## 5.2 Methods

### 5.2.1 Experimental

All standards were purchased from Sigma Aldrich at ≥ 99% purity and verified using powder X-ray diffraction (PXRD). The samples were first ground and then powder data were collected at 100 K by averaging four phi-scans, each covering 180° using a Bruker KAPPA APEX DUO diffractometer with an APEX II CCD and Cu Kα radiation ($\lambda$ = 1.5418 Å). The resulting Debye rings were then integrated yielding a PXRD pattern. The same diffractometer was used to collect unit cell dimensions at 100 K using single crystal X-ray diffraction (SC-XRD) on all three standards.

Low-frequency Raman spectra were obtained using an Ondax (Monrovia, CA) THz-Raman system in a backscattering geometry, with laser excitation centered at 784.7 nm and fiber-coupled to an Andor Shamrock 750 spectrograph equipped with an iDus 416 CCD. Samples were held under vacuum in a Janis ST-100 optical cryostat with glass windows 0.3 m from the edge of the Raman instrument. To secure the sample, the powdered sample was packed between glass plates in a custom brass chamber. Spectra (Stokes component) were collected up to a 300 cm$^{-1}$ shift from the Rayleigh line using a 3 second exposure time with an average of 225 acquisitions at room temperature (293 K) and at liquid-nitrogen temperature (78 K). The approximate spectral resolution was 0.6 cm$^{-1}$. Due to the significant optical path length between the cryostat and the Raman instrument, narrow interference lines can be seen from the Raman rotational spectra of atmospheric gases.[42] The atmospheric interference below 167 cm$^{-1}$ has been reduced in the final Raman spectra of the solid samples by obtaining a spectrum of air only (**Appendix A**) and subtracting the air peaks from the solid spectra and interpolating using the

Spectragryph spectroscopy software package version 1.2.13 (Friedrich Menges, Obersdorf, Germany). In a typically configured commercial instrument (no external cryostat), this atmospheric correction would not be necessary because of the much smaller optical path length. A comparison of the optical path length effects can be found in **Appendix A**. Peak positions were determined from the final Raman spectra using the Origin 2020 software program (OriginLab Corporation, Northampton, MA, USA).

A TeraFlash fiber-coupled terahertz spectrometer from Toptica Photonics (Munich, Germany) was used to obtain all terahertz time-domain spectra. The system was based on a $\lambda = 1.5$ µm femtosecond fiber laser with an InGaAs 25 µm strip-line photoconductive antenna for terahertz generation and an InGaAs 25 µm dipole photoconductive antenna for terahertz detection. Each sample was ground and mixed with polytetrafluoroethylene (PTFE) and then pressed into a pellet of 13 mm diameter and a thickness of $3.0 \pm 0.1$ mm with a sample concentration of $1.5 \pm 0.1\%$ (w/w). PTFE was chosen as a matrix material to reduce the attenuation of THz radiation below 6 THz.[43] The concentration was chosen so that the maximum absorption was within the dynamic range of the instrument, paying close attention to the higher frequency region.[44] A pure PTFE pellet of comparable size and weight was used as a reference blank. The free-standing pellets were held under vacuum in a cryostat equipped with polymethylpentene (TPX) windows and spectra were obtained at 293 K for all, 65 K for α-lactose monohydrate and biotin, and 50 K for L-cystine. Time-domain terahertz waveforms were collected using a 50 ps window and averaged over 20,000 scans. The waveforms were truncated in the data processing at 28 ps past the THz pulse center to avoid interference from the internal pulse reflection generated at the pellet surface.[45] It is relevant to point out that as pellet thickness increases, the interfering reflection is pushed further out in time and enables a larger time

window of the waveform to be used, ultimately leading to a greater spectral resolution.[46] The data was zero-padded prior to the center of the pulse to include a symmetric number of points to the left and right of the pulse center, smoothing the spectral features without altering the chemical information.[47] The ratio of the truncated sample and blank waveforms were Fourier-transformed using the Blackman window function in Origin 2020, which has been shown to yield dynamic and frequency range improvements.[48] Utilizing a 28 ps time window past the THz pulse center yielded an absorption spectrum from 5 to 167 $cm^{-1}$ (0.15 to 5.0 THz) with a spectral resolution of 1.2 $cm^{-1}$. Two full data collections of sample and blank ratios were acquired and averaged together at room temperature, while 3 full data collections were acquired and averaged at low temperature. All values are reported in terms of extinction coefficient ($\varepsilon$, $M^{-1}cm^{-1}$) and account for the crystallographic unit cell concentration ($Z$).[49] Given the uncertainty in the pellet dimensions and sample concentrations there exists a maximum uncertainty in the extinction coefficients of 6.7%. The Origin 2020 software program was used on the resulting spectra for peak position determinations.

### 5.2.2 Computational

Solid-state density functional theory (ss-DFT) calculations were performed using the CRYSTAL17 software package, which performs *ab initio* calculations employing periodic boundary conditions to account for the crystalline environment of the solids being examined.[50] All starting structures were obtained from low-temperature crystallographic data, as the ss-DFT calculations are effectively performed at 0 K. The structures were allowed to fully optimize, being restrained only by their crystallographic space group symmetries ($\alpha$-lactose monohydrate: $P2_1$, biotin: $P2_12_12_1$, L-cystine: $P6_122$) to an energy convergence of $\Delta E < 10^{-8}$ hartree.

The calculations utilized the def2-TZVP basis set and the Perdew-Burke-Ernzerhof (PBE) density functional.[51, 52] All calculations used Grimme's London dispersion correction (D3) with the Becke-Johnson damping function and included a three-body repulsion term with program default settings to improve the intermolecular force modeling.[53-55] Collectively, the applied method can be referred to as PBE-D3/def2-TZVP. An appropriate number of points in the irreducible Brillouin zone was determined for each system (α-lactose monohydrate: 170, biotin: 216, L-cystine: 50), and the overlap-based truncation tolerances for the Coulomb and exchange integrals were set to $10^{-8}$, $10^{-8}$, $10^{-8}$, $10^{-8}$, $10^{-16}$. Harmonic vibrational frequencies were calculated from the fully optimized structures with a tighter energy convergence of $\Delta E < 10^{-10}$ hartree using a two-point finite difference scheme when calculating the second derivatives of the Hessian matrix to ensure numerical accuracy.[56] Both infrared and Raman intensities were calculated through a coupled-perturbed-Hartree-Fock/Kohn-Sham approach with the inclusion of the Anderson convergence accelerator.[56-60] Raman intensities were further refined by accounting for the temperature of the sample and the wavelength of the incident laser.[60]

## 5.3 Results and Discussion

### 5.3.1 Sample Verification

All three proposed standards have clear experimental PXRD patterns indicating high levels of bulk crystallinity and match predictions of the pure materials based on the known SC-XRD structures (**Appendix A**). The simulated PXRD results from ss-DFT calculated structures also show strong agreement with the experimental data, confirming that the crystallographic forms being examined experimentally are the same being investigated computationally. Special

attention was paid to L-cystine to verify that no impurities from the tetragonal form were present in the bulk sample.

Unit cell determinations from SC-XRD measurements at 100 K were used in a similar fashion as the PXRD results to validate space group symmetries and external crystal lattice dimensions as compared to previous experiments (**Table 5-1**).  Excellent agreement is found between the current crystallography and past reports, providing further confidence that the vibrational spectra and the ss-DFT analyses are both based upon the correct experimental crystal structure that forms under common laboratory conditions.

**Table 5-1.** Crystallographic unit cell dimensions obtained at 100 K using SC-XRD for the proposed molecular standards, α-lactose monohydrate[40], biotin[41], and L-cystine[30] as compared to previously published parameters.

| | α-lactose monohydrate | | biotin | | L-cystine | |
|---|---|---|---|---|---|---|
| | 100 K | Published (150 K) | 100 K | Published (173 K) | 100 K | Published (110 K) |
| a (Å) | 4.755(5) | 4.7830(5) | 5.176(6) | 5.1955(6) | 5.4028(4) | 5.412(1) |
| b (Å) | 21.44(2) | 21.540(2) | 10.288(12) | 10.3017(17) | 5.4028(4) | 5.412(1) |
| c (Å) | 7.729(7) | 7.7599(8) | 20.89(3) | 20.943(2) | 55.965(4) | 55.956(1) |
| α (°) | 90 | 90 | 90 | 90 | 90 | 90 |
| β (°) | 105.95(2) | 105.911(2) | 90 | 90 | 90 | 90 |
| γ (°) | 90 | 90 | 90 | 90 | 120 | 120 |

## 5.3.2 Low-frequency Spectroscopy

The final THz-TDS data for α-lactose monohydrate, biotin, and L-cystine at ambient and cryogenic temperatures can be seen in **Fig. 5-1**. The original waveforms, processed individual data collections, and the final XY data used to compose the final THz-TDS spectral figures are included in **Appendix A.** All the spectra show several clearly identifiable peaks at both normal laboratory temperature and at low temperature. It is important to note that even though the data

collected at low temperature has better resolved features (as is typical)[43, 47, 61], the peaks in the 293 K spectra are still well defined. This indicates that the studied solids could all serve as valid experimental standards under ambient conditions, though the L-cystine terahertz data does appear to be slightly modulated compared to previous reports.[34] The choice of matrix material or the concentration of the sample exceeding the range of the detector could contribute to the peak asymmetry seen in the L-cystine terahertz spectra. All of the terahertz spectra presented suffer from a rising baseline resulting from the non-resonant scattering of radiation[46, 49, 62, 63], however no correction has been made to the presented spectra as applying an unbiased correction across this broad frequency range for a variety of samples and temperatures is not trivial.[47, 64]

The LFRS results for the molecular crystals are shown in **Fig. 5-2** from $5 - 167$ cm$^{-1}$ to match the THz-TDS frequency range and ease comparison. Complete Raman data from $0 - 300$ cm$^{-1}$ is provided in **Appendix A**. The Raman spectrum of α-lactose monohydrate has three significant peaks below 50 cm$^{-1}$, but due to the low scattering efficiency of the sample (approximately ¼ the strength of L-cystine), resolving and identifying peaks beyond this range is difficult.[35] Additionally, α-lactose monohydrate presents some weak fluorescence resulting in a rising baseline and is unclear if this originates from the molecule under study or from a minor impurity. Just as with the terahertz spectra, biotin and L-cystine have a number of clearly identifiable Raman peaks at both temperatures. A spectral feature at an impressively low 9.7 cm$^{-1}$ at 50 K in L-cystine can be clearly discerned and highlights the recent advances in LFRS instrument performance.[12] Experimental positions for all peaks $\leq 167$ cm$^{-1}$ (5 THz) are provided in **Appendix A** for both the THz-TDS and LFRS data.
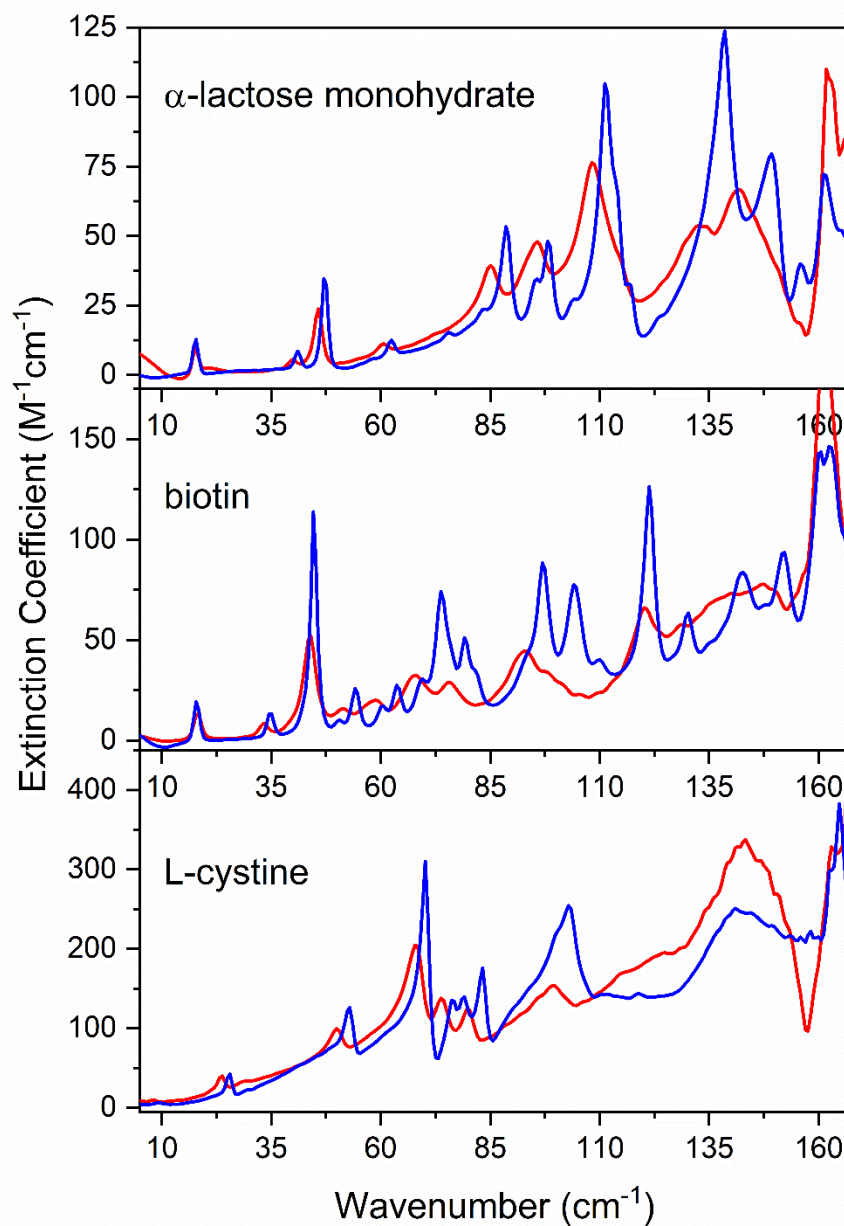
**Figure 5-1.** Terahertz spectra of molecular standards from 5 - 167 cm$^{-1}$ at 293 K (red) and cryogenic temperatures (blue). The cryogenic spectra of α-lactose monohydrate and biotin were taken at 65 K, while L-cystine was 50 K. The 293 K biotin spectra is shown to 175 M$^{-1}$cm$^{-1}$ for clarity, with the off-scale peak at 161.7 cm$^{-1}$ having a maximum intensity of 307 M$^{-1}$cm$^{-1}$.
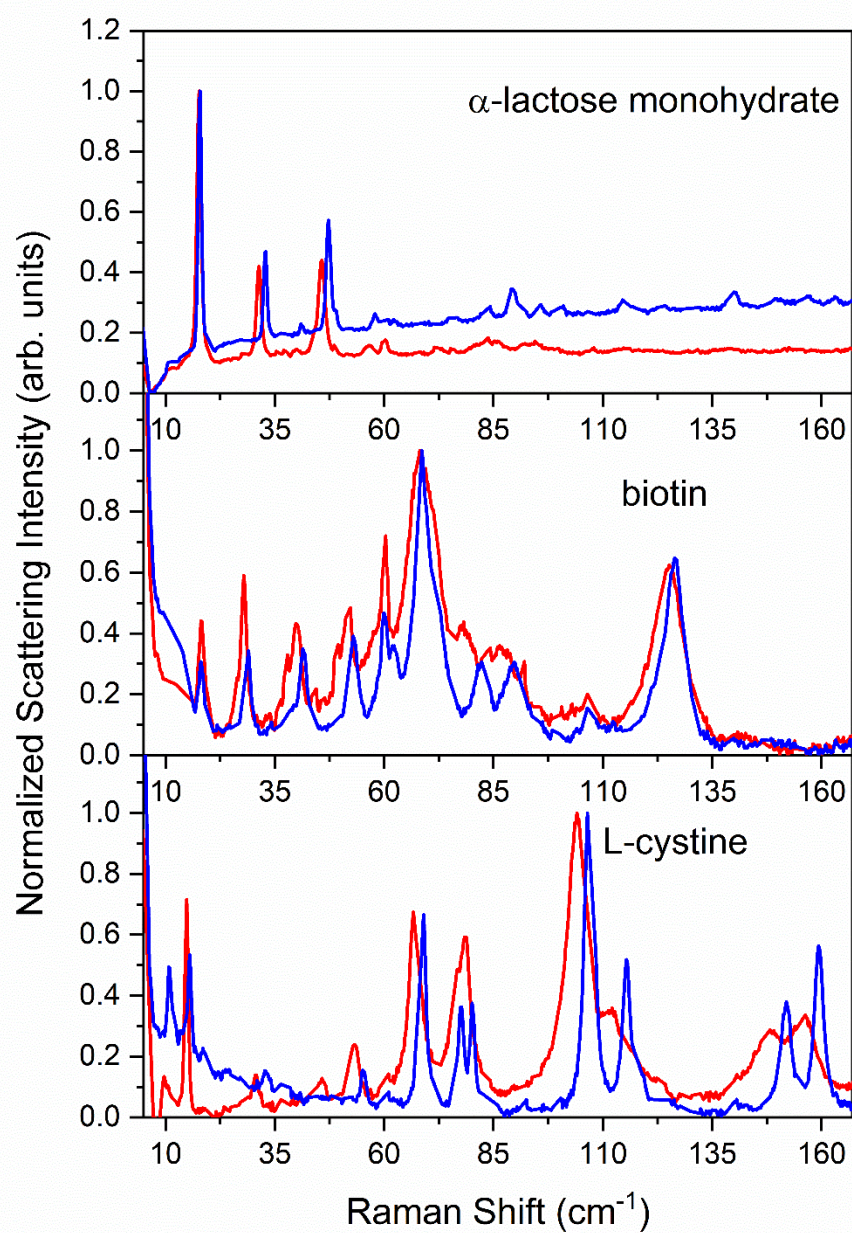
**Figure 5-2.** Raman spectra of molecular standards from 5 - 167 cm^{-1} at 293 K (red) and 78 K (blue). Individual spectra have been intensity normalized to 1 and therefore relative intensities between samples are not comparable.

# 5.3.3 Solid-state Density Functional Theory Calculations

In this work, a typical set of default ss-DFT calculation parameters was chosen that adheres to a level of computational rigor that is generally accepted to be of publication quality and achievable with commercial software and minimal formal training. The same computational methodology was used across all three proposed standards and the lattice dimensions of the fully-optimized ss-DFT structures agree very well with those measured at 100 K using SC-XRD (**Table 5-2**), with the average unsigned error being 0.35%. Since ss-DFT calculations are effectively performed at 0 K, comparison to a low-temperature experimental structure is most appropriate.

**Table 5-2.** Calculated lattice dimensions for α-lactose monohydrate, biotin, and L-cystine compared to 100 K SC-XRD measurements.

| | a (Å) | b (Å) | c (Å) | α (°) | β (°) | γ (°) |
|---|---|---|---|---|---|---|
| α-lactose monohydrate | | | | | | |
| 100 K Exp. | 4.755(5) | 21.44(2) | 7.729(7) | 90 | 105.95(2) | 90 |
| PBE-D3/def2-TZVP | 4.7456 | 21.5875 | 7.7559 | 90 | 106.0994 | 90 |
| Percent Error | -0.20% | 0.69% | 0.35% | - | 0.14% | - |
| biotin | | | | | | |
| 100 K Exp. | 5.176(6) | 10.288(12) | 20.89(3) | 90 | 90 | 90 |
| PBE-D3/def2-TZVP | 5.1685 | 10.3373 | 20.9174 | 90 | 90 | 90 |
| Percent Error | -0.14% | 0.48% | 0.13% | - | - | - |
| L-cystine | | | | | | |
| 100 K Exp. | 5.4028(4) | 5.4028(4) | 55.956(1) | 90 | 90 | 120 |
| PBE-D3/def2-TZVP | 5.4060 | 5.4060 | 56.5076 | 90 | 90 | 120 |
| Percent Error | 0.06% | 0.06% | 0.97% | - | - | - |

Attention was focused on the theoretical agreement with the spectral region below 3.5 THz (117 cm$^{-1}$) with a complete list of calculated frequency positions and intensities for both the IR- and Raman active modes of the solids available in **Appendix A**. The vibrational frequency calculations for α-lactose monohydrate (**Fig. 5-3**) closely match with experiment for the IR-

active vibrations, and further validates why it has been proposed in the past to serve as a

molecular standard for THz-TDS.[17] The ss-DFT prediction for the Raman-active modes (**Figure 5-4**) does well for the strong peaks noted below 50 cm$^{-1}$, but the low scattering efficiency

inherent to the sample at higher Raman shifts makes it difficult to match the predicted

frequencies with experiment and makes it less ideal to serve as a standard for LFRS.[35] Biotin has

numerous well-defined peaks in both the terahertz (**Figure 5-5**) and Raman (**Figure 5-6**) spectra

that can be assigned using ss-DFT across the entire spectral range investigated. The

computational approach applied here also allows for the majority of the peaks in both the

terahertz and Raman spectra of L-cystine (**Figure 5-7**, **Fig 5-8**) to be interpreted, but definitive

assignments for all features is not possible due to the noticeable mismatch in several of the

predicted peak positions and intensities. The origin of the lower performance in the L-cystine

simulations is not clear, but could be tied to the specific structure of this molecule. The largest

deviation between the theoretical and experimental structures of L-cystine occur in the length of

the S-S disulfide bond, with an error that is twice as large as those found in other non-hydrogen

bond lengths. This indicates that the theoretical treatment of this disulfide bond may be the

source of the simulation limitations, but that is speculative. It has been proposed that a hybrid

density functional is a more appropriate choice to properly model disulfide bonds, however the

use of these in solids results in a significant increase in required computational resources and

execution time.[65] The PBE-D3/def2-TZVP frequency calculation for L-cystine took

approximately 20 days on 256 processor cores and the inclusion of a hybrid functional would

more than double the run time, making it impractical to use. Despite imperfections, the general

agreement between experiment and theory confirms that the theoretical approach chosen in this

work is sufficient to adequately model the crystal structures and low-frequency motions of these molecular solids and arrive at meaningful interpretations.

However, if the goal is computational accuracy and not simply demonstrative method benchmarking, there are a multitude of simulation variations that could be explored including hybrid functionals[66-68], larger basis sets[69], plane-wave solutions (e.g. VASP)[70], the quasi-harmonic approximation[71], and *ab initio* molecular dynamics (e.g. CP2K)[72], all coming with various investments of time, computational resources, and user expertise. Each system under study is chemically unique and so choosing simulation parameters specific to each system would provide more chemically accurate results, however such a process is antithetical to the evaluation of the single and widely adopted computational approach utilized here.

The results from the vibrational frequency calculations are able to provide spectral assignments, as well as insight into mode characters, for the majority of the observable terahertz and Raman spectral peaks with tentative correlation tables available in **Appendix A**. To demonstrate this capability, the lowest frequency feature in each spectrum is considered here. The lowest observed vibrational modes in crystalline α-lactose monohydrate and biotin are each vibrations that are both IR- and Raman-active. Their mode characters have already been described in earlier works as rotational, and the current results are consistent with those findings.[37, 38] Interestingly, no solid-state simulations of the low-frequency vibrations of L-cystine have been reported, making the current assignments of the experimental spectrum here particularly useful. The strong hydrogen bonds between L-cystine molecules prevent independent molecular motion, resulting in a mixture of both translational and rotational motion within a single low-frequency vibration of the crystalline solid. The lowest observed terahertz-active peak in crystalline L-cystine (**Figure 5-1**) is found at 9.3 cm$^{-1}$ (at 50 K) which can be

assigned to the mode predicted at 10.72 cm$^{-1}$ by the simulations (**Figure 5-7**). This mode is a combination of rotational and translational motion, where rotational motion can be represented by L-cystine hydrogen-bonded dimers rotating in the *ab* plane while the adjacent rows translate along the *b-axis* as illustrated in **Figure 5-9**. The Raman spectrum (**Figure 5-2**) reveals its first feature at 10.5 cm$^{-1}$ (at 50 K). This peak can be assigned to the mode predicted at 12.21 cm$^{-1}$ by the simulations (**Figure 5-8**) and is also a combination of rotational and translational motion where the L-cystine hydrogen-bonded dimers rotate in the *ab* plane while the adjacent rows translate along the *a*-axis (**Figure 5-10**). These remarkably low-frequency modes make L-cystine a useful benchmark for evaluating the low-frequency response of THz-TDS and LFRS instrumentation.
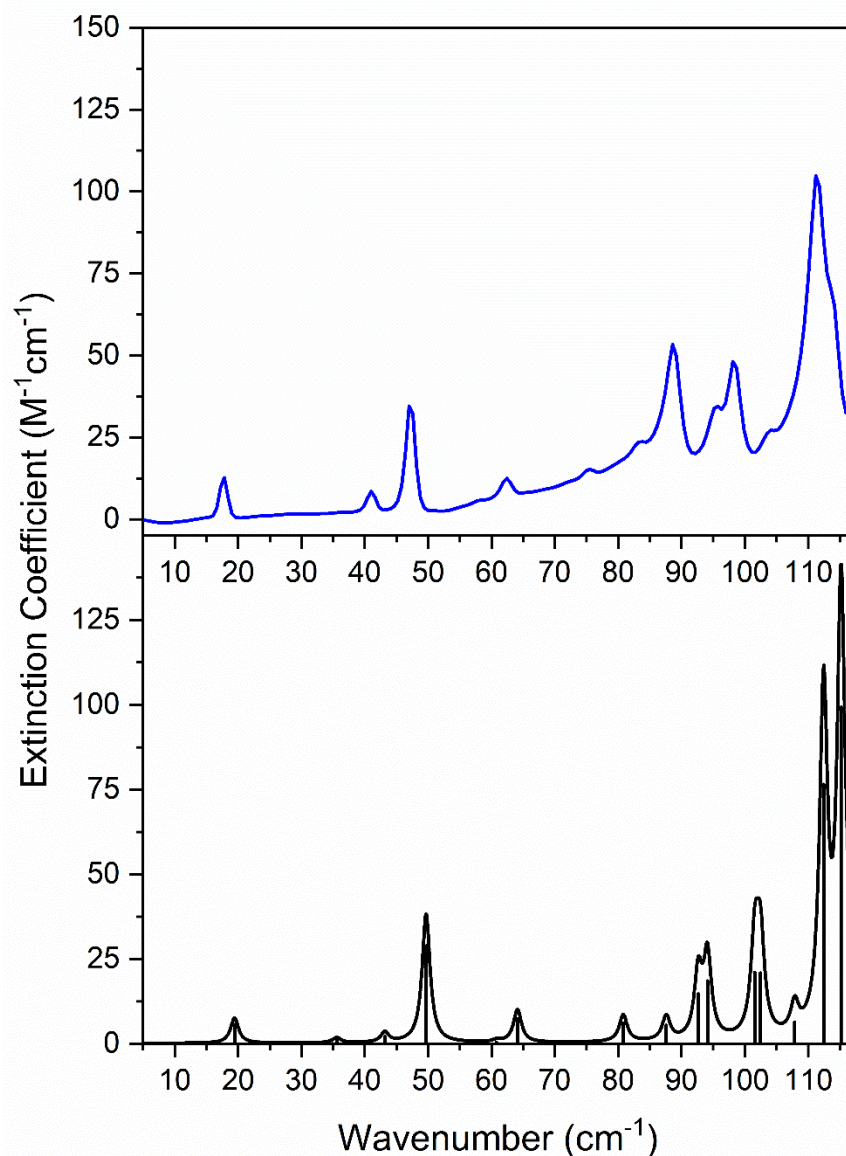
**Figure 5-3.** Experimental (65 K) terahertz spectrum (blue, top) and simulated terahertz spectrum (black, bottom) for α-lactose monohydrate. The simulated spectra have been convolved with Lorentzian line shapes using full-width half-maxima (FWHM) of 1.5 cm^{-1}. The simulated intensity values have been scaled by 0.5 to facilitate comparison with experiment.
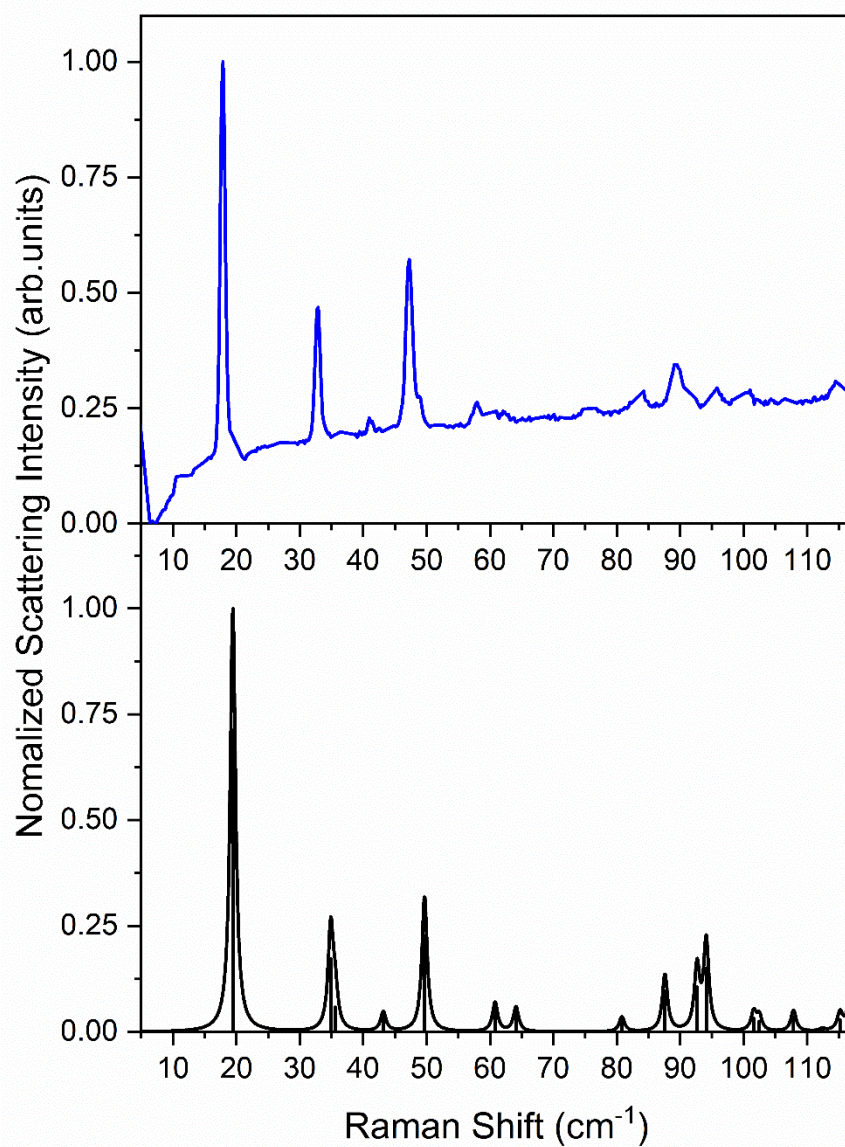
**Figure 5-4.** Experimental (78 K) Raman spectrum (blue, top) and simulated Raman spectrum (black, bottom) for α-lactose monohydrate. The simulated spectra have been convolved with Lorentzian line shapes using full-width half-maxima (FWHM) of 1.0 cm$^{-1}$.
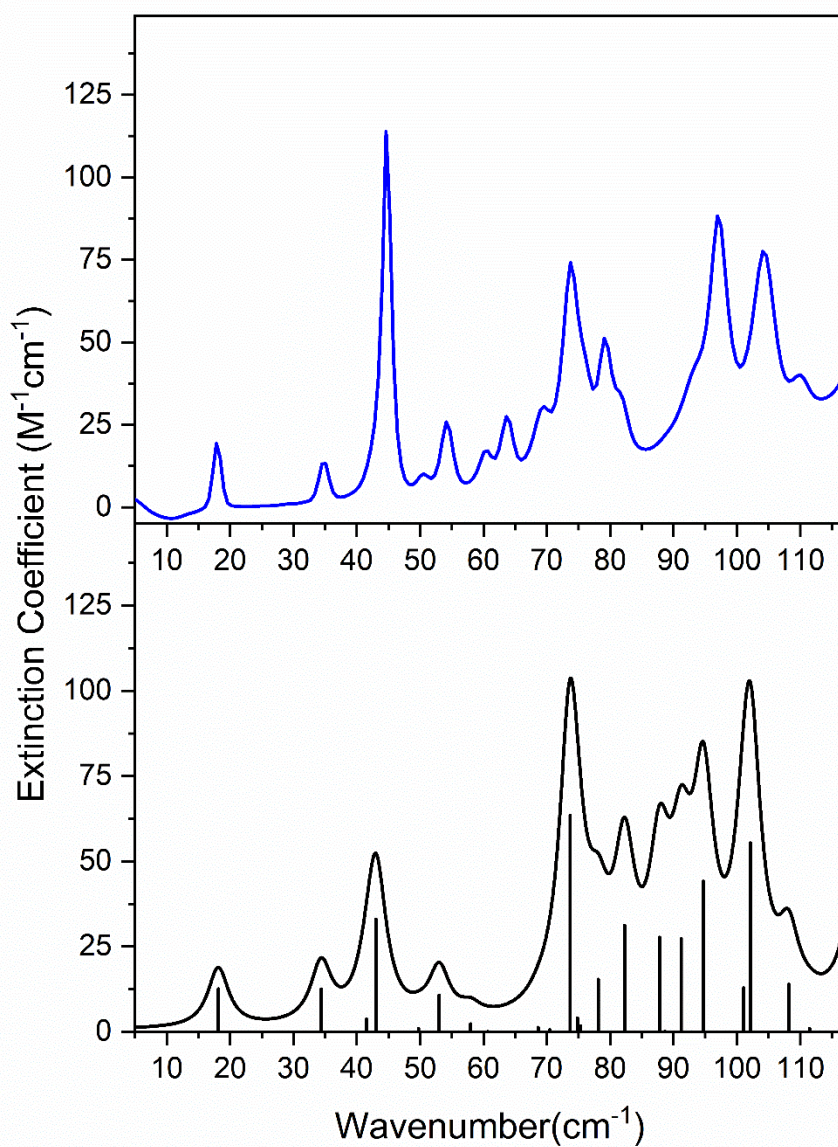
**Figure 5-5.** Experimental (65 K) terahertz spectrum (blue, top) and simulated terahertz spectrum (black, bottom) for biotin. The simulated spectra have been convolved with Lorentzian line shapes using full-width half-maxima (FWHM) of 4.0 cm$^{-1}$.
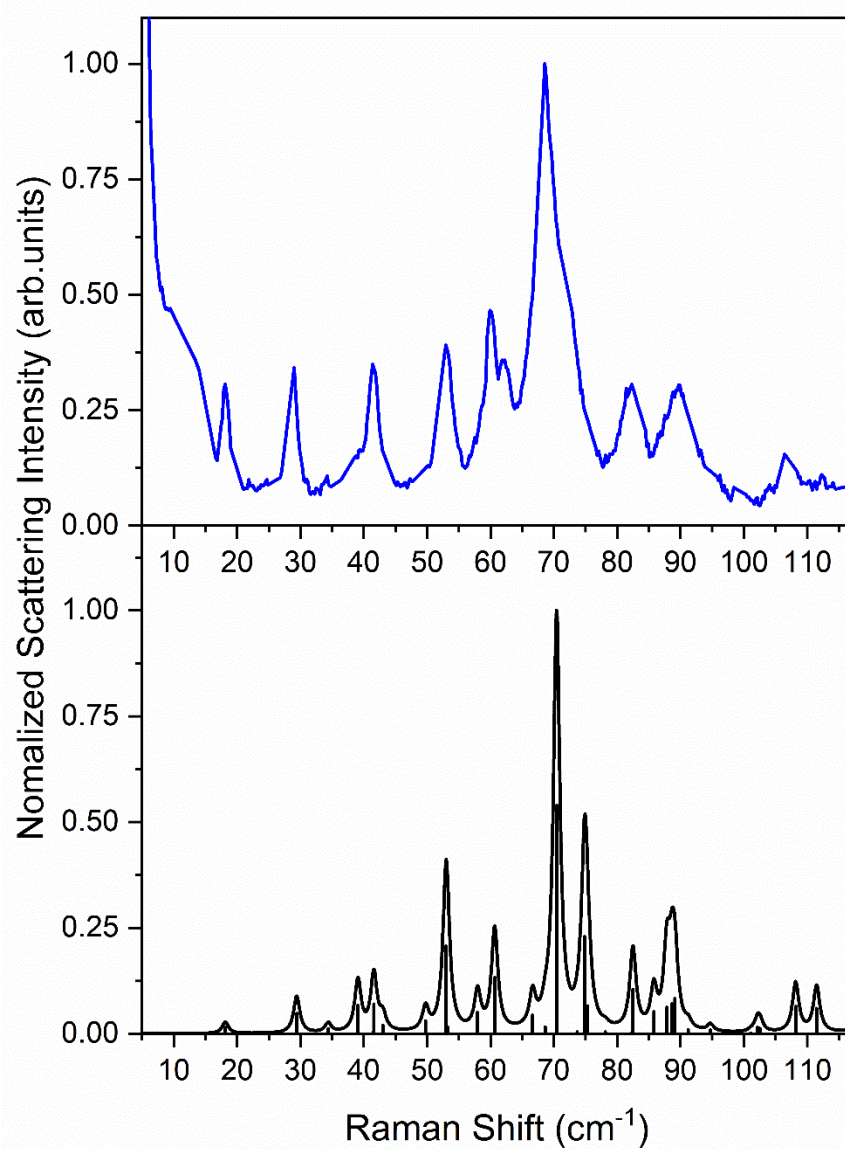
**Figure 5-6.** Experimental (78 K) Raman spectrum (blue, top) and simulated Raman spectrum (black, bottom) for biotin. The simulated spectra have been convolved with Lorentzian line shapes using full-width half-maxima (FWHM) of 1.2 cm$^{-1}$.
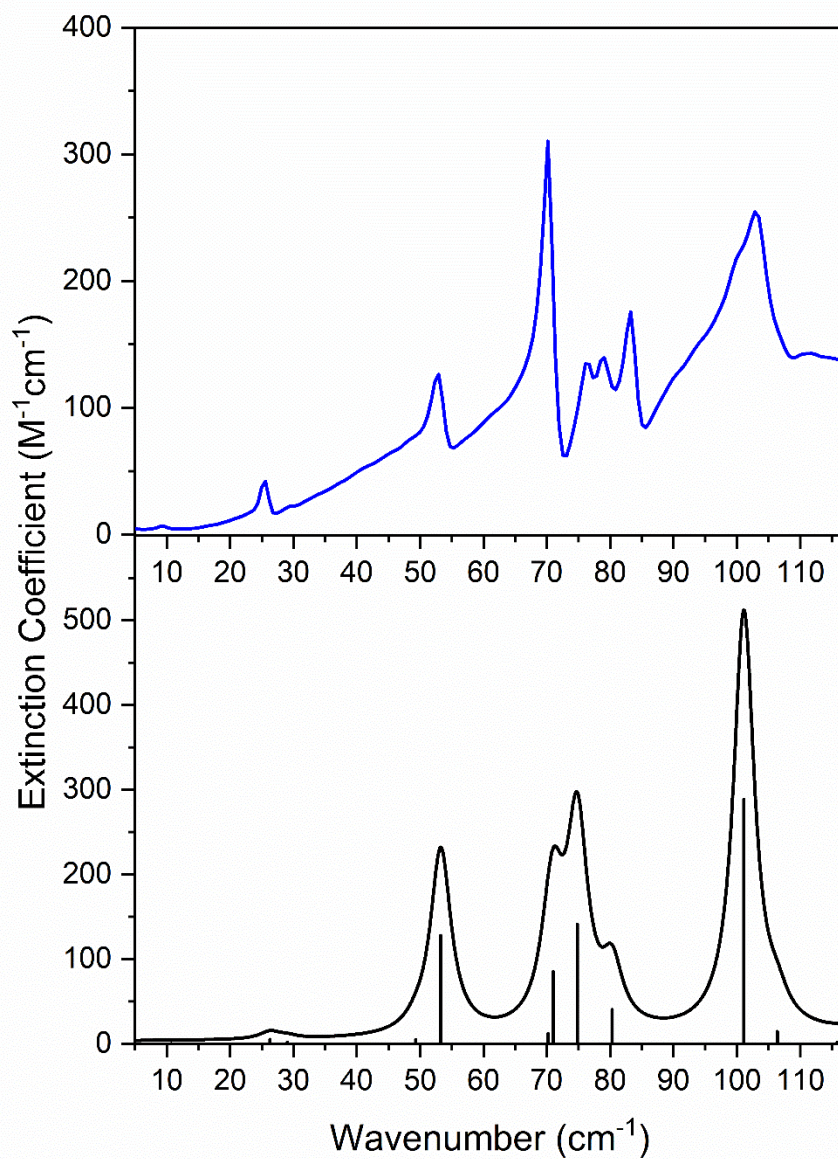
**Figure 5-7.** Experimental (50 K) terahertz spectrum (blue, top) and simulated terahertz spectrum (black, bottom) for L-cystine. The simulated spectra have been convolved with Lorentzian line shapes using full-width half-maxima (FWHM) of 4 cm$^{-1}$.
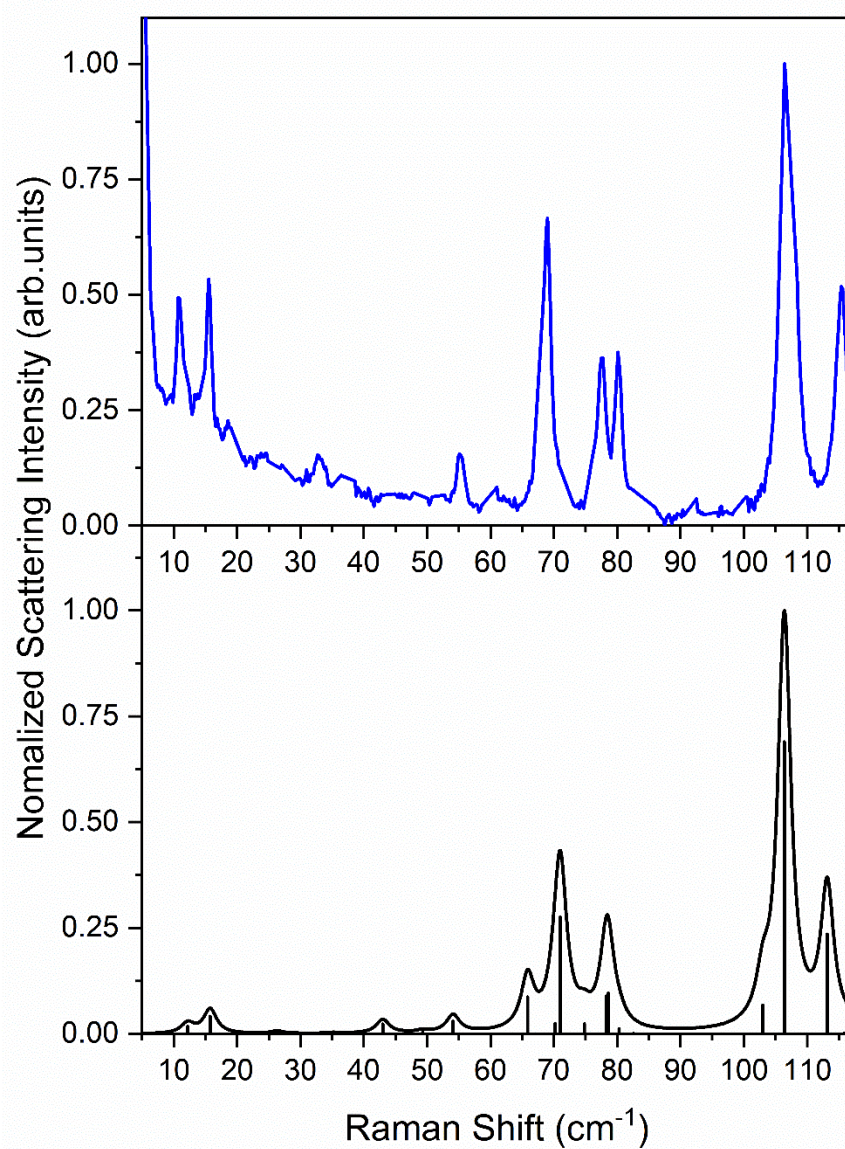
**Figure 5-8.** Experimental (78 K) Raman spectrum (blue, top) and simulated Raman spectrum (black, bottom) for L-cystine. The simulated spectra have been convolved with Lorentzian line shapes using full-width half-maxima (FWHM) of 2.5 cm$^{-1}$.
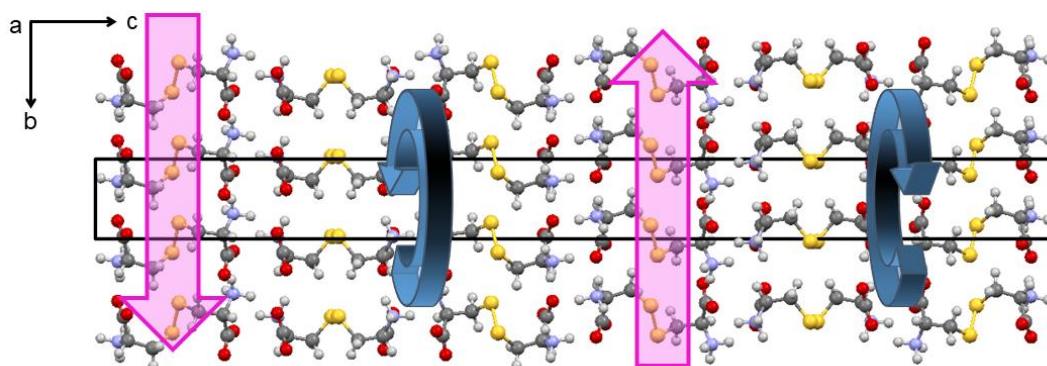
**Figure 5-9.** Rotational and translational mode character of the lowest observed IR-active mode for L-cystine at 9.3 cm$^{-1}$ (calc. 10.72 cm$^{-1}$).
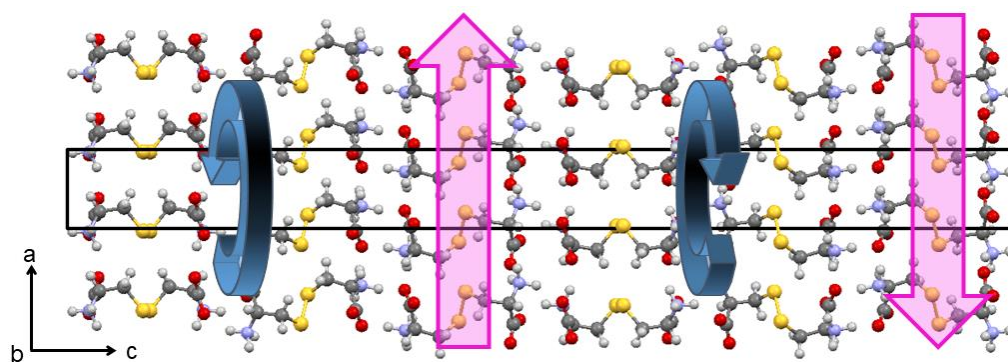


**Figure 5-10.** Rotational and translational mode character of the lowest observed Raman-active mode for L-cystine at 10.5 cm$^{-1}$ (calc. 12.21 cm$^{-1}$).

## 5.4 Conclusions

A series of readily available molecular crystals have been selected and thoroughly evaluated for their potential to serve as spectral standards for both low-frequency terahertz and Raman spectroscopies. Considering their spectra alone, α-lactose monohydrate, biotin, and L-cystine have a multitude of distinguishable peaks below 167 cm$^{-1}$ (5 THz) at room and low temperatures. For this reason, all three spectral standards would provide a strong basis for users to evaluate both their terahertz and Raman instruments over a range of temperatures. However, the molecular standards do vary in performance for the different spectroscopies. While α-lactose monohydrate is more suited for use in terahertz applications, L-cystine is more suited for use in low-frequency Raman applications, with biotin proving to be a strong choices across both forms of low-frequency spectroscopy. Adding to the overall evaluation of these molecular standards, solid-state density functional theory simulations were performed on each using commercially available software at a level of theory that is generally acceptable for publication. The computational analyses of the spectra and crystal structures of the proposed standards were successful and provided useful insights into the origins of the observed spectral features. These results highlight that while specific tuning of computational methods for each crystalline species will always yield the most accurate simulation, reliable and meaningful analyses can be achieved using widely accepted methods (e.g. PBE-D3/def2-ZTVP) that are available in numerous software packages and transferable to diverse solids. In summary, each of the investigated molecular crystals provides useful benchmarks for both experimental and computational studies, but the overall top performing molecular standard across all sample criteria and methods was found to be crystalline biotin.

**Appendix A**

 Unprocessed Raman spectra of atmospheric rotational lines, α-lactose monohydrate, biotin, and L-cystine; Raman spectra of varying optical path lengths and the influence of atmospheric interference; comparison of powder X-ray diffraction patterns for all three standards using ss-DFT, published literature, and experiment; individual trials for THz-TDS; experimental peak positions for both THz-TDS and LFRS for α-lactose monohydrate, biotin, and L-cystine; calculated peaks positions and intensities for both THz-TDS and LFRS for α-lactose monohydrate, biotin, and L-cystine; waveforms for all THz-TDS measurements; processed THz-TDS and LFRS data; CRYSTAL17 input files for the geometry optimization and frequency calculations for α-lactose monohydrate, biotin, and L-cystine; tentative correlation tables between experimental THz-TDS and LFRS peaks and ss-DFT simulations

**Acknowledgements**

## 5.5 References

1.      Larkin, P. *Infrared and Raman Spectroscopy: Principles and Spectral Interpretation*, 1st
        ed.; Elsevier: Amsterdam, 2011.

2.      Stuart, B. H. *Infrared Spectroscopy: Fundamentals and Applications*, John Wiley & Sons
        Ltd.: West Sussex, 2004.

3.      Beard, M. C.;  Turner, G. M.; Schmuttenmaer, C. A. Terahertz Spectroscopy. *J. Phys.
        Chem. B* **2002,** *106* (29), 7146-7159.

4.      Jepsen, P. U.;  Cooke, D. G.; Koch, M. Terahertz Spectroscopy and Imaging – Modern
        Techniques and Applications *Laser Photonics Rev.* **2012,** *6* (3), 418-418.

5.      Kindt, J. T.; Schmuttenmaer, C. A. Far-Infrared Dielectric Properties of Polar Liquids
        Probed by Femtosecond Terahertz Pulse Spectroscopy. *J. Phys. Chem.* **1996,** *100* (24),
        10373-10379.

6.      Zimdars, D.;  White, J.;  Stuk, G.;  Sucha, G.;  Fichter, G.; Williamson, S. L. Time
        Domain Terahertz Imaging of Threats in Luggage and Personnel. *Int. J. High Speed
        Electron. Syst.* **2007,** *17* (2), 271-281.

7.      Guillet, J.;  Roux, M.;  Wang, K.;  Ma, X.;  Fauquet, F.;  Balacey, H.;  Recur, B.;
        Darracq, F.; Mounaix, P. Art Painting Diagnostic Before Restoration with Terahertz and
        Millimeter Waves. *J. Infrared, Millimeter, Terahertz Waves* **2017,** *38* (4), 369-379.

8.      Zeitler, J.;  Taday, P.;  Newnham, D.;  Pepper, M.;  Gordon, K.; Rades, T. Terahertz-
        Pulsed Spectroscopy and Imaging in Pharmaceutical Setting. *J. Pharm. Pharmacol.* **2007,**
        *59*, 209-23.

9. Willett, D. R.; Yilmaz, H.; Wokovich, A. M.; Rodriguez, J. D. Low-frequency Raman Mapping and Multivariate Image Analysis for Complex Drug Products. *American Pharmaceutical Review* **2019,** *22* (3), 48-51.

10. Hisada, H.; Inoue, M.; Koide, T.; Carriere, J.; Heyler, R.; Fukami, T. Direct High-Resolution Imaging of Crystalline Components in Pharmaceutical Dosage Forms Using Low-Frequency Raman Spectroscopy. *Org. Process Res. Dev.* **2015,** *19* (11), 1796-1798.

11. Zhang, X.-C.; Xu, J. *Introduction to THz Wave Photonics*, Springer: New York, 2010.

12. Carriere, J. T.; Havermeyer, F. Ultra-low Frequency Stokes and Anti-Stokes Raman Spectroscopy at 785nm with Volume Volographic Grating Filters. Proceedings of SPIE BiOS, San Francisco, SPIE: San Francisco, 2012.

13. Heyler, R. A.; Carriere, J. T. A.; Havermeyer, F. THz-Raman: Accessing Molecular Structure with Raman Spectroscopy for Enhanced Chemical Identification, Analysis, and Monitoring. Proceedings of SPIE Defense, Security, and Sensing, SPIE: 2013.

14. Hangyo, M.; Tani, M.; Nagashima, T. Terahertz Time-Domain Spectroscopy of Solids: A Review. *Int. J. Infrared Millimeter Waves* **2005,** *26* (12), 1661-1690.

15. Dampf, S. J.; Korter, T. M. Anomalous Temperature Dependence of the Lowest-Frequency Lattice Vibration in Crystalline γ-Aminobutyric Acid. *J. Phys. Chem. A* **2019,** *123* (10), 2058-2064.

16. Fukunaga, K. Construction of Open Terahertz Spectral Database. *J. NICT* **2008,** *55* (1), 61-66.

17.     Naftaly, M. An International Intercomparison of THz Time-domain Spectrometers. Proceedings of 2016 41st International Conference on Infrared, Millimeter, and Terahertz waves (IRMMW-THz), 25-30 Sept. 2016; 2016; pp 1-2.

18.     Hollberg, L.; Oates, C. W.; Curtis, E. A.; Ivanov, E. N.; Diddams, S. A.; Udem, T.; Robinson, H. G.; Bergquist, J. C.; Rafac, R. J.; Itano, W. M.; Drullinger, R. E.; Wineland, D. J. Optical Frequency Standards and Measurements. *IEEE J. Quantum Electron.* **2001,** *37* (12), 1502-1513.

19.     Withayachumnankul, W.; Naftaly, M. Fundamentals of Measurement in Terahertz Time-Domain Spectroscopy. *Journal of Infrared, Millimeter, and Terahertz Wave* **2014,** *35* (8), 610-637.

20.     Ho, L.; Pepper, M.; Taday, P. Signatures and fingerprints. *Nat. Photonics* **2008,** *2*, 541.

21.     Delaney, S. P.; Witko, E. M.; Smith, T. M.; Korter, T. M. Investigating Tautomeric Polymorphism in Crystalline Anthranilic Acid Using Terahertz Spectroscopy and Solid-State Density Functional Theory. *J. Phys. Chem. A* **2012,** *116* (30), 8051-8057.

22.     Socrates, G. *Infrared and Raman Characteristic Group Frequencies: Tables and Charts*, 3 ed.; John Wiley & Sons Ltd.: West Sussex, 2004.

23.     Sholl, D. S.; Steckel, J. A. *Density Functional Theory: A Practical Introduction*, John Wiley & Sons, Inc.: Hoboken, New Jersey, 2009.

24.     Kleist, E. M.; Korter, T. M. Quantitative Analysis of Minium and Vermilion Mixtures Using Low-Frequency Vibrational Spectroscopy. *Anal. Chem.* **2020,** *92*, 1211-1218.

25.     Chernyshov, I. Y.; Vener, M. V.; Feldman, E. V.; Paraschuk, D. Y.; Sosorev, A. Y. Inhibiting Low-frequency Vibrations Explains Exceptionally High Electron Mobility in

2,5-Difluoro-7,7,8,8-tetracyanoquinodimethane (F2-TCNQ) Single Crystals. *J. Phys. Chem. Lett.* **2017,** *8* (13), 2875-2880.

26.     Delaney, S. P.; Korter, T. M. Terahertz Spectroscopy and Computational Investigation of the Flufenamic Acid/Nicotinamide Cocrystal. *J. Phys. Chem. A* **2015,** *119* (13), 3269-3276.

27.     Neu, J.; Stone, E. A.; Spies, J. A.; Storch, G.; Hatano, A. S.; Mercado, B. Q.; Miller, S. J.; Schmuttenmaer, C. A. Terahertz Spectroscopy of Tetrameric Peptides. *J. Phys. Chem. Lett.* **2019,** *10* (10), 2624-2628.

28.     Ruggiero, M. T.; Zhang, W.; Bond, A. D.; Mittleman, D. M.; Zeitler, J. A. Uncovering the Connection Between Low-frequency Dynamics and Phase Transformation Phenomena in Molecular Solids. *Phys. Rev. Lett.* **2018,** *120* (19).

29.     Chaney, M. O.; Steinrauf, L. K. The Crystal and Molecular Structure of Tetragonal l-Cystine. *Acta Crystallographica Section B* **1974,** *30* (3), 711-716.

30.     Dahaoui, S.; Pichon-Pesme, V.; Howard, J. A. K.; Lecomte, C. CCD Charge Density Study on Crystals with Large Unit Cell Parameters: The Case of Hexagonal l-Cystine. *J. Phys. Chem. A* **1999,** *103* (31), 6240-6250.

31.     Kirk, J. H.; Dann, S. E.; Blatchford, C. G. Lactose: A Definitive Guide to Polymorph Determination. *Int. J. Pharm.* **2007,** *334* (1), 103-114.

32.     Zeitler, J. A.; Kogermann, K.; Rantanen, J.; Rades, T.; Taday, P. F.; Pepper, M.; Aaltonen, J.; Strachan, C. J. Drug Hydrate Systems and Dehydration Processes Studied by Terahertz Pulsed Spectroscopy. *Int. J. Pharm.* **2007,** *334* (1), 78-84.

33.     Korter, T. M.; Plusquellic, D. Continuous-wave Terahertz Spectroscopy of Biotin: Vibrational Anharmonicity in the Far-infrared. *Chem. Phys. Lett.* **2004,** *385*, 45-51.

34. Brandt, N. N.; Chikishev, A. Y.; Kargovsky, A. V.; Nazarov, M. M.; Parashchuk, O. D.; Sapozhnikov, D. A.; Smirnova, I. N.; Shkurinov, A. P.; Sumbatyan, N. V. Terahertz Time-domain and Raman Spectroscopy of the Sulfur-containing Peptide Dimers: Low-frequency Markers of Disulfide Bridges. *Vib. Spectrosc.* **2008,** *47* (1), 53-58.

35. Larkin, P. J.; Dabros, M.; Sarsfield, B.; Chan, E.; Carriere, J. T.; Smith, B. C. Polymorph Characterization of Active Pharmaceutical Ingredients (APIs) Using Low-Frequency Raman Spectroscopy. *Appl. Spectrosc.* **2014,** *68* (7), 758-776.

36. Takahashi, M.; Okamura, N.; Ding, X.; Shirakawa, H.; Minamide, H. Intermolecular Hydrogen Bond Stretching Vibrations Observed in Terahertz Spectra of Crystalline Vitamins. *CrystEngComm* **2018,** *20* (14), 1960-1969.

37. Allis, D. G.; Fedor, A. M.; Korter, T. M.; Bjarnason, J. E.; Brown, E. R. Assignment of the Lowest-lying THz Absorption Signatures in Biotin and Lactose Monohydrate by Solid-state Density Functional Theory. *Chem. Phys. Lett.* **2007,** *440* (4), 203-209.

38. Saito, S.; Inerbaev, T.; Mizuseki, H.; Igarashi, N.; Kawazoe, Y. First Principles Calculation of Terahertz Vibrational Modes of a Disaccharide Monohydrate Crystal of Lactose. *Jpn. J. Appl. Phys.* **2006,** *45*, L1156–L1158.

39. Yamamoto, K.; Kabir, M. H.; Tominaga, K. Terahertz Time-domain Spectroscopy of Sulfur-containing Biomolecules. *J. Opt. Soc. Am. B* **2005,** *22* (11), 2417-2426.

40. Smith, J. H.; Dann, S. E.; Elsegood, M. R. J.; Dale, S. H.; Blatchford, C. G. α-Lactose Monohydrate: a Redetermination at 150 K. *Acta Crystallogr., Sect. E: Crystallogr. Commun.* **2005,** *61* (8), o2499-o2501.

41. Altaf, M.; Stoeckli-Evans, H. Chiral One- and Two-Dimensional Silver(I)-Biotin Coordination Polymers. *Acta Crystallogr., Sect. C: Cryst. Struct. Commun.* **2013,** *69* (2), 127-137.

42. Compaan, A.; Wagoner, A.; Aydinli, A. Rotational Raman scattering in the Instructional Laboratory. *Am. J. Phys.* **1994,** *62* (7), 639-645.

43. Fan, W. H.; Burnett, A.; Upadhya, P. C.; Cunningham, J.; Linfield, E. H.; Davies, A. G. Far-Infrared Spectroscopic Characterization of Explosives for Security Applications Using Broadband Terahertz Time-Domain Spectroscopy. *Appl. Spectrosc.* **2007,** *61* (6), 638-643.

44. Jepsen, P. U.; Fischer, B. M. Dynamic Range in Terahertz Time-domain Transmission and Reflection Spectroscopy. *Opt. Lett.* **2005,** *30* (1), 29-31.

45. Neu, J.; Schmuttenmaer, C. A. Tutorial: An Introduction to Terahertz Time Domain Spectroscopy (THz-TDS). *J. Appl. Phys.* **2018,** *124* (23), 231101.

46. Franz, M.; Fischer, B. M.; Walther, M. The Christiansen Effect in Terahertz Time-domain Spectra of Coarse-grained Powders. *Appl. Phys. Lett.* **2008,** *92* (2), 021107.

47. Smith, R. M.; Arnold, M. A. Terahertz Time-Domain Spectroscopy of Solid Samples: Principles, Applications, and Challenges. *Appl. Spectrosc. Rev.* **2011,** *46* (8), 636-679.

48. Vázquez Cabo, J.; Chamorro-Posada, P.; Fraile-Pelaez, J.; Rubinos-Lopez, O.; López-Santos, J. M.; Martin-Ramos, P. Windowing of THz Time-domain Spectroscopy Signals: A Study Based on Lactose. *Opt. Commun.* **2016,** *366*, 386-396.

49. Shen, Y. C.; Taday, P. F.; Pepper, M. Elimination of Scattering Effects in Spectral Measurement of Granulated Materials using Terahertz Pulsed Spectroscopy. *Appl. Phys. Lett.* **2008,** *92* (5), 051103.

50. Dovesi, R.; Erba, A.; Orlando, R.; Zicovich-Wilson, C. M.; Civalleri, B.; Maschio, L.; Rérat, M.; Casassa, S.; Baima, J.; Salustro, S.; Kirtman, B. Quantum-mechanical Condensed Matter Simulations with CRYSTAL. *Wiley Interdiscip. Rev.: Comput. Mol. Sci.* **2018,** *8* (4), e1360.

51. Weigend, F.; Ahlrichs, R. Balanced basis sets of split valence, triple zeta valence and quadruple zeta valence quality for H to Rn: Design and assessment of accuracy. *Phys. Chem. Chem. Phys.* **2005,** *7* (18), 3297-3305.

52. Perdew, J. P.; Burke, K.; Ernzerhof, M. Generalized Gradient Approximation Made Simple. *Phys. Rev. Lett.* **1996,** *77* (18), 3865-3868.

53. Grimme, S.; Antony, J.; Ehrlich, S.; Krieg, H. A Consistent and Accurate ab initio Parametrization of Density Functional Dispersion Correction (DFT-D) for the 94 Elements H-Pu. *J. Chem. Phys.* **2010,** *132* (15), 154104/1-154104/19.

54. Grimme, S.; Ehrlich, S.; Goerigk, L. Effect of the damping function in dispersion corrected density functional theory. *J. Comput. Chem.* **2011,** *32* (7), 1456-1465.

55. Grimme, S.; Hansen, A.; Brandenburg, J. G.; Bannwarth, C. Dispersion-Corrected Mean-Field Electronic Structure Methods. *Chem. Rev.* **2016,** *116* (9), 5105-5154.

56. Anderson, D. G. Iterative Procedures for Nonlinear Integral Equations. *J. Assoc. Comput. Mach.* **1965,** *12* (4), 547-560.

57. Pascale, F.; Zicovich-Wilson, C. M.; López Gejo, F.; Civalleri, B.; Orlando, R.; Dovesi, R. The Calculation of the Vibrational Frequencies of Crystalline Compounds and its Implementation in the CRYSTAL Code. *J. Comput. Chem.* **2004,** *25* (6), 888-897.

58. Zicovich-Wilson, C. M.; Pascale, F.; Roetti, C.; Saunders, V. R.; Orlando, R.; Dovesi, R. Calculation of the Vibration Frequencies of α-quartz: The Effect of Hamiltonian and Basis Set. *J. Comput. Chem.* **2004,** *25* (15), 1873-1881.

59. Maschio, L.; Kirtman, B.; Orlando, R.; Rèrat, M. Ab initio Analytical Infrared Intensities for Periodic Systems through a Coupled Perturbed Hartree-Fock/Kohn-Sham Method. *J. Chem. Phys.* **2012,** *137* (20), 204113.

60. Maschio, L.; Kirtman, B.; Rèrat, M.; Orlando, R.; Dovesi, R. Ab initio Analytical Raman Intensities for Periodic Systems through a Coupled Perturbed Hartree-Fock/Kohn-Sham Method in an Atomic Orbital Basis. II. Validation and Comparison with Experiments. *J. Chem. Phys.* **2013,** *139* (16), 164102/1-164102/9.

61. Xie, A.; He, Q.; Miller, L.; Sclavi, B.; Chance, M. R. Low Frequency Vibrations of Amino Acid Homopolymers Observed by Synchrotron Far-IR Absorption Spectroscopy: Excited State Effects Dominate the Temperature Dependence of the Spectra. *Biopolymers* **1999,** *49* (7), 591-603.

62. Zurk, L. M.; Orlowski, B.; Winebrenner, D. P.; Thorsos, E. I.; Leahy-Hoppa, M. R.; Hayden, L. M. Terahertz Scattering from Granular Material. *J. Opt. Soc. Am. B* **2007,** *24* (9), 2238-2243.

63. Kaushik, M.; Ng, B. W.-H.; Fischer, B. M.; Abbott, D. Terahertz Scattering by Granular Composite Materials: An Effective Medium Theory. *Appl. Phys. Lett.* **2012,** *100* (1), 011107.

64. Leger, M. N.; Ryder, A. G. Comparison of Derivative Preprocessing and Automated Polynomial Baseline Correction Method for Classification and Quantification of Narcotics in Solid Mixtures. *Appl. Spectrosc.* **2006,** *60* (2), 182-193.

65. Jursic, B. S. Computation of Bond Dissociation Energy for Sulfides and Disulfides with ab initio and Density Functional Theory Methods. *International Journal of Quantum Chemistry* **1997,** *62* (3), 291-296.

66. Adamo, C.; Barone, V. Toward Reliable Density Functional Methods Without Adjustable Parameters: The PBE0 Model. *J. Chem. Phys.* **1999,** *110* (13), 6158-6170.

67. Zhao, Y.; Truhlar, D. G. The M06 Suite of Density Functionals for Main Group Thermochemistry, Thermochemical Kinetics, Noncovalent Interactions, Excited States, and Transition Elements: Two New Functionals and Systematic Testing of Four M06-class Functionals and 12 other Functionals. *Theor. Chem. Acc.* **2008,** *120* (1), 215-241.

68. Stephens, P. J.;  Devlin, F. J.;  Chabalowski, C. F.; Frisch, M. J. Ab Initio Calculation of Vibrational Absorption and Circular Dichroism Spectra Using Density Functional Force Fields. *J. Phys. Chem.* **1994,** *98* (45), 11623-11627.

69. Pritchard, B. P.;  Altarawy, D.;  Didier, B.;  Gibson, T. D.; Windus, T. L. New Basis Set Exchange: An Open, Up-to-Date Resource for the Molecular Sciences Community. *J. Chem. Inf. Model.* **2019,** *59* (11), 4814-4820.

70. Kresse, G.; Furthmüller, J. Efficient Iterative Schemes for ab initio Total-energy Calculations using a Plane-wave Basis Set. *Phys. Rev. B* **1996,** *54* (16), 11169-11186.

71. Erba, A.;  Maul, J.; Civalleri, B. Thermal Properties of Molecular Crystals through Dispersion-corrected Quasi-harmonic ab initio Calculations: The Case of Urea. *Chem. Commun.* **2016,** *52* (9), 1820-1823.

72. Ruggiero, M. T.; Zeitler, J. A. Resolving the Origins of Crystalline Anharmonicity Using Terahertz Time-Domain Spectroscopy and ab Initio Simulations. *J. Phys. Chem. B* **2016,** *120* (45), 11733-11739.

# Chapter 6: Anomalous Temperature Dependence of the Lowest-frequency Lattice Vibration in Crystalline γ-Aminobutyric Acid

The material contained within this chapter is published in the Journal of Physical Chemistry A and has been reproduced with permission of the American Chemical Society.

## Abstract

Crystalline γ-aminobutyric acid (GABA) exhibits unusual thermal behavior in a low-frequency lattice vibration that occurs at 37.2 cm$^{-1}$ at 290 K, but decreases dramatically by 34.0% when the sample is cooled to 78 K. Lattice vibrations in molecular crystals are indicators of intermolecular force characteristics and the extraordinary temperature sensitivity of this vibration offers new insight into the local environment within the solid. Solid-state density functional theory simulations of the GABA crystal have found this anomalous frequency shift is based in unexpected differences in the strengths of the intermolecular hydrogen bonds that are cursorily the same. This was accomplished through mapping of the potential energy surfaces governing the terahertz-frequency motions of the GABA solid, and use of the quasi-harmonic approximation to model the response of all the lattice vibrations to temperature-induced unit cell volume changes brought about through the anharmonic character of the intermolecular interactions. The analysis reveals that the vibration in question is rotational in nature and involves the significant distortion of a specific weak intermolecular N–H⋯O hydrogen bond in the crystal that results in its unique thermal response.

## 6.1 Introduction

All crystalline solids possess some degree of anharmonicity in their low-frequency (sub-200 cm$^{-1}$) lattice vibrations, which affects a large number of physical properties including thermal expansion, mechanical elasticity, and dielectric constants.[1,2] Often the magnitude of the anharmonicity is small, and harmonic oscillator models can be used to successfully simulate and assign the low-frequency vibrational spectra of these solids. In molecular crystals, these assignments indicate that the spectra originate from intermolecular translations and rotations and intramolecular torsions, as demonstrated in numerous organic solids of varying complexity.[3,4,5,6] Yet given the non-zero anharmonic character of the potential energy surfaces, these molecular solids do exhibit lattice vibration shifting with temperature changes.

The vast majority of vibrations increase in frequency with sample cooling due to the contracted crystallographic unit cells yielding steeper potential energy surfaces. However, in some cases such as L-tartaric acid[7], ranitidine hydrochloride[8], and sucrose[9], specific vibrations show anomalous behavior with *reduced* vibrational frequencies at lowered temperatures. The magnitude of these negative frequency shifts are typically less than the more common positive shifts, but cannot be explained using simple unit cell volume arguments. Pure harmonic treatments are not able to adequately model such unusual phenomena and any computational analyses of these solids must incorporate vibrational anharmonicity either implicitly or explicitly. [10,11,12,13,14] For periodic solids, the utilization of the quasi-harmonic approximation in solid-state density functional theory simulations provides a powerful tool for investigating anharmonicity.[15,16,17]

The crystalline solid specifically studied here is 4-aminobutyric acid ($C_4H_9NO_2$), more commonly referred to as γ-aminobutyric acid (GABA). GABA is one of the main inhibitory neurotransmitters found in the central nervous system of vertebrates[18] and deficiencies have been linked to various disorders.[19] As a solid sample, GABA is most commonly found in the monoclinic polymorphic form, with GABA molecules existing as zwitterions participating in an extensive intermolecular hydrogen bond network involving the amino and carboxyl groups of adjacent molecules.[20,21]

A combination of experimental and computational methods has been applied in this work to understand the lattice vibrations of crystalline GABA. Single-crystal X-ray diffraction (SC-XRD) was used to verify the polymorph present, as well as observe changes in the GABA unit cell over a range of temperatures. Low-frequency Raman spectroscopy (LFRS) and terahertz time-domain spectroscopy (THz-TDS) were utilized to identify and monitor the shifting of the spectral peaks associated with lattice vibrations as a function of temperature. Solid-state density functional theory (ss-DFT) was then used to model and assign the sub-133 $cm^{-1}$ (sub-4 THz) vibrational frequencies in the observed terahertz spectra. The quasi-harmonic approximation was applied in these simulations to estimate the temperature dependencies of the lattice vibrations, and ultimately investigate the curvatures of the potential energy surfaces that arise from the complex molecular interactions in the GABA crystal.  Together, the low-frequency spectroscopies and solid-state calculations of GABA have revealed that a single infrared-active lattice vibration exhibits a very large anomalous frequency shift with temperature, and that this behavior is connected to the strength of a specific intermolecular hydrogen bond.

## 6.2 Methods

### 6.2.1 Experimental

GABA has been reported in two distinct polymorphic forms, monoclinic and tetragonal, as well as a hexagonal ethanol-solvated cocrystal.[22,23,24] SC-XRD was performed on GABA (Alfa Aesar, 97%, lot: K12Z010) recrystallized from aqueous solution to ensure and verify the presence of the monoclinic form. The structure solved in the present work at 95 K was consistent with the monoclinic results published by Steward, et al.[22] In addition to the complete structure determination at 95 K, the unit cell dimensions of monoclinic GABA were measured over a range of temperatures from 290 K to 100 K.  Measurements were obtained using a Bruker KAPPA APEX DUO diffractometer with an APEX II CCD and Mo Kα radiation ($\lambda = 0.71073$ Å) for full structure determination, while the temperature-dependent measurements were collected using Cu Kα radiation ($\lambda = 1.5418$ Å). Rapid unit cell dimension measurements were obtained using a faster scanning option to quickly monitor temperature trends, at the expense of higher uncertainty in the parameters versus the full structure refinement approach. Powder X-ray diffraction (PXRD) measurements were collected on the same instrument over an average of 4 phi scans (in-plane sample rotation), each sweeping 180° using Cu Kα radiation to obtain Debye rings. The rings were then integrated to obtain a powder pattern and used to verify bulk crystallinity.

Sets of low-frequency Raman data were obtained using an Ondax (Monrovia, CA) THz-Raman system in a backscattering geometry, with laser excitation centered at 784.7 nm and fiber-coupled to an Andor Shamrock 750 spectrograph equipped with an iDus 416 CCD. Pure GABA was pressed at 2000 psig into a 13 mm diameter free-standing pellet and kept under

vacuum in a Janis ST-100 optical cryostat with glass windows for the duration of the experiment. Minor contributions to the spectra from atmospheric Raman rotational lines have not been accounted for. Data was collected over 225 acquisitions, each with an exposure time of 2 seconds across a range of temperatures from 290 K to 78 K. The useable spectral range was 10 to 300 cm$^{-1}$ with an effective spectral resolution of 0.6 cm$^{-1}$.

Terahertz time-domain spectra were obtained using a TeraFlash all fiber-coupled terahertz spectrometer from Toptica Photonics (Munich, Germany) based on a 1.5 µm femtosecond fiber laser with an InGaAs 25 µm strip-line photoconductive antenna for terahertz generation and an InGaAs 25 µm dipole photoconductive antenna for terahertz detection. The sample was ground and mixed with a polytetrafluoroethylene (PTFE) matrix (1.5% by mass) and then pressed into a pellet (13 mm x 2 mm) at 2000 psig. A pure PTFE pellet was made under the same conditions to serve as a reference. Experimental spectra were then obtained from 290 K to 78 K with the sample and reference held under vacuum in the same cryostat, but with polymethylpentene (TPX) windows. The external optical path was purged with dry $N_2$ gas to reduce interference from atmospheric water. For each trial, the sample and reference blank were scanned over a full 100 ps time window, but data was truncated prior to analysis to 17 ps past the THz pulse center to avoid spurious reflections generated at the pellet surface. The ratio of the Fourier-transformed data of the sample and reference produced terahertz spectra from 10 to 133 cm$^{-1}$ (0.3 to 4.0 THz) with a spectral resolution of approximately 2 cm$^{-1}$. The extinction coefficient ($\varepsilon$) is reported in units of M$^{-1}$cm$^{-1}$ and expressed in terms of crystallographic unit cell concentration ($Z=4$).

## 6.2.2 Computational

All ss-DFT calculations were performed with the CRYSTAL17[25] software package, with the crystalline environment accounted for with periodic boundary conditions. The Perdew-Burke-Ernzerhof (PBE) density functional[26] was used along with def2-TZVPP, a triple-zeta valence basis set with added polarization functions[27]. The calculations were augmented with Grimme's London dispersion correction (D3 with the Becke-Johnson damping function) to better treat weak intermolecular forces.[28,29,30] The structure was fully optimized within the crystallographic space group ($P2_1/c$) to a total energy convergence of $\Delta E < 10^{-8}$ hartree, with starting coordinates from the SC-XRD structure solved at 95 K. Harmonic vibrational frequencies were calculated from the optimized structure with a more stringent energy convergence of $\Delta E < 10^{-10}$ hartree where all bielectronic integrals (Coulomb and exchange) are evaluated exactly with the program keyword NOBIPOLA (i.e. by switching-off the bipolar approximation) and infrared intensities were determined through the Berry phase method[31,32]. The overlap-based truncation tolerances for the Coulomb exchange integrals were set to $10^{-9}$, $10^{-9}$, $10^{-9}$, $10^{-9}$, $10^{-18}$ and the shrinking factor was isotropically set to 5, producing 39 points in the irreducible Brillouin zone for all calculations.

The anharmonicity of the solid-state vibrations was explored in two ways. First, the vibrational potential energy surface for each normal mode in the sub-150 cm$^{-1}$ range was scanned using atomic displacements from the calculated eigenvectors of the fully-optimized structure to determine the deviation of their curvatures from the harmonic limit. The potential energy was also calculated for a series of displacements along each symmetry-unique N-H stretch to probe anharmonicity specifically in the hydrogen bond interactions.[33,34] Second, the quasi-harmonic approximation (QHA) was applied to calculate the phonon frequencies as a function of unit cell

volume to represent the effects of temperature change.[35,36,37,38] This approach used the fully-optimized structure as a starting point and then applied constant volume optimizations at +2% and +4% variations with respect to the unconstrained full optimization volume (later referred to as 0%), then vibrational frequencies for each volume-constrained optimized structure were calculated.

## 6.3 Results and Discussion

### 6.3.1 Experimental Low-frequency Vibrational Spectra

The low-frequency lattice vibrations of crystalline GABA were measured using both LFRS and THz-TDS to access all of the vibrations present in the sample, and these spectra are shown in **Figure 6-1** and **Figure 6-2** respectively. Each experiment revealed a significant number of peaks present in the sub-133 cm$^{-1}$ range. The room-temperature THz-TDS data is consistent with that previously reported.[39,40] In both spectroscopies, the spectral features generally narrow and shift to higher frequencies in response to cooling as the crystallographic unit cell changes with temperature.
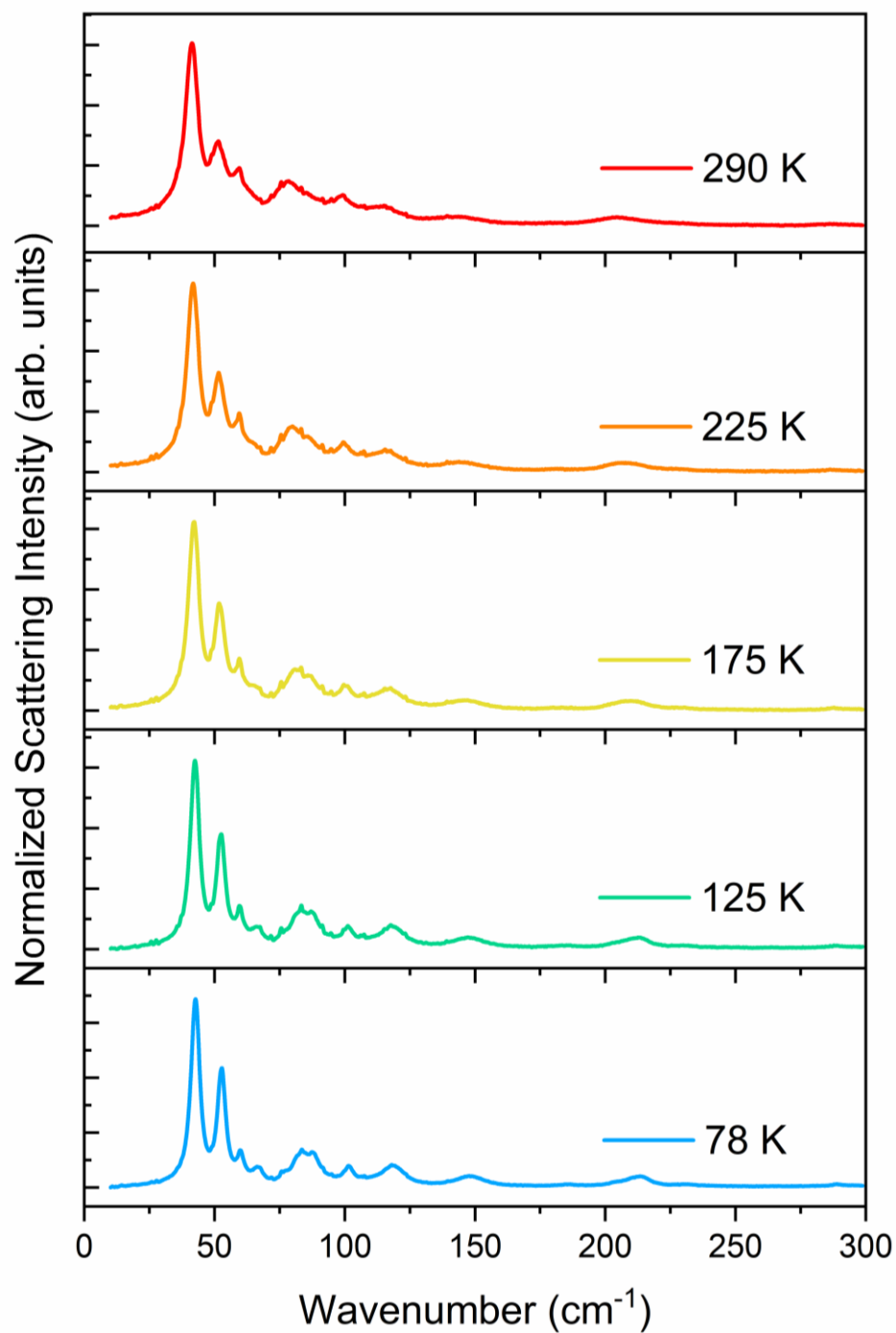
**Figure 6-1.** Temperature-dependent LFRS spectra from 10 cm$^{-1}$ to 300 cm$^{-1}$ of GABA recorded from 290 K to 78 K.
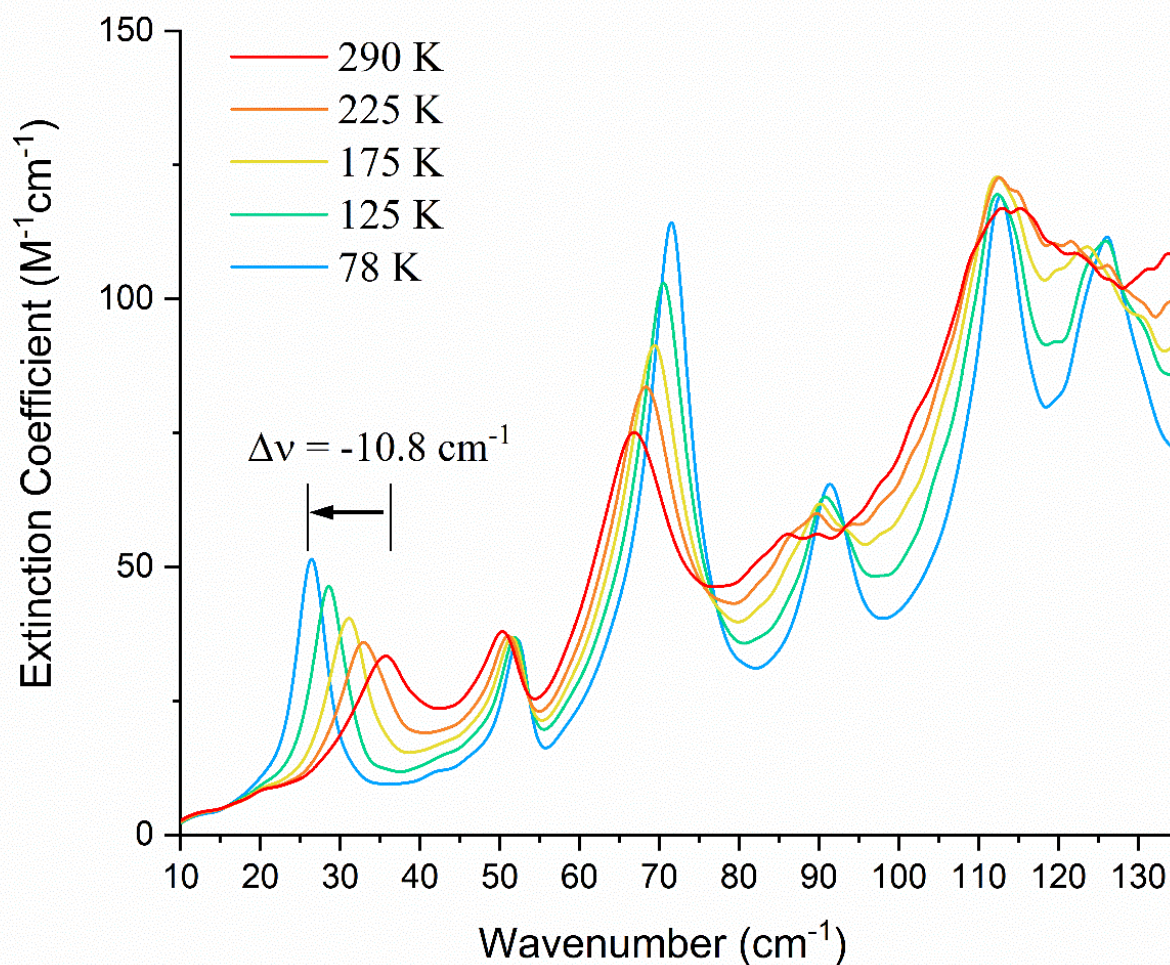
**Figure 6-2.** Temperature-dependent THz-TDS spectra from 290 K to 78 K of GABA. Note the anomalous frequency shifting of the lowest feature.

The Raman data show that all of the Raman-active modes shift to higher frequency at reduced temperatures, as would be expected from a contracted unit cell volume. The THz-TDS results are largely in agreement with this same trend, except for a significant deviation in the thermal behavior of the lowest absorption feature that appears at 37.2 cm$^{-1}$ at 290 K, but is found

at 26.4 cm$^{-1}$ at 78 K. Not only is the direction of the shift anomalous for such a temperature change, but the magnitude of -34.0% is remarkable as well.

Given the strong dependence of the lattice vibrations on the temperature of crystalline GABA, it is reasonable to consider that the origin of the odd shifting may be revealed using X-ray diffraction measurements. PXRD data (see **Appendix B**) does not show any polymorph changes in the bulk sample over the 290 K to 100 K range, with the monoclinic form preserved throughout. Temperature-dependent SC-XRD provides specific structural data that can reveal the presence of negative thermal expansion which could lead to the atypical lattice vibration trend.[41] However, the lattice dimensions for GABA shown in **Table 6-1** obtained using rapid SC-XRD unit cell measurements do not indicate any unusual changes. Cooling of the monoclinic GABA crystal reduces the unit cell volume as expected, with no obvious negative thermal expansion character. Although the *a*-axis becomes slightly larger upon cooling, the change is only slightly outside the measurement error. Given the lack of an irregular thermal-structural relationship in the GABA crystal, the behavior of the lowest-frequency mode necessitates additional study to understand its nature.

**Table 6-2.** SC-XRD measured unit cell dimensions of GABA from 290 K to 100 K.

|  | **290 K** | **240 K** | **180 K** | **150 K** | **100 K** |
|---|---|---|---|---|---|
| **$a$ (Å)** | 7.174(5) | 7.183(6) | 7.200(6) | 7.195(6) | 7.202(4) |
| **$b$ (Å)** | 10.107(8) | 10.074(9) | 10.045(8) | 10.010(7) | 9.972(5) |
| **$c$ (Å)** | 8.242(6) | 8.230(6) | 8.224(6) | 8.206(6) | 8.192(4) |
| **$\beta$ (°)** | 110.90(2) | 110.81(3) | 110.67(3) | 110.59(2) | 110.49(2) |
| **$Volume$ (Å$^3$)** | 558.2(1.2) | 556.7(1.3) | 556.5(1.3) | 553.2(1.1) | 551.1(9) |

## 6.3.2 Structural and Harmonic Vibrational Simulations

The result of the ss-DFT geometry optimization of crystalline GABA was compared to the SC-XRD results (**Table 6-2**) to evaluate the quality of the structure produced computationally. The optimization reveals that only the length of the crystallographic *b*-axis shows significant deviation from the SC-XRD dimensions, while the remaining lattice dimensions are in very good agreement with the X-ray structure. The *b*-axis is the most impacted by temperature (see **Table 6-1**), and consequently the 0 K ss-DFT results would be expected to have the largest difference in this axis. In terms of the internal structure of the GABA molecule, the simulation yielded very good root-mean-squared deviations (RMSDs) for bonds (0.0070 Å), angles (0.29°), and bond dihedral angles (2.09°) as compared to the SC-XRD results.

**Table 6-3.** Comparison of the SC-XRD experimental and ss-DFT simulated unit cell lattice dimensions for GABA.

|  | SC-XRD (95 K) | PBE-D3/def2-TZVPP | Error |
|---|---|---|---|
| **a (Å)** | 7.2130(3) | 7.2917 | 1.09% |
| **b (Å)** | 9.9914(5) | 9.7731 | -2.18% |
| **c (Å)** | 8.2113(4) | 8.1817 | -0.36% |
| **β (°)** | 110.553(3) | 110.613 | 0.05% |
| **Volume (Å³)** | 554.10(5) | 545.72 | -1.51% |

The optimized structure of crystalline GABA was then used as the basis for a complete frequency analysis of the infrared- and Raman-active lattice vibrations. Since the ss-DFT simulations are performed at effectively 0 K, the calculated spectra should most closely match with those measured at 78 K, the lowest temperature utilized experimentally. The frequency analysis (scaled by 0.90) provided good agreement with the 78 K THz-TDS spectrum as seen in **Figure 6-3**, with all features assignable. In order to address the contraction of the *b*-axis that is seen computationally, a fixed-lattice geometry optimization and frequency calculation were performed using the 95 K X-ray dimensions. The resulting vibrations required a more modest frequency scalar of 0.95 to be applied to best match the experiment (see **Appendix B**), indicating that the lattice dimension mismatch between theory and experiment is at least partially responsible for the need of global frequency scaling.
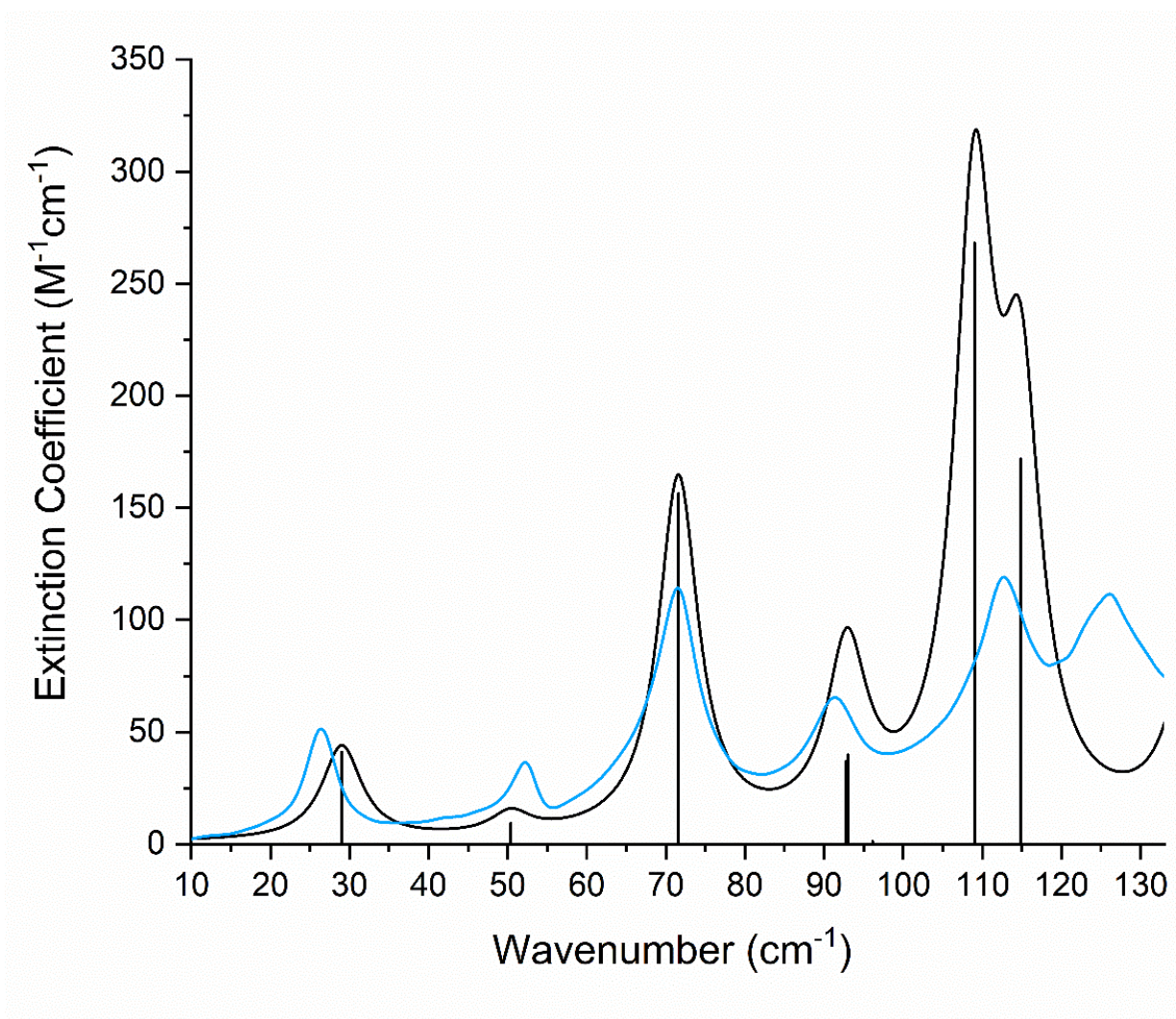
**Figure 6-3.** Overlay of the simulated THz-TDS spectrum (black, frequency-scaled by 0.90) with the 78 K experimental data (blue) for GABA. The simulated spectrum is convolved with an empirical Lorentzian line shape with a full-width-at-half-maximum (FWHM) of 6.8 cm$^{-1}$.

The vibrational simulations are clearly sufficient for the complete assignment of the 78 K spectrum (full list of calculated vibrations available in **Appendix B**). Therefore, the calculated eigenvectors could be used to map out the potential energy surfaces for each vibration in order to investigate the origin of the unusual peak shifting seen in the THz-TDS data. Scanning along the vibrational potential energy surface of each ≤150 cm$^{-1}$ mode reveals that only the lowest-frequency mode (referred hereafter as $\nu_1$) shows a large deviation from the classical harmonic energy as seen in **Figure 6-4**, while the remaining modes (such as $\nu_3$) follow the harmonic approximation very closely (see **Appendix B**). For this reason, evaluating the phonon frequencies using the harmonic approximation may be reasonable for most of the lattice vibrations, but will not be an accurate representation of the $\nu_1$ mode at elevated temperatures.
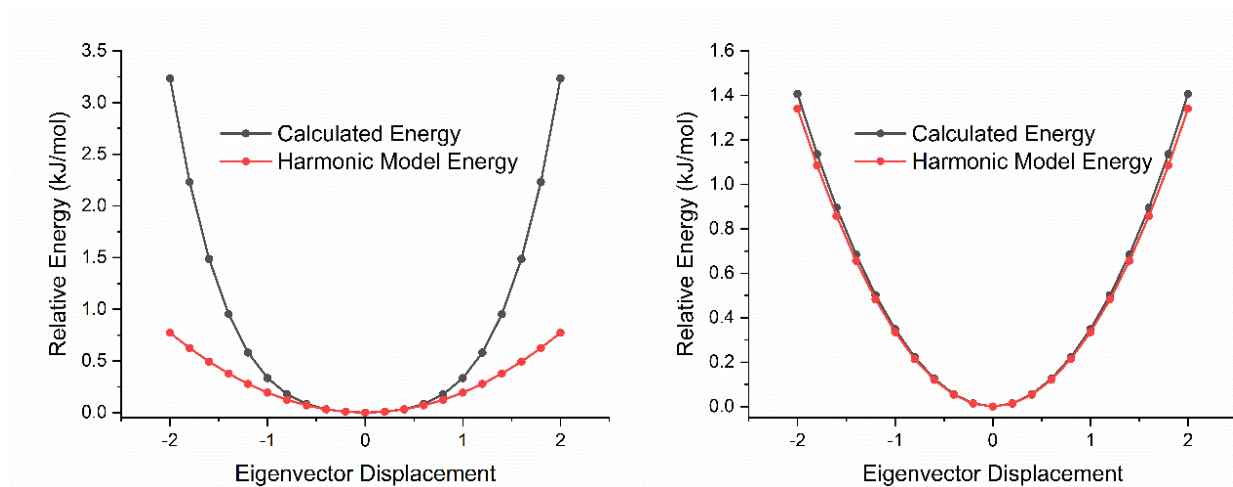


**Figure 6-4.** Potential energy curves for the eigenvector displaced atoms of the two lowest frequency IR-active modes, $\nu_1$ (scaled 29.0 cm$^{-1}$) and $\nu_3$ (scaled 50.4 cm$^{-1}$), predicted for crystalline GABA.

### 6.3.3 Quasi-Harmonic Approximation Simulations

To account for temperature effects, and to identify and understand the basis for the apparent strong anharmonicity in the lowest-frequency mode, the quasi-harmonic approximation was utilized to mimic the thermal behavior of the solid by changing its unit cell volume. The external lattice dimensions change as expected under the volume-constrained optimized geometries, as seen in **Table 6-3**. The QHA results follow the trend of the SC-XRD temperature-dependent unit cell checks (**Table 6-1**), with the crystallographic *b*-axis exhibiting the largest change as a function of constrained volume optimization.

**Table 6-3.** Quasi-harmonic approximation ss-DFT predicted lattice dimensions and resulting $\nu_1$ frequencies for GABA with 0% to 4% unit cell volume expansions.

|  | 0% | +2% | +4% |
|---|---|---|---|
| ***Volume*** $(\text{Å}^3)$ | 545.7 | 556.8 | 567.9 |
| ***a*** $(\text{Å})$ | 7.292 | 7.308 | 7.326 |
| ***b*** $(\text{Å})$ | 9.773 | 9.932 | 10.087 |
| ***c*** $(\text{Å})$ | 8.182 | 8.216 | 8.255 |
| ***β*** $(°)$ | 110.61 | 111.00 | 111.40 |
| **Predicted $\nu_1$ (cm$^{-1}$, unscaled)** | 32.3 | 39.9 | 46.4 |

Expansion and contraction of the GABA unit cell in the QHA approach yields vibrational simulations that are able to reproduce the large red-shift of the $\nu_1$ mode with volume contraction (approximating cooling), and the blue-shift of other vibrations (**Figure 6-5**). The QHA calculation predicts $\nu_1$ to shift by 14.1 cm$^{-1}$ (-43.7.0%) as the volume contracts from +4% to 0% which is a larger volume change than the experimental observations listed in **Table 6-1**, but does confirm and emphasize the anomalous behavior of $\nu_1$. It should be noted that some simulated modes show slight frequency increases or effectively no change with unit cell expansion, but these very small shifts may be obscured by the experimental peak widths or may fall within the uncertainties arising from the convergence thresholds of the calculations.
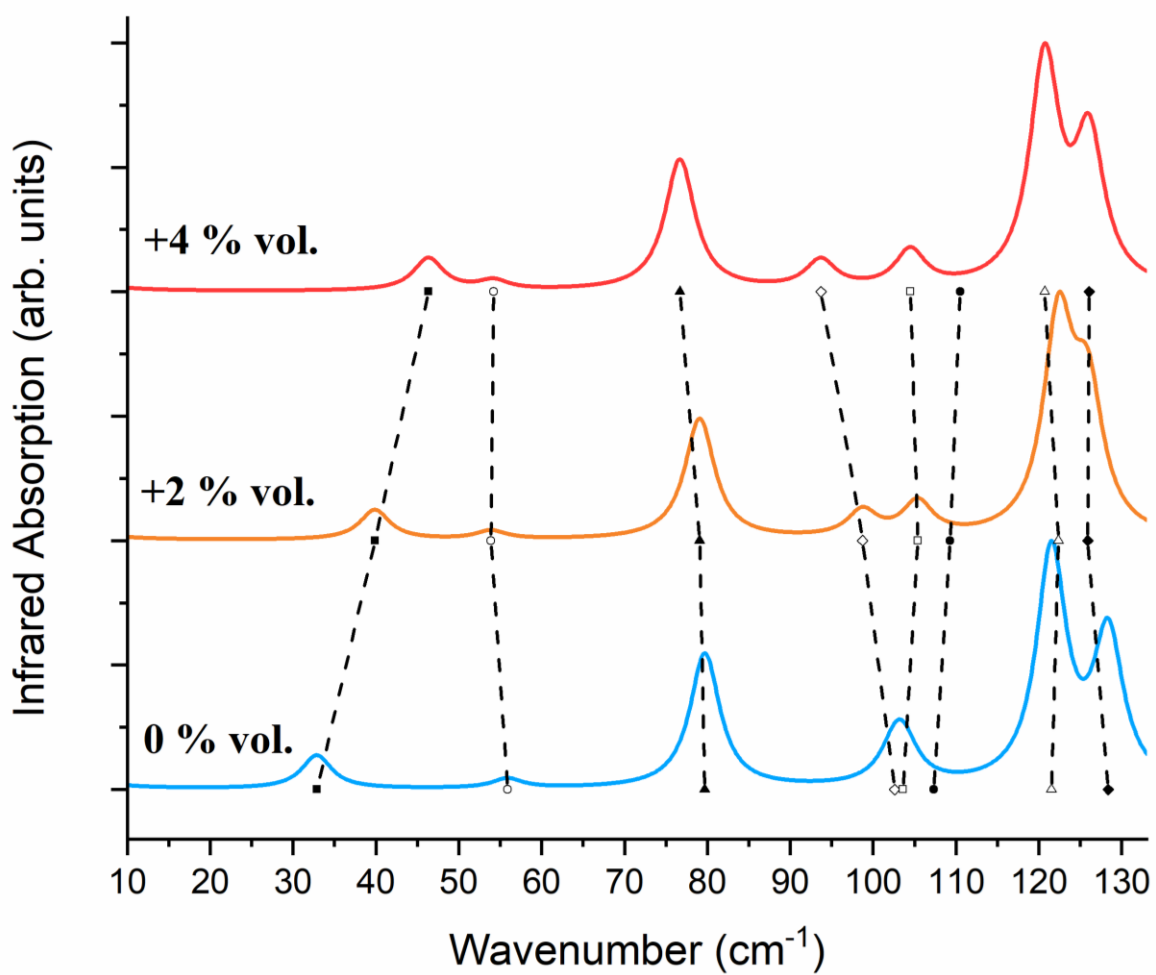
**Figure 6-5.** Quasi-harmonic approximation ss-DFT simulated terahertz spectra of GABA (y-axis offset for clarity) from 0% to +4% volume change. Frequencies are unscaled.

### 6.3.4 Molecular Origin of the Vibrational Shift

The most significant intermolecular force present in solid-state GABA is hydrogen bonding. The hydrogen bonding is accomplished through the $-NH_3^+$ and $-COO^-$ groups, leading to three symmetry-unique $N-HA\cdots OB$ interactions to consider (**Figure 6-6**). Analyzing the eigenvector results from the frequency calculations enables the study of the specific atomic displacements within each normal mode of vibration. While many different normal modes affect the geometries of these three hydrogen bonds, $\nu_1$ is distinct in its strong influence on HB3 in particular. The $\nu_1$ mode results in the largest positional changes in the atoms comprising $N-H3\cdots O2$ (HB3 in **Figure 6-6**), indicating that the distortion of HB3 may be responsible for the unusual shifting seen in the terahertz region for this lowest-frequency lattice vibration.
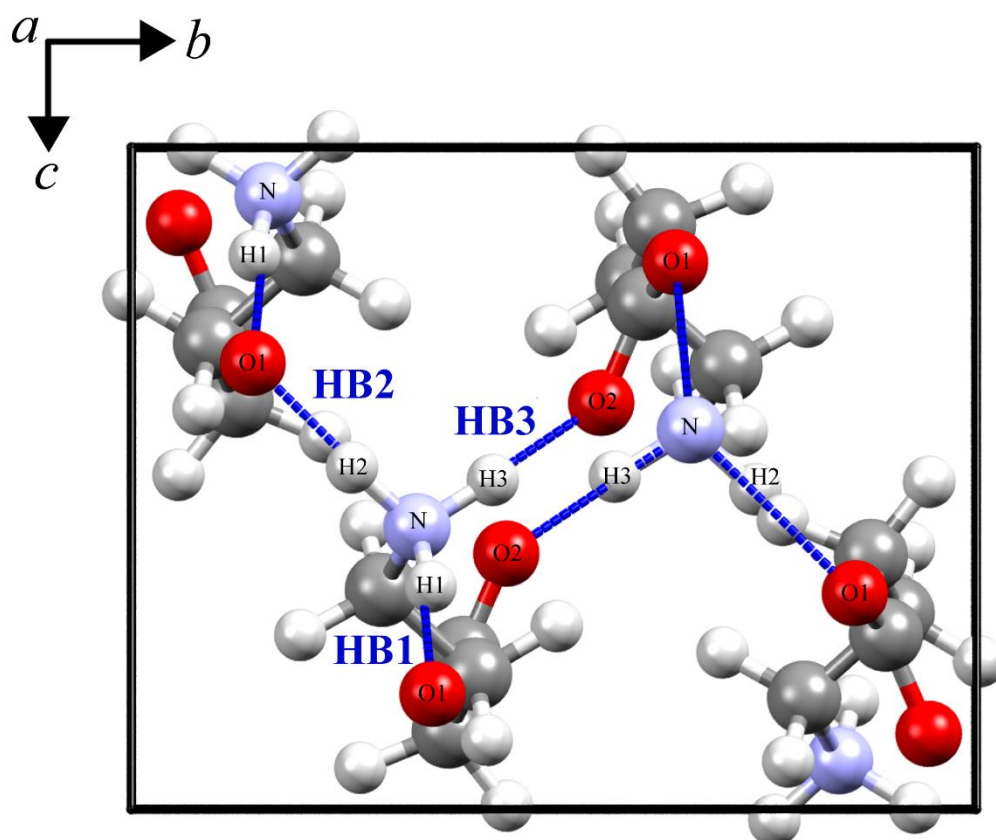
**Figure 6-6.** Monoclinic GABA unit cell highlighting the three symmetry-unique hydrogen bonds designated HB1, HB3, and HB3.

However, the similarities in heavy atom (N···O) separations gathered from SC-XRD measurements do not immediately indicate that a particular hydrogen bond is unique. The X-ray structure points to HB2 being the strongest of the three unique hydrogen bonds, having the marginally shortest bond distance between the heavy atoms (N–H1···O1: 2.76 Å, N–H2···O1: 2.73 Å, N–H3···O2: 2.75 Å) and a bond angle (N–H1···O1: 168.69°, N–H2···O1: 170.87°, N–H3···O2: 163.79°) closest to 180°. HB3 is geometrically the least optimal of the three, possessing the largest deviation from hydrogen bond linearity. These trends in the hydrogen bonds are seen and maintained throughout the QHA simulations, regardless of unit cell volume. Examining the N–H bonds in the simulations supports the HB3 interaction being the weakest, with it having the shortest N–H distance and therefore stronger covalent character as compared to the other N–H bonds in the crystal. These observations suggest that HB3 will be the easiest to distort of the three symmetrically-unique hydrogen bonds.

Potential energy curves calculated along each symmetrically-unique N–H covalent bond (equivalent to a stretching vibration) suggests that the N–H3 bond is the most harmonic of the three (**Figure 6-7**). This specific interaction has the steepest potential when examining the relative energies of the displaced N–HA hydrogens, which is consistent with the structural simulation showing the hydrogen bond geometry of HB3 to be strained and therefore weaker. The incongruity of HB3 may be a contributing factor in the observed lattice dimension behavior of crystalline GABA (**Table 6-2**). The HB3 interaction is predominately oriented along the crystallographic *b*-axis, the same axis that was most difficult to reproduce computationally and also the most sensitive to experimental temperature.
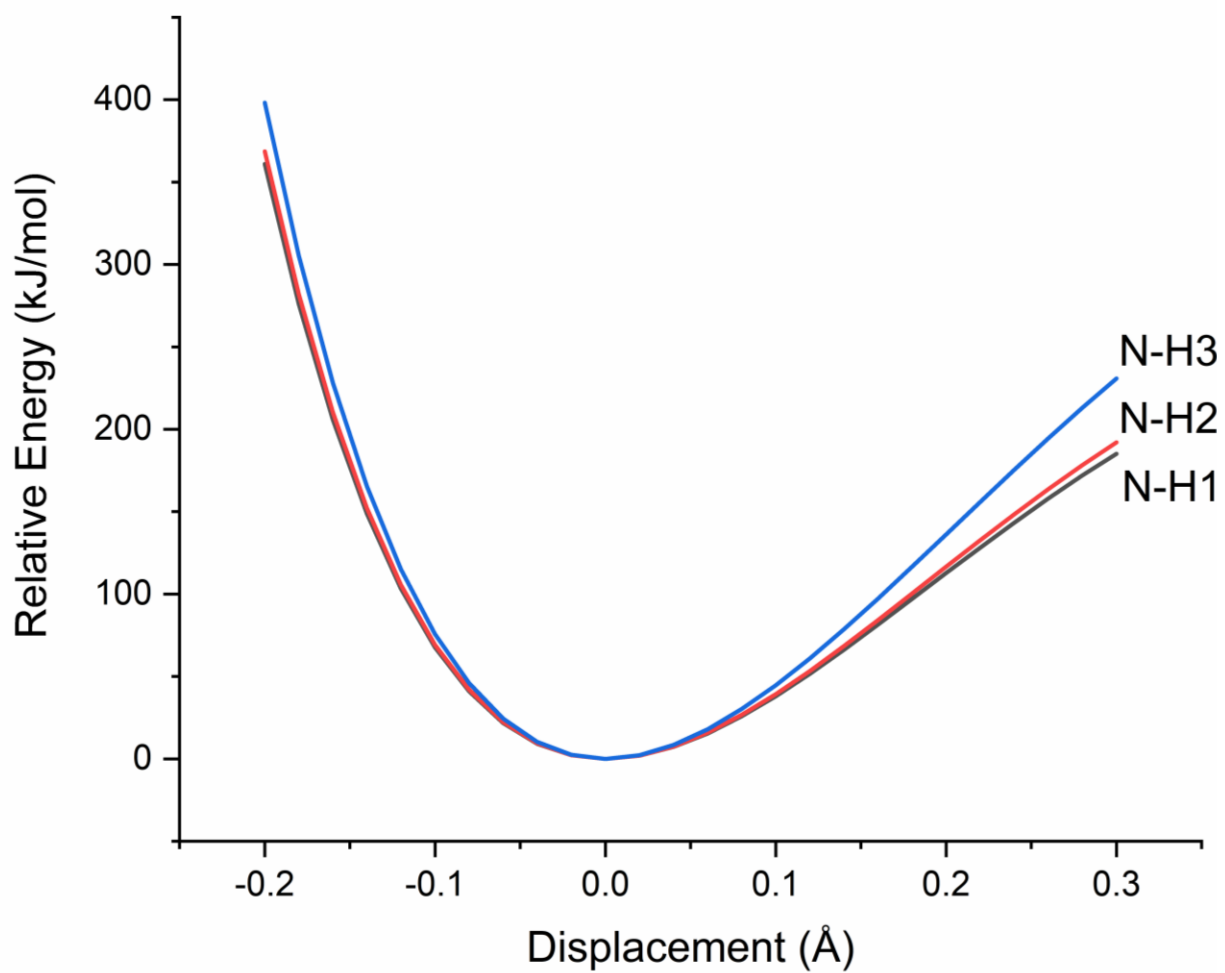
**Figure 6-7.** Potential energy curves of displaced N–HA hydrogens (N–H stretching) in crystalline GABA.

The N–HA hydrogen bonds can be further explored by treating each as an independent oscillator in the crystal and numerically solving the time-independent Schrödinger equation using the Numerov method to characterize the covalent bond stretching potential energies.[34] This approach permits the bonding character at specific positions in the molecule to be independently evaluated. The analysis (**Table 4**) predicts the N–H3 stretch of HB3 to exhibit the highest fundamental frequency (and highest force constant), indicative of the strongest covalent bond order and therefore the weakest intermolecular hydrogen bonding. This specific stretching vibration also shows the largest sensitivity over the range of unit cell volume expansion calculations, increasing by twice as much as the other hydrogen bond coordinates.

**Table 6-4.** Calculated fundamental anharmonic frequencies (cm$^{-1}$) of each N–HA stretching vibration over a series of unit cell volume expansions.

| Unit cell volume change | N–H1 | N–H2 | N–H3 |
|:---:|:---:|:---:|:---:|
| 0% | 2363.5 | 2411.4 | 2637.0 |
| +2% | 2355.6 | 2419.9 | 2655.5 |
| +4% | 2348.0 | 2427.0 | 2675.5 |

Perhaps even more interesting is the trend in the magnitude of the anharmonic constants predicted across the unit cell volume expansions, where the value decreases for HB3 as the unit cell volume increases (**Figure 6-8**).
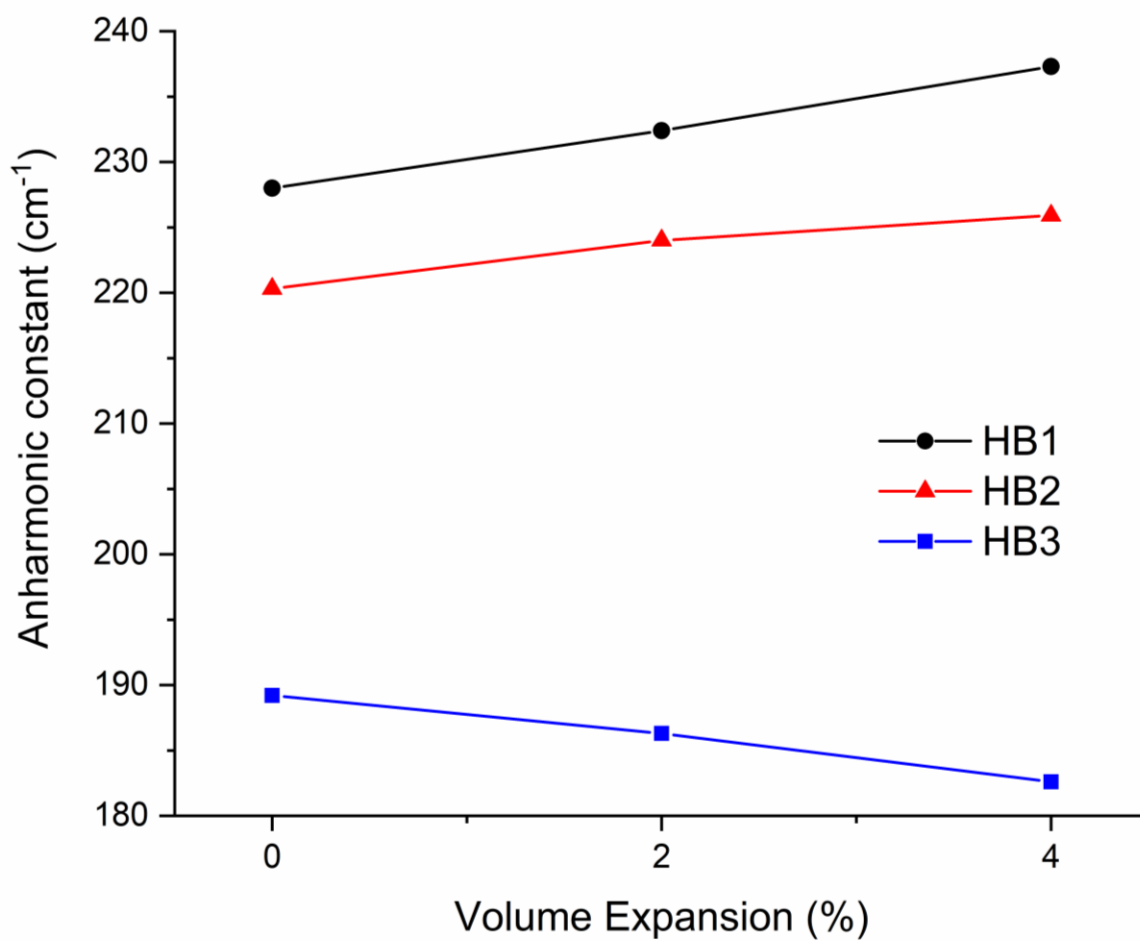
**Figure 6-8.** Anharmonic vibrational constants for N–HA stretching in each symmetry-unique hydrogen bond across unit cell volume expansions.

## 6.4 Conclusions

Crystalline GABA exhibits the largest reported anomalous red-shift of a lattice vibration upon cooling of an organic molecular solid. The trend identified experimentally with terahertz spectroscopy can be reproduced using solid-state density functional theory, and the combined approach allows for a detailed investigation of the intermolecular forces acting within the solid. Quasi-harmonic approximation simulations are not only able to replicate the temperature response of the 37.2 cm$^{-1}$ peak (at 290 K) observed in the THz-TDS spectrum, but the rigorous DFT treatment of the solid is also able to explain its origin. The unexpected temperature shift of the lowest-frequency vibration can be linked to the distortion of a specific weak intermolecular hydrogen bond in solid GABA. The key importance of this disparity in the hydrogen bonding interactions has been revealed through examination of the atomic displacements of the lattice vibrations and mapping of their potential energy surfaces. This study has highlighted the unique anharmonic character of the 37.2 cm$^{-1}$ mode in crystalline GABA, and shown that the temperature sensitivity of the N–H3···O2 hydrogen bond ultimately drives the observed anomalous frequency shift of this terahertz lattice vibration.

**Appendix B**

Powder X-ray diffraction patterns for experimental and simulated GABA, simulated terahertz spectrum from a fixed lattice geometry optimization, potential energy curves for first 20 simulated modes, list of all calculated IR- and Raman-active mode frequencies and intensities, anharmonic calculations for each symmetry-unique N–H bond.

**Acknowledgements**

## 6.5 References

1.    Cowley, R. A. Anharmonic Crystals. *Rep. Prog. Phys.* **1968,** *31* (Pt. 1), 123-66.

2.    Stern, E. A. Theory of the Anharmonic Properties of Solids. *Phys. Rev.* **1958,** *111* (3), 786-797.

3.    Zaczek, A. J.; Korter, T. M. Polymorphism in cis–trans Muconic Acid Crystals and the Role of C–H⋯O Hydrogen Bonds. *Cryst. Growth Des.* **2017,** *17* (8), 4458-4466.

4.    Zhang, F.;  Hayashi, M.;  Wang, H.-W.;  Tominaga, K.;  Kambara, O.;  Nishizawa, J.-i.; Sasaki, T. Terahertz Spectroscopy and Solid-state Density Functional Theory Calculation of Anthracene: Effect of Dispersion Force on the Vibrational Modes. *J. Chem. Phys.* **2014,** *140* (17), 174509/1-174509/10.

5.    Galimberti, D.;  Milani, A.;  Maschio, L.; Castiglioni, C. Intermolecular Modulation of IR Intensities in the Solid State. The Role of Weak Interactions in Polyethylene Crystal: A Computational DFT Study. *J. Chem. Phys.* **2016,** *145* (14), 144901/1-144901/13.

6.    Neu, J.;  Nikonow, H.; Schmuttenmaer, C. A. Terahertz Spectroscopy and Density Functional Theory Calculations of dl-Norleucine and dl-Methionine. *J. Phys. Chem. A* **2018,** *122* (28), 5978-5982.

7.    Witko, E. M.; Korter, T. M. Investigation of the Low-Frequency Vibrations of Crystalline Tartaric Acid Using Terahertz Spectroscopy and Solid-State Density Functional Theory. *J. Phys. Chem. A* **2011,** *115* (35), 10052-10058.

8.    Wallace, V. P.;  Taday, P. F.;  Fitzgerald, A. J.;  Woodward, R. M.;  Cluff, J.;  Pye, R. J.; Arnone, D. D. Terahertz Pulsed Imaging and Spectroscopy for Biomedical and Pharmaceutical Applications. *Faraday Discuss.* **2004,** *126* (0), 255-263.

9.  Walther, M.;  Fischer, B. M.; Uhd Jepsen, P. Noncovalent Intermolecular Forces in Polycrystalline and Amorphous Saccharides in the Far Infrared. *Chem. Phys.* **2003,** *288* (2), 261-268.

10. Dove, M. T. *Introduction to Lattice Dynamics*, Cambridge University Press: Cambridge, 1993.

11. Monserrat, B.;  Drummond, N. D.; Needs, R. J. Anharmonic Vibrational Properties in Periodic Systems: Energy, Electron-phonon Coupling, and Stress. *Phys. Rev. B* **2013,** *87* (14), 144302.

12. Bihary, Z.;  Gerber, R. B.; Apkarian, V. A. Vibrational Self-consistent Field Approach to Anharmonic Spectroscopy of Molecules in Solids: Application to Iodine in Argon Matrix. *J. Chem. Phys.* **2001,** *115* (6), 2695-2701.

13. Drummond, N. D.;  Monserrat, B.;  Lloyd-Williams, J. H.;  Ríos, P. L.;  Pickard, C. J.; Needs, R. J. Quantum Monte Carlo Study of the Phase Diagram of Solid Molecular Hydrogen at Extreme Pressures. *Nat. Commun.* **2015,** *6*, 7794.

14. Ruggiero, M. T.; Zeitler, J. A. Resolving the Origins of Crystalline Anharmonicity Using Terahertz Time-Domain Spectroscopy and ab Initio Simulations. *The Journal of Physical Chemistry B* **2016,** *120* (45), 11733-11739.

15. Kern, G.;  Kresse, G.; Hafner, J. Ab initio Calculation of the Lattice Dynamics and Phase Diagram of Boron Nitride. *Phys. Rev. B* **1999,** *59* (13), 8551-8559.

16. Ruggiero, M. T.;  Zeitler, J. A.; Erba, A. Intermolecular Anharmonicity in Molecular Crystals: Interplay Between Experimental Low-frequency Dynamics and Quantum Quasi-harmonic Simulations of Solid Purine. *Chem. Commun.* **2017,** *53* (26), 3781-3784.

17. Pavone, P.; Karch, K.; Schütt, O.; Strauch, D.; Windl, W.; Giannozzi, P.; Baroni, S. Ab initio Lattice Dynamics of Diamond. *Phys. Rev. B* **1993,** *48* (5), 3156-3163.

18. Davidson, N. *Neurotransmitter Amino Acids*, Academic: 1976.

19. Gajcy, K.; Lochynski, S.; Librowski, T. A Role of GABA Analogues in the Treatment of Neurological Diseases. *Curr. Med. Chem.* **2010,** *17* (22), 2338-2347.

20. Craven, B. M.; Weber, H.-P. Charge Density in the Crystal Structure of g-aminobutyric Acid at 122 K - An Intramolecular Methylene H Bridge. *Acta Crystallogr., Sect. B: Struct. Sci., Cryst. Eng. Mater.* **1983,** *39* (6), 743-748.

21. Weber, H.-P.; Craven, B. M.; McMullan, R. K. The Neutron Structure of and Thermal Motion in γ-Aminobutyric Acid (GABA) at 122 K. *Acta Crystallographica, Section B: Structural Science* **1983,** *39* (3), 360-366.

22. Steward, E. G.; Player, R. B.; Warner, D. Crystal and Molecular Structure of γ-Aminobutyric Acid Determined at Low Temperature. *Acta Crystallogr., Sect. B: Struct. Sci., Cryst. Eng. Mater.* **1973,** *29* (Pt. 10), 2038-40.

23. Dobson, A. J.; Gerkin, R. E. γ-Aminobutyric Acid: a Novel Tetragonal Phase. *Acta Crystallogr., Sect. C: Cryst. Struct. Commun.* **1996,** *C52* (12), 3075-3078.

24. de Vries, E. J. C.; Levendis, D. C.; Reece, H. A. A Hexagonal Solvate of the Neurotransmitter γ-Aminobutyric Acid. *CrystEngComm* **2011,** *13* (10), 3334-3337.

25. Dovesi, R.; Erba, A.; Orlando, R.; Zicovich-Wilson, C. M.; Civalleri, B.; Maschio, L.; Rérat, M.; Casassa, S.; Baima, J.; Salustro, S.; Kirtman, B. Quantum-mechanical Condensed Matter Simulations with CRYSTAL. *Wiley Interdisc. Rev.: Comput. Mol. Sci.* **2018,** *8* (4), e1360.

26. Perdew, J. P.;  Burke, K.; Ernzerhof, M. Generalized Gradient Approximation Made Simple. *Phys. Rev. Lett.* **1996,** *77* (18), 3865-3868.

27. Weigend, F.; Ahlrichs, R. Balanced Basis Sets of Split Valence, Triple Zeta Valence and Quadruple Zeta Valence Quality for H to Rn: Design and Assessment of Accuracy. *Phys. Chem. Chem. Phys.* **2005,** *7* (18), 3297-3305.

28. Grimme, S.;  Antony, J.;  Ehrlich, S.; Krieg, H. A Consistent and Accurate ab initio Parametrization of Density Functional Dispersion Correction (DFT-D) for the 94 Elements H-Pu. *J. Chem. Phys.* **2010,** *132* (15), 154104/1-154104/19.

29. Grimme, S.;  Ehrlich, S.; Goerigk, L. Effect of the Damping Function in Dispersion Corrected Density Functional Theory. *J. Comput. Chem.* **2011,** *32* (7), 1456-1465.

30. Grimme, S.;  Hansen, A.;  Brandenburg, J. G.; Bannwarth, C. Dispersion-Corrected Mean-Field Electronic Structure Methods. *Chem. Rev.* **2016,** *116* (9), 5105-5154.

31. Noel, Y.;  Zicovich-Wilson, C. M.;  Civalleri, B.;  D'Arco, P.; Dovesi, R. Polarization Properties of ZnO and BeO: An ab initio Study through the Berry Phase and Wannier Functions Approaches. *Phys. Rev. B* **2001,** *65* (1), 014111.

32. Pascale, F.;  Zicovich-Wilson, C. M.;  López Gejo, F.;  Civalleri, B.;  Orlando, R.;  Dovesi, R. The calculation of the vibrational frequencies of crystalline compounds and its implementation in the CRYSTAL code. *J. Comput. Chem.* **2004,** *25* (6), 888-897.

33. Pascale, F.;  Tosoni, S.;  Zicovich-Wilson, C.;  Ugliengo, P.;  Orlando, R.; Dovesi, R. Vibrational spectrum of Brucite, $Mg(OH)_2$: A Periodic ab initio Quantum Mechanical Calculation Including OH Anharmonicity. *Chem. Phys. Lett.* **2004,** *396* (4), 308-315.

34.    Lindberg, B. A New Efficient Method for Calculation of Energy Eigenvalues and

Eigenstates of the One-dimensional Schrödinger Equation. *J. Chem. Phys.* **1988,** *88* (6),

3805-3810.

35.    Erba, A. On Combining Temperature and Pressure Effects on Structural Properties of

Crystals with Standard ab initio Techniques. *J. Chem. Phys.* **2014,** *141* (12), 124115/1-

124115/9.

36.    Erba, A.;  Shahrokhi, M.;  Moradian, R.; Dovesi, R. On How Differently the Quasi-

Harmonic Approximation Works for Two Isostructural Crystals: Thermal Properties of

Periclase and Lime. *J. Chem. Phys.* **2015,** *142* (4), 044114/1-044114/9.

37.    Erba, A.;  Maul, J.;  De La Pierre, M.; Dovesi, R. Structural and Elastic Anisotropy of

Crystals at High Pressures and Temperatures from Quantum Mechanical Methods: The

Case of $Mg_2SiO_4$ Forsterite. *J. Chem. Phys.* **2015,** *142* (20), 204502/1-204502/11.

38.    Erba, A.;  Maul, J.;  Itou, M.;  Dovesi, R.; Sakurai, Y. Anharmonic Thermal Oscillations

of the Electron Momentum Distribution in Lithium Fluoride. *Phys. Rev. Lett.* **2015,** *115*

(11), 117402/1-117402/5.

39.    Peng, Y.;  Yuan, X.;  Zou, X.;  Chen, W.;  Huang, H.;  Zhao, H.;  Song, B.;  Chen, L.;

Zhu, Y. Terahertz Identification and Quantification of Neurotransmitter and Neurotrophy

Mixture. *Biomed. Opt. Express* **2016,** *7* (11), 4472-4479.

40.    Du, Y.;  Xue, J.;  Cai, Q.; Zhang, Q. Spectroscopic Investigation on Structure and pH

Dependent Cocrystal Formation Between γ-Aminobutyric Acid and Benzoic Acid.

*Spectrochim. Acta, Part A* **2018,** *191*, 377-381.

41.    Evans, J. S. O.;  Mary, T. A.;  Vogt, T.;  Subramanian, M. A.; Sleight, A. W. Negative

Thermal Expansion in $ZrW_2O_8$ and $HfW_2O_8$. *Chem. Mater.* **1996,** *8* (12), 2809-2823.

# Chapter 7: Evaluation of Functionals and Basis Sets for the Accurate Modeling of Crystalline β-triglycine using Solid-state Density Functional Theory

**ABSTRACT**

Advancements in computational models have enabled a better understanding of the structures and vibrational motions of crystalline biomolecules. The wide variety of options that are available for performing these simulations make it challenging to select the appropriate parameters to achieve a desired level of accuracy. Low-frequency vibrational spectroscopy ($<$ 200 cm$^{-1}$) is a promising benchmark for evaluating the quality of solid-state simulations. Low-frequency vibrations can be used to verify that not only are the covalent bonds of the molecule well represented, but the weak intermolecular forces that hold the solid together are also accurately modeled. A solid-state density functional theory methodology to model crystalline β-triglycine was developed and verified through X-ray diffraction and low-frequency vibrational spectroscopy measurements. A generalized gradient approximation and hybrid functional were tested with a series of basis sets, ultimately yielding that PBE0-D3/VTZP combination as the best approach for replicating the experimental observations.

## 7.1 Introduction

Crystalline molecular solids are remarkable benchmarks for testing and developing new computational models as these samples have well defined structures given their periodicity, but they are simultaneously highly challenging due to the need of the model to treat both covalent and noncovalent forces well. To properly model the complex bonding scheme within molecules and the weak intermolecular forces that hold the solids together, rigorous solid-state computational methodologies are necessary.[1-3] Numerous approaches exist for simulating molecular solids, including force field and semi-empirical methods, but *ab initio* methods allow for the most flexibility when encountering diverse chemical environments. Regardless of the model origin, the treatment of crystalline materials is accomplished through the application of periodic boundary conditions in the calculations so that packing interactions are well represented, and boundary interface problems are avoided. A commonly applied computational method, and the one used in this work, is solid-state density functional theory (ss-DFT) which draws on both aspects to provide excellent reproduction of experimental results.[4-7] The accuracy of these models can be validated through comparisons with experimental observations such as solid-state NMR and mid-infrared spectroscopies. While these traditional comparisons are valuable, new insights into model quality can be achieved by the replication of low-frequency vibrational spectra, as weak noncovalent interactions dominate in the low-frequency region between 10 and 200 $cm^{-1}$ (0.3 – 6 THz).[8-11]

Studies of biomolecules have been met with varying rates of success, with challenges often attributed to their large size and complex bonding patterns. Oligopeptides are a sub-set of proteins used to form cocrystals, serve as templates for solvent-free green synthesis, and can act as catalysts.[12-14] They are generally between 2 and 20 amino acids in length, making them more

approachable for *ab initio* ss-DFT investigations. The crystal structure of several glycine oligomers are known, but the focus of the current work is on triglycine (Gly-Gly-Gly). Triglycine has a well characterized crystal structure and has been observed in two polymorph forms, α and β. The β form is the more common of the triglycine polymorphs that have been reported, with only a single occurrence of α-triglycine in the literature.[15, 16] X-ray diffraction studies reveal that the β polymorph of triglycine (β-triglycine) is a zwitterion, composed of an extensive network of inter- and intramolecular hydrogen bonds.[17-19] β-triglycine crystallizes in the triclinic space group $P\bar{1}$ as two symmetry unique molecules arranged in antiparallel β sheets through a classic head-to-tail fashion (**Figure 7-1**).[20] Temperature studies of β-triglycine have shown that upon cooling, the unit cell contracts without changing the conformation of the molecules, preserving the hydrogen bonding scheme regardless of temperature.[21] Investigations into β-triglycine have previously focused on the low-frequency vibrational spectra, electronic structure, degradation in the presence of changing pH, and the applications of amorphous films.[22-28]

The pre-existing structural information and vibrational analyses makes β-triglycine an ideal candidate for evaluating the ability of a solid-state model to capture the weak intermolecular forces that hold crystalline oligopeptides together. In this work, β-triglycine was modeled using *ab initio* solid-state density functional theory with a variety of functional and basis set combinations. Each methodology was tested for its ability to reproduce the structure observed using X-ray diffraction, as well as the low-frequency vibrations observed via terahertz and Raman spectroscopies.
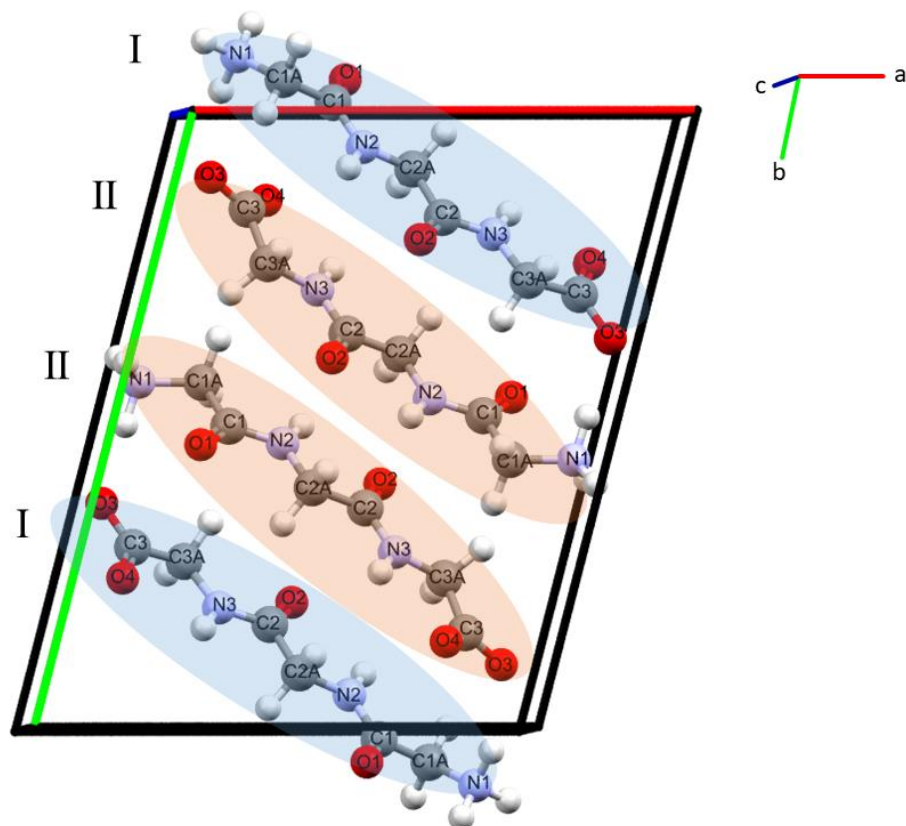
**Figure 7-1.** Labeling scheme of a unit cell of crystalline β-triglycine, with two symmetry unique molecules (I and II).[21]

## 7.2 Methods

### 7.2.1 Experimental

β-triglycine (glycly-glycl-glycine, CAS Number: 556-33-2) was purchased from Acros Organics as an off-white powder. The pulverized sample was analyzed using powder X-ray diffraction (PXRD) to verify bulk crystallinity using a Bruker D2 Phaser equipped with a LYNXEYE silicon strip detector utilizing Cu Kα radiation ($\lambda = 1.5406$ Å). The data was collected over a range of 10-70° with a step size of 0.02° with each step taking 2 seconds. The resulting experimental powder pattern was compared to and found to match the simulated powder pattern from previously published single-crystal X-ray measurements.[20]

Low-frequency Raman spectroscopy (LFRS) was performed using an Ondax (Coherent) THz-Raman system in a backscattering geometry (laser excitation centered at $\lambda = 784.7$ nm) fiber-coupled to an Andor Shamrock 750 spectrograph equipped with an iDus 416 CCD. The commercial system was modified to allow for the collection of cryogenic measurements by removing the standard sample holder and inserting a Janis ST-100 optical cryostat with glass windows 0.3 m from the edge of the Raman instrument. A custom-built brass chamber was used as a sample holder, pressing the powder between two glass plates. Data was collected using a 3 second exposure time with 225 acquisitions at both room (295 K (±1)) and liquid nitrogen (78 K (±1)) temperature up to 400 cm$^{-1}$ past the Rayleigh line. The resulting spectral resolution was approximately 0.6 cm$^{-1}$. Atmospheric interference ($N_2$ and $O_2$ rotational transitions) was observed in the final spectra due to the modifications of the path length from the instrument to the sample.[29] To account for this, the peaks attributed to rotational transitions were identified

from a spectrum taken of only air, and then subtracted from the original data using the Spectragryph spectroscopy software (version 1.2.13).[30]

Terahertz (THz) time-domain spectra were collected using a TeraFlash fiber-coupled terahertz spectrometer from Toptica Photonics at 295($\pm$1) and 25 K ($\pm$5). The spectrometer consisted of a $\lambda$ = 1.5 $\mu$m fiber laser coupled to an InGaAs 25 $\mu$m strip-line photoconductive antenna and an InGaAs 25 $\mu$m dipole photoconductive antenna for terahertz generation and detection, respectively. $\beta$-triglycine was ground and mixed with polytetrafluoroethylene (PTFE) and then pressed into a pellet (13 mm x 3 mm) with a final sample concentration of 2.5 % (w/w). A pure PTFE pellet was made of comparable size to serve as a reference. A 50 ps window was averaged over 20000 scans providing time-domain terahertz waveforms for both the sample and reference. Each data collection was processed by truncating the waveform 28 ps past the THz pulse center to exclude interference from a reflection generated by the surface of the pellet. The remaining waveform was then symmetrically zero-padded on both sides of the THz pulse center to a total of 1121 data points. The ratio of the processed sample and blank waveforms was Fourier-transformed using a Blackman window in Origin 2020, resulting in final spectra from 10 – 120 cm$^{-1}$ with a spectral resolution of 1.2 cm$^{-1}$. Spectral intensities account for the total contents of the crystallographic unit cell ($Z$ = 4) and are reported in terms of extinction coefficient, $\varepsilon$ (M$^{-1}$cm$^{-1}$). Experimental peak positions for both LFRS and THz cryogenic spectra < 100 cm$^{-1}$ were fit using the Lorentzian peak function in Origin 2020.[30]

## 7.2.2 Computational

All calculations were performed using the *ab initio* solid-state density functional theory software package, CRYSTAL17.[31]   Geometry optimizations and harmonic frequency calculations were performed to an energy convergence of $\Delta E < 10^{-8}$ and $\Delta E < 10^{-10}$ hartree, respectively. The starting coordinates and lattice dimensions were obtained from published single-crystal X-ray diffraction (SC-XRD) measurements for a cryogenic structure given the unit cell dimensions of $a = 11.585$ Å, $b = 14.603$ Å, $c = 4.800$ Å, $\alpha = 89.28°$, $\beta = 95.55°$, and $\gamma = 104.484°$.[21] Functionals used included the generalized gradient approximation (GGA), PBE[32], and the global hybrid, PBE0[33]. Both functionals were augmented with the DFT-D3 dispersion correction with Becke-Johnson damping scheme (BJ) and the Axelrod-Teller-Muto three-body repulsion term ($E^{ABC}$) with program default settings (D3(BJ)+$E^{ABC}$), further referred to as simply -D3, to account for weak intermolecular forces such as London dispersion interactions.[34-36] Basis sets used included: 6-311G(d,p), POB-TZVP-rev2, and VTZP composed of 1200 atomic orbitals (436 shells), 1200 atomic orbitals (592 shells), and 1304 atomic orbitals (696 shells), respectively. [37, 38] All basis sets were obtained from the Basis Set Exchange with the VTZP basis set used in this work modified from the original VTZ basis set to include polarization functions.[39, 40] This basis set is built from the same principles as the well-known def2-TZVP basis set and performs similarly, but incurs less computational cost and results in fewer electronic convergence problems in periodic systems.[41, 42] The def2-TZVP basis set was tested here in combination with a hybrid functional and was found to have convergence problems and was not further pursued. The basis set superposition error (BSSE) for each basis set was calculated using the counterpoise method from a combination of single molecule and unit cell single point energy calculations.[43]

For all calculations, 260 k-points were used in the irreducible Brillouin zone with the overlap-based truncation tolerances for the Coulomb and exchange integrals set to $10^{-10}$, $10^{-10}$, $10^{-10}$, $10^{-15}$, and $10^{-30}$ to properly sample the system.[44] Harmonic vibrational frequencies were calculated from the optimized structures using a stricter energy convergence criterion of $\Delta E <$ $10^{-10}$ hartree. Both Raman and IR intensities were calculated using a coupled-perturbed-Hartree-Fock/Kohn-Sham approach with an additional Anderson convergence accelerator.[45-47] The Raman intensities were then refined by accounting for the temperature of the sample as well as the wavelength of the incident laser.[48] In final comparisons, the calculated frequency positions and intensities were convolved using a Lorentzian line shape and a full-width at half-maximum (FWHM) of 2.0 cm$^{-1}$ and 2.4 cm$^{-1}$ for Raman and terahertz spectra, respectively. The strongest performing functional and basis set combination was used for mode assignments and descriptions by visualizing the eigenvectors for each vibrational frequency below 120 cm$^{-1}$ and examining the resultant motion.

## 7.3 Results and Discussion

### 7.3.1 Experimental

The sample received matched the predicted PXRD pattern from experiment, confirming that the sample was not only crystalline, but was the expected β-triglycine polymorph (**Appendix C**). Both the Raman (**Figure 7-2**) and terahertz (**Figure 7-3**) spectra revealed a significant number of peaks for β-triglycine at both room and cryogenic temperatures. The large number of discernable peaks at cryogenic temperature provided numerous opportunities for a comprehensive evaluation of the different theories used.
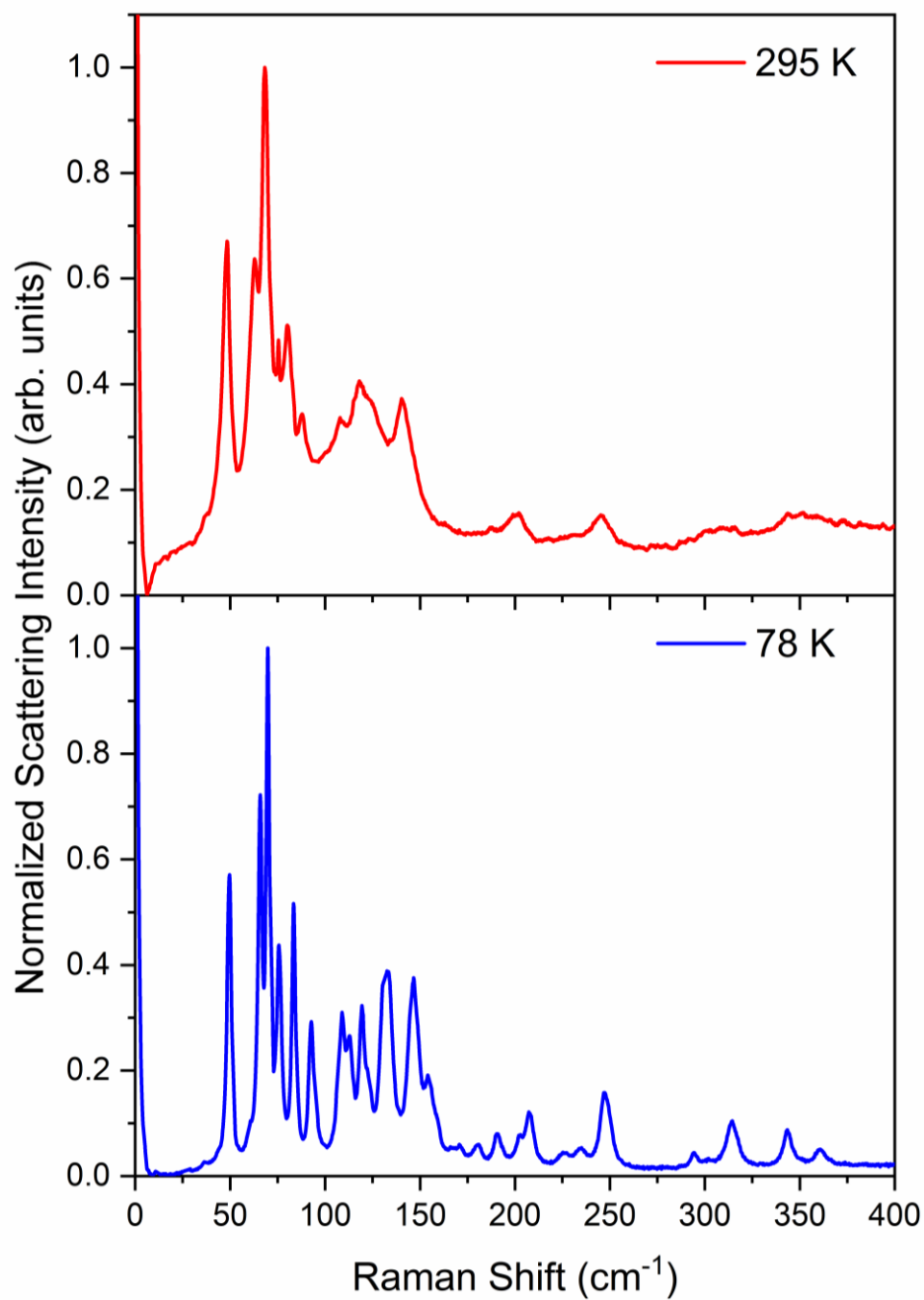
**Figure 7-2.** Low-frequency Raman spectra (0 – 400 cm$^{-1}$) of β-triglycine at 295 K (red, top) and 78 K (blue, bottom).
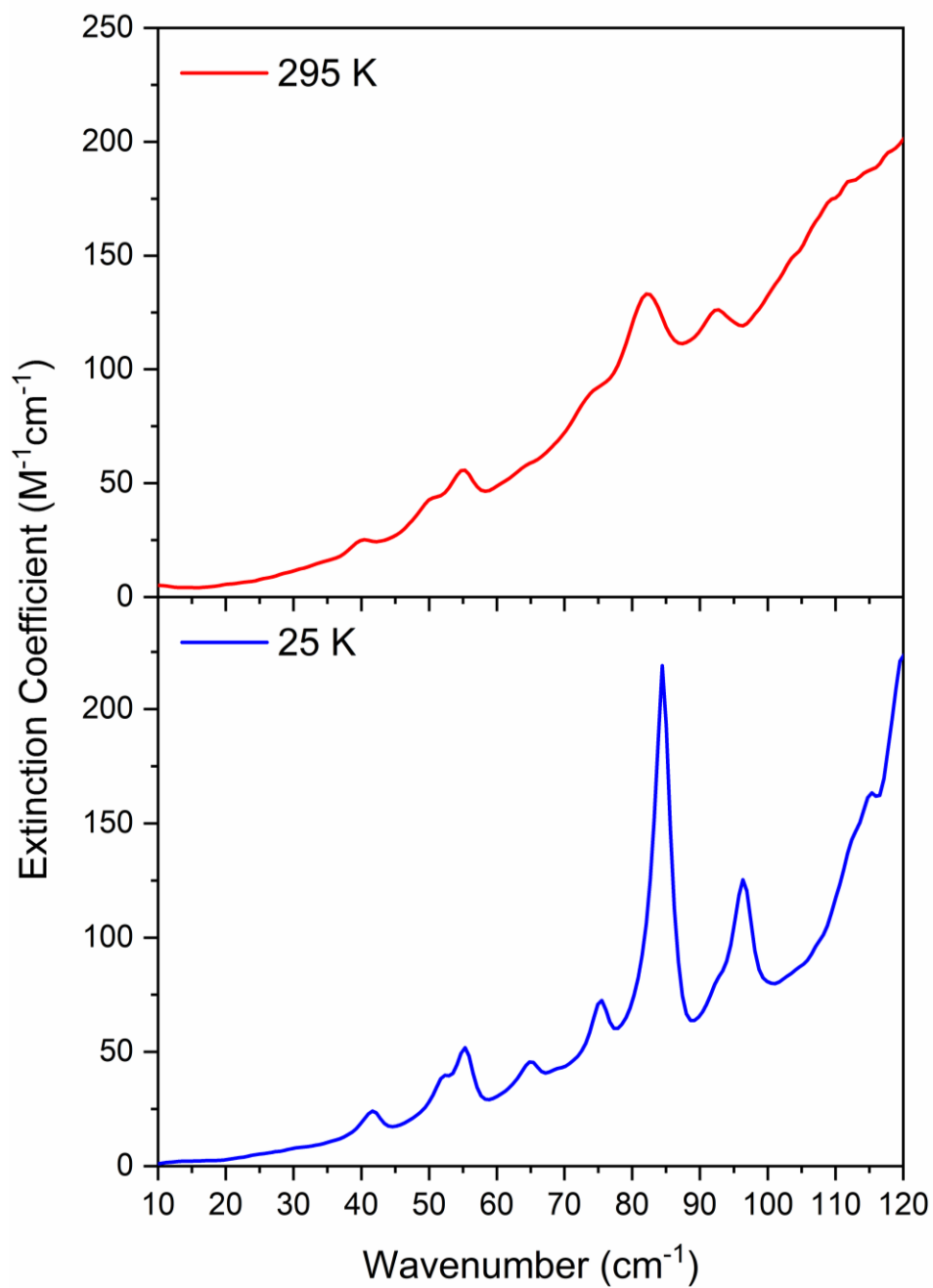
**Figure 7-3.** Terahertz time-domain spectra (10 – 120 cm$^{-1}$) of β-triglycine at 295 K (red, top) and 25 K (blue, bottom).

## 7.3.2 Computational

### 7.3.2.1. Relative Time Factors

While a more complex functional or larger basis set tends to increase the accuracy of a computational model, they also increase the time required to complete a calculation. To accurately compare the timing information across different functional and basis set combinations, calculations were performed on crystalline β-triglycine using the same hardware and the time was reported at equal points in the calculation. As expected, the use of a hybrid functional and increasing basis set size increased the computational cost (**Figure 7-4**). When performing gas phase calculations this increased cost is typically a factor of minutes while with solid-state calculations the increased cost can be a factor of weeks over hundreds of processors. This clearly demonstrates that there can be a large time penalty for the combined use of hybrid functionals and large basis sets and that the user will ultimately have to select the specific methodology based on time constraints.
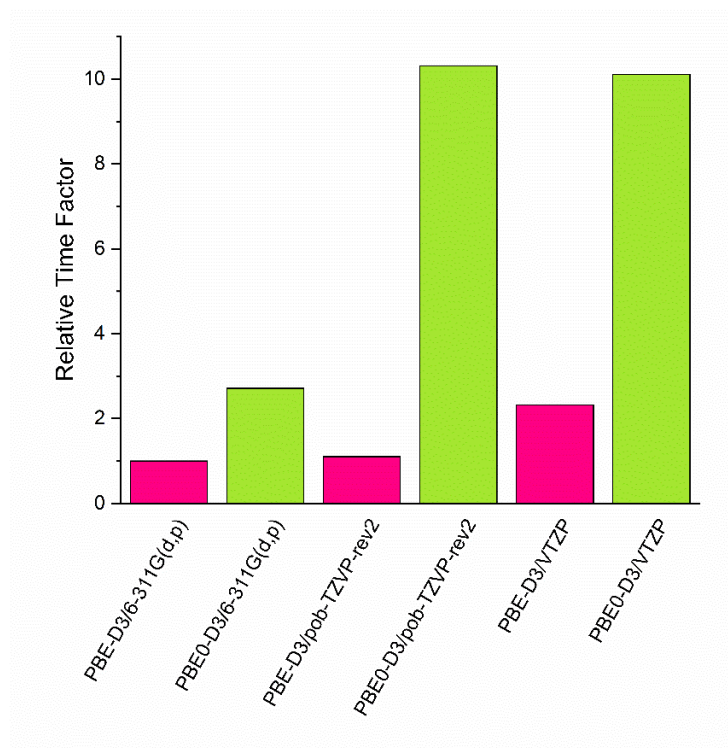
**Figure 7-4.** Relative time factors for β-triglycine using a range of functionals and basis sets.

### 7.3.2.2 Structural Optimizations

To thoroughly evaluate each functional and basis set combination, the geometry optimizations were bound only by space group symmetry, allowing the both the external lattice dimensions and internal structural components to be compared to experiment. Given that all calculations are performed at 0 K, the most appropriate comparisons came from cryogenic SC-XRD and vibrational spectroscopy measurements.

Externally, there were large variations between the calculated and reported lattice dimensions for the crystallographic unit cell of β-triglycine across the functionals and basis sets used. As shown in **Figure 7-4**, the hybrid functional (PBE0) contracted the unit cell more than its GGA counterpart (PBE), regardless of the basis set used. However, without the inclusion of the dispersion correction, the unit cell volume was consistently overestimated, reaching an error of > 14 % when modeled using PBE/VTZP (**Appendix C**). This demonstrated that even in a strongly hydrogen bonded zwitterion where the dispersion correction between 20 and 25 % of the total cohesion energy of the unit cell, and less than 1 % of the total energy of the whole solid, it is still necessary. Errors in unit cell volume alone were enough to reinforce the necessity of using the dispersion correction, and so all further discussions in this work toward developing a methodology to model crystalline β-triglycine include the dispersion correction. Using the average unsigned error across the three unique crystallographic axes, the functional and basis set combinations ranked in the following order from smallest to largest deviation from experiment: PBE0-D3/VTZP, PBE-D3/6-311G(d,p), PBE0-D3/6-311G(d,p), PBE-D3/VTZP, PBE0-D3/pob-TZVP-rev2, PBE-D3/pob-TZVp-rev2 (**Figure 7-5**).
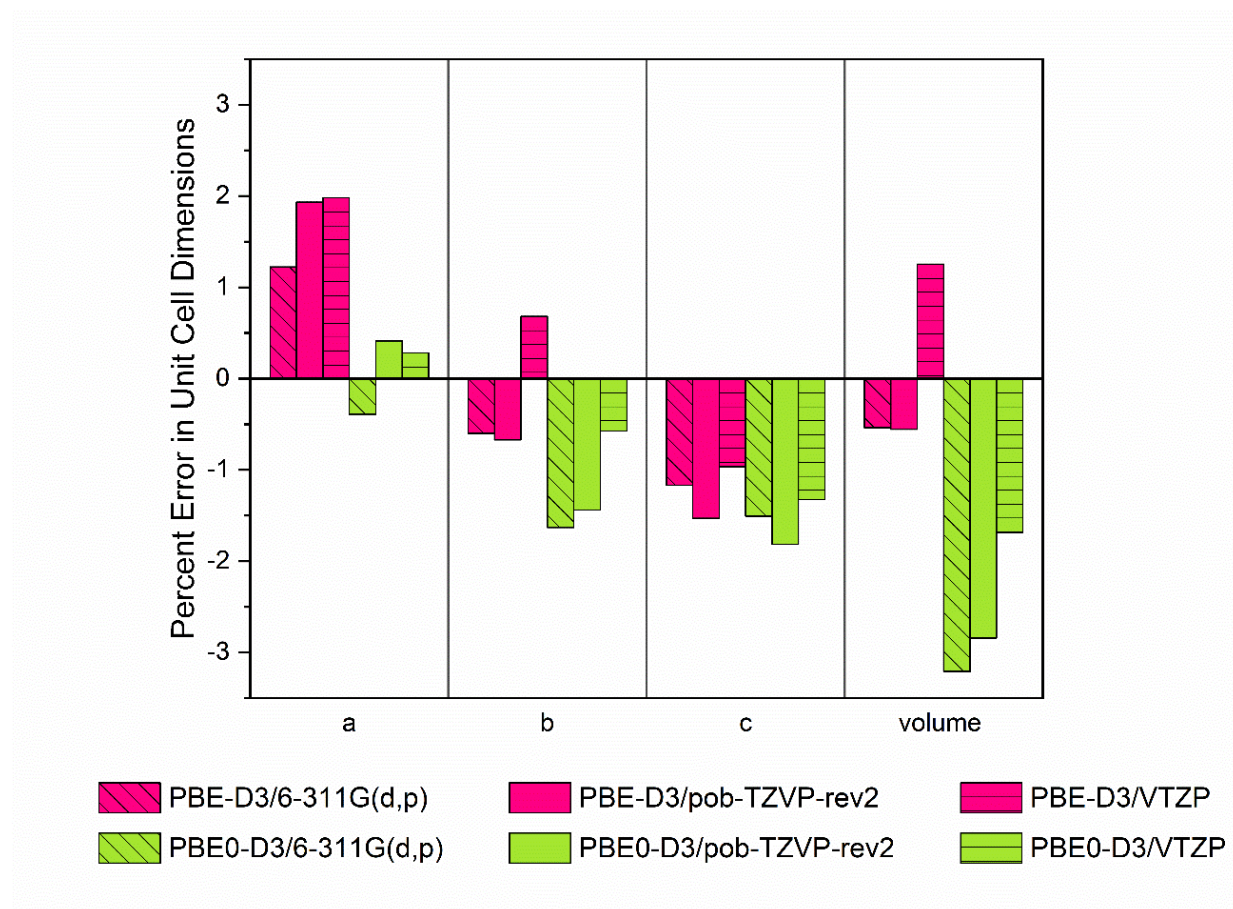
**Figure 7-5.** Signed percent errors in calculated lattice dimensions of β-triglycine compared to published SC-XRD measurements.

While the two symmetry unique molecules were conformationally very similar to each other, the complex hydrogen bonding arrangement caused molecule I and II to differ in the C2-C2A and C2A-N2 dihedral angles along the peptide backbone (**Figure 7-1**). The deviation between the optimized internal components (bond distances, bond angles, and dihedral angles) compared to SC-XRD measurements for each symmetry unique molecule are found in **Appendix C** with similar results seen between molecule I and molecule II. Similar to the trends established by external crystallographic parameter comparisons, the internal coordinates were also often overestimated with the PBE-D3 and underestimated with PBE0-D3. Average RMSD values indicated that, regardless of the basis set chosen, the hybrid structure produced a better internal structure in terms of bond distances, bond angles, and dihedral angles as seen in **Table 7-1** with individual basis set RMSD values provided in **Appendix C**. The hydrogen bonding was also well modeled across the functionals and basis sets tested, with the largest error across 11 unique hydrogen bonds presenting deviations of less than 0.1 Å in terms of acceptor to donor distance (**Appendix C**). Combining the external and internal structural comparisons, the PBE0-D3 functional with the VTZP basis set yielded a structure most similar to experiment.

**Table 7-1.** Average RMSD for heavy atom bond distances, bond angles, and dihedral angles across all basis sets for the structures calculated using PBE-D3 and PBE0-D3.

|  | PBE-D3 | PBE0-D3 |
| --- | --- | --- |
| Bond Distances (Å) | 0.0096 | 0.0063 |
| Bond Angles (°) | 0.46 | 0.31 |
| Dihedral Angles (°) | 1.63 | 0.94 |

## 7.3.2.3 Cohesion Energies and Basis Set Superposition Error

To evaluate a fundamental difference between the basis sets studied, the basis set superposition error (BSSE) was considered for each. BSSE calculations were performed on multiple structures to not only evaluate the BSSE inherent to the basis set, but also how that same BSSE was affected by changing lattice dimensions and atomic positions. Due to the zwitterionic character of the triglycine molecules, PBE-D3 was unable to account for a single molecule in a vacuum, and so all BSSE calculations were performed using PBE0-D3 functional.[49-51] The BSSE present in each basis set was evaluated using two different starting structures. The first starting structure came from the published 123 K SC-XRD measurements to keep all lattice dimensions and atomic positions equal, changing only the basis set. The second starting structure came from the optimized geometry for each basis set studied, changing the lattice dimensions and atomic positions for each calculation. The calculated BSSE of each unit cell for all structures considered is reported in **Table 2**, where regardless of the starting lattice dimensions and relative positions investigated, the BSSE remained relatively unchanged for each basis set. The differences in basis set composition led to differences in the calculated cohesion energy even after BSSE corrections, and the structures that suffered from the largest amount of BSSE resulted in overly contracted lattice dimensions due to falsely imposed binding. **Table 2** also revealed that VTZP has only a third of the BSSE present compared to the smaller basis set of 6-311G(d,p) furthering the argument to use PBE0-D3/VTZP as the methodology to model crystalline β-triglycine.

**Table 7-2.** Total BSSE (kJ/mol), corrected cohesion energy (kJ/mol), and the percentage of cohesion energy attributed to BSSE per unit cell of crystalline β-triglycine compared across multiple structures.

| | Fixed lattice, fixed positions | | | Relaxed lattice, relaxed positions | | |
|---|---|---|---|---|---|---|
| | Total BSSE | Corrected Cohesion | Percent Cohesion | Total BSSE | Corrected Cohesion | Percent Cohesion |
| PBE0-D3/6-311G(d,p) | 306 | -2108 | 14.5 % | 314 | -2117 | 14.8 % |
| PBE0-D3/pob-TZVP-rev2 | 187 | -2093 | 8.9 % | 195 | -2107 | 9.3 % |
| PBE0-D3/VTZP | 91 | -2103 | 4.3 % | 93 | -2115 | 4.4 % |

### 7.3.2.4 Vibrational Frequency Analysis

All functional and basis set combinations generally predicted the correct pattern of vibrational peak positions and intensities from $10 - 120$ cm$^{-1}$ when compared to experiment. However, the predicted spectra suffered from some amount of shifting of the frequency positions in each comparison. As expected, the crystal structures that had larger volumes typically predicted the vibrations at a lower frequency than is seen experimentally, while the structures that had smaller volumes typically predicted the vibrations at higher frequencies than the experiment (**Figure 7-6** and **Figure 7-7**). The structure produced using PBE-D3/VTZP was the only methodology tested that resulted in an overall overestimation of the unit cell volume, and this becomes very evident as the harmonic frequency calculation suffered from a significant underestimation in predicted vibrational frequency values.
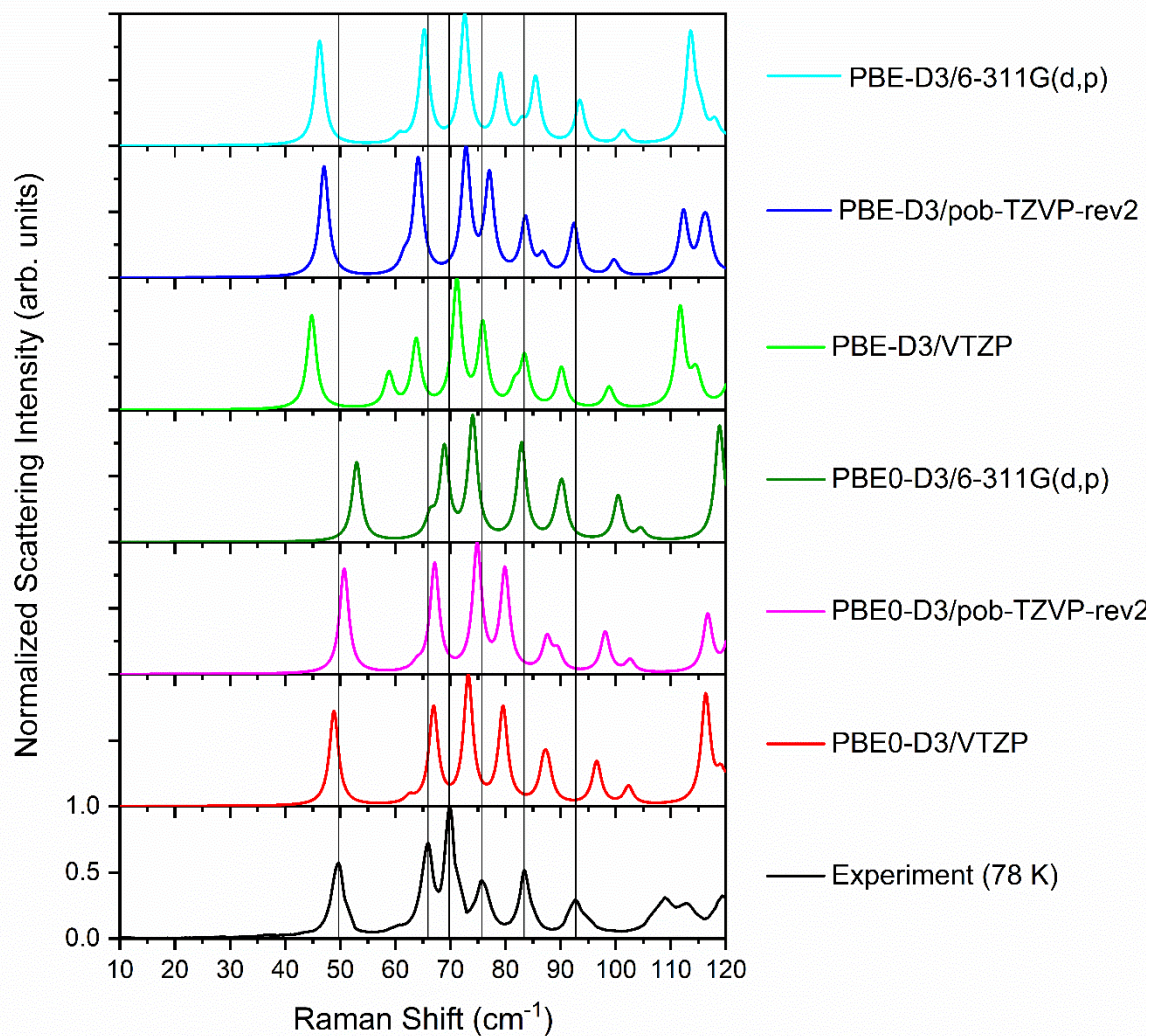
**Figure 7-6.** Experimental (78 K) low-frequency Raman spectrum (black) and simulated Raman spectra across multiple basis set and functional combinations. Vertical black lines denote experimental peak positions.
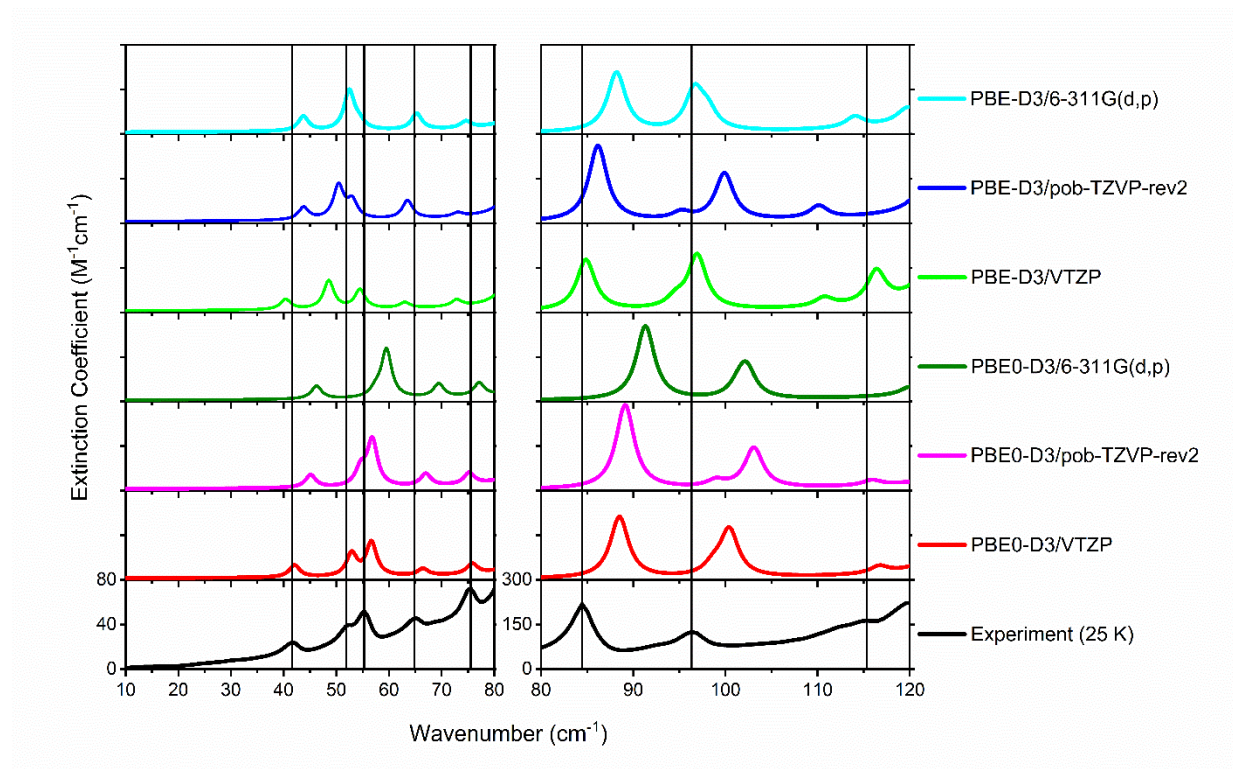
**Figure 7-7.** Experimental (25 K) terahertz spectrum (black) and simulated terahertz spectra across multiple functional and basis set combinations. Vertical black lines denote experimental peak positions. To better show the low intensity peaks, the spectra have a maximum absorption of 80 $M^{-1}cm^{-1}$ in the 10-80 $cm^{-1}$ range and 300 $M^{-1}cm^{-1}$ in the 80-120 $cm^{-1}$ range.

The top candidate from the structural comparisons (PBE0-D3/VTZP) continued to perform well, with an average RMSD of 2.7 cm$^{-1}$ between the calculated and experimental low-frequency vibrational spectra. However, when looking at the deviation between the calculated and experimental frequencies the top performers were in fact PBE-D3/POB-TZVP-rev2 and PBE-D3/6-311G(d,p) with an average RMSD of 2.1 cm$^{-1}$ across both the terahertz and Raman frequencies as seen in **Appendix C**. The large amount of BSSE present in calculations performed using the 6-311G(d,p) and POB-TZVP-rev2 basis set yielded what appeared to be good frequency agreement, but these positive results occurred potentially for the wrong reasons.

To address the shifting due to the contraction or expansion of lattice dimensions from experiment, the lattice dimensions were fixed at the experimentally observed values. However, it should be noted that imposing any restrictions on the unit cell dimensions or atomic positions induces strain on the calculation that may have unintended consequences on the simulation results. The PBE0-D3/VTZP fixed-lattice calculation had an average RMSD of 1.8 cm-1 across both form of vibrational spectroscopies as compared to the 2.7 cm$^{-1}$ seen using the fully optimized structure demonstrating how sensitive the frequencies are to lattice dimensions (**Figure 7-8**).

The combination of structural optimization analysis, vibrational frequency analysis, and basis set superposition error calculations all indicate that PBE0-D3/VTZP provides generally good agreement to experiment, and these simulations allowed for spectral assignments to be made and for the mode character of each individual vibration $< 120$ cm$^{-1}$ to be described as seen in **Table 7-3**.
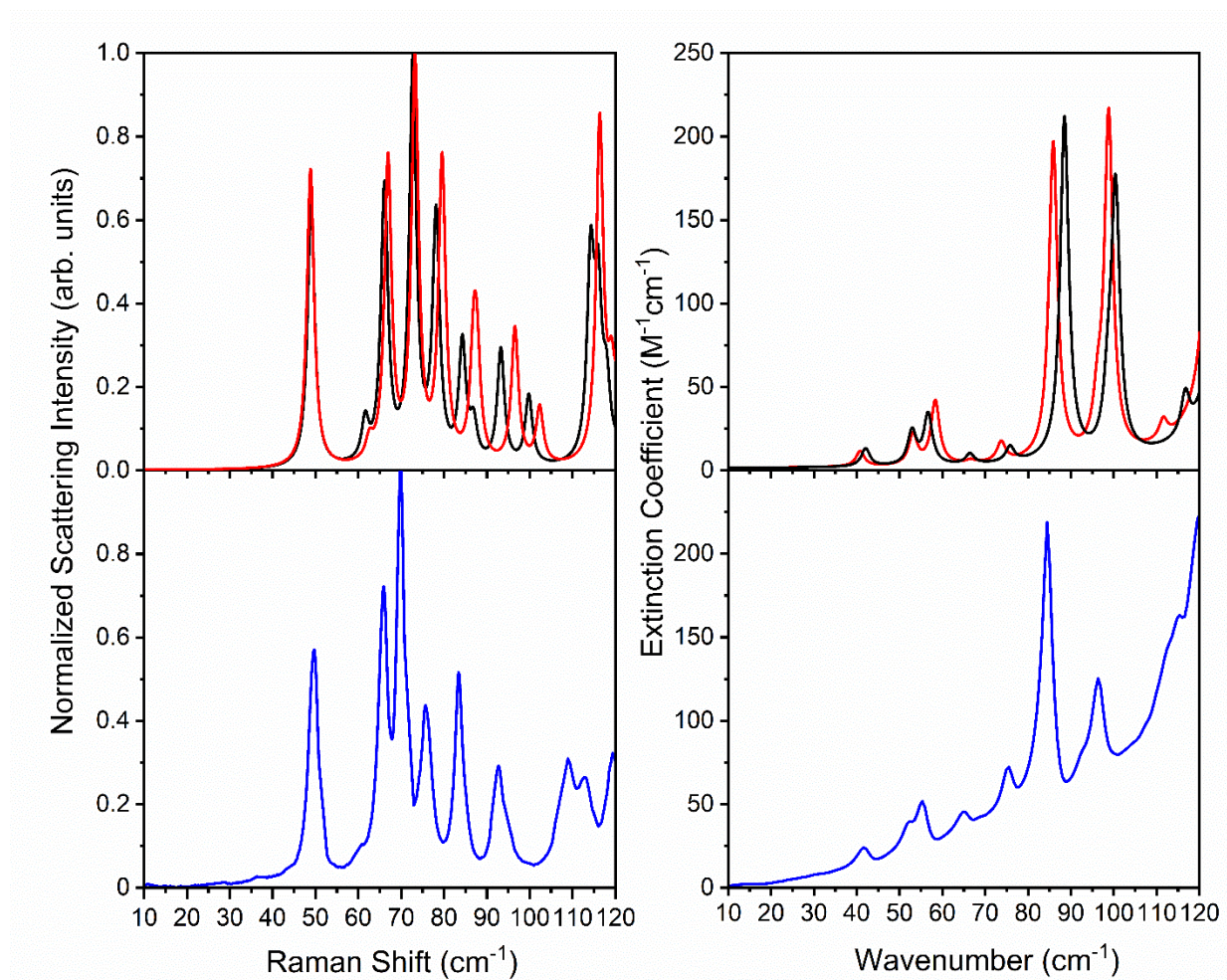
**Figure 7-8.** Comparison of low-temperature experimental β-triglycine spectra (blue) and predicted spectra from fixed-lattice (black) and full geometry (red) optimizations for LFRS (left) and THz-TDS (right).

**Table 7-3.** Spectral assignment*s* and mode character description*s* for the IR and Raman vibrational frequencies of crystalline β-triglycine below 120 cm$^{-1}$.

| Observed | | Calculated | | Mode description |
|---|---|---|---|---|
| Raman | Terahertz | Raman | Terahertz | |
| | 41.6 | | 42.10 | Rigid rotation of molecules I and II in the *b/c* plane |
| 49.7 | | 48.84 | | Internal torsion about C1A-C1 dihedral angle in molecule I and C2A-C2 dihedral angle in molecule II |
| | 51.9 | | 52.91 | Bending of molecule II in the *b/c* plane |
| | 55.3 | | 56.66 | Intramolecular torsion of the amino end of molecule I and carboxyl end of molecule II |
| | | 62.58 | | Internal torsion of carboxyl end of molecule I and amino end of molecule II |
| | 64.8 | | 66.44 | Rigid rotation of molecule II along the *c*-axis |
| 65.9 | | 66.93 | | In-phase torsion of the amino group of molecule I |
| 69.7 | | 73.23 | | Out-of-phase torsion of the amino group of molecule I |
| | 75.5 | | 75.79 | In-phase torsion of the carboxyl group of molecule II |
| 75.7 | | 79.55 | | Out-of-phase torsion of the carboxyl group of molecule II |
| 83.4 | | 86.95 | | Translation of molecule II in the *a/c* plane |
| | | 87.71 | | Translation of molecule I in along the *a-axis* |
| | 84.4 | | 88.50 | Localized twist of O1in molecule I |
| 92.8 | | 96.55 | | Localized twist of O2 in molecule II |
| | | | 98.70 | Torsion throughout the triglycine molecules |
| | 96.3 | | 100.43 | Internal torsion centered about the C3A-C3 dihedral angle of molecule II |
| 108.9 | | 102.34 | | Intramolecular torsion of the carboxyl end of molecule I |
| 112.8 | | 116.36 | | Internal torsion centered about the C3A-C3 dihedral angle |
| | 115.4 | | 116.70 | In plane bend of molecule I in the *a/b* plane |
| 119.4 | | 119.10 | | Torsion about the C3A-N3 dihedral angle of molecule II |

## 7.4 Conclusions

The functional and basis set combinations that were examined in this work were generally able to replicate the general packing arrangement and low-frequency vibrations for crystalline β-triglycine. The need to include the D3(BJ)+$E^{ABC}$ dispersion correction was easily established through the optimization of the unit cell volume, as the implementation of the dispersion correction lowered the average error across all basis sets in unit cell volume when compared to experiment from 10% to -1 % across the functional and basis set combinations. The PBE0 hybrid functional proved to be superior to PBE in terms of achieving both external and internal structural parameters that were most similar to those obtained experimentally. In terms of basis sets, both 6-311G(d,p) and VTZP performed well at capturing the proper geometry and the low-frequency vibrations, however the BSSE contributions must be considered. The basis set, 6-311G(d,p), artificially added over 300 kJ/mol to a unit cell of β-triglycine, over three times the BSSE that was present with VTZP. The VTZP basis set deserves recognition for the ability to run successfully with a hybrid functional, something that has proven elusive to other similarly sized basis sets. This basis set should be further explored using other oligopeptides of differing lengths and compositions. Combining all factors considered in replicating the external structure, internal structure, and low-frequency vibrations of crystalline β-triglycine, PBE0-D3/VTZP is the top performing methodology tested here and is widely available in numerous software packages.

**Appendix C**

The predicted and experimental powder X-ray diffraction patterns, percent error of unit cell volume across functional and basis set combinations tested with and without the dispersion correction, deviation between predicted and experimental heavy atom bond distances, bond angles, dihedral angles, hydrogen bond distances, and vibrational frequencies for crystalline β-triglycine as well as a fully labeled asymmetric unit. RMSD values for heavy atom bond distances, bond angles, dihedral angles and average frequency for the peaks identified $< 100$ cm$^{-1}$

## 7.5 References

1.  Zhang, F.; Wang, H.-W.; Tominaga, K.; Hayashi, M. Intramolecular Vibrations in Low-Frequency Normal Modes of Amino Acids: l-Alanine in the Neat Solid State. *J. Phys. Chem. A* **2015,** *119* (12), 3008-3022.

2.  Dampf, S. J.; Korter, T. M. Crystalline Molecular Standards for Low-Frequency Vibrational Spectroscopies. *J. Infrared, Millimeter, Terahertz Waves* **2020,** *41* (11), 1284-1300.

3.  Mazurek, A. H.; Szeleszczuk, Ł.; Pisklak, D. M. Periodic DFT Calculations-Review of Applications in the Pharmaceutical Sciences. *Pharmaceutics* **2020,** *12* (5), 415.

4.  Islam, M. M.; Costa, D.; Calatayud, M.; Tielens, F. Characterization of SupportedVvanadium Oxide Species on Silica: A Periodic DFT Investigation. *J. Phys. Chem. C* **2009,** *113* (24), 10740-10746.

5.  Levina, E. O.; Chernyshov, I. Y.; Voronin, A. P.; Alekseiko, L. N.; Stash, A. I.; Vener, M. V. Solving the Enigma of Weak Fluorine Contacts in the Solid State: A Periodic DFT Study of Fluorinated Organic Crystals. *RSC Adv.* **2019,** *9* (22), 12520-12537.

6.  Bilski, P.; Druzbicki, K.; Jenczyk, J.; Mielcarek, J.; Wasicki, J. Molecular and Vibrational Dynamics in the Cholesterol-lowering Agent Lovastatin: Solid-state NMR, Inelastic Neutron Scattering, and Periodic DFT Study. *J. Phys. Chem. B* **2017,** *121* (13), 2776-2787.

7.  Manin, A. N.; Voronin, A. P.; Manin, N. G.; Vener, M. V.; Shishkina, A. V.; Lermontov, A. S.; Perlovich, G. L. Salicylamide Cocrystals: Screening, Crystal Structure, Sublimation Thermodynamics, Dissolution, and Solid-state DFT Calculations. *J. Phys. Chem. B* **2014,** *118* (24), 6803-6814.

8.      Banks, P. A.;  Song, Z.; Ruggiero, M. T. Assessing the Performance of Density Functional Theory Methods on the Prediction of Low-Frequency Vibrational Spectra. *J. Infrared, Millimeter, Terahertz Waves* **2020,** *41* (11), 1411-1429.

9.      Rexrode, N. R.;  Orien, J.; King, M. D. Effects of Solvent Stabilization on Pharmaceutical Crystallization: Investigating Conformational Polymorphism of Probucol Using Combined Solid-State Density Functional Theory, Molecular Dynamics, and Terahertz Spectroscopy. *J. Phys. Chem. A* **2019,** *123* (32), 6937-6947.

10.     Davis, M. P.;  Mohara, M.;  Shimura, K.; Korter, T. M. Simulation and Assignment of the Terahertz Vibrational Spectra of Enalapril Maleate Cocrystal Polymorphs. *J. Phys. Chem. A* **2020,** *124* (47), 9793-9800.

11.     Schweitzer-Stenner, R. Advances in Vibrational Spectroscopy as a Sensitive Probe of Peptide and Protein Structure: A Critical Review. *Vib. Spectrosc.* **2006,** *42* (1), 98-117.

12.     Malipeddi, H.;  Das, P.; Karigar, A. Green Technique-solvent Free Synthesis and its Advantages. *Int. J. Res. Ayurveda Pharm.* **2011,** *2*, 1079-1086.

13.     Tanaka, K.; Toda, F. Solvent-Free Organic Synthesis. *Chem. Rev.* **2000,** *100* (3), 1025-1074.

14.     Seitz, A.;  Wende, R. C.;  Roesner, E.;  Niedek, D.;  Topp, C.;  Colgan, A. C.; McGarrigle, E. M.; Schreiner, P. R. Site-Selective Acylation of Pyranosides with Oligopeptide Catalysts. *J. Org. Chem.* **2021,** *86* (5), 3907-3922.

15.     Lenel, F. V. The Structures of Some Simple Glycine Polypeptides. *Z. Kristallogr., Kristallgeom., Kristallphys., Kristallchem.* **1932,** *81*, 224-9.

16.     Yakel, H. L.; Hughes, E. W. The Unit-cell Dimensions and Space Groups of Two Modifications of Crystalline Glycylglycylglycine. *Acta Crystallogr.* **1952,** *5* (6), 847-848.

17.  Juliano Jr, T. R.; Korter, T. M. Terahertz Vibrations of Crystalline Acyclic and Cyclic Diglycine: Benchmarks for London Force Correction Models. *J. Phys. Chem. A* **2013,** *117* (40), 10504-10512.

18.  Ivanova, B. B.; Kolev, T.; Zareva, S. Y. Solid-state IR–LD Spectroscopic and Theoretical Analysis of Glycine-containing Peptides and their Hydrochlorides. *Biopolymers* **2006,** *82* (6), 587-596.

19.  Smith, A. J.; Ali, F. I.; Soldatov, D. V. Glycine Homopeptides: The Effect of the Chain Length on the Crystal Structure and Solid State Reactivity. *CrystEngComm* **2014,** *16* (31), 7196-7208.

20.  Srikrishnan, T.: Winiewica, R.: Parthasarathy, R. New Patterns of Hydrogen Bonded Interactions Between Polypeptide Chains. *Int. J. Pept. Protein Res.* **1982,** *19* (2), 103-113.

21.  Pichon-Pesme, V.; Lecomte, C. Experimental Charge Density and Electrostatic Potential of Triglycine. *Acta Crystallogr., Sect. B: Struct. Sci., Cryst. Eng. Mater.* **1998,** *54* (4), 485-493.

22.  Sundius, T.; Bandekar, J.; Krimm, S. Vibrational Analysis of Crystalline Triglycine. *J. Mol. Struct.* **1989,** *214*, 119-42.

23.  Rutz, F.; Wilk, R.; Kleine-Ostmann, T.; Grunenberg, J.; Koch, M. Experimental and Theoretical Study of the THz Absorption Spectra of Selected Tripeptides. *Proc. SPIE* **2005,** *5727* (Terahertz and Gigahertz Electronics and Photonics IV), 12-19.

24.  Kawaguchi, S.; Kambara, O.; Ponseca, C. S., Jr.; Shibata, M.; Kandori, H.; Tominaga, K. Low-frequency Dynamics of Biological Molecules Studied by Terahertz Time-domain Spectroscopy. *J. Spectrosc.* **2010,** *24* (1,2), 153-158.

25.  Kutteruf, M. R.;  Brown, C. M.;  Iwaki, L. K.;  Campbell, M. B.;  Korter, T. M.; Heilweil, E. J. Terahertz Spectroscopy of Short-chain Polypeptides. *Chem. Phys. Lett.* **2003,** *375* (3), 337-343.

26.  Weinhardt, L.;  Benkert, A.;  Meyer, F.;  Blum, M.;  Hauschild, D.;  Wilks, R. G.;  Baer, M.;  Yang, W.;  Zharnikov, M.;  Reinert, F.; Heske, C. Local Electronic Structure of the Peptide Bond Probed by Resonant Inelastic Soft X-ray Scattering. *Phys. Chem. Chem. Phys.* **2019,** *21* (24), 13207-13214.

27.  Sun, Y.;  Frenkel-Pinter, M.;  Liotta, C. L.; Grover, M. A. The pH Dependent Mechanisms of Non-enzymatic Peptide Bond Cleavage Reactions. *Phys. Chem. Chem. Phys.* **2020,** *22* (1), 107-113.

28.  Morozova, A. S.;  Ziganshina, S. A.;  Bukharaev, A. A.;  Ziganshin, M. A.; Gerasimov, A. V. Features of the Self-organization of Films Based on Triglycine under the Influence of Vapors of Organic Compounds. *J. Surf. Invest.: X-Ray, Synchrotron Neutron Tech.* **2020,** *14* (3), 499-506.

29.  Compaan, A.;  Wagoner, A.; Aydinli, A. Rotational Raman scattering in the Instructional Laboratory. *Am. J. Phys.* **1994,** *62* (7), 639-645.

30.  *Origin*, 2020; OriginLab Corporation: Northampton, MA, USA.

31.  Dovesi, R.;  Erba, A.;  Orlando, R.;  Zicovich-Wilson, C. M.;  Civalleri, B.;  Maschio, L.;  Rérat, M.;  Casassa, S.;  Baima, J.;  Salustro, S.; Kirtman, B. Quantum-mechanical Condensed Matter Simulations with CRYSTAL. *Wiley Interdiscip. Rev.: Comput. Mol. Sci.* **2018,** *8* (4), e1360.

32.  Perdew, J. P.;  Burke, K.; Ernzerhof, M. Generalized Gradient Approximation Made Simple. *Phys. Rev. Lett.* **1996,** *77* (18), 3865-3868.

33.     Adamo, C.; Barone, V. Toward Reliable Density Functional Methods Without Adjustable

        Parameters: The PBE0 Model. *J. Chem. Phys.* **1999,** *110* (13), 6158-6170.

34.     Grimme, S.;  Antony, J.;  Ehrlich, S.; Krieg, H. A Consistent and Accurate ab initio

        Parametrization of Density Functional Dispersion Correction (DFT-D) for the 94

        Elements H-Pu. *J. Chem. Phys.* **2010,** *132* (15), 154104/1-154104/19.

35.     Grimme, S.;  Ehrlich, S.; Goerigk, L. Effect of the damping function in dispersion

        corrected density functional theory. *J. Comput. Chem.* **2011,** *32* (7), 1456-1465.

36.     Grimme, S.;  Hansen, A.;  Brandenburg, J. G.; Bannwarth, C. Dispersion-Corrected

        Mean-Field Electronic Structure Methods. *Chem. Rev.* **2016,** *116* (9), 5105-5154.

37.     Schäfer, A.;  Horn, H.; Ahlrichs, R. Fully Optimized Contracted Gaussian Basis Sets for

        Atoms Li to Kr. *J. Chem. Phys.* **1992,** *97* (4), 2571-2577.

38.     Pritchard, B. P.;  Altarawy, D.;  Didier, B.;  Gibson, T. D.; Windus, T. L. New Basis Set

        Exchange: An Open, Up-to-Date Resource for the Molecular Sciences Community. *J.

        Chem. Inf. Model.* **2019,** *59* (11), 4814-4820.

39.     Feller, D. The Role of Databases in Support of Computational Chemistry Calculations. *J.

        Comput. Chem.* **1996,** *17* (13), 1571-1586.

40.     Schuchardt, K. L.;  Didier, B. T.;  Elsethagen, T.;  Sun, L.;  Gurumoorthi, V.;  Chase, J.;

        Li, J.; Windus, T. L. Basis Set Exchange:  A Community Database for Computational

        Sciences. *J. Chem. Inf. Model.* **2007,** *47* (3), 1045-1052.

41.     Banks, P. A.;  Song, Z.; Ruggiero, M. T. Assessing the Performance of Density

        Functional Theory Methods on the Prediction of Low-Frequency Vibrational Spectra.

        *Journal of Infrared, Millimeter, and Terahertz Waves* **2020**.

42. Weigend, F.; Ahlrichs, R. Balanced Basis Sets of Split Valence, Triple Zeta Valence and Quadruple Zeta Valence Quality for H to Rn: Design and Assessment of Accuracy. *Phys. Chem. Chem. Phys.* **2005,** *7* (18), 3297-3305.

43. Boys, S. F.; Bernardi, F. The Calculation of Small Molecular Interactions by the Differences of Separate Total Energies. Some Procedures with Reduced Errors. *Mol. Phys.* **1970,** *19* (4), 553-566.

44. Kratzer, P.; Neugebauer, J. The Basics of Electronic Structure Theory for Periodic Systems. *Front. Chem.* **2019,** *7* (106).

45. Pascale, F.; Zicovich-Wilson, C. M.; López Gejo, F.; Civalleri, B.; Orlando, R.; Dovesi, R. The Calculation of the Vibrational Frequencies of Crystalline Compounds and its Implementation in the CRYSTAL Code. *J. Comput. Chem.* **2004,** *25* (6), 888-897.

46. Zicovich-Wilson, C. M.; Pascale, F.; Roetti, C.; Saunders, V. R.; Orlando, R.; Dovesi, R. Calculation of the Vibration Frequencies of α-quartz: The Effect of Hamiltonian and Basis Set. *J. Comput. Chem.* **2004,** *25* (15), 1873-1881.

47. Anderson, D. G. Iterative Procedures for Nonlinear Integral Equations. *J. Assoc. Comput. Mach.* **1965,** *12* (4), 547-560.

48. Maschio, L.; Kirtman, B.; Rerat, M.; Orlando, R.; Dovesi, R. Ab initio Analytical Raman Intensities for Periodic Systems through a Coupled Perturbed Hartree-Fock/Kohn-Sham Method in an Atomic Orbital Basis. I. Theory. *J. Chem. Phys.* **2013,** *139* (16), 164101/1-164101/13.

49. Chowdhry, B. Z.; Dines, T. J.; Jabeen, S.; Withnall, R. Vibrational Spectra of α-Amino Acids in the Zwitterionic State in Aqueous Solution and the Solid State: DFT

Calculations and the Influence of Hydrogen Bonding. *J. Phys. Chem. A* **2008,** *112* (41), 10333-10347.

50.     Červinka, C.; Fulem, M. Cohesive Properties of the Crystalline Phases of Twenty Proteinogenic α-Amino Acids from First-principles Calculations. *Phys. Chem. Chem. Phys.* **2019,** *21* (34), 18501-18515.

51.     Marchese Robinson, R. L.;  Geatches, D.;  Morris, C.;  Mackenzie, R.;  Maloney, A. G. P.;  Roberts, K. J.;  Moldovan, A.;  Chow, E.;  Pencheva, K.; Vatvani, D. R. M. Evaluation of Force-Field Calculations of Lattice Energies on a Large Public Dataset, Assessment of Pharmaceutical Relevance, and Comparison to Density Functional Theory. *J. Chem. Inf. Model.* **2019,** *59* (11), 4778-4792.

# Chapter 8: Reflections

Studying the effects of not only a multitude of density functionals and basis sets, but specific software parameters, has led to a better understanding of the correlation between theory and experiments seen across quantum mechanical models. In the case of γ-aminobutyric acid (GABA), the anomalous response of the lowest-frequency terahertz-active vibration to temperature is now being used to monitor the temperature of cryogenic experiments in other laboratories as it is currently the largest anomalous temperature shift reported for a molecular solid. To capture the lowest-frequency terahertz-active vibration, the implementation of very stringent convergence criteria was required. By computing all 2 electron integrals exactly, as opposed to using the default overlap thresholds, the lowest calculated frequency shifted by almost 6 %. Overall, GABA turned out to be an amazing solid showing unprecedented behavior from both experimental and computational perspectives.

Similar in importance for creating a more stringent simulation through the calculation of electron integrals, is the addition of a three-body dispersion term. It has been found across three molecular crystals that the inclusion of a three-body dispersion term that serves as a repulsive term in the treatment of weak intermolecular forces produced more realistic representations of packing arrangements and therefore low-frequency vibrations. While the implementation of these additional keywords and parameters may seem small, the sensitivity of the low-frequency region apparently demands them. Despite having a magnitude of only 2% of the cohesion energy, the three-body term has remarkably demonstrated its utility in the simulation of organic molecular crystals.

When choosing an appropriate computational methodology, a comprehensive approach should be used to determine the most appropriate functional and basis set for the system being studied. The role that each parameter has on the final optimized geometry, vibrational frequencies, and calculated energies must be considered. For the oligopeptide, β-triglycine, the use of a hybrid functional (PBE0) was found to produce both internal and external structural dimensions that more closely resembled experiment than a generalized gradient approximation of the same family (PBE). The need for a dispersion correction was also reinforced as without it the external lattice parameters were consistently overestimated. β-triglycine also proved to be an excellent test system for the deceiving effects that basis set superposition error (BSSE) can have on a calculation. While the use of certain basis sets appeared to replicate the low-frequency vibrations, the large percentage of the cohesion energy that was attributed to basis set superposition error could not be ignored. The BSSE analysis demonstrated that for solid-state density functional simulations, one needs to use as large a basis set as possible, not only to achieve chemical accuracy in the molecular structures, but to also avoid the pitfall of cohesion artifacts caused by small basis sets.

Collectively, the work presented in this dissertation has demonstrated that the simulation of structures and vibrations in molecular solids can be very successful, but that a great amount of care and attention to detail is needed in their use. A fruitful research direction for future projects would be a systematic investigation of density functionals, basis sets, and other calculation parameters applied to a wide variety of molecular solids such as weakly bound carbazole or the chloride salt of the pharmaceutical drug, Baclofen.  The work presented here has provided a great amount of new and useful insight into the best practices for performing these simulations, but also shows that every sample exhibits its own unique challenges and surprises.

# Appendix A: Supporting Information for Chapter 5

**Table of Contents:**

**Table A-8.** Mode labels, vibrational frequencies, symmetry representations, and IR/Raman intensities for crystalline biotin simulated using ss-DFT.

**Table A-9.** Mode labels, vibrational frequencies, symmetry representations, and IR/Raman intensities for crystalline L-cystine simulated using ss-DFT.

**Table A-10.** Tentative correlation table between the observed peaks for the terahertz spectra of crystalline α-lactose monohydrate (5 - 167 cm$^{-1}$) at 65 K and ss-DFT simulations.

**Table A-11.** Tentative correlation table between the observed peaks for the Raman spectra of crystalline α-lactose monohydrate (5 - 167 cm$^{-1}$) at 78 K and ss-DFT simulations.

**Table A-12.** Tentative correlation table between the observed peaks for the terahertz spectra of crystalline biotin (5 - 167 cm$^{-1}$) at 65 K and ss-DFT simulations.

**Table A-13.** Tentative correlation table between the observed peaks for the Raman spectra of crystalline biotin (5 - 167 cm$^{-1}$) at 78 K and ss-DFT simulations.

**Table A-14.** Tentative correlation table between the observed peaks for the terahertz spectra of crystalline L-cystine (5 - 167 cm$^{-1}$) at 50 K and ss-DFT simulations.

**Table A-15.** Tentative correlation table between the observed peaks for the Raman spectra of crystalline L-cystine (5 - 167 cm$^{-1}$) at 78 K and ss-DFT simulations.

Input file for α-lactose monohydrate geometry optimization

Input file for α-lactose monohydrate frequency calculation

Input file for biotin geometry optimization

Input file for biotin frequency calculation

Input file for L-cystine geometry optimization

Input file for L-cystine frequency calculation

DOI containing XY data for all THz-TDS waveforms and processed THz-TDS and LFRS data
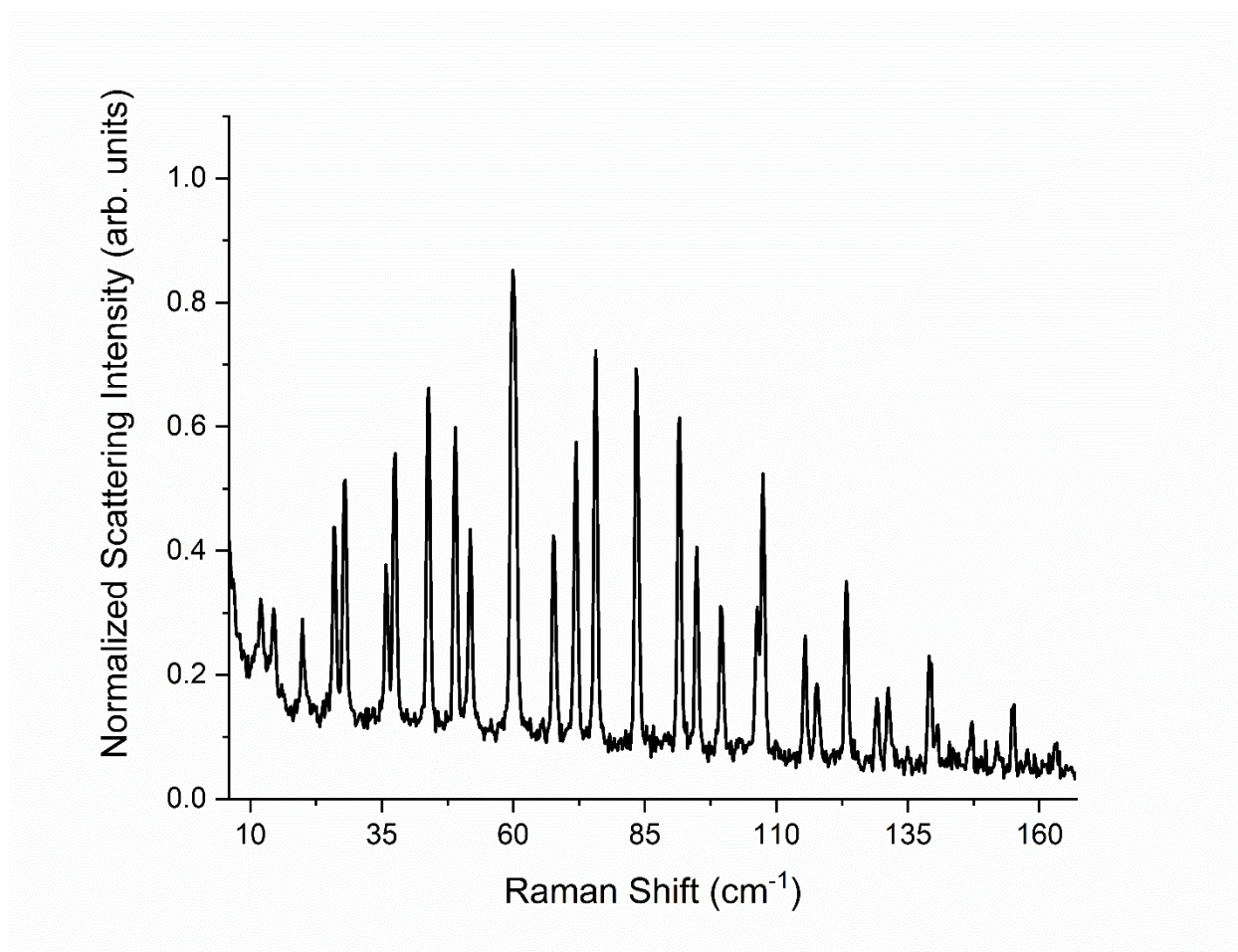
**Figure A-1.** Raman spectrum of atmospheric rotational lines taken at 293 K.
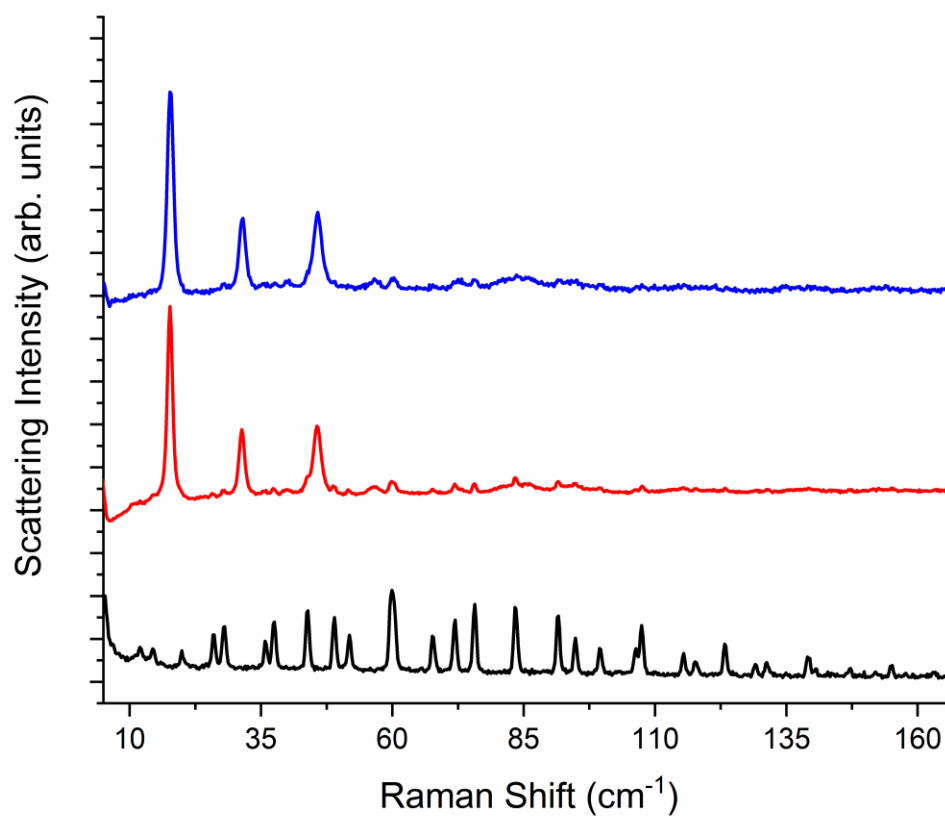
**Figure A-2.** Offset of Raman spectra of short path length for α-lactose monohydrate (blue, top), long path length for α-lactose monohydrate (red, middle) and air (black, bottom) all taken at 293 K. Path length refers to the distance traveled by the excitation laser to the sample.
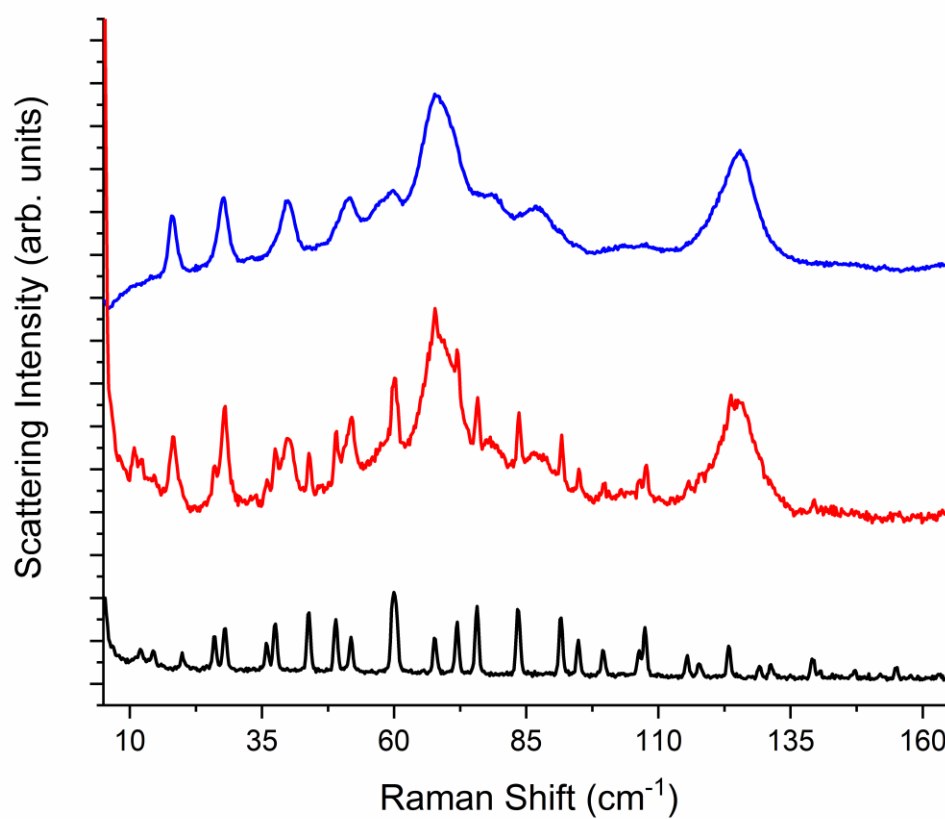
**Figure A-3.** Offset of Raman spectra of short path length for biotin (blue, top), long path length for biotin (red, middle) and air (black, bottom) all taken at 293 K. Path length refers to the distance traveled by the excitation laser to the sample.
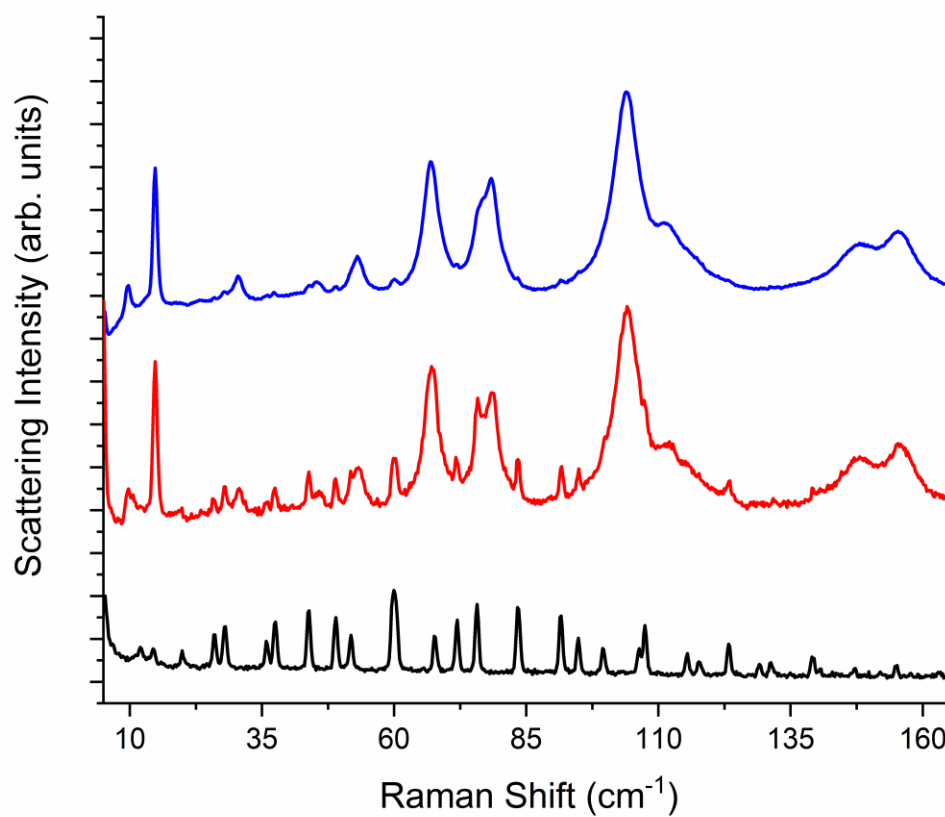
**Figure A-4.** Offset of Raman spectra of short path length for L-cystine (blue, top), long path length for L-cystine (red, middle) and air (black, bottom) all taken at 293 K. Path length refers to the distance traveled by the excitation laser to the sample.
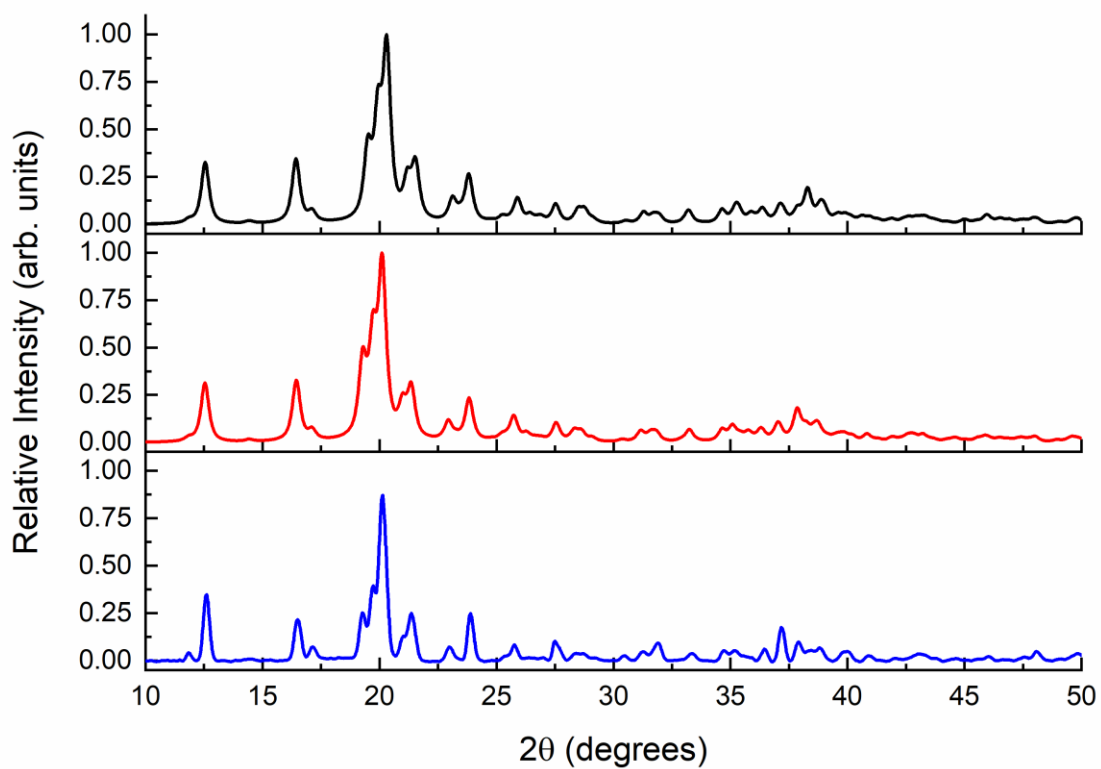
**Figure A-5.** Ss-DFT simulated powder X-ray diffraction pattern (black, top) with the predicted SC-XRD powder pattern (red, middle) and 100 K experimental data (blue, bottom) for crystalline α-lactose monohydrate.
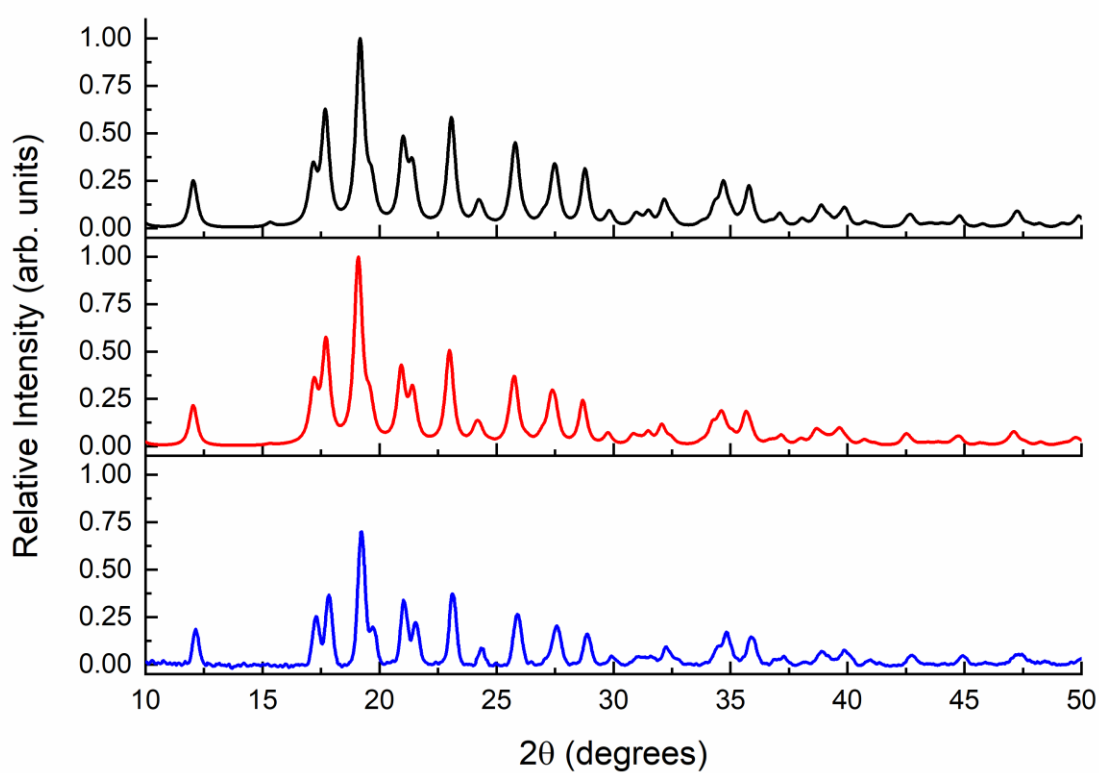
**Figure A-6.** Ss-DFT simulated powder X-ray diffraction pattern (black, top) with the predicted SC-XRD powder pattern (red, middle) and 100 K experimental data (blue, bottom) for crystalline biotin.
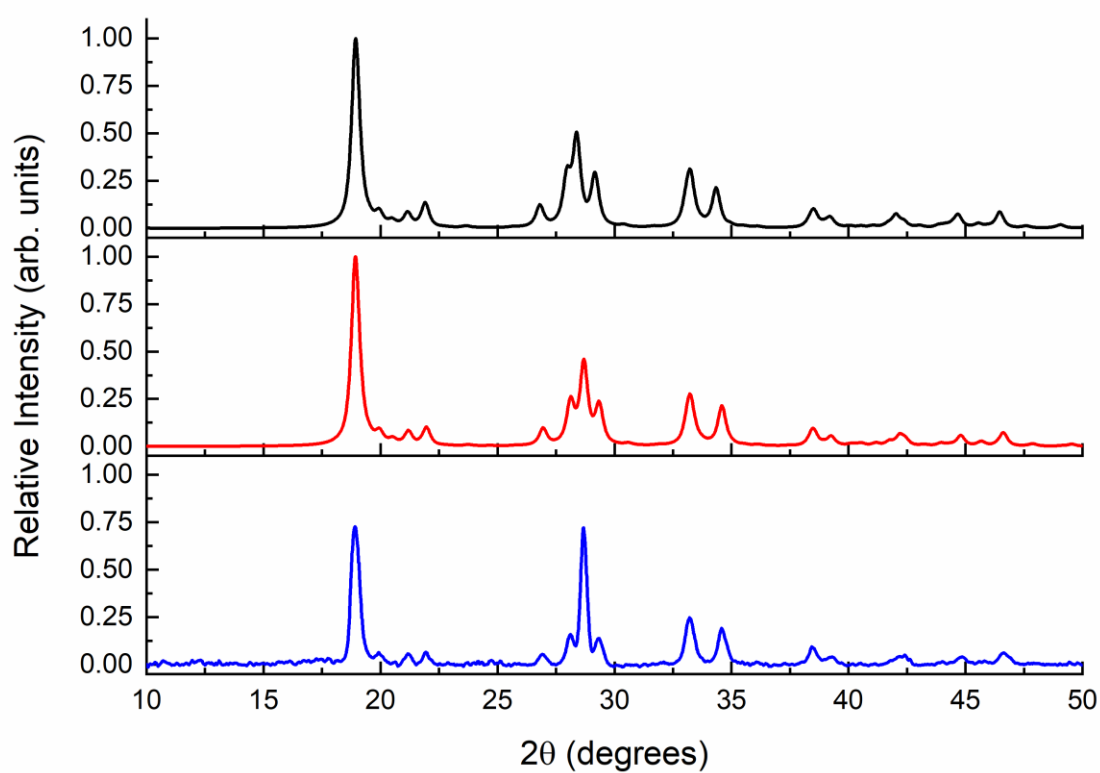
**Figure A-7.** Ss-DFT simulated powder X-ray diffraction pattern (black, top) with the predicted SC-XRD powder pattern (red, middle) and 100 K experimental data (blue, bottom) for crystalline L-cystine.
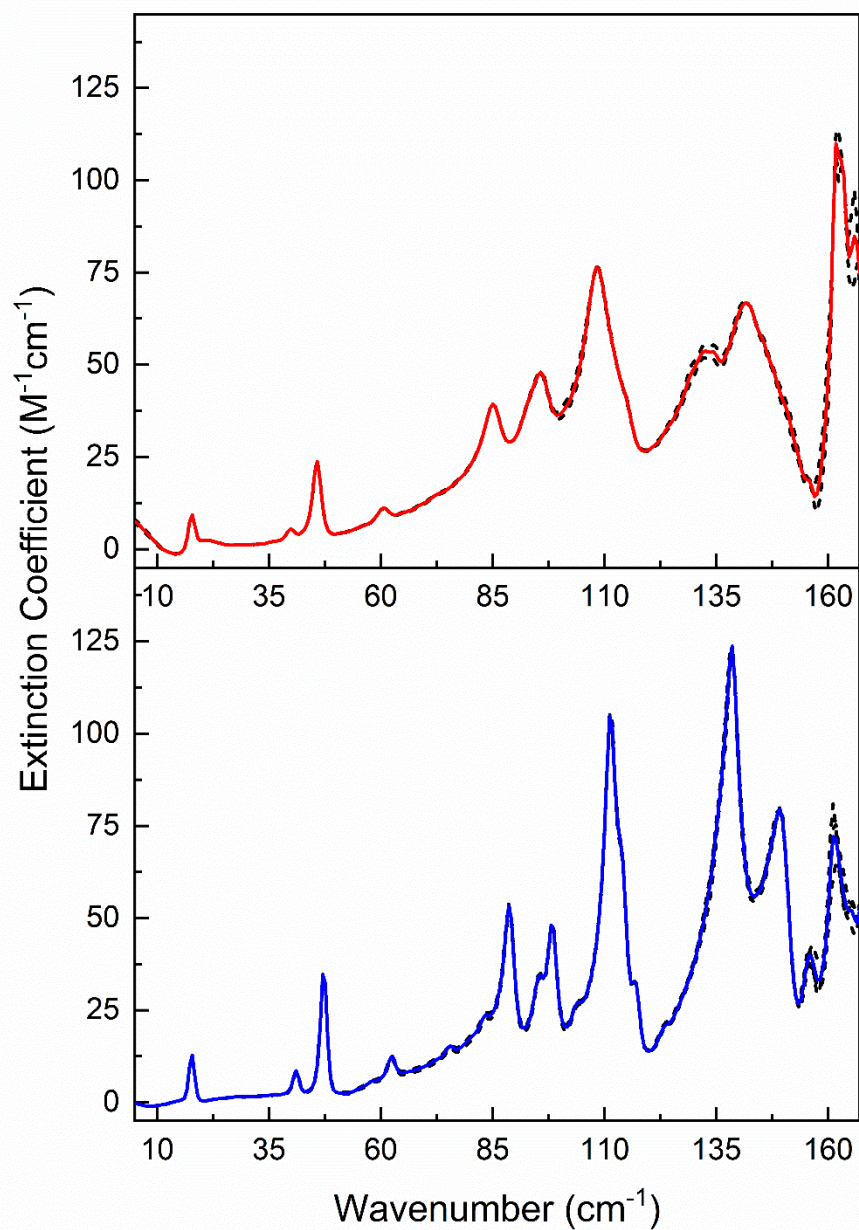
**Figure A-8.** Individual trials (dashed lines) and average (solid) THz-TDS data for crystalline α-lactose monohydrate at 293 K (top) and 78K (bottom).
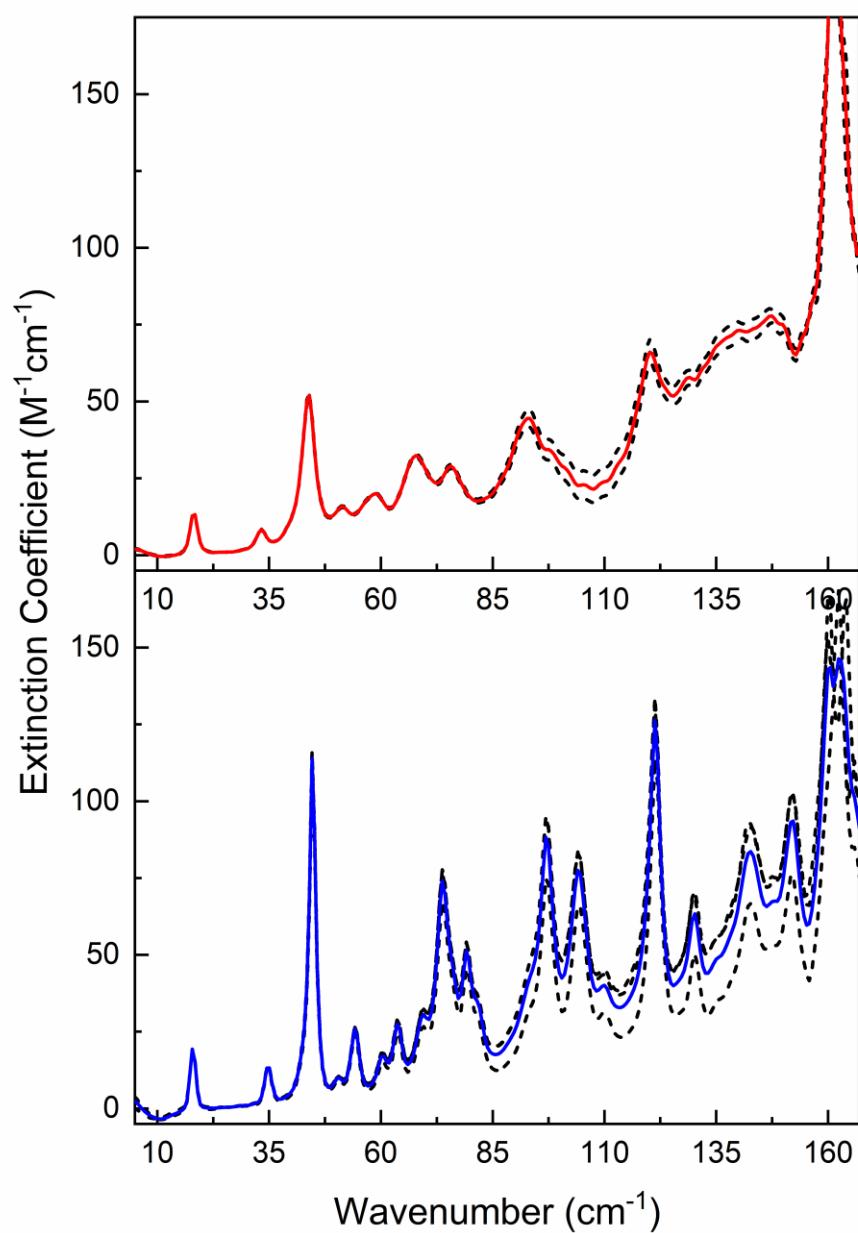
**Figure A-9.** Individual trials (dashed lines) and average (solid) THz-TDS data for crystalline biotin at 293 K (top) and 78K (bottom). The 293 K biotin spectra is shown to 175 $M^{-1}cm^{-1}$ for clarity.
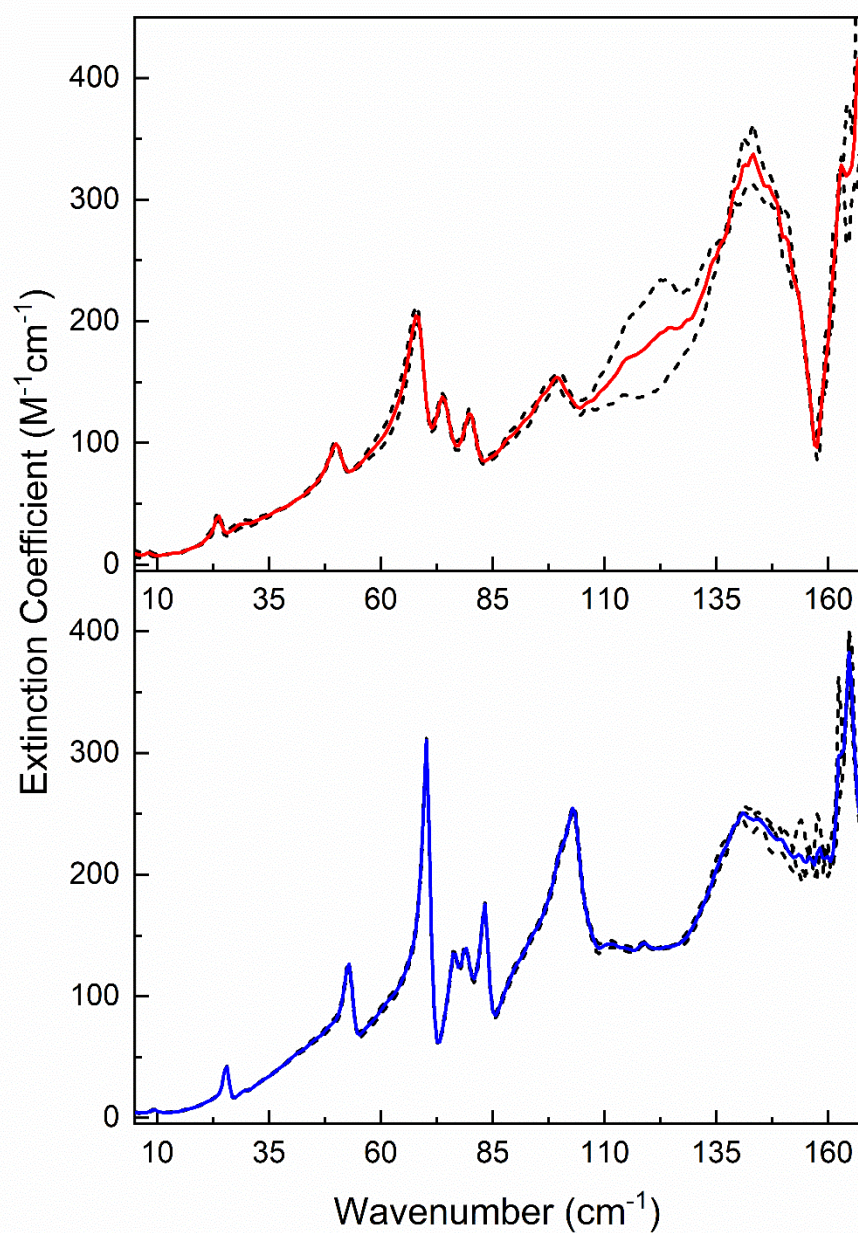
**Figure A-10.** Individual trials (dashed lines) and average (solid) THz-TDS data for crystalline L-cystine at 293 K (top) and 78K (bottom).
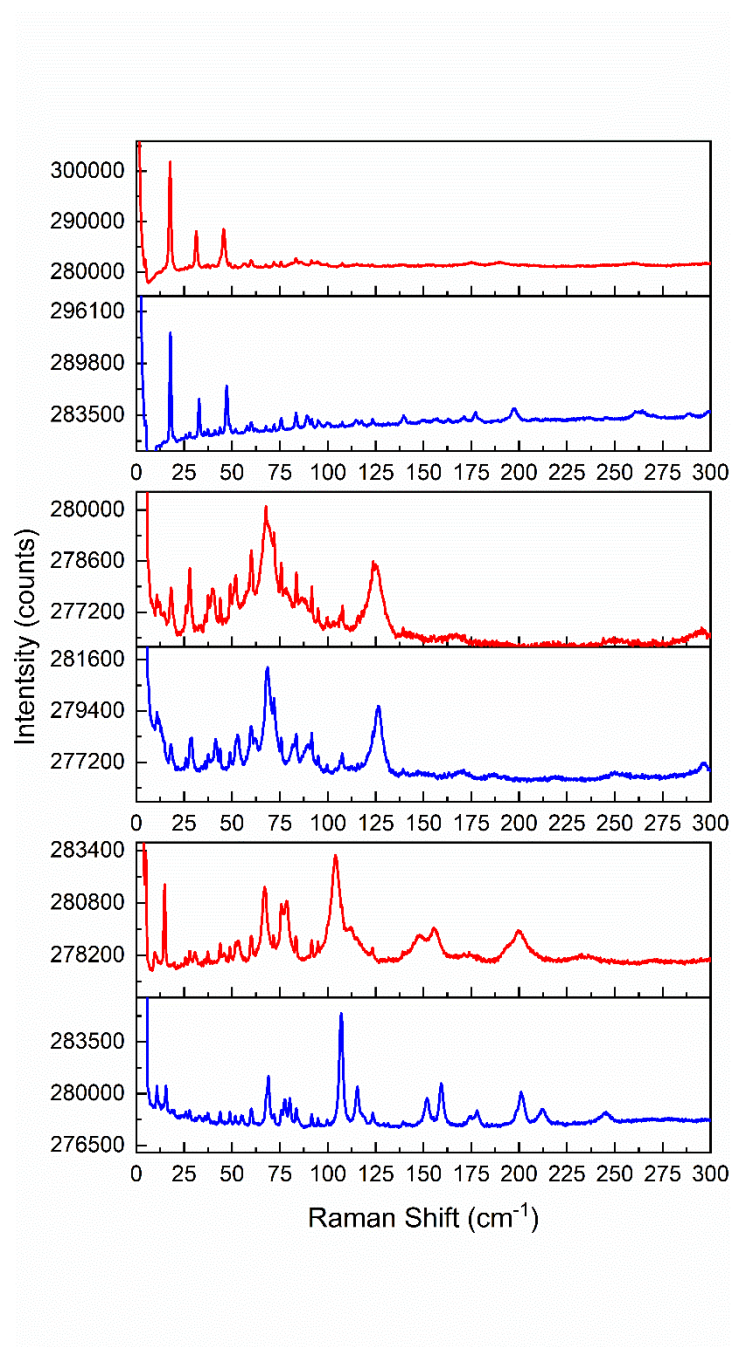
**Figure A-11.** Raw Raman spectra of molecular standards (top: α-lactose monohydrate, middle: biotin, bottom: L-cystine) at 293 K (red) and 78 K (blue) from 0 – 300 cm⁻¹.
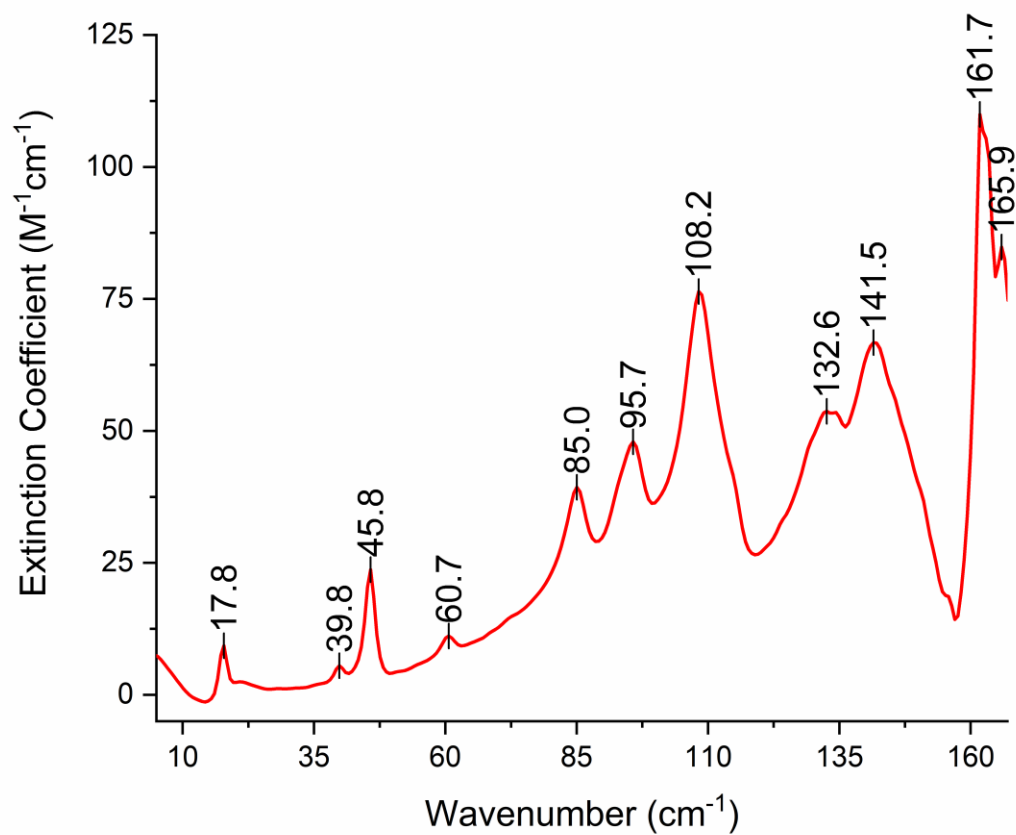
**Figure A-12.** Terahertz spectrum of crystalline α-lactose monohydrate (5 - 167 cm$^{-1}$) at 293 K with peak centers identified.
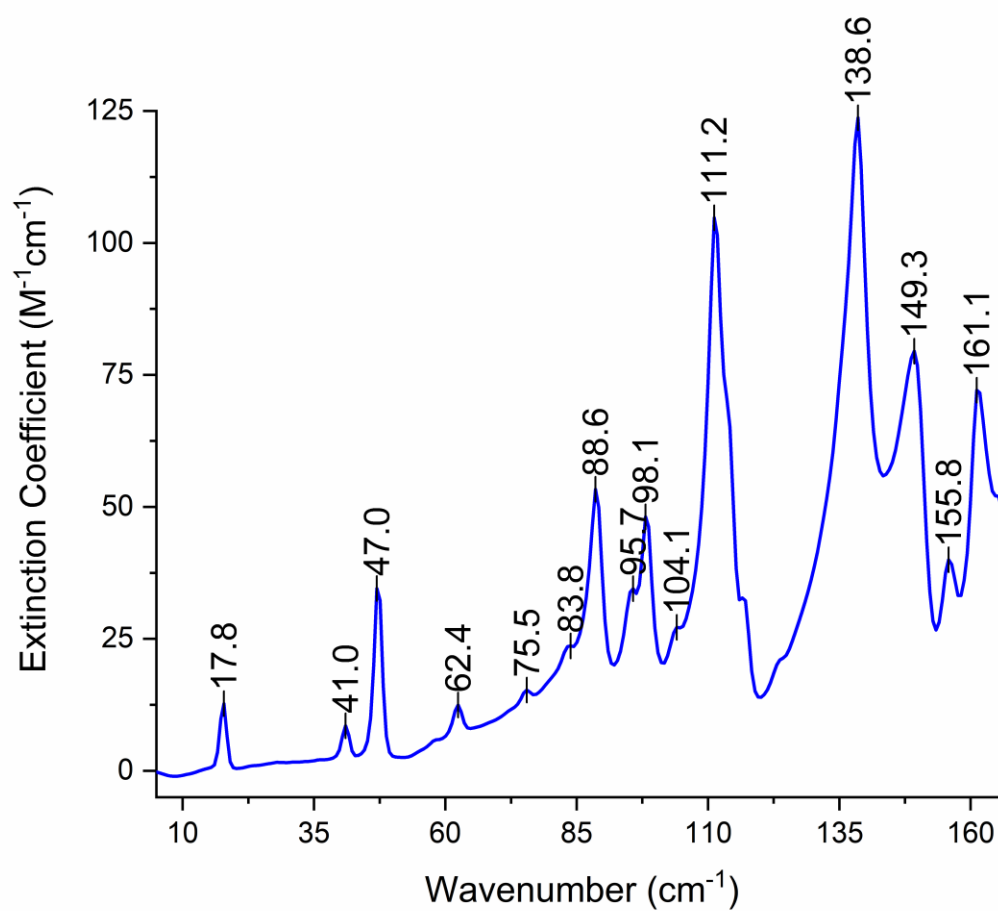
**Figure A-13.** Terahertz spectrum of crystalline α-lactose monohydrate (5 - 167 cm$^{-1}$) at 65 K with peak centers identified.
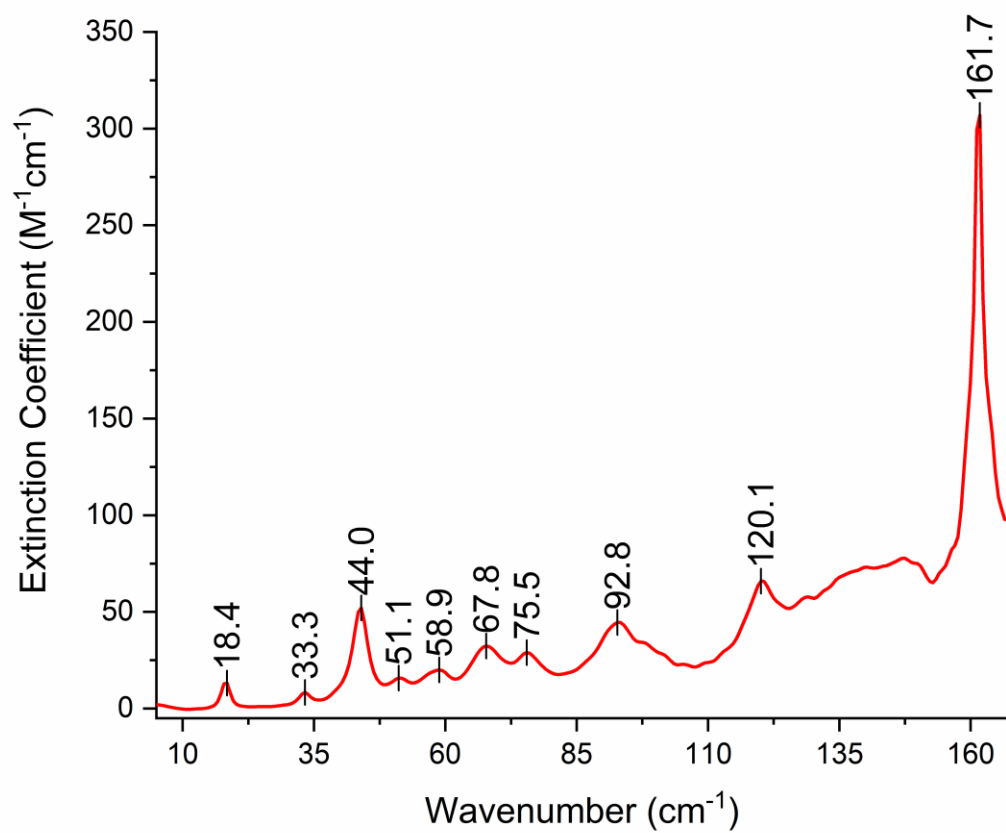
**Figure A-14.** Terahertz spectrum of crystalline biotin (5 - 167 cm$^{-1}$) at 293 K with peak centers identified.
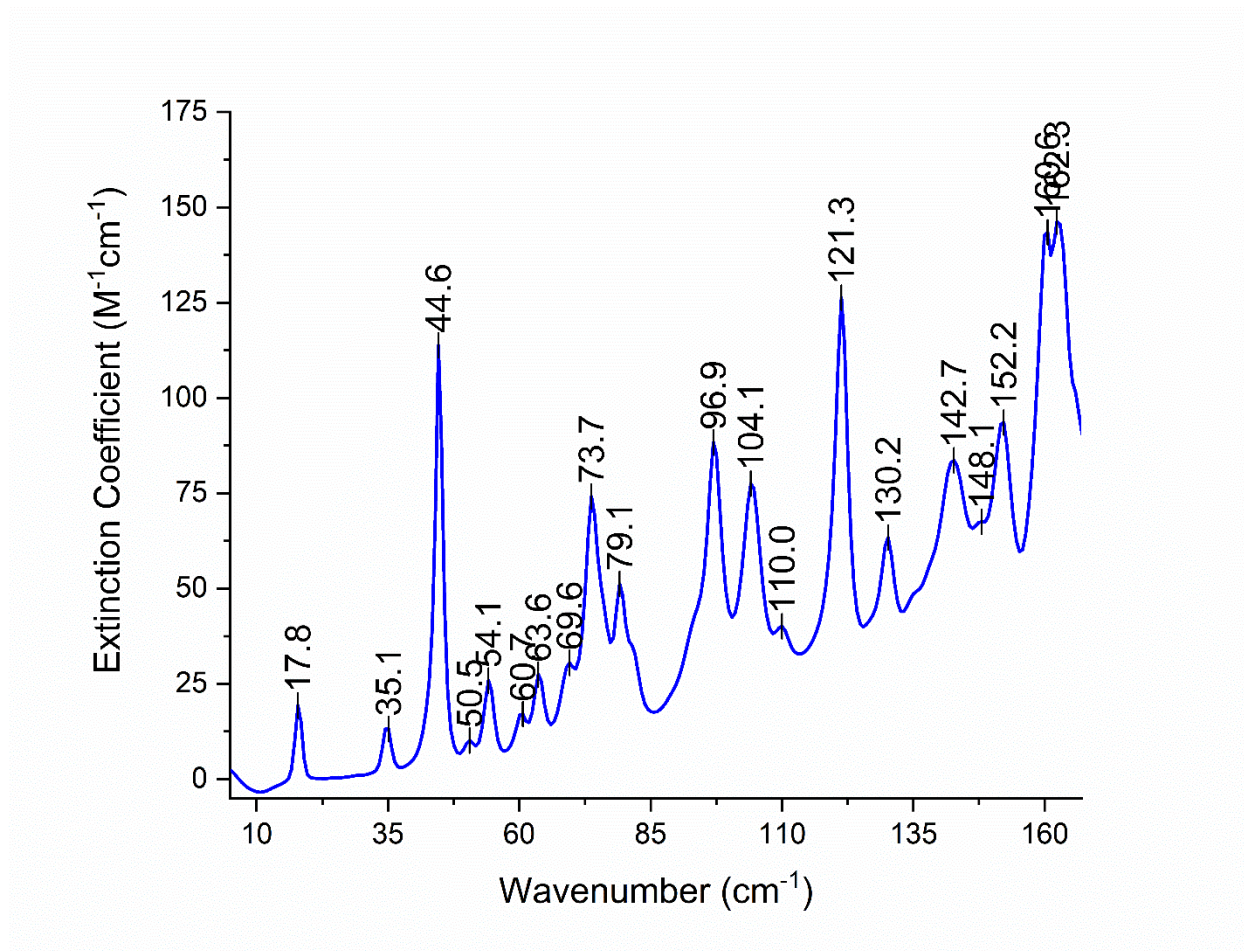
**Figure A-15.** Terahertz spectrum of crystalline biotin (5 - 167 cm⁻¹) at 65 K with peak centers identified.
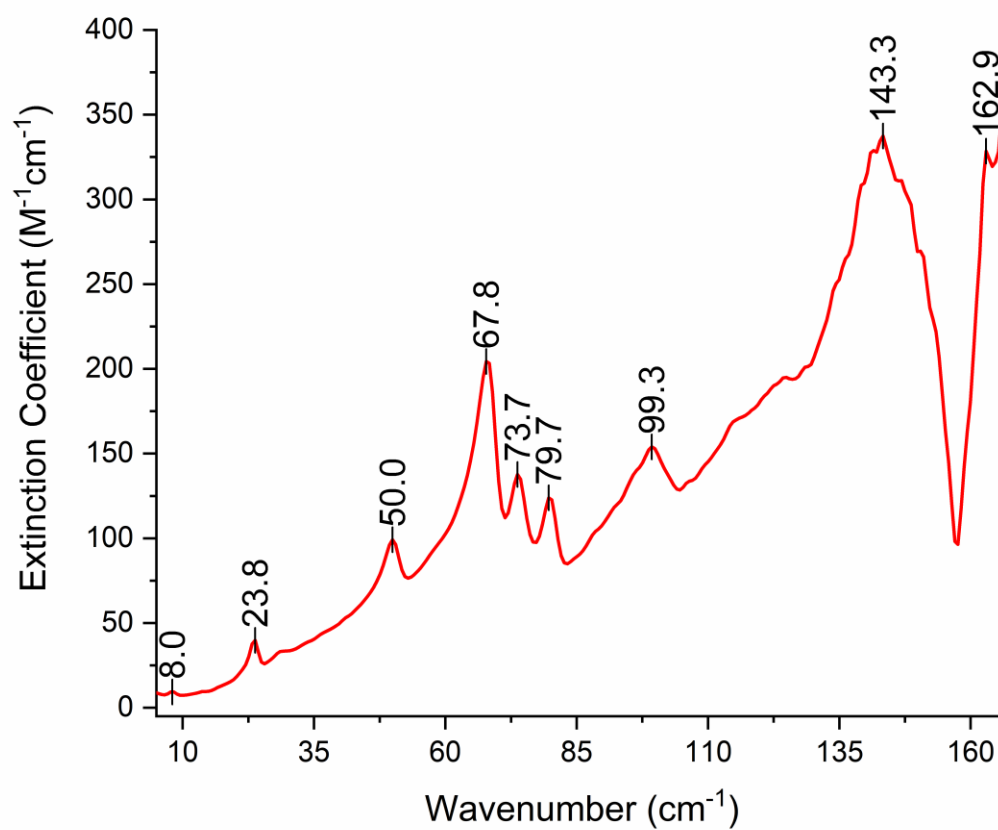
**Figure A-16.** Terahertz spectrum of crystalline L-cystine (5-167 cm$^{-1}$) at 293 K with peak centers identified.
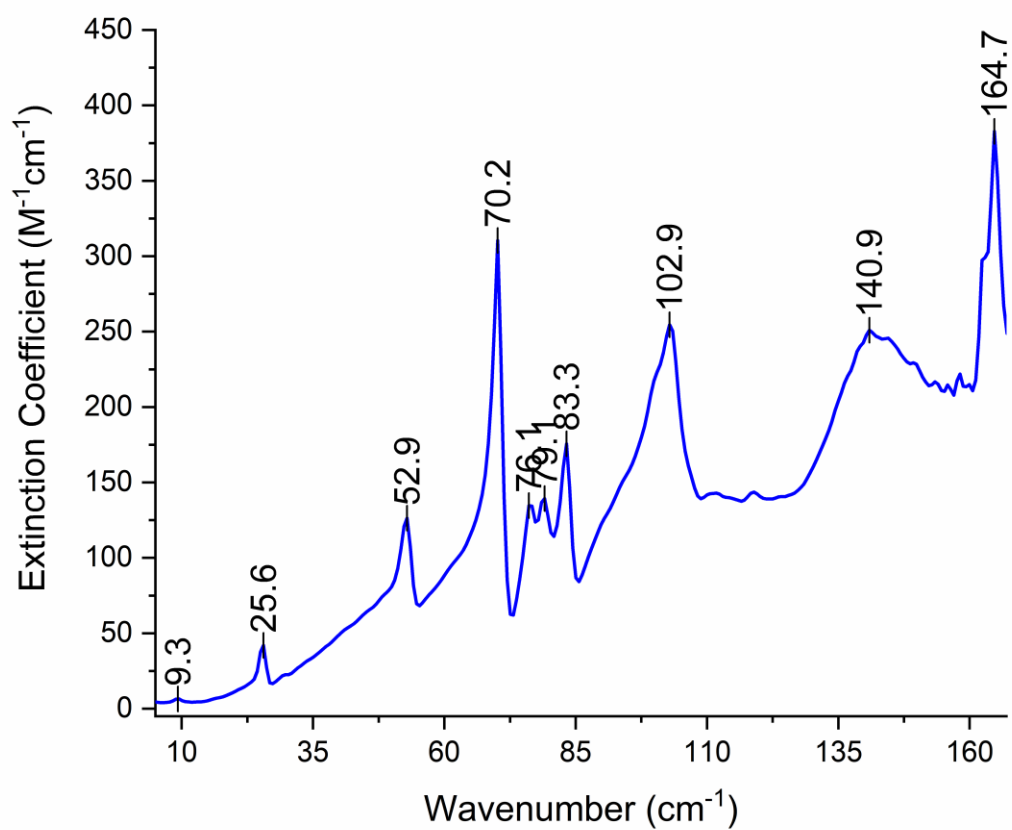
**Figure A-17.** Terahertz spectrum of crystalline L-cystine (5 - 167 cm^{-1}) at 50 K with peak identified.
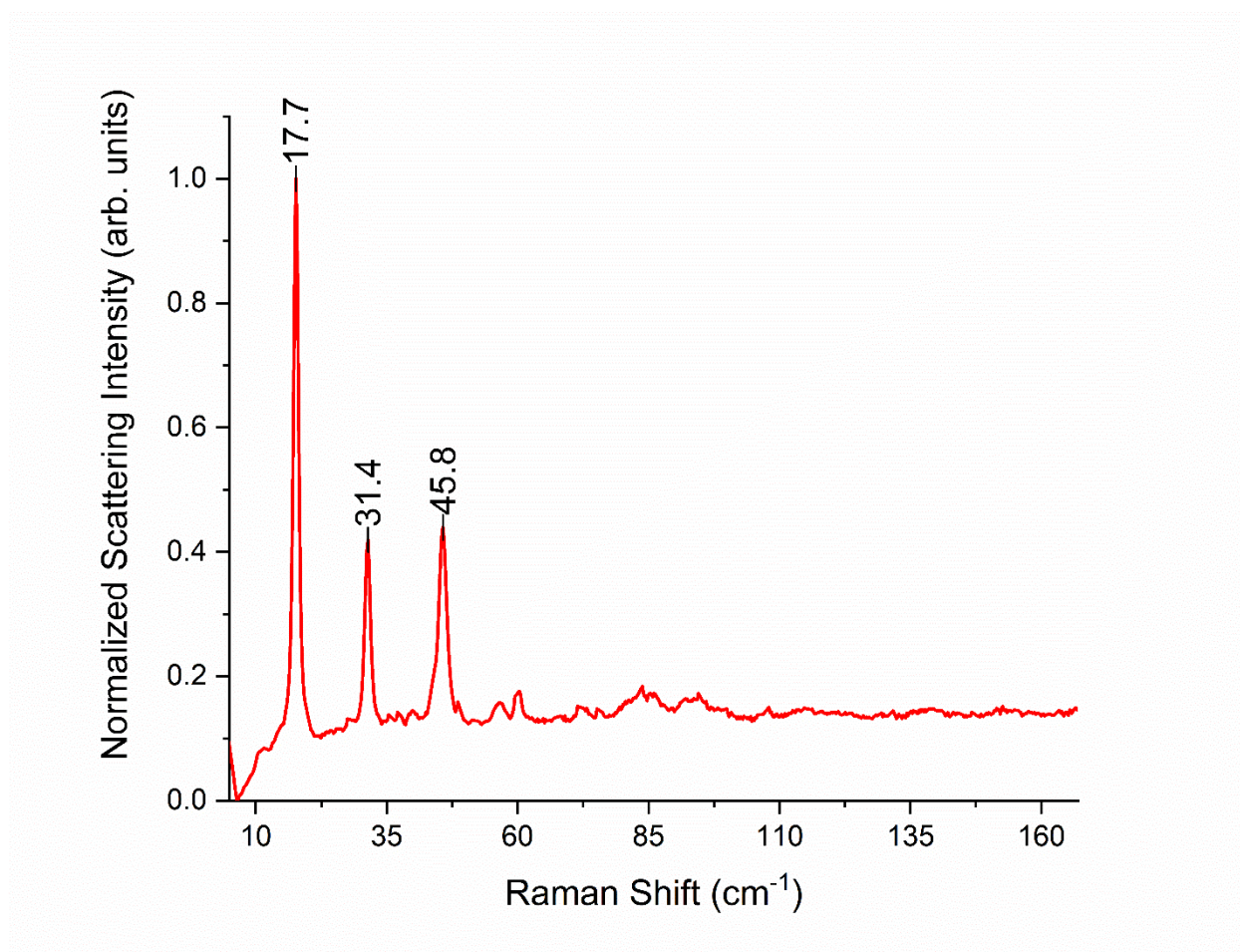
**Figure A-18.** Raman spectrum of crystalline α-lactose monohydrate (5 - 167 cm^{-1}) at 293 K with peak centers identified.
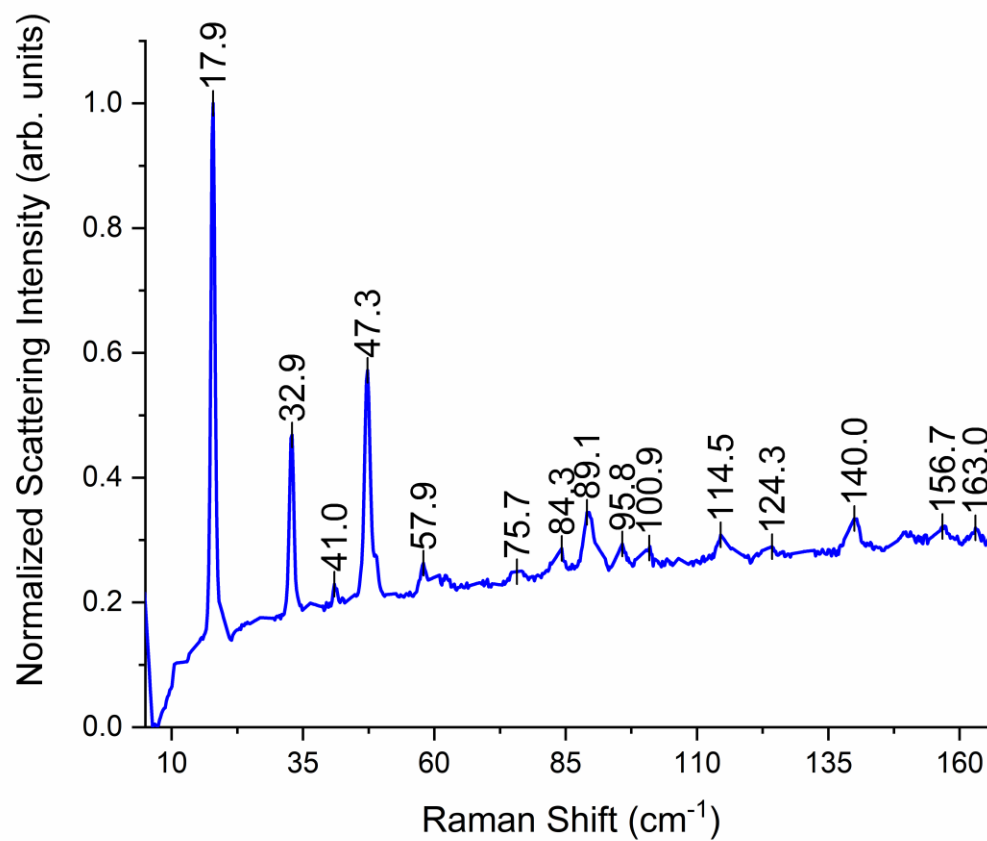
**Figure A-19.** Raman spectrum of crystalline α-lactose monohydrate (5 - 167 cm$^{-1}$) at 78 K with peak centers identified.
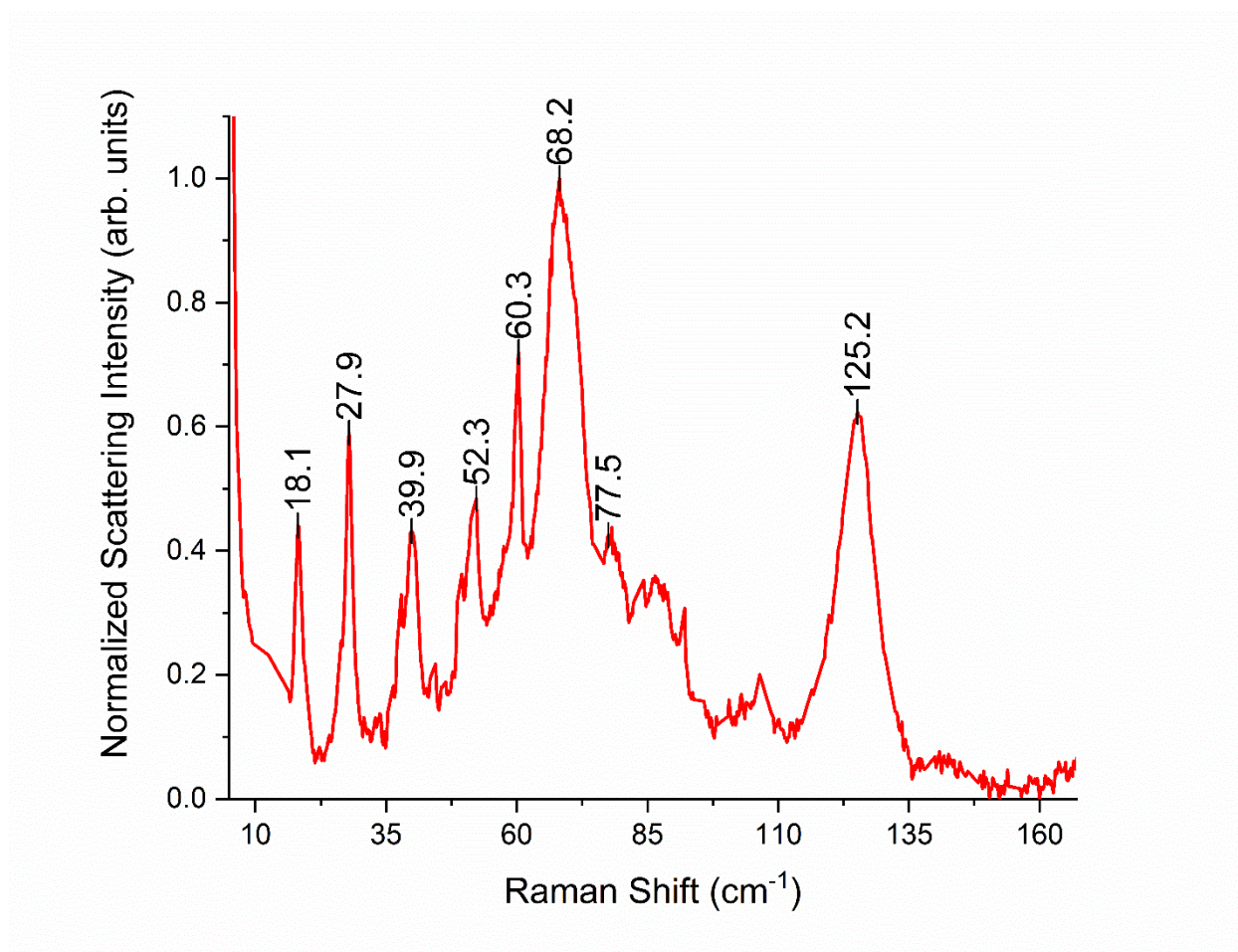
**Figure A-20.** Raman spectrum of crystalline biotin (5 - 167 cm$^{-1}$) at 293 K with peak centers identified.
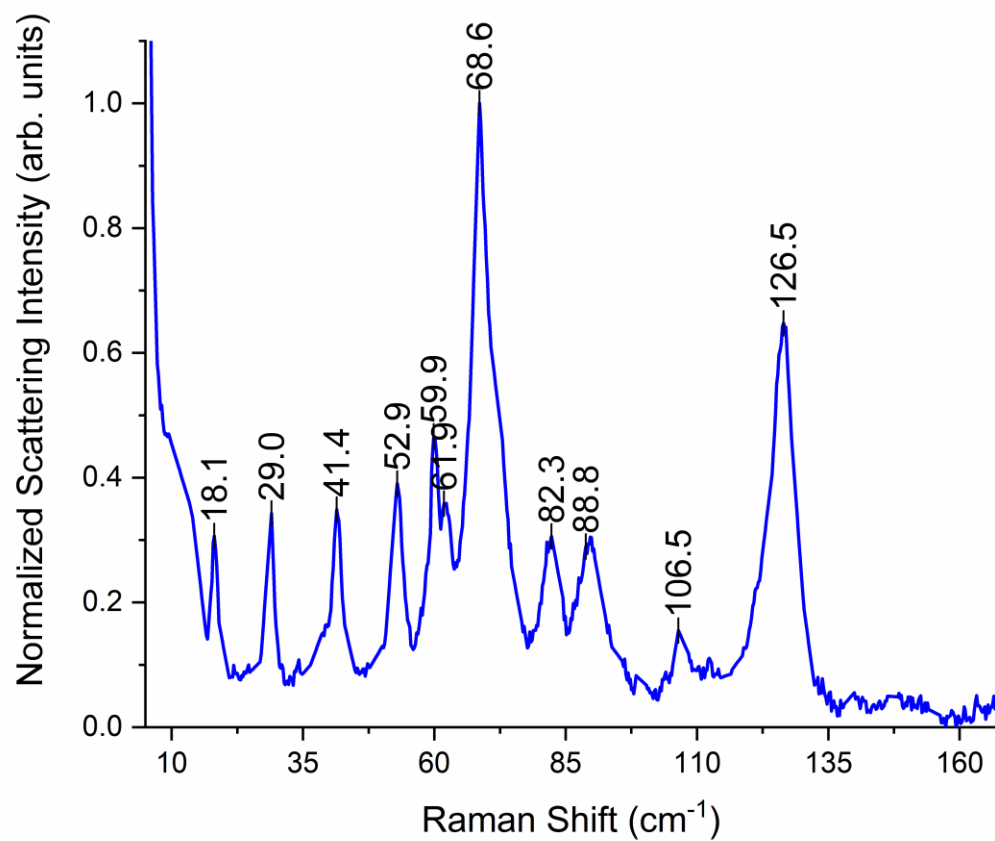
**Figure A-21.** Raman spectrum of crystalline biotin (5 - 167 cm$^{-1}$) at 78 K with peak centers identified.
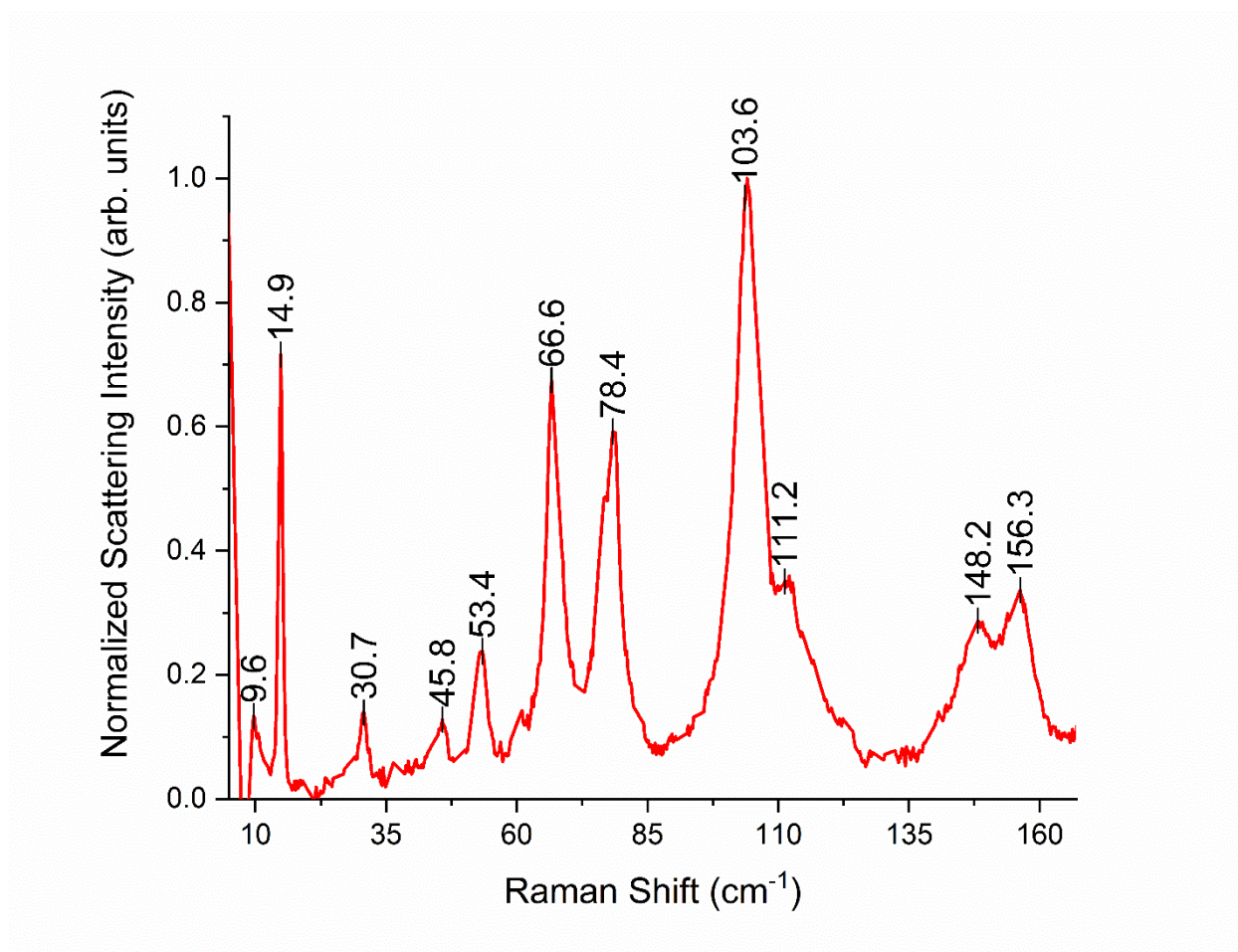
**Figure A-22.** Raman spectrum of crystalline L-cystine (5 - 167 cm$^{-1}$) at 293 K with peak centers identified.
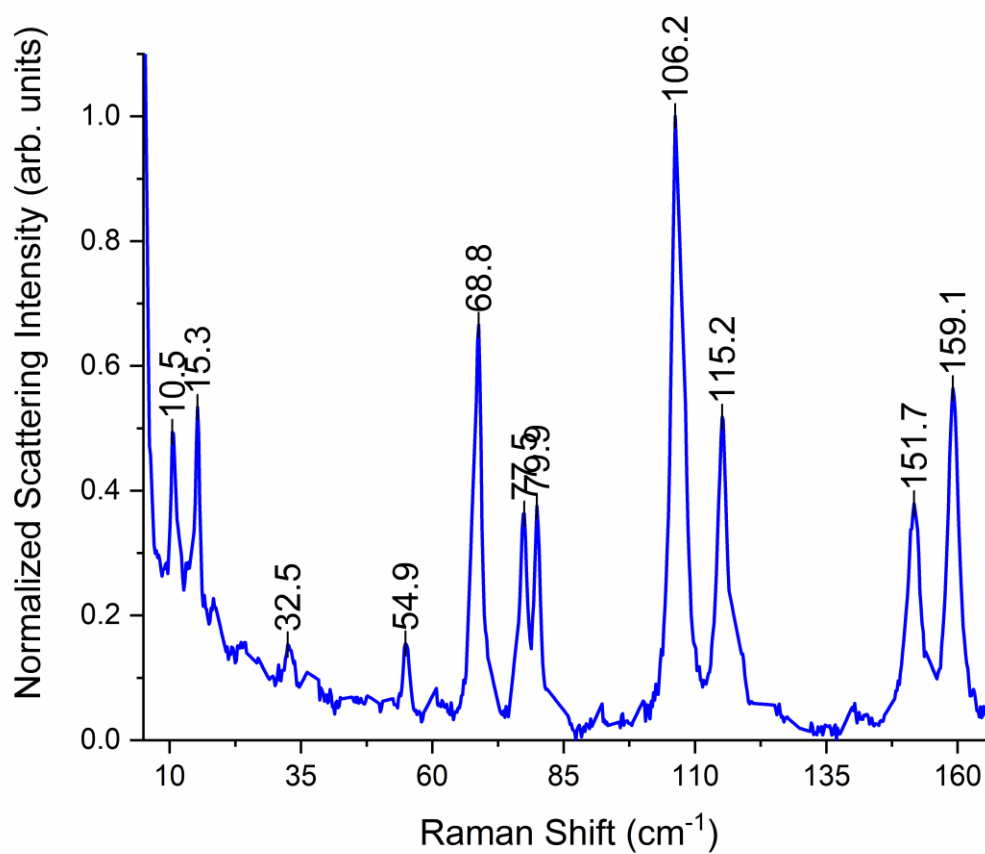
**Figure A-23.** Raman spectrum of crystalline L-cystine (5 - 167 cm$^{-1}$) at 78 K with peak centers identified.

**Table A-1.** Peak positions for the terahertz spectra of crystalline α-lactose monohydrate (5 - 167 cm$^{-1}$) at 293 K and 65 K.

| 293 K | | 65 K | |
|---|---|---|---|
| Frequency | | Frequency | |
| cm$^{-1}$ | THz | cm$^{-1}$ | THz |
| 17.8 | 0.54 | 17.8 | 0.54 |
| 39.8 | 1.20 | 41.0 | 1.23 |
| 45.8 | 1.37 | 47.0 | 1.41 |
| 60.7 | 1.82 | 62.4 | 1.87 |
| 85.0 | 2.55 | 75.5 | 2.27 |
| 95.7 | 2.87 | 83.8 | 2.52 |
| 108.2 | 3.25 | 88.6 | 2.66 |
| 132.6 | 3.98 | 95.7 | 2.87 |
| 141.5 | 4.25 | 98.1 | 2.94 |
| 161.7 | 4.85 | 104.1 | 3.12 |
| 165.9 | 4.98 | 111.2 | 3.34 |
| | | 138.6 | 4.16 |
| | | 149.3 | 4.48 |
| | | 155.8 | 4.67 |
| | | 161.1 | 4.83 |

**Table A-2.** Peak positions for the terahertz spectra of crystalline biotin (5 - 167 cm$^{-1}$) at 293 K and 65 K.

| 293 K | | 65 K | |
| --- | --- | --- | --- |
| Frequency | | Frequency | |
| cm$^{-1}$ | THz | cm$^{-1}$ | THz |
| 18.4 | 0.55 | 17.8 | 0.54 |
| 33.3 | 1.00 | 35.1 | 1.05 |
| 44.0 | 1.32 | 44.6 | 1.34 |
| 51.1 | 1.53 | 50.5 | 1.52 |
| 58.9 | 1.77 | 54.1 | 1.62 |
| 67.8 | 2.03 | 60.7 | 1.82 |
| 75.5 | 2.27 | 63.6 | 1.91 |
| 92.8 | 2.78 | 69.6 | 2.09 |
| 120.1 | 3.60 | 73.7 | 2.21 |
| 161.7 | 4.85 | 79.1 | 2.37 |
| | | 96.9 | 2.91 |
| | | 104.1 | 3.12 |
| | | 110.0 | 3.30 |
| | | 121.3 | 3.64 |
| | | 130.2 | 3.91 |
| | | 142.7 | 4.28 |
| | | 148.1 | 4.44 |
| | | 152.2 | 4.57 |
| | | 160.6 | 4.82 |
| | | 162.3 | 4.87 |

**Table A-3.** Peak positions for the terahertz spectra of crystalline L-cystine (5 - 167 cm$^{-1}$) at 293 K and 50 K.

| 293 K | | 50 K | |
|---|---|---|---|
| Frequency | | Frequency | |
| cm$^{-1}$ | THz | cm$^{-1}$ | THz |
| 8.0 | 0.24 | 9.3 | 0.28 |
| 23.8 | 0.71 | 25.6 | 0.77 |
| 50.0 | 1.50 | 52.9 | 1.59 |
| 67.8 | 2.03 | 70.2 | 2.11 |
| 73.7 | 2.21 | 76.1 | 2.28 |
| 79.7 | 2.39 | 79.1 | 2.37 |
| 99.3 | 2.98 | 83.3 | 2.50 |
| 143.3 | 4.30 | 102.9 | 3.09 |
| 162.9 | 4.89 | 140.9 | 4.23 |
| | | 164.7 | 4.94 |

**Table A-4.** Peak positions for the Raman spectra of crystalline α-lactose monohydrate (5 - 167 cm$^{-1}$) at 293 K and 78 K.

| 293 K | | 78 K | |
|---|---|---|---|
| Frequency | | Frequency | |
| cm$^{-1}$ | THz | cm$^{-1}$ | THz |
| 17.7 | 0.53 | 17.9 | 0.54 |
| 31.4 | 0.94 | 32.9 | 0.99 |
| 45.8 | 1.37 | 41.0 | 1.23 |
| | | 47.3 | 1.42 |
| | | 57.9 | 1.74 |
| | | 75.7 | 2.27 |
| | | 84.3 | 2.53 |
| | | 89.1 | 2.67 |
| | | 95.8 | 2.87 |
| | | 100.9 | 3.03 |
| | | 114.5 | 3.44 |
| | | 124.3 | 3.73 |
| | | 140.0 | 4.20 |
| | | 156.7 | 4.70 |
| | | 163.0 | 4.89 |

**Table A-5.** Peak positions for the Raman spectra of crystalline biotin (5 - 167 cm$^{-1}$) at 293 K and 78 K.

| 293 K | | 78 K | |
| --- | --- | --- | --- |
| Frequency | | Frequency | |
| cm$^{-1}$ | THz | cm$^{-1}$ | THz |
| 18.1 | 0.54 | 18.1 | 0.54 |
| 27.9 | 0.84 | 29.0 | 0.87 |
| 39.9 | 1.20 | 41.4 | 1.24 |
| 52.3 | 1.57 | 52.9 | 1.59 |
| 60.3 | 1.81 | 59.9 | 1.80 |
| 68.2 | 2.05 | 61.9 | 1.86 |
| 77.5 | 2.33 | 68.6 | 2.06 |
| 125.2 | 3.76 | 82.3 | 2.47 |
| | | 88.8 | 2.67 |
| | | 106.5 | 3.19 |
| | | 126.5 | 3.79 |

**Table A-6.** Peak positions for the Raman spectra of crystalline L-cystine (5 - 167 cm$^{-1}$) at 293 K and 78 K.

| 293 K | | 78 K | |
| --- | --- | --- | --- |
| Frequency | | Frequency | |
| cm$^{-1}$ | THz | cm$^{-1}$ | THz |
| 9.6 | 0.29 | 10.5 | 0.49 |
| 14.9 | 0.45 | 15.3 | 0.53 |
| 30.7 | 0.92 | 32.5 | 0.15 |
| 45.8 | 1.37 | 54.9 | 0.16 |
| 53.4 | 1.60 | 68.8 | 0.67 |
| 66.6 | 2.00 | 77.5 | 0.36 |
| 78.4 | 2.35 | 79.9 | 0.38 |
| 103.6 | 3.11 | 106.2 | 1.00 |
| 111.2 | 3.34 | 115.2 | 0.52 |
| 148.2 | 4.45 | 151.7 | 0.38 |
| 156.3 | 4.69 | 159.1 | 0.56 |

**Table A-7.** Mode labels, vibrational frequencies, symmetry representations, and IR/Raman intensities for crystalline α-lactose monohydrate simulated using ss-DFT.

| Frequency | | Symmetry representation | Intensity | |
|---|---|---|---|---|
| cm$^{-1}$ | THz | | IR (km/mol) | Raman (arb. Units) |
| 19.4441 | 0.5829 | A | 0.81 | 106.79 |
| 34.8735 | 1.0455 | A | 0.01 | 25.97 |
| 35.5762 | 1.0665 | A | 0.16 | 8.66 |
| 43.1646 | 1.2940 | A | 0.32 | 4.88 |
| 49.6656 | 1.4889 | B | 4.13 | 34.04 |
| 60.7892 | 1.8224 | B | 0.07 | 7.31 |
| 64.1179 | 1.9222 | B | 1.05 | 6.24 |
| 80.8105 | 2.4226 | B | 0.86 | 3.70 |
| 87.5963 | 2.6261 | A | 0.78 | 14.28 |
| 92.6547 | 2.7777 | B | 2.10 | 15.85 |
| 94.1053 | 2.8212 | A | 2.65 | 22.60 |
| 101.5874 | 3.0455 | A | 3.01 | 4.77 |
| 102.4690 | 3.0719 | B | 2.99 | 3.73 |
| 107.8672 | 3.2338 | A | 0.92 | 5.28 |
| 112.4351 | 3.3707 | B | 10.94 | 0.57 |
| 115.1928 | 3.4534 | B | 14.19 | 4.25 |
| 117.2567 | 3.5153 | A | 2.66 | 20.68 |
| 118.4583 | 3.5513 | B | 1.02 | 3.89 |
| 126.2434 | 3.7847 | A | 0.61 | 3.31 |
| 140.1306 | 4.2010 | A | 0.01 | 13.53 |
| 142.6420 | 4.2763 | B | 21.41 | 3.85 |
| 150.5342 | 4.5129 | B | 3.87 | 0.38 |
| 152.7000 | 4.5778 | A | 17.70 | 11.25 |
| 158.5223 | 4.7524 | B | 14.03 | 13.07 |
| 164.3266 | 4.9264 | A | 5.24 | 1.05 |
| 170.0589 | 5.0982 | B | 1.61 | 14.74 |
| 172.2988 | 5.1654 | A | 6.36 | 33.12 |
| 179.3188 | 5.3758 | A | 3.10 | 16.65 |
| 179.5974 | 5.3842 | B | 1.78 | 5.84 |
| 183.8152 | 5.5106 | B | 39.29 | 0.62 |
| 191.1686 | 5.7311 | A | 1.16 | 7.49 |
| 200.1152 | 5.9993 | A | 1.24 | 42.43 |
| 201.0012 | 6.0259 | B | 37.43 | 17.11 |
| 210.6668 | 6.3156 | A | 11.61 | 11.48 |

| 214.9028 | 6.4426 | B | 21.00 | 5.64 |
|---|---|---|---|---|
| 227.7719 | 6.8284 | A | 2.88 | 3.75 |
| 228.0992 | 6.8382 | B | 15.89 | 4.37 |
| 237.2297 | 7.1120 | B | 6.36 | 5.47 |
| 243.0562 | 7.2866 | A | 0.78 | 9.33 |
| 257.6971 | 7.7256 | A | 0.99 | 25.89 |
| 259.7883 | 7.7883 | B | 17.12 | 5.20 |
| 273.2411 | 8.1916 | A | 1.95 | 14.12 |
| 275.3660 | 8.2553 | B | 90.26 | 2.46 |
| 286.9244 | 8.6018 | A | 25.97 | 13.32 |
| 291.9811 | 8.7534 | B | 2.20 | 10.44 |
| 297.8525 | 8.9294 | B | 33.81 | 3.27 |
| 299.9148 | 8.9912 | A | 30.45 | 25.25 |
| 309.1152 | 9.2670 | A | 31.73 | 8.21 |
| 315.4260 | 9.4562 | B | 52.96 | 0.56 |
| 334.5622 | 10.0299 | B | 16.29 | 10.53 |
| 340.6773 | 10.2132 | A | 3.40 | 27.73 |
| 344.1153 | 10.3163 | A | 6.64 | 33.04 |
| 348.4563 | 10.4465 | B | 28.03 | 8.21 |
| 355.2854 | 10.6512 | B | 10.84 | 19.81 |
| 357.1259 | 10.7064 | A | 36.67 | 71.18 |
| 358.0685 | 10.7346 | B | 14.02 | 8.88 |
| 360.7826 | 10.8160 | A | 25.58 | 41.40 |
| 367.0522 | 11.0039 | A | 55.20 | 83.06 |
| 371.4453 | 11.1357 | B | 62.75 | 8.56 |
| 373.8607 | 11.2081 | A | 0.85 | 121.48 |
| 375.8441 | 11.2675 | B | 35.27 | 15.21 |
| 388.1120 | 11.6353 | A | 1.67 | 19.64 |
| 391.0300 | 11.7228 | B | 62.73 | 37.17 |
| 399.0647 | 11.9637 | B | 42.33 | 47.22 |
| 400.7387 | 12.0138 | A | 24.45 | 28.83 |
| 419.3822 | 12.5728 | A | 0.27 | 7.02 |
| 420.1215 | 12.5949 | B | 2.90 | 6.45 |
| 430.5871 | 12.9087 | A | 11.72 | 17.20 |
| 431.1529 | 12.9256 | B | 22.69 | 1.08 |
| 443.3351 | 13.2909 | A | 4.74 | 20.66 |
| 443.8015 | 13.3048 | B | 29.76 | 4.16 |
| 460.1456 | 13.7948 | B | 9.80 | 6.89 |
| 461.9711 | 13.8495 | A | 3.12 | 66.69 |

| 469.7557 | 14.0829 | A | 5.20 | 152.67 |
|---|---|---|---|---|
| 472.1449 | 14.1545 | B | 8.05 | 4.66 |
| 539.6154 | 16.1773 | A | 3.34 | 30.98 |
| 541.8867 | 16.2454 | B | 106.86 | 13.25 |
| 545.8484 | 16.3641 | B | 6.00 | 40.25 |
| 551.7954 | 16.5424 | A | 65.20 | 20.96 |
| 558.6350 | 16.7475 | A | 7.29 | 12.16 |
| 561.5514 | 16.8349 | B | 37.99 | 6.28 |
| 576.4245 | 17.2808 | B | 26.39 | 5.09 |
| 577.8753 | 17.3243 | A | 0.02 | 3.44 |
| 601.0290 | 18.0184 | A | 0.79 | 6.42 |
| 601.7426 | 18.0398 | B | 21.89 | 4.37 |
| 609.0490 | 18.2588 | A | 4.54 | 21.41 |
| 611.6455 | 18.3367 | B | 53.32 | 3.25 |
| 618.6554 | 18.5468 | B | 95.64 | 4.48 |
| 619.6290 | 18.5760 | A | 2.37 | 19.14 |
| 637.5277 | 19.1126 | A | 9.92 | 10.81 |
| 638.5385 | 19.1429 | B | 34.72 | 3.61 |
| 681.8498 | 20.4413 | A | 1.59 | 13.69 |
| 682.2162 | 20.4523 | B | 512.37 | 13.79 |
| 692.3471 | 20.7560 | B | 115.06 | 1.14 |
| 694.2113 | 20.8119 | A | 2.86 | 47.04 |
| 709.6091 | 21.2735 | A | 24.67 | 9.84 |
| 712.8294 | 21.3701 | B | 264.04 | 4.90 |
| 719.6056 | 21.5732 | A | 39.70 | 19.07 |
| 720.1558 | 21.5897 | B | 45.18 | 15.10 |
| 757.8993 | 22.7212 | B | 213.41 | 4.50 |
| 759.6572 | 22.7739 | A | 25.09 | 20.96 |
| 770.4615 | 23.0979 | A | 35.98 | 5.20 |
| 771.2325 | 23.1210 | B | 105.84 | 5.44 |
| 788.0961 | 23.6265 | A | 485.86 | 36.14 |
| 794.0150 | 23.8040 | B | 2.95 | 5.24 |
| 831.5554 | 24.9294 | B | 4.50 | 8.89 |
| 832.1808 | 24.9482 | A | 10.19 | 62.33 |
| 843.1963 | 25.2784 | A | 176.16 | 16.42 |
| 846.2777 | 25.3708 | B | 44.41 | 0.42 |
| 853.0602 | 25.5741 | A | 109.65 | 87.18 |
| 854.1711 | 25.6074 | B | 16.36 | 2.10 |
| 862.0903 | 25.8448 | A | 126.84 | 53.15 |

| 864.0953 | 25.9049 | B | 237.40 | 18.56 |
|---|---|---|---|---|
| 881.7063 | 26.4329 | A | 98.28 | 11.36 |
| 883.7853 | 26.4952 | B | 69.15 | 8.84 |
| 885.6784 | 26.5520 | A | 225.86 | 18.51 |
| 885.8991 | 26.5586 | B | 50.56 | 16.10 |
| 894.7647 | 26.8244 | A | 14.68 | 37.45 |
| 898.4923 | 26.9361 | B | 85.50 | 14.72 |
| 909.6905 | 27.2718 | B | 62.00 | 0.66 |
| 910.3801 | 27.2925 | A | 64.77 | 33.43 |
| 934.2160 | 28.0071 | B | 118.75 | 19.98 |
| 934.6129 | 28.0190 | A | 4.58 | 8.92 |
| 941.1859 | 28.2160 | A | 4.46 | 37.02 |
| 941.5166 | 28.2260 | B | 9.00 | 10.86 |
| 973.3031 | 29.1789 | A | 137.93 | 12.98 |
| 975.3721 | 29.2409 | B | 43.28 | 5.07 |
| 986.9102 | 29.5868 | B | 58.15 | 6.02 |
| 988.3607 | 29.6303 | A | 3.64 | 13.67 |
| 994.3804 | 29.8108 | A | 525.75 | 30.82 |
| 1000.1998 | 29.9852 | B | 1186.88 | 6.76 |
| 1004.9903 | 30.1289 | A | 56.59 | 10.54 |
| 1005.9292 | 30.1570 | B | 390.85 | 0.36 |
| 1012.3187 | 30.3486 | A | 124.26 | 26.00 |
| 1014.4728 | 30.4131 | B | 46.40 | 12.39 |
| 1029.1091 | 30.8519 | A | 13.61 | 4.39 |
| 1029.6897 | 30.8693 | B | 34.96 | 24.14 |
| 1036.8541 | 31.0841 | A | 26.11 | 77.06 |
| 1038.0887 | 31.1211 | B | 28.29 | 6.59 |
| 1041.5740 | 31.2256 | A | 203.46 | 9.03 |
| 1043.2488 | 31.2758 | B | 13.29 | 0.57 |
| 1050.5460 | 31.4946 | A | 200.45 | 55.11 |
| 1052.1103 | 31.5415 | B | 429.27 | 21.95 |
| 1059.5078 | 31.7632 | A | 181.85 | 12.50 |
| 1060.5207 | 31.7936 | B | 31.12 | 4.23 |
| 1067.6356 | 32.0069 | A | 69.00 | 137.34 |
| 1068.6061 | 32.0360 | B | 0.66 | 22.24 |
| 1069.9713 | 32.0769 | A | 142.80 | 95.76 |
| 1072.8926 | 32.1645 | B | 92.51 | 11.24 |
| 1078.4127 | 32.3300 | A | 45.71 | 17.49 |
| 1080.2348 | 32.3846 | B | 126.05 | 14.70 |

| | | | | |
|---|---|---|---|---|
| 1084.7212 | 32.5191 | A | 0.88 | 6.97 |
| 1085.0819 | 32.5299 | B | 178.52 | 8.03 |
| 1097.5814 | 32.9047 | B | 15.56 | 26.18 |
| 1097.7132 | 32.9086 | A | 120.48 | 47.35 |
| 1100.7558 | 32.9998 | A | 262.44 | 16.42 |
| 1106.3686 | 33.1681 | B | 101.13 | 3.77 |
| 1112.5753 | 33.3542 | A | 5.77 | 18.71 |
| 1113.3397 | 33.3771 | B | 3.33 | 0.75 |
| 1114.4801 | 33.4113 | A | 13.59 | 36.89 |
| 1114.9005 | 33.4239 | B | 48.04 | 3.21 |
| 1122.5370 | 33.6528 | B | 554.44 | 10.70 |
| 1122.6740 | 33.6569 | A | 14.78 | 12.17 |
| 1122.9718 | 33.6658 | A | 0.01 | 65.23 |
| 1123.6037 | 33.6848 | B | 51.70 | 0.29 |
| 1146.8462 | 34.3816 | A | 196.70 | 12.36 |
| 1149.5487 | 34.4626 | B | 72.09 | 4.63 |
| 1187.8966 | 35.6122 | B | 92.51 | 1.25 |
| 1187.9553 | 35.6140 | A | 0.26 | 2.67 |
| 1202.7821 | 36.0585 | B | 30.41 | 8.31 |
| 1203.1561 | 36.0697 | A | 0.19 | 3.64 |
| 1205.8563 | 36.1507 | A | 1.37 | 17.57 |
| 1206.2326 | 36.1619 | B | 2.97 | 6.02 |
| 1227.8339 | 36.8095 | B | 15.91 | 12.51 |
| 1227.8505 | 36.8100 | A | 0.26 | 7.89 |
| 1240.7944 | 37.1981 | A | 5.13 | 73.48 |
| 1241.0836 | 37.2067 | B | 7.56 | 21.90 |
| 1248.2975 | 37.4230 | A | 12.01 | 15.77 |
| 1248.7492 | 37.4366 | B | 68.04 | 7.60 |
| 1251.0552 | 37.5057 | A | 17.27 | 20.27 |
| 1253.7751 | 37.5872 | B | 39.87 | 41.05 |
| 1259.0711 | 37.7460 | B | 25.23 | 5.86 |
| 1262.8729 | 37.8600 | A | 6.02 | 94.95 |
| 1268.4370 | 38.0268 | A | 0.00 | 0.90 |
| 1269.3671 | 38.0547 | B | 6.86 | 49.73 |
| 1272.3161 | 38.1431 | A | 46.59 | 26.82 |
| 1273.2911 | 38.1723 | B | 8.30 | 23.23 |
| 1278.6228 | 38.3321 | B | 11.46 | 4.57 |
| 1278.8757 | 38.3397 | A | 0.60 | 8.97 |
| 1297.1197 | 38.8867 | B | 10.36 | 30.32 |

| 1297.3193 | 38.8927 | A | 16.91 | 45.27 |
|-----------|---------|---|--------|-------|
| 1307.3677 | 39.1939 | A | 0.43 | 56.92 |
| 1309.0739 | 39.2450 | B | 21.01 | 4.37 |
| 1314.6867 | 39.4133 | B | 30.39 | 24.24 |
| 1315.6560 | 39.4424 | A | 2.68 | 26.17 |
| 1317.9474 | 39.5111 | B | 2.36 | 60.50 |
| 1318.8380 | 39.5378 | A | 0.00 | 37.02 |
| 1321.0939 | 39.6054 | A | 0.57 | 5.32 |
| 1321.1194 | 39.6062 | B | 17.01 | 24.48 |
| 1322.5067 | 39.6478 | A | 118.26 | 16.07 |
| 1323.3716 | 39.6737 | B | 94.66 | 25.88 |
| 1329.0895 | 39.8451 | A | 9.04 | 34.93 |
| 1329.7711 | 39.8655 | B | 12.04 | 24.65 |
| 1333.3238 | 39.9720 | A | 11.47 | 38.70 |
| 1334.9012 | 40.0193 | B | 79.31 | 0.60 |
| 1341.2347 | 40.2092 | A | 24.24 | 2.42 |
| 1341.4116 | 40.2145 | B | 21.58 | 3.39 |
| 1349.2563 | 40.4497 | B | 17.73 | 4.08 |
| 1350.9813 | 40.5014 | A | 2.55 | 4.51 |
| 1361.8221 | 40.8264 | A | 40.38 | 47.82 |
| 1362.4716 | 40.8459 | B | 4.11 | 4.35 |
| 1364.6257 | 40.9104 | A | 18.20 | 12.13 |
| 1365.1163 | 40.9252 | B | 86.25 | 1.82 |
| 1375.9122 | 41.2488 | A | 0.01 | 17.85 |
| 1376.4677 | 41.2655 | B | 60.44 | 6.81 |
| 1383.1981 | 41.4672 | A | 12.49 | 36.31 |
| 1383.3527 | 41.4719 | B | 4.45 | 6.39 |
| 1406.6466 | 42.1702 | B | 124.91 | 17.60 |
| 1406.9035 | 42.1779 | A | 10.29 | 22.54 |
| 1411.6922 | 42.3215 | A | 38.27 | 7.59 |
| 1411.7538 | 42.3233 | B | 110.90 | 0.25 |
| 1429.4538 | 42.8539 | B | 112.58 | 3.61 |
| 1429.8503 | 42.8658 | A | 12.70 | 5.65 |
| 1431.8829 | 42.9268 | A | 61.76 | 2.09 |
| 1432.3730 | 42.9415 | B | 90.50 | 19.39 |
| 1434.0245 | 42.9910 | B | 75.32 | 3.21 |
| 1434.5163 | 43.0057 | A | 8.85 | 7.01 |
| 1434.9946 | 43.0201 | A | 0.71 | 25.38 |
| 1436.9937 | 43.0800 | B | 6.06 | 16.08 |

| 1449.2135 | 43.4463 | B | 15.23 | 19.67 |
|---|---|---|---|---|
| 1449.2700 | 43.4480 | A | 4.84 | 32.42 |
| 1468.4165 | 44.0220 | B | 176.56 | 0.84 |
| 1469.8314 | 44.0644 | A | 0.55 | 8.34 |
| 1471.0217 | 44.1001 | A | 0.68 | 7.17 |
| 1472.0009 | 44.1295 | B | 224.42 | 9.53 |
| 1631.3892 | 48.9078 | A | 7.27 | 9.13 |
| 1631.4376 | 48.9093 | B | 327.54 | 0.68 |
| 2880.2624 | 86.3481 | B | 74.54 | 27.43 |
| 2880.2968 | 86.3491 | A | 3.09 | 189.87 |
| 2926.5897 | 87.7370 | B | 28.26 | 15.11 |
| 2926.6588 | 87.7390 | A | 0.05 | 110.17 |
| 2932.8391 | 87.9243 | B | 41.25 | 24.17 |
| 2934.3172 | 87.9686 | A | 0.03 | 1000.00 |
| 2938.4467 | 88.0924 | A | 15.24 | 106.34 |
| 2938.8347 | 88.1040 | B | 3.86 | 1.06 |
| 2956.3480 | 88.6291 | A | 21.59 | 7.40 |
| 2956.3614 | 88.6295 | B | 126.57 | 0.24 |
| 2957.8356 | 88.6737 | B | 5.50 | 50.63 |
| 2958.1510 | 88.6831 | A | 0.12 | 327.20 |
| 2959.9478 | 88.7370 | A | 111.72 | 230.57 |
| 2960.4208 | 88.7512 | B | 341.70 | 61.86 |
| 2961.9569 | 88.7972 | A | 29.62 | 383.14 |
| 2962.0450 | 88.7999 | B | 24.22 | 18.02 |
| 2968.5273 | 88.9942 | B | 37.69 | 59.83 |
| 2969.1975 | 89.0143 | A | 13.86 | 907.30 |
| 2978.7592 | 89.3010 | B | 139.61 | 0.62 |
| 2978.9044 | 89.3053 | A | 88.34 | 152.47 |
| 2984.8850 | 89.4846 | A | 45.92 | 477.48 |
| 2984.9996 | 89.4880 | B | 4144.90 | 0.14 |
| 2997.6904 | 89.8685 | B | 977.12 | 15.94 |
| 2997.8958 | 89.8747 | A | 10.93 | 29.36 |
| 3007.0674 | 90.1496 | A | 1002.09 | 748.96 |
| 3010.7935 | 90.2613 | B | 2363.55 | 45.13 |
| 3030.7703 | 90.8602 | A | 359.26 | 59.46 |
| 3032.4142 | 90.9095 | B | 943.11 | 0.85 |
| 3044.8095 | 91.2811 | B | 11.03 | 33.53 |
| 3044.8859 | 91.2834 | A | 0.21 | 80.62 |
| 3051.5092 | 91.4819 | A | 8.83 | 496.00 |

| | | | | |
|---|---|---|---|---|
| 3051.5652 | 91.4836 | B | 4853.50 | 17.98 |
| 3060.8847 | 91.7630 | B | 22.96 | 3.79 |
| 3060.9676 | 91.7655 | A | 9.56 | 138.29 |
| 3190.2695 | 95.6419 | A | 2187.50 | 131.56 |
| 3197.9668 | 95.8726 | B | 1592.44 | 121.14 |
| 3223.4408 | 96.6363 | A | 4.79 | 176.07 |
| 3223.9619 | 96.6519 | B | 2698.16 | 16.57 |
| 3235.1512 | 96.9874 | A | 573.88 | 327.17 |
| 3236.2877 | 97.0215 | B | 4752.25 | 22.02 |
| 3276.9812 | 98.2414 | A | 66.38 | 62.40 |
| 3277.4969 | 98.2569 | B | 194.35 | 58.12 |
| 3327.1868 | 99.7466 | A | 4942.50 | 500.21 |
| 3349.2404 | 100.4077 | B | 259.40 | 18.46 |
| 3351.6690 | 100.4805 | B | 30.78 | 0.63 |
| 3351.7002 | 100.4814 | A | 10.84 | 4.99 |
| 3527.8630 | 105.7627 | A | 630.21 | 120.49 |
| 3530.6500 | 105.8462 | B | 561.64 | 46.37 |

**Table A-8.** Mode labels, vibrational frequencies, symmetry representations, and IR/Raman intensities for crystalline biotin simulated using ss-DFT.

| Frequency | | Symmetry representation | Intensity | |
|---|---|---|---|---|
| cm⁻¹ | THz | | IR (km/mol) | Raman (arb. Units) |
| 18.1304 | 0.5435 | B1 | 2.52 | 6.68 |
| 29.4060 | 0.8816 | A | inactive | 21.45 |
| 34.3676 | 1.0303 | B1 | 2.51 | 5.47 |
| 39.0644 | 1.1711 | A | inactive | 30.32 |
| 41.5293 | 1.2450 | B3 | 0.75 | 2.45 |
| 41.5824 | 1.2466 | A | inactive | 31.45 |
| 43.0083 | 1.2894 | B2 | 6.61 | 9.11 |
| 49.7455 | 1.4913 | B3 | 0.18 | 13.69 |
| 52.9894 | 1.5886 | B1 | 2.15 | 93.28 |
| 53.2057 | 1.5951 | A | inactive | 7.50 |
| 57.9510 | 1.7373 | B2 | 0.47 | 22.68 |
| 60.6493 | 1.8182 | B3 | 0.01 | 59.86 |
| 66.6649 | 1.9986 | A | inactive | 19.76 |
| 68.6355 | 2.0576 | B3 | 0.25 | 7.12 |
| 70.4565 | 2.1122 | B2 | 0.13 | 242.86 |
| 73.6898 | 2.2092 | B3 | 12.69 | 2.18 |
| 74.8702 | 2.2446 | B1 | 0.81 | 103.33 |
| 75.3423 | 2.2587 | B2 | 0.35 | 29.65 |
| 78.1471 | 2.3428 | B2 | 3.08 | 2.08 |
| 82.2866 | 2.4669 | B1 | 6.24 | 0.85 |
| 82.5037 | 2.4734 | A | inactive | 47.02 |
| 85.8007 | 2.5722 | A | inactive | 23.50 |
| 87.8114 | 2.6325 | B1 | 5.54 | 15.91 |
| 87.8687 | 2.6342 | B3 | 0.32 | 28.17 |
| 88.6505 | 2.6577 | B2 | 0.03 | 31.78 |
| 89.1244 | 2.6719 | A | inactive | 37.52 |
| 91.2291 | 2.7350 | B3 | 5.46 | 4.31 |
| 94.7242 | 2.8398 | B1 | 8.82 | 4.22 |
| 101.0810 | 3.0303 | B2 | 2.58 | 0.77 |
| 102.1425 | 3.0622 | B3 | 11.07 | 6.66 |
| 102.5600 | 3.0747 | A | inactive | 5.59 |
| 108.1842 | 3.2433 | B2 | 2.80 | 29.05 |
| 111.4882 | 3.3423 | B1 | 0.19 | 26.99 |
| 119.5173 | 3.5830 | B2 | 8.85 | 19.37 |
| 124.0319 | 3.7184 | B1 | 0.80 | 37.10 |

| 126.3905 | 3.7891 | A | inactive | 157.75 |
|---|---|---|---|---|
| 127.9458 | 3.8357 | B3 | 8.18 | 0.01 |
| 135.9831 | 4.0767 | B2 | 0.20 | 0.69 |
| 135.9901 | 4.0769 | A | inactive | 6.93 |
| 140.1328 | 4.2011 | B1 | 1.81 | 0.03 |
| 142.4787 | 4.2714 | B3 | 1.40 | 2.84 |
| 143.9487 | 4.3155 | B1 | 3.45 | 3.54 |
| 147.2955 | 4.4158 | B2 | 8.01 | 0.22 |
| 149.1212 | 4.4705 | A | inactive | 38.08 |
| 149.2133 | 4.4733 | B3 | 0.00 | 2.51 |
| 156.8380 | 4.7019 | B1 | 17.16 | 0.36 |
| 159.6733 | 4.7869 | B2 | 2.08 | 20.16 |
| 161.6497 | 4.8461 | A | inactive | 10.08 |
| 163.7994 | 4.9106 | B3 | 3.06 | 2.57 |
| 174.9027 | 5.2435 | B2 | 19.29 | 21.29 |
| 177.9355 | 5.3344 | A | inactive | 24.71 |
| 179.5124 | 5.3816 | B3 | 69.01 | 0.00 |
| 182.3969 | 5.4681 | B1 | 0.12 | 4.94 |
| 191.9521 | 5.7546 | B2 | 34.62 | 0.58 |
| 194.1201 | 5.8196 | B3 | 12.90 | 0.95 |
| 196.0732 | 5.8781 | A | inactive | 58.54 |
| 198.2409 | 5.9431 | B1 | 39.85 | 3.15 |
| 213.0901 | 6.3883 | A | inactive | 12.53 |
| 214.0602 | 6.4174 | B3 | 29.69 | 1.62 |
| 215.7803 | 6.4689 | B2 | 29.74 | 1.98 |
| 216.1534 | 6.4801 | B1 | 10.38 | 5.78 |
| 238.4158 | 7.1475 | B2 | 5.20 | 0.47 |
| 244.4665 | 7.3289 | B3 | 8.10 | 0.40 |
| 250.3129 | 7.5042 | A | inactive | 21.35 |
| 254.1250 | 7.6185 | B1 | 9.96 | 9.10 |
| 284.5042 | 8.5292 | B3 | 16.31 | 4.67 |
| 285.0117 | 8.5444 | B2 | 0.01 | 18.02 |
| 293.8647 | 8.8098 | A | inactive | 75.99 |
| 295.2332 | 8.8509 | B1 | 35.34 | 2.65 |
| 301.5883 | 9.0414 | B1 | 14.62 | 1.57 |
| 303.3498 | 9.0942 | A | inactive | 16.41 |
| 316.8703 | 9.4995 | B3 | 20.66 | 4.06 |
| 321.4153 | 9.6358 | B2 | 64.93 | 1.09 |
| 361.3720 | 10.8337 | B1 | 2.59 | 34.66 |
| 362.2876 | 10.8611 | B3 | 53.02 | 2.04 |
| 364.1237 | 10.9162 | B2 | 33.47 | 1.24 |

| | | | | |
|---|---|---|---|---|
| 364.8536 | 10.9380 | A | inactive | 48.37 |
| 420.5090 | 12.6065 | B3 | 36.13 | 1.34 |
| 422.9297 | 12.6791 | A | inactive | 32.80 |
| 423.6828 | 12.7017 | B1 | 0.73 | 0.86 |
| 424.8960 | 12.7381 | B2 | 2.49 | 10.36 |
| 437.2586 | 13.1087 | B1 | 33.39 | 1.68 |
| 437.4612 | 13.1148 | B3 | 4.21 | 14.12 |
| 437.7469 | 13.1233 | B2 | 71.93 | 0.07 |
| 438.7128 | 13.1523 | A | inactive | 12.80 |
| 460.0048 | 13.7906 | A | inactive | 18.12 |
| 460.2455 | 13.7978 | B1 | 58.69 | 4.03 |
| 461.6709 | 13.8405 | B3 | 9.46 | 4.37 |
| 464.0915 | 13.9131 | B2 | 76.40 | 8.70 |
| 526.6927 | 15.7898 | A | inactive | 7.79 |
| 527.4974 | 15.8140 | B3 | 9.15 | 2.15 |
| 531.5026 | 15.9340 | B1 | 112.78 | 0.53 |
| 532.6904 | 15.9697 | B2 | 8.59 | 2.83 |
| 556.5222 | 16.6841 | A | inactive | 44.32 |
| 557.6005 | 16.7164 | B2 | 22.54 | 30.44 |
| 557.8633 | 16.7243 | B3 | 11.23 | 4.20 |
| 558.8718 | 16.7546 | B1 | 0.05 | 0.59 |
| 595.7926 | 17.8614 | B3 | 0.11 | 31.07 |
| 596.7801 | 17.8910 | B1 | 60.56 | 47.63 |
| 597.3674 | 17.9086 | B2 | 5.33 | 3.01 |
| 597.6726 | 17.9178 | A | inactive | 171.49 |
| 602.4904 | 18.0622 | B1 | 8.39 | 0.71 |
| 602.5743 | 18.0647 | B2 | 414.83 | 5.55 |
| 611.4456 | 18.3307 | B3 | 121.65 | 1.57 |
| 614.1397 | 18.4114 | A | inactive | 3.91 |
| 624.7151 | 18.7285 | B3 | 1.81 | 4.39 |
| 625.8994 | 18.7640 | B2 | 7.21 | 11.74 |
| 630.9676 | 18.9159 | B1 | 7.19 | 15.13 |
| 632.2812 | 18.9553 | A | inactive | 61.63 |
| 641.9795 | 19.2461 | A | inactive | 63.38 |
| 646.2083 | 19.3728 | B1 | 224.30 | 2.74 |
| 652.2178 | 19.5530 | B2 | 13.10 | 15.80 |
| 654.9783 | 19.6358 | B3 | 30.87 | 2.78 |
| 675.3571 | 20.2467 | B3 | 2.23 | 0.00 |
| 676.0617 | 20.2678 | A | inactive | 210.62 |
| 677.5095 | 20.3112 | B1 | 70.64 | 0.91 |
| 678.5617 | 20.3428 | B2 | 123.28 | 6.96 |

| 698.7667 | 20.9485 | A | inactive | 60.73 |
|---|---|---|---|---|
| 699.5556 | 20.9721 | B3 | 138.46 | 8.29 |
| 706.4939 | 21.1802 | B1 | 875.15 | 16.79 |
| 716.5682 | 21.4822 | B2 | 180.45 | 7.63 |
| 720.4087 | 21.5973 | B2 | 17.25 | 12.25 |
| 721.8768 | 21.6413 | B3 | 26.29 | 1.24 |
| 724.1951 | 21.7108 | B1 | 23.58 | 6.13 |
| 724.7311 | 21.7269 | A | inactive | 31.28 |
| 727.9915 | 21.8246 | B1 | 53.20 | 9.49 |
| 728.2954 | 21.8337 | A | inactive | 50.52 |
| 729.2863 | 21.8635 | B2 | 229.32 | 0.36 |
| 729.5504 | 21.8714 | B3 | 50.13 | 3.98 |
| 736.0067 | 22.0649 | B1 | 5.65 | 1.32 |
| 736.5626 | 22.0816 | A | inactive | 5.75 |
| 739.1176 | 22.1582 | B3 | 14.30 | 6.58 |
| 740.0596 | 22.1864 | B2 | 63.95 | 2.01 |
| 743.6650 | 22.2945 | B3 | 89.85 | 3.29 |
| 744.6408 | 22.3238 | B2 | 74.20 | 1.22 |
| 744.9786 | 22.3339 | A | inactive | 3.83 |
| 745.6112 | 22.3529 | B1 | 49.20 | 5.99 |
| 803.6373 | 24.0924 | B2 | 1.24 | 2.19 |
| 805.6063 | 24.1515 | B3 | 0.57 | 11.90 |
| 805.7985 | 24.1572 | A | inactive | 18.05 |
| 807.2144 | 24.1997 | B1 | 13.06 | 0.24 |
| 827.5750 | 24.8101 | A | inactive | 5.45 |
| 828.0816 | 24.8253 | B3 | 112.15 | 0.00 |
| 828.1045 | 24.8259 | B2 | 22.26 | 20.08 |
| 828.3730 | 24.8340 | B1 | 7.17 | 5.32 |
| 830.9203 | 24.9104 | B1 | 13.72 | 16.66 |
| 833.3336 | 24.9827 | A | inactive | 76.49 |
| 833.8630 | 24.9986 | B3 | 23.88 | 0.51 |
| 834.2280 | 25.0095 | B2 | 7.95 | 3.95 |
| 875.2441 | 26.2392 | B3 | 10.49 | 0.55 |
| 875.6719 | 26.2520 | A | inactive | 31.26 |
| 875.8726 | 26.2580 | B1 | 37.43 | 0.95 |
| 876.4932 | 26.2766 | B2 | 60.44 | 0.87 |
| 888.1657 | 26.6265 | B3 | 35.55 | 10.40 |
| 888.3323 | 26.6315 | B2 | 4.55 | 0.68 |
| 889.7930 | 26.6753 | B1 | 0.13 | 3.41 |
| 890.2512 | 26.6891 | A | inactive | 36.50 |
| 913.4034 | 27.3831 | B2 | 31.66 | 1.38 |

| 914.5890 | 27.4187 | A | inactive | 48.05 |
|---|---|---|---|---|
| 914.6723 | 27.4212 | B3 | 28.71 | 0.92 |
| 915.5240 | 27.4467 | B1 | 50.31 | 0.21 |
| 938.5229 | 28.1362 | B1 | 0.15 | 2.16 |
| 940.5425 | 28.1968 | B3 | 5.64 | 5.75 |
| 941.4077 | 28.2227 | A | inactive | 40.55 |
| 944.0127 | 28.3008 | B2 | 69.02 | 4.34 |
| 968.6855 | 29.0405 | A | inactive | 28.50 |
| 969.9891 | 29.0795 | B2 | 1.60 | 3.39 |
| 970.2516 | 29.0874 | B3 | 4.01 | 1.24 |
| 971.8372 | 29.1349 | B1 | 1.53 | 2.42 |
| 1012.2372 | 30.3461 | B3 | 37.54 | 19.69 |
| 1013.4564 | 30.3827 | B1 | 47.53 | 0.60 |
| 1013.6712 | 30.3891 | B2 | 27.05 | 0.04 |
| 1013.6837 | 30.3895 | A | inactive | 83.48 |
| 1017.7887 | 30.5125 | B1 | 41.15 | 0.16 |
| 1018.3049 | 30.5280 | B3 | 20.29 | 5.23 |
| 1018.3857 | 30.5304 | A | inactive | 28.01 |
| 1018.9971 | 30.5488 | B2 | 0.52 | 1.23 |
| 1024.3008 | 30.7078 | A | inactive | 34.52 |
| 1024.6757 | 30.7190 | B2 | 2.95 | 11.54 |
| 1025.2384 | 30.7359 | B1 | 0.19 | 3.47 |
| 1025.2777 | 30.7371 | B3 | 0.24 | 19.15 |
| 1039.6332 | 31.1674 | B3 | 3.85 | 2.28 |
| 1039.9854 | 31.1780 | B1 | 11.04 | 2.79 |
| 1040.9627 | 31.2073 | A | inactive | 69.69 |
| 1041.3258 | 31.2182 | B2 | 26.98 | 26.25 |
| 1055.8275 | 31.6529 | B2 | 0.38 | 0.08 |
| 1055.9200 | 31.6557 | B1 | 7.39 | 1.51 |
| 1055.9726 | 31.6573 | A | inactive | 119.58 |
| 1056.0705 | 31.6602 | B3 | 18.31 | 30.72 |
| 1068.4929 | 32.0326 | B2 | 0.23 | 5.09 |
| 1068.8076 | 32.0420 | A | inactive | 15.32 |
| 1070.9633 | 32.1067 | B3 | 85.55 | 3.61 |
| 1071.2595 | 32.1156 | B1 | 39.12 | 1.17 |
| 1091.9326 | 32.7353 | B3 | 23.11 | 6.57 |
| 1092.2719 | 32.7455 | B1 | 3.19 | 2.40 |
| 1092.6057 | 32.7555 | A | inactive | 14.41 |
| 1092.6354 | 32.7564 | B2 | 5.89 | 1.03 |
| 1107.4702 | 33.2011 | B3 | 13.05 | 2.06 |
| 1109.0195 | 33.2476 | A | inactive | 4.29 |

| 1109.6290 | 33.2658 | B1 | 350.49 | 0.73 |
|---|---|---|---|---|
| 1111.4151 | 33.3194 | B2 | 110.09 | 0.49 |
| 1114.8677 | 33.4229 | A | inactive | 14.28 |
| 1115.3164 | 33.4363 | B3 | 1.44 | 0.18 |
| 1117.0971 | 33.4897 | B1 | 35.69 | 0.31 |
| 1118.3912 | 33.5285 | B2 | 402.63 | 0.00 |
| 1126.3333 | 33.7666 | A | inactive | 15.37 |
| 1126.8602 | 33.7824 | B2 | 3.69 | 0.55 |
| 1127.8495 | 33.8121 | B1 | 28.42 | 0.36 |
| 1128.5898 | 33.8343 | B3 | 14.97 | 3.99 |
| 1144.3431 | 34.3065 | B2 | 0.42 | 2.18 |
| 1144.3991 | 34.3082 | B1 | 89.42 | 0.37 |
| 1145.5506 | 34.3427 | B3 | 63.90 | 4.10 |
| 1145.9433 | 34.3545 | A | inactive | 4.88 |
| 1182.4103 | 35.4478 | A | inactive | 75.56 |
| 1182.7801 | 35.4589 | B2 | 3.41 | 4.84 |
| 1184.2359 | 35.5025 | B1 | 16.38 | 9.36 |
| 1184.4289 | 35.5083 | B3 | 49.58 | 0.82 |
| 1191.9601 | 35.7341 | B1 | 1.19 | 4.44 |
| 1192.2105 | 35.7416 | B3 | 1.91 | 1.84 |
| 1192.5519 | 35.7518 | A | inactive | 28.71 |
| 1193.1694 | 35.7703 | B2 | inactive | 9.04 |
| 1215.4367 | 36.4379 | B3 | 14.42 | 0.75 |
| 1215.9590 | 36.4535 | B1 | 20.29 | 0.06 |
| 1216.1147 | 36.4582 | B2 | 6.13 | 7.40 |
| 1216.3203 | 36.4644 | A | inactive | 26.51 |
| 1227.4895 | 36.7992 | B2 | 0.13 | 2.68 |
| 1228.0697 | 36.8166 | B3 | 28.07 | 2.16 |
| 1229.9783 | 36.8738 | B1 | 8.94 | 0.41 |
| 1230.6055 | 36.8926 | A | inactive | 1.96 |
| 1239.0114 | 37.1446 | A | inactive | 2.98 |
| 1239.3416 | 37.1545 | B1 | 4.83 | 2.66 |
| 1242.5436 | 37.2505 | B2 | 26.89 | 9.25 |
| 1243.8808 | 37.2906 | B3 | 0.13 | 4.51 |
| 1259.6332 | 37.7629 | B3 | 463.00 | 7.65 |
| 1260.0338 | 37.7749 | B2 | 2.52 | 1.05 |
| 1260.0605 | 37.7757 | B1 | 0.35 | 0.00 |
| 1261.1852 | 37.8094 | A | inactive | 36.19 |
| 1267.5139 | 37.9991 | A | inactive | 19.79 |
| 1270.4994 | 38.0886 | B2 | 1.57 | 6.23 |
| 1271.3427 | 38.1139 | B1 | 138.77 | 0.15 |

| 1273.0879 | 38.1662 | B3 | 18.94 | 0.64 |
|---|---|---|---|---|
| 1276.5604 | 38.2703 | B3 | 76.63 | 13.08 |
| 1276.9533 | 38.2821 | B2 | 13.30 | 18.38 |
| 1280.3002 | 38.3824 | A | inactive | 0.77 |
| 1280.8646 | 38.3994 | B1 | 45.40 | 4.38 |
| 1288.9652 | 38.6422 | A | inactive | 19.06 |
| 1294.3195 | 38.8027 | B1 | 10.10 | 3.21 |
| 1294.3724 | 38.8043 | B2 | 8.32 | 51.77 |
| 1295.2620 | 38.8310 | B3 | 12.83 | 0.74 |
| 1295.9170 | 38.8506 | A | inactive | 8.69 |
| 1296.9492 | 38.8816 | B2 | 0.11 | 4.01 |
| 1297.2870 | 38.8917 | B1 | 76.07 | 0.98 |
| 1297.3453 | 38.8934 | B3 | 29.72 | 7.62 |
| 1302.3865 | 39.0446 | B3 | 132.81 | 5.72 |
| 1303.7785 | 39.0863 | A | inactive | 48.86 |
| 1308.9086 | 39.2401 | B2 | 78.36 | 4.10 |
| 1310.0540 | 39.2744 | B1 | 454.38 | 17.18 |
| 1310.4407 | 39.2860 | B1 | 172.74 | 8.55 |
| 1311.7447 | 39.3251 | B2 | 80.17 | 7.93 |
| 1311.8702 | 39.3289 | A | inactive | 3.20 |
| 1312.5885 | 39.3504 | B3 | 51.40 | 10.05 |
| 1319.1047 | 39.5458 | B1 | 431.15 | 1.96 |
| 1320.4866 | 39.5872 | A | inactive | 1.30 |
| 1322.0929 | 39.6353 | B3 | 567.34 | 1.71 |
| 1324.8749 | 39.7187 | B2 | 375.81 | 0.01 |
| 1340.8157 | 40.1966 | B3 | 0.47 | 21.53 |
| 1341.0863 | 40.2048 | B1 | 22.46 | 8.58 |
| 1345.1423 | 40.3264 | B2 | 3.16 | 0.14 |
| 1345.5750 | 40.3393 | A | inactive | 5.81 |
| 1350.4653 | 40.4859 | A | inactive | 10.05 |
| 1351.3769 | 40.5133 | B2 | 0.67 | 1.30 |
| 1355.5061 | 40.6370 | B1 | 22.15 | 0.01 |
| 1356.0936 | 40.6547 | B3 | 0.41 | 0.03 |
| 1357.5081 | 40.6971 | B2 | 57.03 | 1.16 |
| 1358.8581 | 40.7375 | B1 | 33.43 | 0.53 |
| 1365.6416 | 40.9409 | B3 | 12.77 | 25.95 |
| 1365.8764 | 40.9479 | A | inactive | 100.38 |
| 1408.7519 | 42.2333 | A | inactive | 32.10 |
| 1408.9563 | 42.2394 | B3 | 75.59 | 1.57 |
| 1411.3650 | 42.3117 | B2 | 9.63 | 17.02 |
| 1412.3426 | 42.3410 | B1 | 11.01 | 2.47 |

| 1413.4039 | 42.3728 | A | inactive | 12.01 |
|---|---|---|---|---|
| 1415.3802 | 42.4320 | B1 | 6.78 | 5.42 |
| 1415.4274 | 42.4334 | B2 | 2.16 | 3.20 |
| 1415.6237 | 42.4393 | B3 | 53.81 | 2.25 |
| 1418.1966 | 42.5165 | B3 | 47.40 | 4.30 |
| 1418.3505 | 42.5211 | B2 | 0.10 | 5.04 |
| 1418.8100 | 42.5349 | A | inactive | 29.41 |
| 1419.0527 | 42.5421 | B1 | 47.69 | 11.34 |
| 1427.7638 | 42.8033 | A | inactive | 28.65 |
| 1428.1025 | 42.8134 | B3 | 7.00 | 0.58 |
| 1428.2133 | 42.8168 | B2 | 124.22 | 7.01 |
| 1428.2187 | 42.8169 | B1 | 59.60 | 17.53 |
| 1437.1653 | 43.0851 | B3 | 3.91 | 19.64 |
| 1437.5256 | 43.0959 | A | inactive | 32.26 |
| 1437.7155 | 43.1016 | B2 | 24.80 | 1.34 |
| 1437.7598 | 43.1030 | B1 | 10.83 | 28.99 |
| 1451.4784 | 43.5142 | B2 | 56.24 | 3.68 |
| 1451.5330 | 43.5159 | A | inactive | 5.46 |
| 1454.8265 | 43.6146 | B1 | 18.06 | 4.20 |
| 1454.9218 | 43.6175 | B3 | 33.16 | 0.71 |
| 1462.4534 | 43.8433 | A | inactive | 27.66 |
| 1462.7245 | 43.8514 | B3 | 489.77 | 1.25 |
| 1468.4459 | 44.0229 | B1 | 129.05 | 0.00 |
| 1469.1939 | 44.0453 | B2 | 142.35 | 2.22 |
| 1488.2820 | 44.6176 | B1 | 21.75 | 0.03 |
| 1488.3485 | 44.6196 | B2 | 200.31 | 4.30 |
| 1492.1837 | 44.7345 | A | inactive | 5.95 |
| 1492.3869 | 44.7406 | B3 | 223.60 | 5.66 |
| 1599.9236 | 47.9645 | A | inactive | 142.10 |
| 1600.0933 | 47.9696 | B3 | 295.86 | 29.28 |
| 1617.5906 | 48.4941 | B1 | 1235.22 | 1.40 |
| 1622.2462 | 48.6337 | B2 | 297.12 | 0.32 |
| 1657.8841 | 49.7021 | A | inactive | 26.29 |
| 1659.0851 | 49.7381 | B3 | 3423.27 | 1.03 |
| 1684.5631 | 50.5019 | B1 | 2840.03 | 6.76 |
| 1699.8592 | 50.9605 | B2 | 2308.77 | 0.02 |
| 2316.0926 | 69.4347 | A | inactive | 88.73 |
| 2317.1417 | 69.4662 | B3 | 951.46 | 121.27 |
| 2331.9018 | 69.9087 | B1 | 6656.23 | 28.52 |
| 2356.6246 | 70.6498 | B2 | 7790.37 | 26.40 |
| 2950.7299 | 88.4607 | B2 | 3.23 | 12.07 |

| 2950.7476 | 88.4612 | A | inactive | 82.12 |
|---|---|---|---|---|
| 2950.9580 | 88.4675 | B1 | 64.83 | 14.81 |
| 2951.1113 | 88.4721 | B3 | 14.74 | 7.31 |
| 2958.2509 | 88.6861 | B2 | 101.58 | 2.01 |
| 2958.7385 | 88.7008 | B1 | 0.00 | 0.04 |
| 2958.7640 | 88.7015 | B3 | 96.58 | 14.48 |
| 2959.1780 | 88.7139 | A | inactive | 1000.00 |
| 2963.5425 | 88.8448 | B3 | 15.96 | 26.78 |
| 2963.5445 | 88.8448 | B1 | 0.14 | 68.03 |
| 2963.5462 | 88.8449 | A | inactive | 71.20 |
| 2963.6395 | 88.8477 | B2 | 0.67 | 10.95 |
| 2973.1383 | 89.1324 | B1 | 51.59 | 12.01 |
| 2973.1448 | 89.1326 | B2 | 124.86 | 0.30 |
| 2973.3196 | 89.1379 | B3 | 9.85 | 16.87 |
| 2973.5906 | 89.1460 | A | inactive | 237.68 |
| 2986.2198 | 89.5246 | B3 | 138.96 | 16.66 |
| 2986.2714 | 89.5262 | B2 | 1.55 | 0.87 |
| 2986.5248 | 89.5338 | A | inactive | 165.62 |
| 2986.5374 | 89.5341 | B1 | 2.33 | 24.50 |
| 2988.4101 | 89.5903 | B3 | 7.18 | 2.15 |
| 2988.5065 | 89.5932 | B1 | 4.90 | 55.80 |
| 2988.5737 | 89.5952 | B2 | 1.25 | 19.50 |
| 2989.2210 | 89.6146 | A | inactive | 560.26 |
| 2990.4755 | 89.6522 | B3 | 2.88 | 27.08 |
| 2990.5241 | 89.6537 | B1 | 1.11 | 139.77 |
| 2990.6774 | 89.6583 | A | inactive | 67.29 |
| 2990.7176 | 89.6595 | B2 | 5.22 | 12.34 |
| 2999.7477 | 89.9302 | B2 | 17.99 | 1.02 |
| 2999.8092 | 89.9320 | B1 | 3.58 | 0.04 |
| 2999.8552 | 89.9334 | A | inactive | 157.32 |
| 2999.8879 | 89.9344 | B3 | 13.54 | 10.91 |
| 3003.5493 | 90.0441 | A | inactive | 88.49 |
| 3003.5642 | 90.0446 | B2 | 111.25 | 17.26 |
| 3003.7626 | 90.0505 | B1 | 1.20 | 0.00 |
| 3003.7939 | 90.0515 | B3 | 14.28 | 1.91 |
| 3018.9886 | 90.5070 | B1 | 8.06 | 13.51 |
| 3018.9953 | 90.5072 | B3 | 166.06 | 4.09 |
| 3019.7254 | 90.5291 | B2 | 43.65 | 8.84 |
| 3019.7910 | 90.5311 | A | inactive | 20.06 |
| 3034.0414 | 90.9583 | B2 | 10.92 | 25.83 |
| 3034.0906 | 90.9597 | B1 | 0.05 | 28.94 |

| 3034.3741 | 90.9682 | B3 | 4.48 | 24.56 |
|---|---|---|---|---|
| 3034.4544 | 90.9707 | A | inactive | 306.63 |
| 3054.4617 | 91.5705 | B1 | 0.61 | 13.73 |
| 3054.4999 | 91.5716 | B3 | 95.34 | 2.43 |
| 3054.5709 | 91.5737 | A | inactive | 39.45 |
| 3054.6651 | 91.5766 | B2 | 3.10 | 0.62 |
| 3064.3261 | 91.8662 | B1 | 2.15 | 86.18 |
| 3064.3382 | 91.8665 | B3 | 0.00 | 0.43 |
| 3064.3477 | 91.8668 | A | inactive | 15.56 |
| 3064.4268 | 91.8692 | B2 | 12.88 | 6.84 |
| 3269.3599 | 98.0129 | A | inactive | 241.20 |
| 3269.8639 | 98.0281 | B3 | 5426.71 | 1.77 |
| 3279.1533 | 98.3065 | B2 | 806.59 | 7.10 |
| 3280.0765 | 98.3342 | B1 | 67.41 | 43.17 |
| 3402.3954 | 102.0012 | A | inactive | 152.10 |
| 3402.6796 | 102.0098 | B3 | 176.74 | 32.20 |
| 3405.2560 | 102.0870 | B1 | 1562.10 | 3.68 |
| 3409.2880 | 102.2079 | B2 | 1017.11 | 10.32 |

**Table A-9.** Mode labels, vibrational frequencies, symmetry representations, and IR/Raman intensities for crystalline L-cystine simulated using ss-DFT.

| Frequency | | Symmetry representation | Intensity | |
|---|---|---|---|---|
| cm$^{-1}$ | THz | | IR (km/mol) | Raman (arb. Units) |
| 10.7231 | 0.3215 | A2 | 0.08 | inactive |
| 12.2051 | 0.3659 | E2 | inactive | 1.73 |
| 15.7526 | 0.4723 | A1 | inactive | 4.10 |
| 21.6078 | 0.6478 | B2 | inactive | inactive |
| 26.2916 | 0.7882 | E1 | 1.27 | 0.42 |
| 27.4655 | 0.8234 | B1 | inactive | inactive |
| 29.0278 | 0.8702 | E1 | 0.47 | 0.02 |
| 35.1315 | 1.0532 | E2 | inactive | 0.15 |
| 42.9987 | 1.2891 | E2 | inactive | 2.29 |
| 49.2947 | 1.4778 | E1 | 1.18 | 0.37 |
| 53.2425 | 1.5962 | A2 | 31.94 | inactive |
| 53.4200 | 1.6015 | B1 | inactive | inactive |
| 53.5505 | 1.6054 | B2 | inactive | inactive |
| 54.0832 | 1.6214 | E2 | inactive | 2.95 |
| 65.8808 | 1.9751 | E2 | inactive | 8.68 |
| 70.2051 | 2.1047 | E1 | 3.02 | 2.45 |
| 71.0276 | 2.1294 | A1 | inactive | 27.57 |
| 71.0327 | 2.1295 | A2 | 21.31 | inactive |
| 74.8157 | 2.2429 | E1 | 35.26 | 2.32 |
| 76.9018 | 2.3055 | B1 | inactive | inactive |
| 78.2667 | 2.3464 | E2 | inactive | 8.90 |
| 78.6107 | 2.3567 | A1 | inactive | 9.63 |
| 79.4483 | 2.3818 | B2 | inactive | inactive |
| 80.1998 | 2.4043 | B1 | inactive | inactive |
| 80.3232 | 2.4080 | E1 | 10.10 | 1.22 |
| 82.5666 | 2.4753 | E2 | inactive | 0.08 |
| 90.7120 | 2.7195 | B2 | inactive | inactive |
| 101.1171 | 3.0314 | A2 | 72.13 | inactive |
| 102.9947 | 3.0877 | E2 | inactive | 6.79 |
| 106.4023 | 3.1899 | E1 | 3.62 | 68.95 |
| 113.1676 | 3.3927 | E2 | inactive | 23.51 |
| 115.8603 | 3.4734 | E1 | 0.38 | 0.12 |
| 120.3680 | 3.6085 | B2 | inactive | inactive |
| 120.5630 | 3.6144 | A1 | inactive | 6.58 |

| 129.8551 | 3.8930 | B1 | inactive | inactive |
|---|---|---|---|---|
| 138.6171 | 4.1556 | E2 | inactive | 0.13 |
| 144.4010 | 4.3290 | B1 | inactive | inactive |
| 147.1037 | 4.4101 | E2 | inactive | 5.36 |
| 151.7839 | 4.5504 | E1 | 17.60 | 31.64 |
| 154.0333 | 4.6178 | E1 | 63.96 | 3.26 |
| 158.6900 | 4.7574 | A1 | inactive | 29.52 |
| 163.9367 | 4.9147 | A2 | 97.57 | inactive |
| 168.2627 | 5.0444 | A2 | 1.75 | inactive |
| 171.3089 | 5.1357 | A1 | inactive | 17.90 |
| 173.0334 | 5.1874 | E1 | 7.32 | 5.64 |
| 178.5242 | 5.3520 | E2 | inactive | 16.68 |
| 180.7582 | 5.4190 | B1 | inactive | inactive |
| 186.5517 | 5.5927 | E1 | 121.45 | 1.51 |
| 196.1363 | 5.8800 | B2 | inactive | inactive |
| 196.2665 | 5.8839 | E2 | inactive | 0.32 |
| 200.6378 | 6.0150 | E1 | 230.24 | 37.09 |
| 200.9928 | 6.0256 | A1 | inactive | 2.27 |
| 205.7272 | 6.1675 | E2 | inactive | 13.88 |
| 214.6371 | 6.4347 | B1 | inactive | inactive |
| 217.4154 | 6.5180 | B2 | inactive | inactive |
| 218.1284 | 6.5393 | A2 | 3.39 | inactive |
| 218.7321 | 6.5574 | E1 | 0.35 | 4.18 |
| 219.2616 | 6.5733 | E2 | inactive | 11.25 |
| 250.1398 | 7.4990 | E1 | 1128.76 | 0.23 |
| 250.2877 | 7.5034 | A1 | inactive | 28.58 |
| 250.4085 | 7.5071 | E2 | inactive | 6.70 |
| 252.0688 | 7.5568 | A2 | 1244.25 | inactive |
| 253.7920 | 7.6085 | B1 | inactive | inactive |
| 254.2398 | 7.6219 | B2 | inactive | inactive |
| 263.4463 | 7.8979 | E2 | inactive | 0.00 |
| 274.4818 | 8.2288 | E1 | 1.34 | 2.44 |
| 305.3259 | 9.1534 | A1 | inactive | 21.52 |
| 308.7450 | 9.2559 | E1 | 69.04 | 13.52 |
| 314.3995 | 9.4255 | E2 | inactive | 11.56 |
| 318.7183 | 9.5549 | B1 | inactive | inactive |
| 319.9039 | 9.5905 | B2 | inactive | inactive |
| 321.4191 | 9.6359 | A2 | 124.32 | inactive |
| 322.6404 | 9.6725 | E2 | inactive | 8.21 |

| | | | | |
|---|---|---|---|---|
| 324.5248 | 9.7290 | E1 | 39.31 | 2.62 |
| 397.6336 | 11.9208 | A1 | inactive | 1.68 |
| 398.0055 | 11.9319 | E1 | 14.40 | 0.76 |
| 399.0012 | 11.9618 | E2 | inactive | 12.79 |
| 399.6793 | 11.9821 | B1 | inactive | inactive |
| 402.5844 | 12.0692 | A2 | 139.55 | inactive |
| 403.2673 | 12.0896 | B2 | inactive | inactive |
| 403.8946 | 12.1085 | E2 | inactive | 0.03 |
| 404.8131 | 12.1360 | E1 | 1267.43 | 1.00 |
| 445.0280 | 13.3416 | A2 | 3.00 | inactive |
| 445.6671 | 13.3608 | E1 | 686.99 | 0.03 |
| 447.1805 | 13.4061 | E2 | inactive | 5.76 |
| 448.4244 | 13.4434 | B2 | inactive | inactive |
| 450.8338 | 13.5157 | B1 | inactive | inactive |
| 451.9060 | 13.5478 | E2 | inactive | 3.49 |
| 453.1123 | 13.5840 | E1 | 445.81 | 21.38 |
| 453.5785 | 13.5979 | A1 | inactive | 0.36 |
| 480.9295 | 14.4179 | A1 | inactive | 1000.00 |
| 480.9577 | 14.4188 | E2 | inactive | 461.61 |
| 480.9581 | 14.4188 | B2 | inactive | inactive |
| 481.0119 | 14.4204 | E1 | 3.85 | 1.41 |
| 529.7018 | 15.8801 | B1 | inactive | inactive |
| 530.1335 | 15.8930 | E2 | inactive | 0.33 |
| 531.2902 | 15.9277 | E1 | 767.99 | 0.36 |
| 531.8826 | 15.9454 | A2 | 32.22 | inactive |
| 533.1996 | 15.9849 | A1 | inactive | 8.57 |
| 533.9803 | 16.0083 | E1 | 35.45 | 2.97 |
| 534.6120 | 16.0273 | E2 | inactive | 3.77 |
| 534.8672 | 16.0349 | B2 | inactive | inactive |
| 556.8852 | 16.6950 | A2 | 35.19 | inactive |
| 557.3895 | 16.7101 | E1 | 0.66 | 0.00 |
| 557.5293 | 16.7143 | E2 | inactive | 13.41 |
| 557.5938 | 16.7162 | B2 | inactive | inactive |
| 573.1366 | 17.1822 | E1 | 31.17 | 0.97 |
| 573.1958 | 17.1840 | E2 | inactive | 5.59 |
| 573.2484 | 17.1856 | A1 | inactive | 2.93 |
| 573.2497 | 17.1856 | B1 | inactive | inactive |
| 599.1011 | 17.9606 | A2 | 0.04 | inactive |
| 599.6286 | 17.9764 | E1 | 76.13 | 2.46 |

| 600.9030 | 18.0146 | E2 | inactive | 5.94 |
|---|---|---|---|---|
| 601.8602 | 18.0433 | B1 | inactive | inactive |
| 606.1887 | 18.1731 | B2 | inactive | inactive |
| 607.1825 | 18.2029 | E2 | inactive | 5.32 |
| 608.6118 | 18.2457 | E1 | 192.39 | 0.02 |
| 609.2894 | 18.2660 | A1 | inactive | 26.98 |
| 663.9133 | 19.9036 | B2 | inactive | inactive |
| 663.9830 | 19.9057 | E2 | inactive | 10.39 |
| 664.0614 | 19.9081 | E1 | 457.54 | 10.34 |
| 664.0929 | 19.9090 | A2 | 0.05 | inactive |
| 669.1736 | 20.0613 | A1 | inactive | 12.87 |
| 669.4803 | 20.0705 | E1 | 6.57 | 6.18 |
| 669.8229 | 20.0808 | E2 | inactive | 14.32 |
| 669.9620 | 20.0850 | B1 | inactive | inactive |
| 758.1926 | 22.7300 | A2 | 232.43 | inactive |
| 760.4990 | 22.7992 | E1 | 9.94 | 1.85 |
| 761.5401 | 22.8304 | E2 | inactive | 0.47 |
| 762.3706 | 22.8553 | B1 | inactive | inactive |
| 764.6834 | 22.9246 | B2 | inactive | inactive |
| 765.5350 | 22.9502 | E2 | inactive | 2.16 |
| 766.5228 | 22.9798 | E1 | 87.00 | 0.11 |
| 766.9142 | 22.9915 | A1 | inactive | 82.49 |
| 828.7915 | 24.8465 | E1 | 244.77 | 0.26 |
| 828.7977 | 24.8467 | A1 | inactive | 0.42 |
| 828.9603 | 24.8516 | E2 | inactive | 0.00 |
| 829.0583 | 24.8545 | B1 | inactive | inactive |
| 830.0673 | 24.8848 | B2 | inactive | inactive |
| 830.3110 | 24.8921 | E2 | inactive | 0.35 |
| 830.6770 | 24.9031 | E1 | 681.42 | 2.94 |
| 830.6841 | 24.9033 | A2 | 20.29 | inactive |
| 855.9715 | 25.6614 | A1 | inactive | 18.74 |
| 856.1702 | 25.6673 | E1 | 0.18 | 1.97 |
| 856.8752 | 25.6885 | E2 | inactive | 0.56 |
| 857.3360 | 25.7023 | A2 | 289.60 | inactive |
| 857.3681 | 25.7032 | B2 | inactive | inactive |
| 858.4242 | 25.7349 | B1 | inactive | inactive |
| 858.8409 | 25.7474 | E2 | inactive | 0.72 |
| 859.2840 | 25.7607 | E1 | 30.09 | 2.25 |
| 962.0526 | 28.8416 | A2 | 224.08 | inactive |

| 963.2563 | 28.8777 | B1 | inactive | inactive |
|---|---|---|---|---|
| 963.3090 | 28.8793 | E2 | inactive | 0.15 |
| 963.4302 | 28.8829 | E1 | 47.49 | 2.71 |
| 963.7249 | 28.8917 | A1 | inactive | 11.05 |
| 963.8383 | 28.8951 | E1 | 146.07 | 5.83 |
| 964.0010 | 28.9000 | E2 | inactive | 8.87 |
| 964.1192 | 28.9036 | B2 | inactive | inactive |
| 1038.7731 | 31.1416 | A1 | inactive | 3.21 |
| 1038.8449 | 31.1438 | E1 | 521.17 | 7.10 |
| 1038.9686 | 31.1475 | E2 | inactive | 0.06 |
| 1039.0852 | 31.1510 | B1 | inactive | inactive |
| 1040.0716 | 31.1806 | B2 | inactive | inactive |
| 1040.1402 | 31.1826 | E2 | inactive | 4.28 |
| 1040.3068 | 31.1876 | E1 | 3.76 | 3.52 |
| 1040.3101 | 31.1877 | A2 | 16.91 | inactive |
| 1088.6043 | 32.6355 | A2 | 205.61 | inactive |
| 1089.7389 | 32.6695 | E1 | 49.52 | 0.15 |
| 1089.8461 | 32.6728 | E2 | inactive | 2.41 |
| 1089.9862 | 32.6770 | B1 | inactive | inactive |
| 1090.0752 | 32.6796 | B2 | inactive | inactive |
| 1090.2371 | 32.6845 | E2 | inactive | 15.83 |
| 1090.3079 | 32.6866 | E1 | 89.28 | 4.78 |
| 1090.3257 | 32.6871 | A1 | inactive | 2.03 |
| 1125.4837 | 33.7412 | A2 | 785.08 | inactive |
| 1130.5935 | 33.8943 | E1 | 187.26 | 18.98 |
| 1131.9319 | 33.9345 | E2 | inactive | 6.35 |
| 1133.3299 | 33.9764 | B2 | inactive | inactive |
| 1134.4147 | 34.0089 | B1 | inactive | inactive |
| 1135.8036 | 34.0505 | E2 | inactive | 0.62 |
| 1137.1750 | 34.0917 | E1 | 22.00 | 0.01 |
| 1137.6704 | 34.1065 | A1 | inactive | 19.50 |
| 1175.1210 | 35.2292 | B1 | inactive | inactive |
| 1175.2322 | 35.2326 | E2 | inactive | 8.16 |
| 1175.5389 | 35.2418 | E1 | 357.40 | 1.05 |
| 1175.7146 | 35.2470 | A2 | 2.43 | inactive |
| 1180.7005 | 35.3965 | A1 | inactive | 6.51 |
| 1180.7986 | 35.3995 | E1 | 101.61 | 20.20 |
| 1181.0707 | 35.4076 | E2 | inactive | 5.62 |
| 1181.1792 | 35.4109 | B2 | inactive | inactive |

| 1242.3076 | 37.2434 | A2 | 6.06 | inactive |
|-----------|---------|-----|----------|----------|
| 1242.5196 | 37.2498 | E1 | 70.62 | 0.14 |
| 1243.0352 | 37.2653 | E2 | inactive | 0.61 |
| 1243.3262 | 37.2740 | B1 | inactive | inactive |
| 1254.6683 | 37.6140 | B2 | inactive | inactive |
| 1254.8457 | 37.6193 | E2 | inactive | 0.23 |
| 1255.1701 | 37.6291 | E1 | 154.64 | 1.40 |
| 1255.4173 | 37.6365 | A1 | inactive | 0.07 |
| 1282.3221 | 38.4430 | B1 | inactive | inactive |
| 1282.6598 | 38.4532 | E2 | inactive | 2.65 |
| 1283.4441 | 38.4767 | E1 | 674.67 | 2.06 |
| 1283.9460 | 38.4917 | A1 | inactive | 9.41 |
| 1286.5961 | 38.5712 | A2 | 187.68 | inactive |
| 1287.9234 | 38.6110 | E1 | 26.09 | 5.62 |
| 1288.5241 | 38.6290 | E2 | inactive | 8.94 |
| 1288.7858 | 38.6368 | B2 | inactive | inactive |
| 1322.0906 | 39.6353 | B1 | inactive | inactive |
| 1322.2563 | 39.6402 | E2 | inactive | 5.40 |
| 1322.6433 | 39.6518 | A2 | 178.03 | inactive |
| 1322.7587 | 39.6553 | E1 | 776.58 | 3.92 |
| 1323.1350 | 39.6666 | A1 | inactive | 56.15 |
| 1323.9751 | 39.6918 | E1 | 146.34 | 17.56 |
| 1324.3032 | 39.7016 | E2 | inactive | 16.50 |
| 1324.4415 | 39.7058 | B2 | inactive | inactive |
| 1363.6980 | 40.8826 | A2 | 419.02 | inactive |
| 1365.3732 | 40.9329 | E2 | inactive | 16.73 |
| 1365.4040 | 40.9338 | B1 | inactive | inactive |
| 1365.4589 | 40.9354 | E1 | 811.33 | 0.60 |
| 1366.1399 | 40.9558 | A1 | inactive | 45.93 |
| 1366.1966 | 40.9575 | E1 | 309.44 | 1.48 |
| 1366.4559 | 40.9653 | E2 | inactive | 8.42 |
| 1366.6175 | 40.9702 | B2 | inactive | inactive |
| 1382.1939 | 41.4371 | A2 | 771.55 | inactive |
| 1383.0345 | 41.4623 | B1 | inactive | inactive |
| 1383.7009 | 41.4823 | E2 | inactive | 5.23 |
| 1385.1171 | 41.5248 | E1 | 290.82 | 18.05 |
| 1389.3237 | 41.6509 | A1 | inactive | 9.67 |
| 1390.2138 | 41.6776 | E1 | 3334.80 | 0.01 |
| 1391.5346 | 41.7172 | E2 | inactive | 46.01 |

| 1391.9597 | 41.7299 | B2 | inactive | inactive |
|---|---|---|---|---|
| 1498.6254 | 44.9277 | B1 | inactive | inactive |
| 1498.6477 | 44.9283 | E2 | inactive | 2.54 |
| 1498.7488 | 44.9314 | E1 | 7058.34 | 0.08 |
| 1498.7833 | 44.9324 | A1 | inactive | 30.27 |
| 1499.4592 | 44.9527 | B2 | inactive | inactive |
| 1499.5192 | 44.9545 | E2 | inactive | 1.43 |
| 1499.6262 | 44.9577 | E1 | 507.07 | 0.36 |
| 1499.6336 | 44.9579 | A2 | 2.18 | inactive |
| 1578.7474 | 47.3297 | B1 | inactive | inactive |
| 1578.8154 | 47.3317 | E2 | inactive | 4.36 |
| 1578.8542 | 47.3329 | A1 | inactive | 1.14 |
| 1578.8623 | 47.3331 | E1 | 4329.61 | 0.30 |
| 1579.5705 | 47.3543 | A2 | 575.60 | inactive |
| 1582.0172 | 47.4277 | E1 | 1627.24 | 0.06 |
| 1582.2325 | 47.4341 | E2 | inactive | 4.26 |
| 1582.3164 | 47.4367 | B2 | inactive | inactive |
| 1591.9006 | 47.7240 | B2 | inactive | inactive |
| 1591.9624 | 47.7258 | E2 | inactive | 2.33 |
| 1592.0240 | 47.7277 | A2 | 27.37 | inactive |
| 1592.0865 | 47.7296 | E1 | 1005.30 | 0.41 |
| 1626.5929 | 48.7640 | E1 | 2023.04 | 0.15 |
| 1626.6277 | 48.7651 | A1 | inactive | 6.76 |
| 1626.6520 | 48.7658 | E2 | inactive | 6.37 |
| 1626.6694 | 48.7663 | B1 | inactive | inactive |
| 1638.6255 | 49.1248 | A2 | 686.58 | inactive |
| 1641.5459 | 49.2123 | B2 | inactive | inactive |
| 1641.5517 | 49.2125 | E2 | inactive | 4.54 |
| 1641.5975 | 49.2139 | E1 | 171.81 | 4.01 |
| 1666.5552 | 49.9621 | A1 | inactive | 1.57 |
| 1666.6230 | 49.9641 | E1 | 143.97 | 2.54 |
| 1666.7460 | 49.9678 | E2 | inactive | 0.85 |
| 1666.8041 | 49.9695 | B1 | inactive | inactive |
| 2758.1359 | 82.6868 | A1 | inactive | 85.98 |
| 2758.1472 | 82.6872 | E2 | inactive | 44.47 |
| 2758.1590 | 82.6875 | B1 | inactive | inactive |
| 2758.2209 | 82.6894 | E1 | 4825.79 | 0.07 |
| 2766.2742 | 82.9308 | B2 | inactive | inactive |
| 2766.3149 | 82.9320 | E2 | inactive | 88.74 |

| 2766.3273 | 82.9324 | A2 | 31.20 | inactive |
|---|---|---|---|---|
| 2766.3698 | 82.9337 | E1 | 22076.93 | 0.37 |
| 2982.3819 | 89.4096 | E2 | inactive | 20.65 |
| 2982.5517 | 89.4147 | B2 | inactive | inactive |
| 2982.7218 | 89.4198 | A1 | inactive | 217.44 |
| 2982.8661 | 89.4241 | E1 | 117.30 | 2.72 |
| 2983.6479 | 89.4475 | A2 | 126.16 | inactive |
| 2983.9818 | 89.4575 | E2 | inactive | 7.61 |
| 2984.0014 | 89.4581 | B1 | inactive | inactive |
| 2984.0212 | 89.4587 | E1 | 197.73 | 0.57 |
| 3017.8180 | 90.4719 | E1 | 313.98 | 14.24 |
| 3017.8283 | 90.4722 | E2 | inactive | 3.89 |
| 3017.8396 | 90.4726 | A2 | 11.46 | inactive |
| 3017.8517 | 90.4729 | E2 | inactive | 53.80 |
| 3017.8597 | 90.4732 | B2 | inactive | inactive |
| 3017.8969 | 90.4743 | B1 | inactive | inactive |
| 3018.2487 | 90.4848 | A1 | inactive | 246.52 |
| 3018.4425 | 90.4906 | E1 | 5630.57 | 9.74 |
| 3033.7550 | 90.9497 | A2 | 36.65 | inactive |
| 3033.7962 | 90.9509 | B2 | inactive | inactive |
| 3033.8082 | 90.9513 | E2 | inactive | 2.04 |
| 3033.8211 | 90.9517 | E1 | 1841.91 | 2.50 |
| 3034.6772 | 90.9773 | A1 | inactive | 3.30 |
| 3034.7062 | 90.9782 | E1 | 6073.50 | 5.91 |
| 3034.7100 | 90.9783 | E2 | inactive | 21.08 |
| 3034.7103 | 90.9783 | B1 | inactive | inactive |
| 3052.4743 | 91.5109 | E1 | 137.21 | 0.05 |
| 3052.4832 | 91.5111 | E2 | inactive | 48.39 |
| 3052.5422 | 91.5129 | B2 | inactive | inactive |
| 3052.6001 | 91.5146 | A1 | inactive | 18.55 |
| 3055.1324 | 91.5906 | B1 | inactive | inactive |
| 3055.1467 | 91.5910 | E2 | inactive | 2.90 |
| 3055.1644 | 91.5915 | E1 | 121.72 | 7.08 |
| 3055.1844 | 91.5921 | A2 | 14.81 | inactive |
| 3118.3107 | 93.4846 | A1 | inactive | 167.75 |
| 3118.3247 | 93.4850 | E2 | inactive | 0.68 |
| 3118.4125 | 93.4877 | B1 | inactive | inactive |
| 3118.5903 | 93.4930 | E1 | 1700.91 | 4.90 |
| 3152.7457 | 94.5169 | A2 | 11193.49 | inactive |

| 3176.1984 | 95.2200 | B2 | inactive | inactive |
| 3176.2586 | 95.2218 | E2 | inactive | 2.21 |
| 3176.2821 | 95.2225 | E1 | 270.31 | 14.92 |

**Table A-10.** Tentative correlation table between the observed peaks for the terahertz spectra of crystalline α-lactose monohydrate (5 - 167 cm⁻¹) at 65 K and ss-DFT simulations.

| Observed (65 K) | | Simulated | |
|---|---|---|---|
| cm⁻¹ | THz | cm⁻¹ | THz |
| 17.8 | 0.54 | 19.4441 | 0.5829 |
| - | - | 34.8735 (unassigned) | 1.0455 (unassigned) |
| - | - | 35.5762 (unassigned) | 1.0665 (unassigned) |
| 41.0 | 1.23 | 43.1646 | 1.294 |
| 47.0 | 1.41 | 49.6656 | 1.4889 |
| - | - | 60.7892 (unassigned) | 1.8224 (unassigned) |
| 62.4 | 1.87 | 64.1179 | 1.9222 |
| 75.5 | 2.27 | 80.8105 | 2.4226 |
| 83.8 | 2.52 | 87.5963 | 2.6261 |
| 88.6 | 2.66 | 92.6547 | 2.7777 |
| 95.7 | 2.87 | 94.1053 | 2.8212 |
| 98.1 | 2.94 | 101.5874 | 3.0455 |
| - | - | 102.4690 (unassigned) | 3.0719 (unassigned) |
| 104.1 | 3.12 | 107.8672 | 3.2338 |
| - | - | 112.4351 (unassigned) | 3.3707 (unassigned) |
| 111.2 | 3.34 | 115.1928 | 3.4534 |
| - | - | 117.2567 (unassigned) | 3.5153 (unassigned) |
| - | - | 118.4583 (unassigned) | 3.5513 (unassigned) |
| - | - | 126.2434 (unassigned) | 3.7847 (unassigned) |
| - | - | 140.1306 (unassigned) | 4.201 (unassigned) |
| 138.6 | 4.16 | 142.6420 | 4.2763 |
| - | - | 150.5342 (unassigned) | 4.5129 (unassigned) |
| 149.3 | 4.48 | 152.7000 | 4.5778 |
| 155.8 | 4.67 | 158.5223 | 4.7524 |
| 161.1 | 4.83 | 164.3266 | 4.9264 |

**Table A-11.** Tentative correlation table between the observed peaks for the Raman spectra of crystalline α-lactose monohydrate (5 - 167 cm$^{-1}$) at 78 K and ss-DFT simulations.

| Observed (78 K) | | Simulated | |
|---|---|---|---|
| cm$^{-1}$ | THz | cm$^{-1}$ | THz |
| 17.9 | 0.54 | 19.4441 | 0.5829 |
| 32.9 | 0.99 | 34.8735 | 1.0455 |
| - | - | 35.5762 (unassigned) | 1.0665 (unassigned) |
| 41.0 | 1.23 | 43.1646 | 1.2940 |
| 47.3 | 1.42 | 49.6656 | 1.4889 |
| 57.9 | 1.74 | 60.7892 | 1.8224 |
| 75.7 | 2.27 | 64.1179 | 1.9222 |
| 84.3 | 2.53 | 80.8105 | 2.4226 |
| 89.1 | 2.67 | 87.5963 | 2.6261 |
| - | - | 92.6547 (unassigned) | 2.7777 (unassigned) |
| 95.8 | 2.87 | 94.1053 | 2.8212 |
| 100.9 | 3.03 | 101.5874 | 3.0455 |
| - | - | 102.469 (unassigned) | 3.0719 (unassigned) |
| - | - | 107.8672 (unassigned) | 3.2338 (unassigned) |
| - | - | 112.4351 (unassigned) | 3.3707 (unassigned) |
| - | - | 115.1928 (unassigned) | 3.4534 (unassigned) |
| 114.5 | 3.44 | 117.2567 | 3.5153 |
| - | - | 118.4583 (unassigned) | 3.5513 (unassigned) |
| 124.3 | 3.73 | 126.2434 | 3.7847 |
| 140.0 | 4.20 | 140.1306 | 4.2010 |
| - | - | 142.642 (unassigned) | 4.2763 (unassigned) |
| - | - | 150.5342 (unassigned) | 4.5129 (unassigned) |
| - | - | 152.7 (unassigned) | 4.5778 (unassigned) |
| 156.7 | 4.70 | 158.5223 | 4.7524 |
| 163.0 | 4.89 | 164.3266 | 4.9264 |

**Table A-12.** Tentative correlation table between the observed peaks for the terahertz spectra of crystalline biotin (5 - 167 cm$^{-1}$) at 65 K and ss-DFT simulations.

| Observed (65 K) | | Simulated | |
|---|---|---|---|
| cm$^{-1}$ | THz | cm$^{-1}$ | THz |
| 17.8 | 0.54 | 18.1304 | 0.5435 |
| 35.1 | 1.05 | 34.3676 | 1.0303 |
| - | - | 41.5293 (unassigned) | 1.245 (unassigned) |
| 44.6 | 1.34 | 43.0083 | 1.2894 |
| 50.5 | 1.52 | 49.7455 | 1.4913 |
| 54.1 | 1.62 | 52.9894 | 1.5886 |
| - | - | 57.951 (unassigned) | 1.7373 (unassigned) |
| 60.7 | 1.82 | 60.6493 | 1.8182 |
| 63.6 | 1.91 | 68.6355 | 2.0576 |
| 69.6 | 2.09 | 70.4565 | 2.1122 |
| 73.7 | 2.21 | 73.6898 | 2.2092 |
| - | - | 74.8702 (unassigned) | 2.2446 (unassigned) |
| - | - | 75.3423 (unassigned) | 2.2587 (unassigned) |
| 79.1 | 2.37 | 78.1471 | 2.3428 |
| - | - | 82.2866 (unassigned) | 2.4669 (unassigned) |
| - | - | 87.8114 (unassigned) | 2.6325 (unassigned) |
| - | - | 87.8687 (unassigned) | 2.6342 (unassigned) |
| - | - | 88.6505 (unassigned) | 2.6577 (unassigned) |
| - | - | 91.2291 (unassigned) | 2.735 (unassigned) |
| 96.9 | 2.91 | 94.7242 | 2.8398 |
| - | - | 101.081 (unassigned) | 3.0303 (unassigned) |
| 104.1 | 3.12 | 102.1425 | 3.0622 |
| 110.0 | 3.30 | 108.1842 | 3.2433 |
| - | - | 111.4882 (unassigned) | 3.3423 (unassigned) |
| 121.3 | 3.64 | 119.5173 | 3.5830 |
| - | - | 124.0319 (unassigned) | 3.7184 (unassigned) |
| 130.2 | 3.91 | 127.9458 | 3.8357 |
| - | - | 135.9831 (unassigned) | 4.0767 (unassigned) |
| - | - | 140.1328 (unassigned) | 4.2011 (unassigned) |
| - | - | 142.4787 (unassigned) | 4.2714 (unassigned) |
| - | - | 143.9487 (unassigned) | 4.3155 (unassigned) |
| 142.7 | 4.28 | 147.2955 | 4.4158 |
| 148.1 | 4.44 | 149.2133 | 4.4733 |

| 152.2 | 4.57 | 156.8380 | 4.7019 |
|-------|------|----------|--------|
| 160.6 | 4.82 | 159.6733 | 4.7869 |
| 162.3 | 4.87 | 163.7994 | 4.9106 |

**Table A-13.** Tentative correlation table between the observed peaks for the Raman spectra of crystalline biotin (5 - 167 cm$^{-1}$) at 78 K and ss-DFT simulations.

| Observed (78 K) | | Simulated | |
|---|---|---|---|
| cm$^{-1}$ | THz | cm$^{-1}$ | THz |
| 18.1 | 0.54 | 18.1304 | 0.5435 |
| 29.0 | 0.87 | 29.4060 | 1.0303 |
| - | - | 34.3676 (unassigned) | 1.245 (unassigned) |
| 41.4 | 1.24 | 39.0644 | 1.2894 |
| - | - | 41.5293 (unassigned) | 1.4913 (unassigned) |
| - | - | 41.5824 (unassigned) | 1.5886 (unassigned) |
| - | - | 43.0083 (unassigned) | 1.7373 (unassigned) |
| - | - | 49.7455 (unassigned) | 1.8182 (unassigned) |
| 52.9 | 1.59 | 52.9894 | 2.0576 |
| - | - | 53.2057 (unassigned) | 2.1122 (unassigned) |
| 59.9 | 1.80 | 57.9510 | 2.2092 |
| 61.9 | 1.86 | 60.6493 | 2.2446 |
| - | - | 66.6649 (unassigned) | 2.2587 (unassigned) |
| - | - | 68.6355 (unassigned) | 2.3428 (unassigned) |
| 68.6 | 2.06 | 70.4565 | 2.4669 |
| - | - | 73.6898 (unassigned) | 2.6325 (unassigned) |
| - | - | 74.8702 (unassigned) | 2.6342 (unassigned) |
| - | - | 75.3423 (unassigned) | 2.6577 (unassigned) |
| - | - | 78.1471 (unassigned) | 2.735 (unassigned) |
| - | - | 82.2866 (unassigned) | 2.8398 (unassigned) |
| 82.3 | 2.47 | 82.5037 | 3.0303 |
| - | - | 85.8007 (unassigned) | 3.0622 (unassigned) |
| - | - | 87.8114 (unassigned) | 3.2433 (unassigned) |
| - | - | 87.8687 (unassigned) | 3.3423 (unassigned) |
| - | - | 88.6505 (unassigned) | 3.583 (unassigned) |
| 88.8 | 2.67 | 89.1244 | 3.7184 |
| - | - | 91.2291 (unassigned) | 3.8357 (unassigned) |
| - | - | 94.7242 (unassigned) | 4.0767 (unassigned) |
| - | - | 101.081 (unassigned) | 4.2011 (unassigned) |
| - | - | 102.1425 (unassigned) | 4.2714 (unassigned) |
| - | - | 102.5600 (unassigned) | 4.3155 (unassigned) |
| 106.5 | 3.19 | 108.1842 | 4.4158 |
| - | - | 111.4882 (unassigned) | 4.4733 (unassigned) |
| - | - | 119.5173 (unassigned) | 4.7019 (unassigned) |

| - | - | 124.0319 (unassigned) | 4.7869 (unassigned) |
|---|---|---|---|
| 126.5 | 3.79 | 126.3905 | 4.9106 |
| - | - | 127.9458 (unassigned) | 5.2435 (unassigned) |
| - | - | 135.9831 (unassigned) | 5.3816 (unassigned) |
| - | - | 135.9901 (unassigned) | 5.4681 (unassigned) |
| - | - | 140.1328 (unassigned) | 5.7546 (unassigned) |
| - | - | 142.4787 (unassigned) | 5.8196 (unassigned) |
| - | - | 143.9487 (unassigned) | 4.3189 (unassigned) |
| - | - | 147.2955 (unassigned) | 4.4193 (unassigned) |
| - | - | 149.1212 (unassigned) | 4.4741 (unassigned) |
| - | - | 149.2133 (unassigned) | 4.4768 (unassigned) |
| - | - | 156.838 (unassigned) | 4.7053 (unassigned) |
| - | - | 159.6733 (unassigned) | 4.7907 (unassigned) |
| - | - | 161.6497 (unassigned) | 4.8500 (unassigned) |
| - | - | 163.7994 (unassigned) | 4.9145 (unassigned) |

**Table A-14.** Tentative correlation table between the observed peaks for the terahertz spectra of crystalline L-cystine (5 - 167 cm$^{-1}$) at 50 K and ss-DFT simulations.

| Observed (50 K) | | Simulated | |
|---|---|---|---|
| cm$^{-1}$ | THz | cm$^{-1}$ | THz |
| 9.3 | 0.28 | 10.7231 | 0.3215 |
| 25.6 | 0.77 | 26.2916 | 0.7882 |
| - | - | 29.0278 (unassigned) | 0.8702 (unassigned) |
| - | - | 49.2947 (unassigned) | 1.4778 (unassigned) |
| 52.9 | 1.59 | 53.2425 | 1.5962 |
| - | - | 70.2051 (unassigned) | 2.1047 (unassigned) |
| 70.2 | 2.11 | 71.0327 | 2.1295 |
| 76.1 (unassigned) | 2.28 (unassigned) | - | - |
| 79.1 (unassigned) | 2.37 (unassigned) | - | - |
| 83.3 | 2.50 | 74.8157 | 2.2429 |
| - | - | 80.3232 (unassigned) | 2.408 (unassigned) |
| 102.9 | 3.09 | 101.1171 | 3.0314 |
| - | - | 106.4023 (unassigned) | 3.1899 (unassigned) |
| - | - | 115.8603 (unassigned) | 3.4734 (unassigned) |
| - | - | 151.7839 (unassigned) | 4.5504 (unassigned) |
| 140.9 | 4.23 | 154.0333 | 4.6178 |
| - | - | 163.9367 (unassigned) | 4.9147 (unassigned) |
| 164.7 | 4.94 | 168.2627 | 5.0444 |

**Table A-15.** Tentative correlation table between the observed peaks for the Raman spectra of crystalline L-cystine (5 - 167 cm$^{-1}$) at 78 K and ss-DFT simulations.

| Observed (78 K) | | Simulated | |
|---|---|---|---|
| cm$^{-1}$ | THz | cm$^{-1}$ | THz |
| 10.5 | 0.49 | 12.2051 | 0.3659 |
| 15.3 | 0.53 | 15.7526 | 0.4723 |
| - | - | 26.2916 (unassigned) | 0.7882 (unassigned) |
| - | - | 29.0278 (unassigned) | 0.8702 (unassigned) |
| 32.5 | 0.15 | 35.1315 | 1.0532 |
| - | - | 42.9987 (unassigned) | 1.2891 (unassigned) |
| - | - | 49.2947 (unassigned) | 1.4778 (unassigned) |
| 54.9 | 0.16 | 54.0832 | 1.6214 |
| 68.8 | 0.67 | 65.8808 | 1.9751 |
| - | - | 70.2051 (unassigned) | 2.1047 (unassigned) |
| - | - | 71.0276 (unassigned) | 2.1294 (unassigned) |
| - | - | 74.8157 (unassigned) | 2.2429 (unassigned) |
| 77.5 | 0.36 | 78.2667 | 2.3464 |
| 79.9 | 0.38 | 78.6107 | 2.3567 |
| - | - | 80.3232 (unassigned) | 2.408 (unassigned) |
| - | - | 82.5666 (unassigned) | 2.4753 (unassigned) |
| - | - | 102.9947 (unassigned) | 3.0877 (unassigned) |
| 106.2 | 1.00 | 106.4023 | 3.1899 |
| 115.2 | 0.52 | 113.1676 | 3.3927 |
| - | - | 115.8603 (unassigned) | 3.4734 (unassigned) |
| - | - | 120.563 (unassigned) | 3.6144 (unassigned) |
| - | - | 138.6171 (unassigned) | 4.1556 (unassigned) |
| - | - | 147.1037 (unassigned) | 4.4101 (unassigned) |
| 151.7 | 0.38 | 151.7839 | 4.5504 |
| - | - | 154.0333 (unassigned) | 4.6178 (unassigned) |
| 159.1 | 0.56 | 158.6900 | 4.7574 |

**LACTOS11 GEOMETRY OPTIMIZATION**

**CRYSTAL**

**0 0 0**

**4**

**4.7830 21.540 7.7599 105.911**

**48**

| | | | |
|---|---|---|---|
| 1 | 0.3530 | -0.0304 | 0.7625 |
| 1 | -0.1467 | 0.0494 | 0.6322 |
| 1 | -0.1065 | 0.0093 | 0.4019 |
| 1 | 0.4489 | 0.0855 | 0.6738 |
| 1 | 0.2572 | 0.1660 | 0.5474 |
| 1 | 0.4201 | 0.1477 | 0.9200 |
| 1 | -0.0208 | 0.1692 | 0.8833 |
| 1 | 0.5796 | 0.0435 | 0.9901 |
| 1 | 0.5526 | 0.1032 | 1.2414 |
| 1 | 0.2181 | 0.0841 | 1.2094 |
| 1 | 0.3859 | 0.0089 | 1.3672 |
| 1 | -0.0221 | -0.2960 | 0.8191 |
| 1 | -0.4841 | -0.2626 | 0.7136 |
| 1 | 0.3048 | -0.2211 | 0.9721 |
| 1 | -0.0856 | -0.2234 | 1.1546 |
| 1 | -0.1683 | -0.1379 | 0.9577 |
| 1 | 0.2228 | -0.0764 | 1.0755 |
| 1 | 0.2609 | -0.1262 | 0.7605 |
| 1 | -0.3432 | -0.1599 | 0.6155 |
| 1 | -0.1494 | -0.1019 | 0.4084 |
| 1 | 0.0965 | -0.1540 | 0.4269 |
| 1 | -0.4400 | -0.1604 | 0.2395 |
| 1 | 0.6190 | 0.2294 | 0.6160 |
| 1 | 0.7640 | 0.1835 | 0.5480 |

6        0.1611 -0.0141        0.7705

6        0.0574 0.0381 0.6356

6        0.2515 0.0950 0.6874

6        0.2784 0.1128 0.8832

6        0.3853 0.0566 1.0023

6        0.4085 0.0698 1.1971

6        -0.0864        -0.2516        0.8074

6        0.0961 -0.2152        0.9691

6        0.0325 -0.1460        0.9477

6        0.0540 -0.1238        0.7645

6        -0.1351        -0.1637        0.6149

6        -0.1058        -0.1466        0.4311

8        -0.0485        -0.0611        0.7307

8        0.0640 0.0159 0.4648

8        0.1249 0.1441 0.5683

8        0.0032 0.1310 0.9035

8        0.4960 0.0148 1.3010

8        0.1815 0.0062 0.9485

8        -0.3771        -0.2488        0.8105

8        0.0602 -0.2398        1.1327

8        0.2382 -0.1150        1.0912

8        -0.3010        -0.1828        0.2957

8        -0.0445        -0.2271        0.6468

8        0.6064 0.2040 0.5314

OPTGEOM

TOLDEG

0.000010

TOLDEX

0.000040

END

**BASISSET**

**DEF2-TZVP**

**DFT**

**PBE-D**

**XLGRID**

**END**

**DFTD3**

**ABC**

**END**

**MAXCYCLE**

**200**

**SCFDIR**

**TOLINTEG**

**8 8 8 8 16**

**TOLDEE**

**8**

**SHRINK**

**8 8**

**END**

**LACTOS11 FREQUENCY**

**CRYSTAL**

**0 0 0**

**4**

**4.74561167    21.58750942    7.75590551    106.099382**

**48**

| | | | |
|---|---|---|---|
| 1 | 0.37709234714810 | -0.03430376584060 | -0.23210653661860 |
| 1 | -0.15493516554050 | 0.05104201315906 | -0.36161992178500 |
| 1 | -0.14596952161240 | 0.01051422822208 | 0.39729271736240 |
| 1 | 0.49042851307410 | 0.08111248344468 | -0.31675255620200 |
| 1 | 0.32555481176670 | 0.16697837345460 | -0.44535782390260 |
| 1 | 0.46696789798430 | 0.14737778251980 | -0.07129413734677 |
| 1 | 0.01322879082830 | 0.17794954932820 | -0.11407073417800 |
| 1 | -0.38867707219840 | 0.03913000741999 | -0.00705081786719 |
| 1 | -0.40783270727150 | 0.10465315235660 | 0.24902093236950 |
| 1 | 0.21356315341190 | 0.08679929226773 | 0.21594834611020 |
| 1 | 0.35389833123620 | 0.00955656661044 | 0.37924453821030 |
| 1 | -0.03320585000190 | -0.29975829858380 | -0.19063544724990 |
| 1 | 0.47972394033960 | -0.26621381912670 | -0.31545090146240 |
| 1 | 0.30609548460090 | -0.22464535680970 | -0.02755173959230 |
| 1 | -0.11935483580740 | -0.21766789891460 | 0.17177170031120 |
| 1 | -0.20453296800470 | -0.13601992867180 | -0.04333322407356 |
| 1 | 0.21989158589030 | -0.07013655332236 | 0.07181141163667 |
| 1 | 0.27522357330710 | -0.12788180034070 | -0.23635020533820 |
| 1 | -0.37861407774080 | -0.15831974837290 | -0.38856781204160 |
| 1 | -0.14857944546380 | -0.09649557980331 | 0.40907771413890 |
| 1 | 0.11340724662180 | -0.15674231375660 | 0.42676378822480 |
| 1 | -0.47299892927440 | -0.15427294070380 | 0.22329132680390 |
| 1 | -0.31793717925090 | 0.23276432630830 | -0.36754650262360 |
| 1 | -0.17255841516680 | 0.17899101616370 | -0.44774020356360 |

| | | | |
|---|---|---|---|
| 6 | 0.16236165723330 | -0.01550621392205 | -0.22550332304300 |
| 6 | 0.06870247128186 | 0.03719349179543 | -0.36108720614810 |
| 6 | 0.26880113593970 | 0.09326921839976 | -0.30806989794190 |
| 6 | 0.29631808344380 | 0.11134561905100 | -0.11216366053900 |
| 6 | 0.39669363025690 | 0.05466542863171 | 0.00761289379018 |
| 6 | 0.42275840109080 | 0.06870483396201 | 0.20262999928060 |
| 6 | -0.11017666701130 | -0.25138797722080 | -0.19490082386080 |
| 6 | 0.07663224693882 | -0.21607290990640 | -0.03022039277231 |
| 6 | 0.02002037549522 | -0.14634589544580 | -0.05084617803179 |
| 6 | 0.04382796487102 | -0.12428157518260 | -0.23443626642450 |
| 6 | -0.14612495225140 | -0.16389695563830 | -0.38646501955650 |
| 6 | -0.11215713140790 | -0.14643032662310 | 0.43057952473320 |
| 8 | -0.05348926379864 | -0.06126731324645 | -0.26694172206230 |
| 8 | 0.06629952455838 | 0.01478312956487 | 0.46618735268500 |
| 8 | 0.15528440005130 | 0.14246550799140 | -0.42979636646570 |
| 8 | 0.02383042794981 | 0.13270117432590 | -0.09186919359274 |
| 8 | -0.49922191703020 | 0.01381508337435 | 0.30940720513110 |
| 8 | 0.18607563925500 | 0.00506189599850 | -0.04652398298702 |
| 8 | -0.40644312119990 | -0.24826695159130 | -0.19827078526730 |
| 8 | 0.03834028948278 | -0.24052809425500 | 0.13340143602890 |
| 8 | 0.22787914034610 | -0.11546647016440 | 0.09354343813543 |
| 8 | -0.30914817184440 | -0.18127982438650 | 0.29049446176230 |
| 8 | -0.06023912057792 | -0.22714428471850 | -0.35469338279080 |
| 8 | -0.36239925402310 | 0.20165862219810 | -0.46407494896140 |

FREQCALC

NUMDERIV

2

INTENS

INTRAMAN

RAMEXP

**78 784.7**

**INTCPHF**

**ANDERSON**

**ANDERSON2**

**END**

**END**

**BASISSET**

**DEF2-TZVP**

**DFT**

**PBE-D**

**XLGRID**

**END**

**DFTD3**

**ABC**

**END**

**MAXCYCLE**

**200**

**SCFDIR**

**TOLINTEG**

**8 8 8 8 16**

**TOLDEE**

**10**

**SHRINK**

**8 8**

**END**

**BIOTIN12 GEOMETRY OPTIMIZATION**

**CRYSTAL**

**0 0 0**

**19**

**5.1955 10.3017 20.943**

**32**

| | | | |
|---|---|---|---|
| 16 | 0.56496 | 0.37007 | 0.04622 |
| 8 | 0.4697 | 0.48208 | -0.18884 |
| 8 | 0.3843 | 0.69236 | -0.19861 |
| 8 | 0.423 | 0.57414 | 0.24408 |
| 7 | 0.5386 | 0.37186 | 0.2059 |
| 7 | 0.7453 | 0.54283 | 0.17099 |
| 6 | 0.5182 | 0.6058 | -0.17793 |
| 6 | 0.753 | 0.6264 | -0.13749 |
| 6 | 0.7105 | 0.5814 | -0.0684 |
| 6 | 0.9575 | 0.5932 | -0.02951 |
| 6 | 0.9253 | 0.577 | 0.04246 |
| 6 | 0.8745 | 0.4413 | 0.06772 |
| 6 | 0.8828 | 0.4365 | 0.14098 |
| 6 | 0.732 | 0.3151 | 0.16447 |
| 6 | 0.6168 | 0.246 | 0.1062 |
| 6 | 0.5574 | 0.5015 | 0.21013 |
| 1 | 0.436 | 0.333 | 0.2307 |
| 1 | 0.3353 | 0.4754 | -0.2109 |
| 1 | 0.7983 | 0.7198 | -0.1376 |
| 1 | 0.8992 | 0.5778 | -0.1561 |
| 1 | 0.803 | 0.6209 | 0.1756 |
| 1 | 0.574 | 0.6348 | -0.0484 |
| 1 | 0.6522 | 0.4899 | -0.0683 |
| 1 | 1.0343 | 0.6795 | -0.0379 |

```
1        1.0809 0.527   -0.0449
1        1.0833 0.6101 0.0633
1        0.7814 0.6334 0.0563
1        1.0131 0.3829 0.0511
1        1.0649 0.4334 0.1564
1        0.8472 0.2554 0.189
1        0.452  0.2037 0.1176
1        0.7368 0.179  0.0901
OPTGEOM
TOLDEG
0.000010
TOLDEX
0.000040
END
BASISSET
DEF2-TZVP
DFT
PBE-D
XLGRID
END
DFTD3
ABC
END
MAXCYCLE
200
SCFDIR
TOLINTEG
8 8 8 8 16
TOLDEE
8
```

**SHRINK**

**10 10**

**END**

**BIOTIN12 FREQUENCY**

**CRYSTAL**

**0 0 0**

**19**

**5.16853962    10.33726597    20.91739929**

**32**

| | | | |
|---|---|---|---|
| 16 | -0.428599279265400 | 0.368520670211100 | 0.041903619297710 |
| 8 | 0.464499954911700 | 0.486600929048100 | -0.189755451896700 |
| 8 | 0.375894459504400 | -0.301586615180100 | -0.200944178524900 |
| 8 | 0.422053789770100 | -0.426839680028700 | 0.243484938570400 |
| 7 | -0.468154716492400 | 0.369954064591700 | 0.202748532581500 |
| 7 | -0.251841966652500 | -0.457972780231000 | 0.169402063109700 |
| 6 | -0.486949848516500 | -0.389898659292700 | -0.179506175482100 |
| 6 | -0.250468764189200 | -0.367570617322500 | -0.138886699384900 |
| 6 | -0.288743594799400 | -0.413241642955000 | -0.069716683078750 |
| 6 | -0.037594757882600 | -0.404058157719200 | -0.031478648761170 |
| 6 | -0.065542035701390 | -0.422662413775700 | 0.040662222481170 |
| 6 | -0.118173677038800 | 0.441213892732500 | 0.065161845507520 |
| 6 | -0.115259226324900 | 0.435511221716500 | 0.138928989858700 |
| 6 | -0.270384812598200 | 0.314035348250500 | 0.161760115384600 |
| 6 | -0.381253219274600 | 0.245055339184500 | 0.102813554803400 |
| 6 | -0.443940204458800 | -0.499661087190700 | 0.208378473255600 |
| 1 | 0.418619216751100 | 0.317984565506300 | 0.233557197800400 |
| 1 | 0.299330361717600 | 0.473067070908400 | -0.218610923850700 |
| 1 | -0.199260340944400 | -0.264563651880700 | -0.140934811486700 |
| 1 | -0.090247284721790 | -0.422649971882000 | -0.160295092884900 |
| 1 | -0.174135339803400 | -0.367598211353100 | 0.176816022038000 |
| 1 | -0.439712772457700 | -0.354354715869500 | -0.046566604369360 |
| 1 | -0.360239592315500 | 0.486525212425900 | -0.070025528396680 |
| 1 | 0.046506778840460 | -0.307376676120300 | -0.039568952492860 |

| 1 | 0.104469468970100 | -0.473454669131800 | -0.050629074237950 |
| 1 | 0.117789001338200 | -0.392788968910700 | 0.063363562149400 |
| 1 | -0.216204381870600 | -0.357317448506700 | 0.059247692835100 |
| 1 | 0.034045753363850 | 0.375463679219900 | 0.047566149336070 |
| 1 | 0.087836602551780 | 0.432334342298000 | 0.154770681444500 |
| 1 | -0.148172416645900 | 0.247030600775900 | 0.189064257798100 |
| 1 | 0.434646791609700 | 0.196692136390500 | 0.113273072680300 |
| 1 | -0.242096826865900 | 0.172974464165100 | 0.085069017728660 |

FREQCALC

NUMDERIV

2

INTENS

INTRAMAN

RAMEXP

78 784.7

INTCPHF

ANDERSON

ANDERSON2

END

END

BASISSET

DEF2-TZVP

DFT

PBE-D

XLGRID

END

DFTD3

ABC

END

MAXCYCLE

**200**

**SCFDIR**

**TOLINTEG**

**8 8 8 8 16**

**TOLDEE**

**10**

**SHRINK**

**10 10**

**END**

**LCYSYI14 GEOMETRY OPTIMIZATION**

**CRYSTAL**

**0 0 0**

**178**

**5.412   55.956**

**13**

| | | | |
|---|---|---|---|
| 16 | 0.03234 | 0.8306 | 0.0798 |
| 8 | 0.0738 | 1.225 | 0.02275 |
| 6 | -0.172 | 1.0311 | 0.02913 |
| 8 | -0.383 | 1.0614 | 0.0323 |
| 6 | -0.2129 | 0.732 | 0.03332 |
| 6 | -0.2656 | 0.6395 | 0.05941 |
| 7 | 0.032 | 0.7173 | 0.02317 |
| 1 | -0.31048 | 0.42059 | 0.06023 |
| 1 | -0.44231 | 0.65857 | 0.06635 |
| 1 | -0.40397 | 0.57561 | 0.0241 |
| 1 | 0.01816 | 0.52107 | 0.02503 |
| 1 | 0.22427 | 0.86655 | 0.03052 |
| 1 | 0.04481 | 0.75936 | 0.00508 |

**OPTGEOM**

**TOLDEG**

**0.000010**

**TOLDEX**

**0.000040**

**END**

**BASISSET**

**DEF2-TZVP**

**DFT**

**PBE-D**

**XLGRID**

**END**

**DFTD3**

**ABC**

**END**

**MAXCYCLE**

**200**

**SCFDIR**

**TOLINTEG**

**8 8 8 8 16**

**TOLDEE**

**8**

**SHRINK**

**8 8**

**END**

**LCYSYI14 FREQUENCY**

**CRYSTAL**

**0 0 0**

**178**

**5.40602794    56.50761595**

**13**

| | | | |
|---|---|---|---|
| **16** | **0.038023345941950** | **-0.167299467559200** | **0.079622726968190** |
| **8** | **0.057374599044590** | **0.226561311614400** | **0.022522239852360** |
| **6** | **-0.186092863217500** | **0.027191932894760** | **0.029491161273430** |
| **8** | **-0.399739238314200** | **0.054635191014430** | **0.033186579209200** |
| **6** | **-0.218468996430700** | **-0.268970528689000** | **0.033617188032410** |
| **6** | **-0.261786366477000** | **-0.361081029051200** | **0.059467316299950** |
| **7** | **0.023395768592480** | **-0.282888107435200** | **0.022518821248180** |
| **1** | **-0.308043389477300** | **0.416238304291900** | **0.060437606292820** |
| **1** | **-0.448275798867300** | **-0.354798028648300** | **0.066370897664110** |
| **1** | **-0.413954871331300** | **-0.426599742362100** | **0.024485330162670** |
| **1** | **0.005982587433721** | **-0.487437837527400** | **0.023758015071360** |
| **1** | **0.224304827044000** | **-0.136143447897600** | **0.029451056989460** |
| **1** | **0.019591732577360** | **-0.239249577472500** | **0.004607609577265** |

**FREQCALC**

**NUMDERIV**

**2**

**INTENS**

**INTRAMAN**

**RAMEXP**

**78 784.7**

**INTCPHF**

**ANDERSON**

**ANDERSON2**

**END**

**END**

**BASISSET**

**DEF2-TZVP**

**DFT**

**PBE-D**

**XLGRID**

**END**

**DFTD3**

**ABC**

**END**

**MAXCYCLE**

**200**

**SCFDIR**

**TOLINTEG**

**8 8 8 8 16**

**TOLDEE**

**10**

**SHRINK**

**8 8**

**END**

XY data for all THz-TDS waveforms and processed THz-TDS and LFRS data can be found

using the DOI: https://doi.org/10.1007/s10762-020-00725-y

# Appendix B: Supporting Information for Chapter 6

**Table of Contents:**

**Table B-1**. Mode labels, vibrational frequencies, symmetry representations, and IR/Raman intensities for crystalline GABA simulated using ss-DFT.

**Table B-2.** Anharmonic calculations for N–H1 across unit cell volume expansions.

**Table B-3.** Anharmonic calculations for N–H2 across unit cell volume expansions.

**Table B-4.** Anharmonic calculations for N–H3 across unit cell volume expansions.

**Figure B-3.** PXRD patterns of GABA at 300 K (red), 100 K (blue), and simulated from the 95 K single crystal coordinates (black).
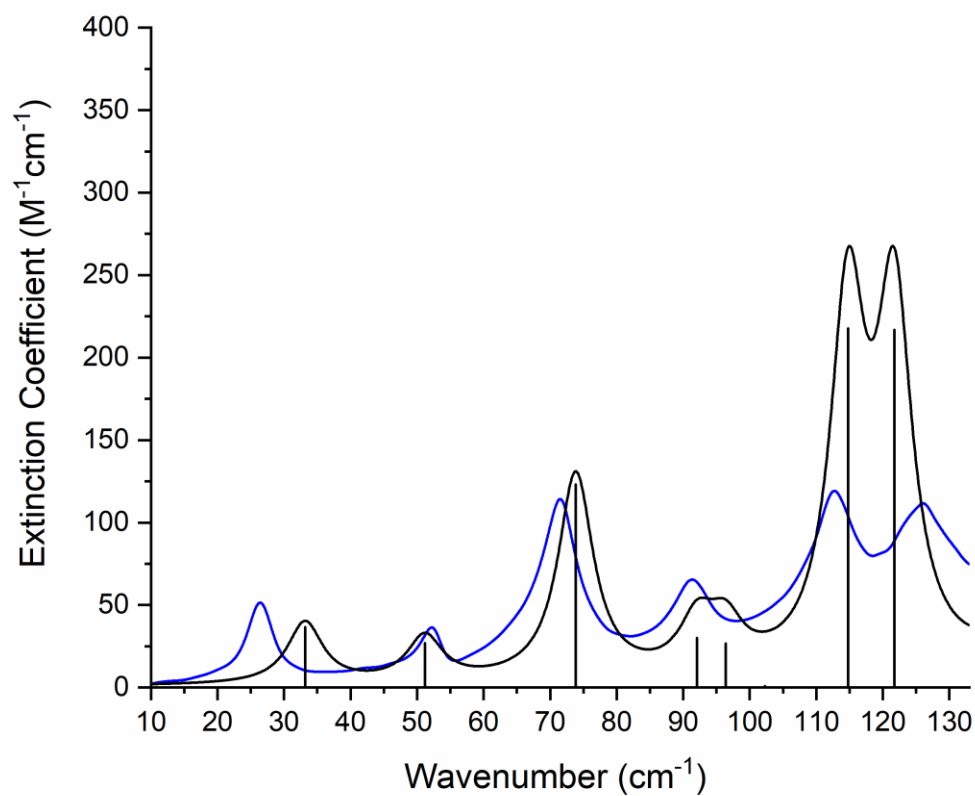
**Figure B-2.** Overlay of the simulated THz-TDS spectrum (frequencies scaled by 0.95) from a fixed lattice geometry optimization (black) with the 78 K experimental data (blue) for GABA. The simulated spectrum is convolved with an empirical Lorentzian line shape with a full-width-at-half-maximum (FWHM) of 6.8 cm⁻¹.
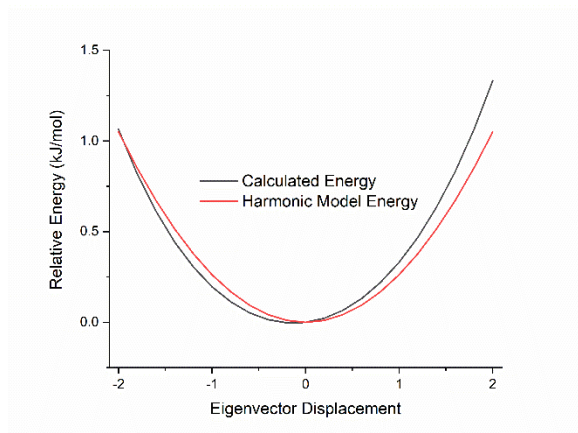
**Figure B-3.** Relative total energy compared to the harmonic energy for $\nu_2$.
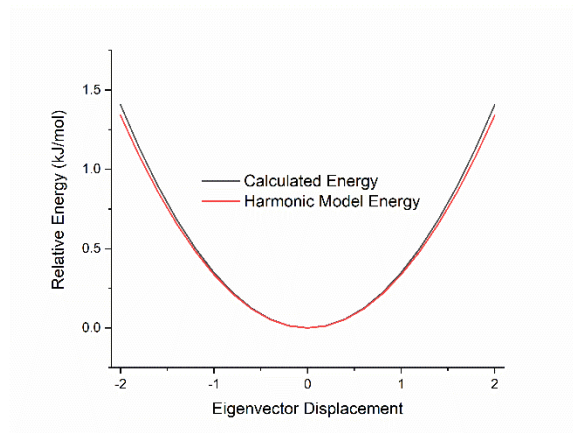


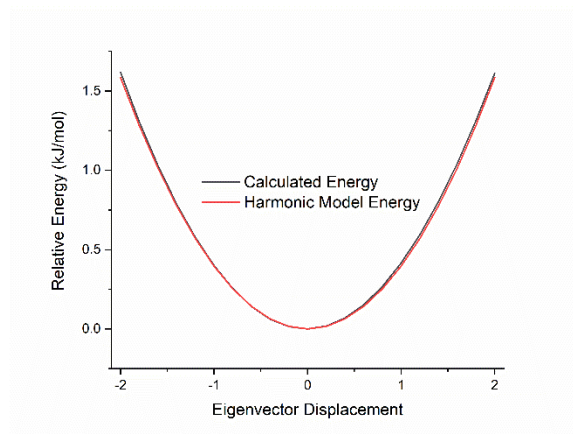**Figure B-4.** Relative total energy compared to the harmonic energy for $\nu_3$.
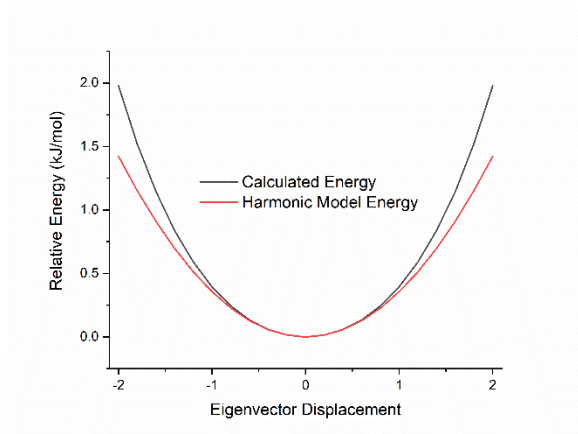


**Figure B-5.** Relative total energy compared to the harmonic energy for $\nu_4$.



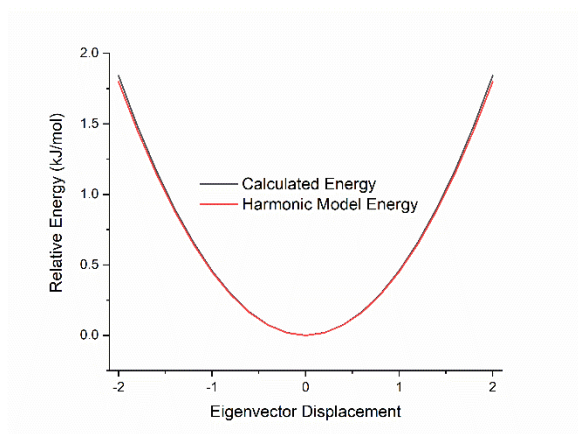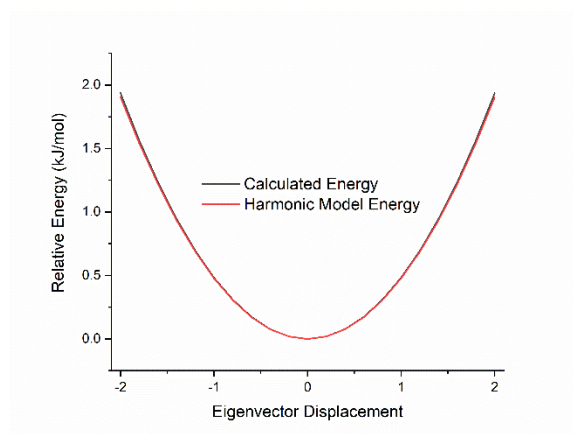**Figure B-6.** Relative total energy compared to the harmonic energy for $\nu_5$.



**Figure B-7.** Relative total energy compared to the harmonic energy for $\nu_6$.



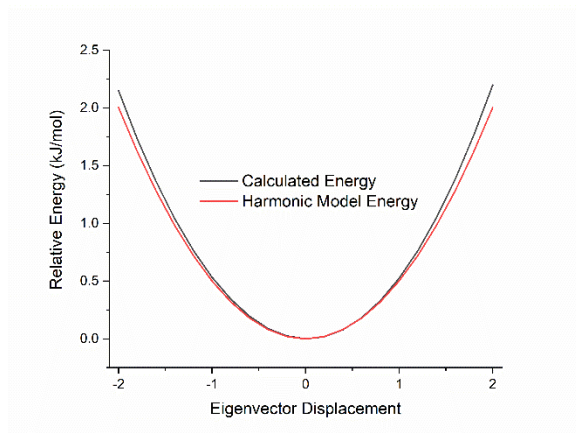**Figure B-8.** Relative total energy compared to the harmonic energy for $\nu_7$.

**Figure B-9.** Relative total energy compared to the harmonic energy for $\nu_8$.
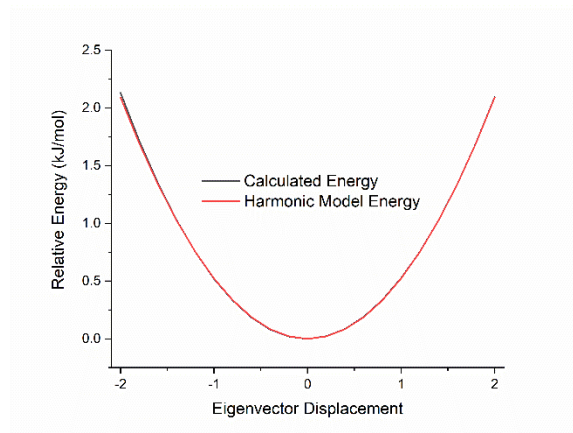


**Figure B-10.** Relative total energy compared to the harmonic energy for $\nu_9$.



**Figure B-11**. Relative total energy compared to the harmonic energy for $\nu_{10}$.



**Figure B-12.** Relative total energy compared to the harmonic energy for $\nu_{11}$.

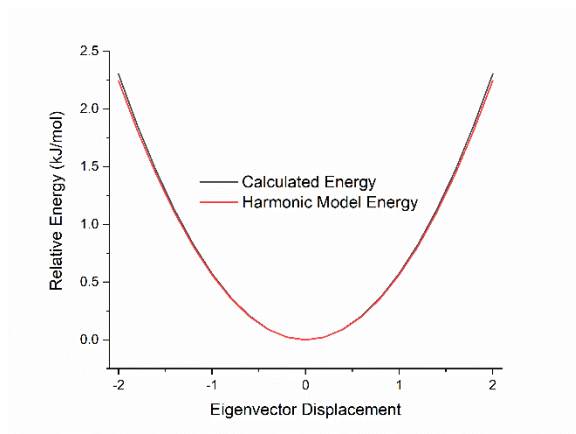

**Figure B-13.** Relative total energy compared to the harmonic energy for $\nu_{12}$.

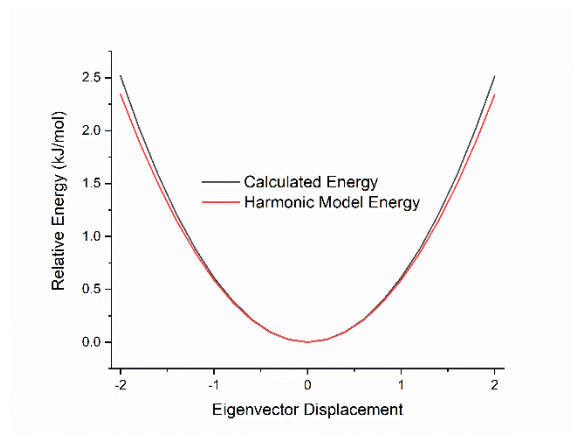

**Figure B-14.** Relative total energy compared to the harmonic energy for $\nu_{13}$.

**Figure B-15.** Relative total energy compared to the harmonic energy for $\nu_{14}$.



**Figure B-16.** Relative total energy compared to the harmonic energy for $\nu_{15}$.



**Figure B-17.** Relative total energy compared to the harmonic energy for $\nu_{16}$.



**Figure B-18.** Relative total energy compared to the harmonic energy for $\nu_{17}$.



**Figure B-19.** Relative total energy compared to the harmonic energy for $\nu_{18}$.
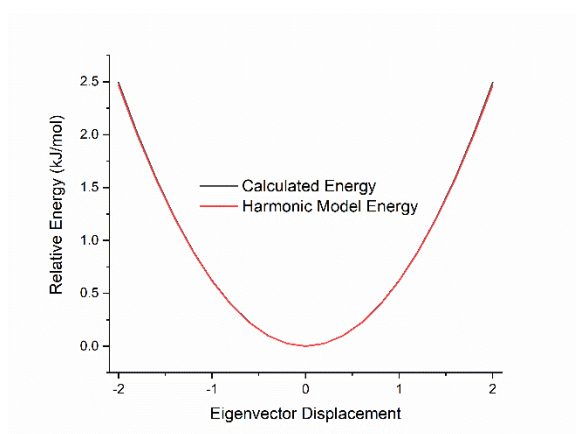


**Figure B-20.** Relative total energy compared to the harmonic energy for $\nu_{19}$.
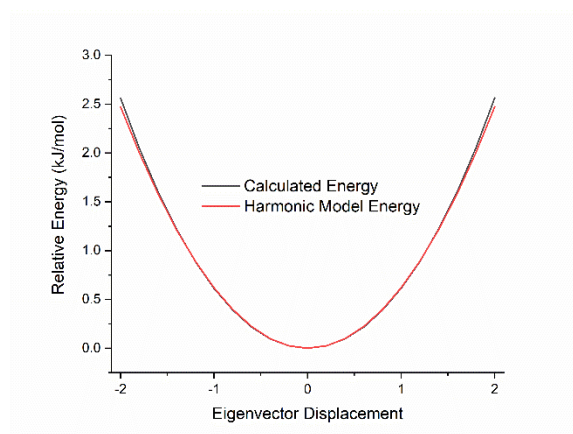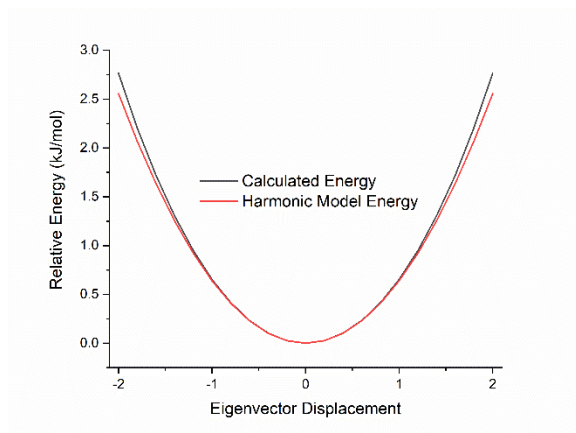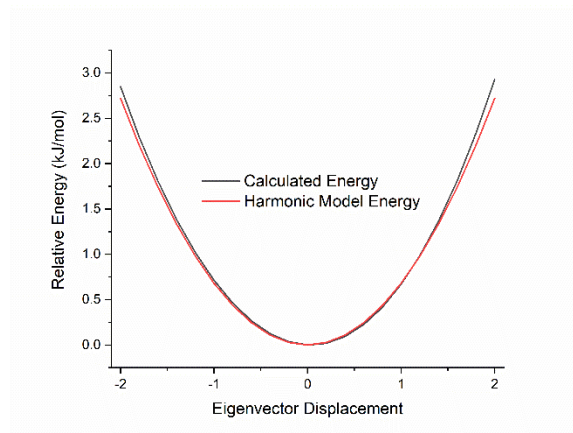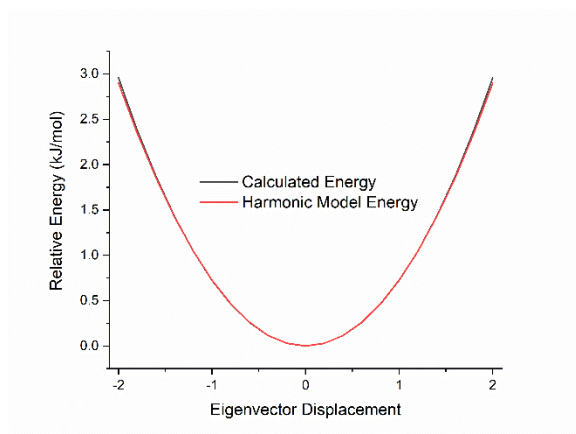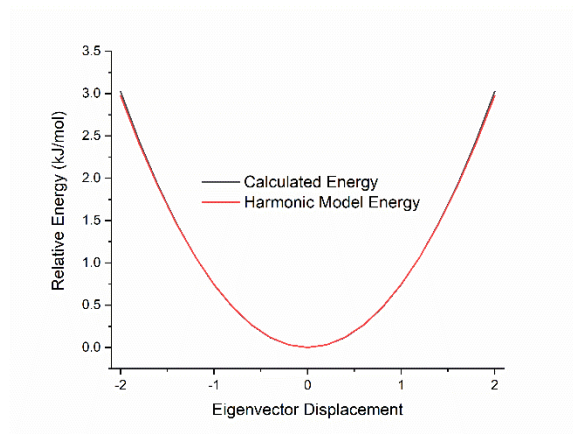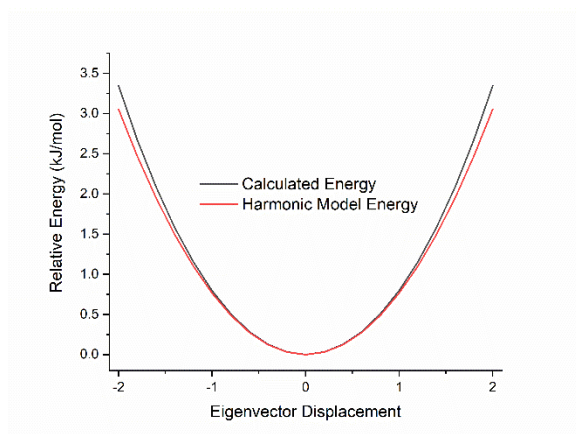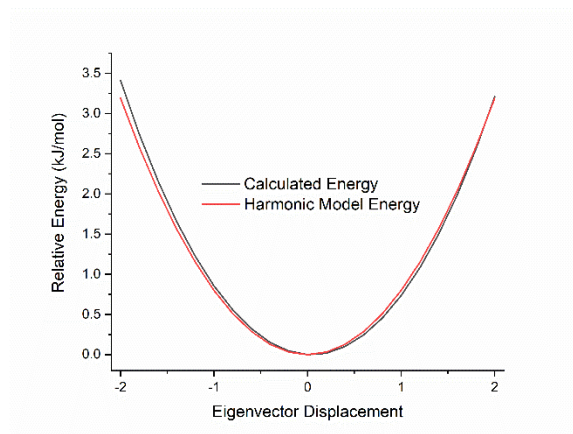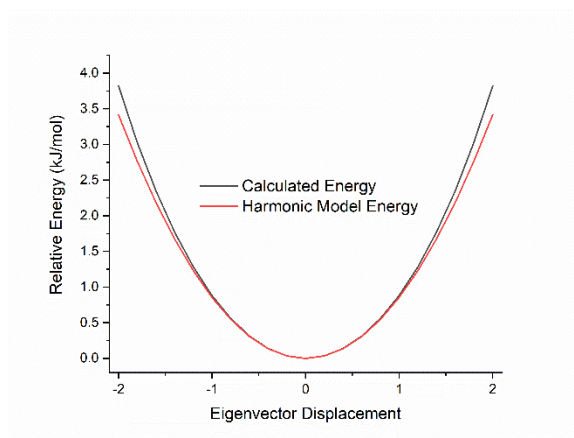
**Figure S21.** Relative total energy compared to the harmonic energy for $\nu_{20}$.

**Table B-1.** Mode labels, vibrational frequencies, symmetry representations, and IR/Raman intensities for crystalline GABA simulated using ss-DFT.

| Mode label (v) | Frequencies | | Symmetry representation | Intensity | |
|---|---|---|---|---|---|
| | cm$^{-1}$ | THz | | IR (km/mol) | Raman (arb. Units) |
| 1 | 32.2503 | 0.9668 | Bu | 10.28 | |
| 2 | 43.8737 | 1.3153 | Ag | | 355.48 |
| 3 | 55.9917 | 1.6786 | Au | 2.36 | |
| 4 | 59.4509 | 1.7823 | Bg | | 379.75 |
| 5 | 66.1818 | 1.9841 | Ag | | 25.14 |
| 6 | 75.1415 | 2.2527 | Bg | | 36.17 |
| 7 | 79.5252 | 2.3841 | Au | 39.11 | |
| 8 | 83.7827 | 2.5117 | Ag | | 25.26 |
| 9 | 87.3872 | 2.6198 | Ag | | 45.87 |
| 10 | 93.7647 | 2.8110 | Bg | | 21.2 |
| 11 | 97.8720 | 2.9341 | Bg | | 243.85 |
| 12 | 103.0457 | 3.0892 | Bu | 9.22 | |
| 13 | 103.3435 | 3.0982 | Au | 9.97 | |
| 14 | 106.7981 | 3.2017 | Au | 0.32 | |
| 15 | 113.6612 | 3.4075 | Ag | | 31.14 |
| 16 | 121.1360 | 3.6316 | Bu | 67.06 | |
| 17 | 124.2683 | 3.7255 | Bg | | 26.64 |
| 18 | 127.6021 | 3.8254 | Bu | 42.99 | |
| 19 | 133.2920 | 3.9960 | Ag | | 77.26 |
| 20 | 142.7648 | 4.2800 | Bg | | 3.89 |
| 21 | 151.5973 | 4.5448 | Ag | | 158.02 |
| 22 | 152.2333 | 4.5638 | Bu | 24.94 | |
| 23 | 153.0054 | 4.5870 | Au | 1.23 | |
| 24 | 168.4892 | 5.0512 | Au | 14.34 | |
| 25 | 195.2613 | 5.8538 | Au | 232.43 | |
| 26 | 195.7729 | 5.8691 | Bg | | 17.76 |
| 27 | 203.2510 | 6.0933 | Bu | 97.05 | |
| 28 | 211.7363 | 6.3477 | Ag | | 9.02 |
| 29 | 219.2525 | 6.5730 | Bg | | 35.98 |
| 30 | 226.8069 | 6.7995 | Ag | | 42.36 |
| 31 | 243.0902 | 7.2877 | Bg | | 2.13 |
| 32 | 272.8320 | 8.1793 | Au | 82.46 | |
| 33 | 275.4524 | 8.2579 | Bu | 12.29 | |

| 34 | 292.9524 | 8.7825 | Bu | 587.07 | |
| 35 | 294.6086 | 8.8321 | Ag | | 9.71 |
| 36 | 299.3363 | 8.9739 | Au | 30.12 | |
| 37 | 299.7816 | 8.9872 | Bg | | 3.51 |
| 38 | 329.9514 | 9.8917 | Ag | | 33.72 |
| 39 | 333.5227 | 9.9988 | Au | 180 | |
| 40 | 336.9189 | 10.1006 | Bg | | 32.24 |
| 41 | 342.0875 | 10.2555 | Bu | 40.44 | |
| 42 | 401.1797 | 12.0271 | Bu | 169.69 | |
| 43 | 406.3381 | 12.1817 | Ag | | 37.1 |
| 44 | 408.8416 | 12.2568 | Au | 30.03 | |
| 45 | 418.9863 | 12.5609 | Bg | | 48.06 |
| 46 | 564.4215 | 16.9209 | Bg | | 13.52 |
| 47 | 565.5371 | 16.9544 | Au | 29.01 | |
| 48 | 569.7261 | 17.0800 | Ag | | 61.07 |
| 49 | 572.2264 | 17.1549 | Bu | 139.99 | |
| 50 | 572.6690 | 17.1682 | Au | 10.6 | |
| 51 | 573.2400 | 17.1853 | Bg | | 15.44 |
| 52 | 579.0819 | 17.3604 | Bu | 7.54 | |
| 53 | 581.9180 | 17.4455 | Ag | | 32.29 |
| 54 | 628.4185 | 18.8395 | Bu | 110.72 | |
| 55 | 631.5085 | 18.9321 | Ag | | 37.16 |
| 56 | 632.6032 | 18.9650 | Au | 27.97 | |
| 57 | 632.7413 | 18.9691 | Bg | | 0.56 |
| 58 | 651.8890 | 19.5431 | Au | 4.28 | |
| 59 | 653.1563 | 19.5811 | Bg | | 8.07 |
| 60 | 657.5294 | 19.7122 | Ag | | 6.41 |
| 61 | 662.8053 | 19.8704 | Bu | 9.64 | |
| 62 | 756.0198 | 22.6649 | Au | 48.6 | |
| 63 | 765.0329 | 22.9351 | Ag | | 28.7 |
| 64 | 770.6240 | 23.1027 | Bu | 187.26 | |
| 65 | 772.2366 | 23.1511 | Bg | | 5.47 |
| 66 | 857.8260 | 25.7170 | Ag | | 176.77 |
| 67 | 860.8721 | 25.8083 | Bu | 43.34 | |
| 68 | 864.2250 | 25.9088 | Bg | | 3.26 |
| 69 | 865.0758 | 25.9343 | Au | 21.84 | |
| 70 | 875.5931 | 26.2496 | Ag | | 85.38 |
| 71 | 879.8570 | 26.3775 | Bg | | 8.9 |
| 72 | 879.8788 | 26.3781 | Bu | 3.83 | |

| | | | | | |
|---|---|---|---|---|---|
| **73** | 880.6383 | 26.4009 | Au | 5.78 | |
| **74** | 986.6620 | 29.5794 | Ag | | 50.41 |
| **75** | 987.7838 | 29.6130 | Bg | | 23.06 |
| **76** | 989.4238 | 29.6622 | Bu | 59.23 | |
| **77** | 994.2315 | 29.8063 | Au | 9.79 | |
| **78** | 1005.8700 | 30.1552 | Bg | | 4.29 |
| **79** | 1006.1950 | 30.1650 | Bu | 136.34 | |
| **80** | 1008.2570 | 30.2268 | Au | 6.85 | |
| **81** | 1008.4940 | 30.2339 | Ag | | 83.31 |
| **82** | 1026.1660 | 30.7637 | Ag | | 26.18 |
| **83** | 1028.8450 | 30.8440 | Bu | 7.58 | |
| **84** | 1029.0980 | 30.8516 | Bg | | 4.99 |
| **85** | 1031.9310 | 30.9365 | Au | 6.01 | |
| **86** | 1063.2040 | 31.8741 | Bu | 53.24 | |
| **87** | 1065.3200 | 31.9375 | Au | 1.38 | |
| **88** | 1069.4220 | 32.0605 | Bg | | 34.24 |
| **89** | 1069.8210 | 32.0724 | Ag | | 40.57 |
| **90** | 1123.8720 | 33.6928 | Au | 33.96 | |
| **91** | 1125.4740 | 33.7409 | Ag | | 12.73 |
| **92** | 1125.4830 | 33.7411 | Bu | 102.98 | |
| **93** | 1129.2650 | 33.8545 | Bg | | 9.51 |
| **94** | 1170.7910 | 35.0994 | Au | 9.58 | |
| **95** | 1172.1720 | 35.1408 | Bg | | 11.23 |
| **96** | 1174.1560 | 35.2003 | Ag | | 5.62 |
| **97** | 1174.2260 | 35.2024 | Bu | 38.69 | |
| **98** | 1246.5720 | 37.3713 | Bu | 21.6 | |
| **99** | 1250.8490 | 37.4995 | Bg | | 27.62 |
| **100** | 1252.1960 | 37.5399 | Ag | | 14.09 |
| **101** | 1254.1540 | 37.5986 | Au | 5.08 | |
| **102** | 1271.1920 | 38.1094 | Bu | 95.27 | |
| **103** | 1275.3500 | 38.2340 | Bg | | 20.31 |
| **104** | 1279.0460 | 38.3448 | Ag | | 39.88 |
| **105** | 1280.4470 | 38.3868 | Au | 30.73 | |
| **106** | 1295.5570 | 38.8398 | Bu | 478.57 | |
| **107** | 1299.3290 | 38.9529 | Au | 21.31 | |
| **108** | 1302.9480 | 39.0614 | Bg | | 38.12 |
| **109** | 1304.7960 | 39.1168 | Ag | | 149.21 |
| **110** | 1334.4290 | 40.0052 | Bg | | 10.67 |
| **111** | 1336.0120 | 40.0526 | Bu | 120.74 | |

| 112 | 1337.4630 | 40.0961 | Au | 15.88 | |
|-----|-----------|---------|----|-------|-----|
| 113 | 1340.0890 | 40.1748 | Ag | | 24.11 |
| 114 | 1349.2540 | 40.4496 | Ag | | 26.9 |
| 115 | 1352.1920 | 40.5377 | Bu | 22.24 | |
| 116 | 1353.8380 | 40.5870 | Au | 0.51 | |
| 117 | 1355.0340 | 40.6229 | Bg | | 3.07 |
| 118 | 1371.1000 | 41.1045 | Au | 44.21 | |
| 119 | 1371.6450 | 41.1209 | Bu | 457.95 | |
| 120 | 1373.3460 | 41.1719 | Bg | | 20.39 |
| 121 | 1374.4630 | 41.2054 | Ag | | 116.98 |
| 122 | 1377.8770 | 41.3077 | Bg | | 17.22 |
| 123 | 1378.9010 | 41.3384 | Bu | 1150.47 | |
| 124 | 1381.6500 | 41.4208 | Au | 0.03 | |
| 125 | 1386.6220 | 41.5699 | Ag | | 48.81 |
| 126 | 1418.6080 | 42.5288 | Bg | | 61.93 |
| 127 | 1418.8120 | 42.5349 | Ag | | 54.3 |
| 128 | 1420.2980 | 42.5795 | Bu | 103.37 | |
| 129 | 1422.5030 | 42.6456 | Au | 88.25 | |
| 130 | 1424.0420 | 42.6917 | Ag | | 44.51 |
| 131 | 1426.3690 | 42.7615 | Bu | 121.39 | |
| 132 | 1427.4830 | 42.7949 | Bg | | 41.03 |
| 133 | 1432.6570 | 42.9500 | Au | 77.37 | |
| 134 | 1446.3480 | 43.3604 | Au | 1.66 | |
| 135 | 1451.1390 | 43.5041 | Bg | | 10.38 |
| 136 | 1459.0300 | 43.7406 | Ag | | 44.69 |
| 137 | 1465.5880 | 43.9372 | Bu | 49.4 | |
| 138 | 1507.6700 | 45.1988 | Au | 508 | |
| 139 | 1522.8740 | 45.6546 | Bu | 1161.56 | |
| 140 | 1538.7820 | 46.1315 | Bg | | 6.74 |
| 141 | 1543.8160 | 46.2824 | Ag | | 83.54 |
| 142 | 1571.2150 | 47.1038 | Ag | | 8.4 |
| 143 | 1580.2800 | 47.3756 | Au | 526.59 | |
| 144 | 1582.4940 | 47.4420 | Bg | | 16.35 |
| 145 | 1586.2340 | 47.5541 | Bu | 2956.93 | |
| 146 | 1645.7730 | 49.3390 | Ag | | 4.9 |
| 147 | 1647.4840 | 49.3903 | Bg | | 6.29 |
| 148 | 1647.4880 | 49.3904 | Au | 69.52 | |
| 149 | 1648.2430 | 49.4131 | Bu | 67.83 | |
| 150 | 1667.3460 | 49.9858 | Ag | | 9.28 |

| 151 | 1668.0720 | 50.0075 | Au | 0.03 | |
|-----|-----------|---------|-----|---------|--------|
| 152 | 1669.0740 | 50.0376 | Bu | 149.09 | |
| 153 | 1669.2760 | 50.0436 | Bg | | 5.24 |
| 154 | 2738.6230 | 82.1018 | Bu | 8084.74 | |
| 155 | 2739.0910 | 82.1159 | Ag | | 693.32 |
| 156 | 2791.6850 | 83.6926 | Bg | | 97.71 |
| 157 | 2792.1150 | 83.7055 | Au | 550.92 | |
| 158 | 2852.1100 | 85.5041 | Au | 4719.55 | |
| 159 | 2858.4630 | 85.6946 | Ag | | 337.87 |
| 160 | 2868.3630 | 85.9914 | Bu | 5367.01 | |
| 161 | 2878.0970 | 86.2832 | Bg | | 202.2 |
| 162 | 2953.5320 | 88.5447 | Ag | | 42.07 |
| 163 | 2958.0300 | 88.6795 | Bg | | 253.56 |
| 164 | 2959.4700 | 88.7227 | Au | 396.26 | |
| 165 | 2960.7210 | 88.7602 | Bu | 121.7 | |
| 166 | 2961.7870 | 88.7921 | Bg | | 144.54 |
| 167 | 2967.6790 | 88.9688 | Ag | | 479.51 |
| 168 | 2970.2600 | 89.0462 | Au | 1275.64 | |
| 169 | 2976.0940 | 89.2210 | Bu | 1406.11 | |
| 170 | 2983.6790 | 89.4485 | Au | 251.91 | |
| 171 | 2984.3240 | 89.4678 | Bg | | 6.31 |
| 172 | 2987.9650 | 89.5769 | Bu | 814.18 | |
| 173 | 2993.0440 | 89.7292 | Ag | | 809.79 |
| 174 | 3000.0540 | 89.9394 | Bu | 35.42 | |
| 175 | 3000.0780 | 89.9401 | Bg | | 225.24 |
| 176 | 3000.6440 | 89.9570 | Au | 14.51 | |
| 177 | 3000.7210 | 89.9593 | Ag | | 143.92 |
| 178 | 3005.8820 | 90.1141 | Bu | 668.4 | |
| 179 | 3006.9910 | 90.1473 | Au | 33.44 | |
| 180 | 3007.7190 | 90.1691 | Bg | | 36.22 |
| 181 | 3014.6430 | 90.3767 | Ag | | 1000 |
| 182 | 3030.0710 | 90.8393 | Au | 14.29 | |
| 183 | 3030.2910 | 90.8458 | Bg | | 57 |
| 184 | 3031.4340 | 90.8801 | Bu | 15.96 | |
| 185 | 3031.7310 | 90.8890 | Ag | | 256.55 |
| 186 | 3062.8960 | 91.8233 | Au | 0.33 | |
| 187 | 3063.8110 | 91.8507 | Bg | | 33.11 |
| 188 | 3065.2430 | 91.8937 | Bu | 16.12 | |
| 189 | 3065.9850 | 91.9159 | Ag | | 65.67 |

**Table B-2.** Anharmonic calculations for N–H1 across unit cell volume expansions.

| | 0% | +2% | +4% |
|---|---|---|---|
| **N–H1** | | | |
| *Fundamental anharmonic frequency (cm⁻¹)* | 2363.5 | 2355.6 | 2348.0 |
| *First overtone (cm⁻¹)* | 4271.0 | 4246.5 | 4221.5 |
| *Harmonic frequency (cm⁻¹)* | 2819.6 | 2820.3 | 2822.6 |
| *Anharmonic constant (cm⁻¹)* | 228.0 | 232.4 | 237.3 |

**Table B-3.** Anharmonic calculations for N–H2 across unit cell volume expansions.

| | 0% | +2% | +4% |
|---|---|---|---|
| **N–H2** | | | |
| *Fundamental anharmonic frequency (cm⁻¹)* | 2411.4 | 2419.9 | 2427.0 |
| *First overtone (cm⁻¹)* | 4382.2 | 4391.8 | 4402.1 |
| *Harmonic frequency (cm⁻¹)* | 2852.0 | 2867.8 | 2878.8 |
| *Anharmonic constant (cm⁻¹)* | 220.3 | 224.0 | 225.9 |

**Table B-4.** **A**nharmonic calculations for N–H3 across unit cell volume expansions.

| | 0% | +2% | +4% |
|---|---|---|---|
| **N–H3** | | | |
| *Fundamental anharmonic frequency (cm$^{-1}$)* | 2637.0 | 2655.5 | 2675.5 |
| *First overtone (cm$^{-1}$)* | 4895.5 | 4938.4 | 4985.7 |
| *Harmonic frequency (cm$^{-1}$)* | 3015.4 | 3028.2 | 3040.7 |
| *Anharmonic constant (cm$^{-1}$)* | 189.2 | 186.3 | 182.6 |

**Appendix C: Supporting Information for Chapter 7**
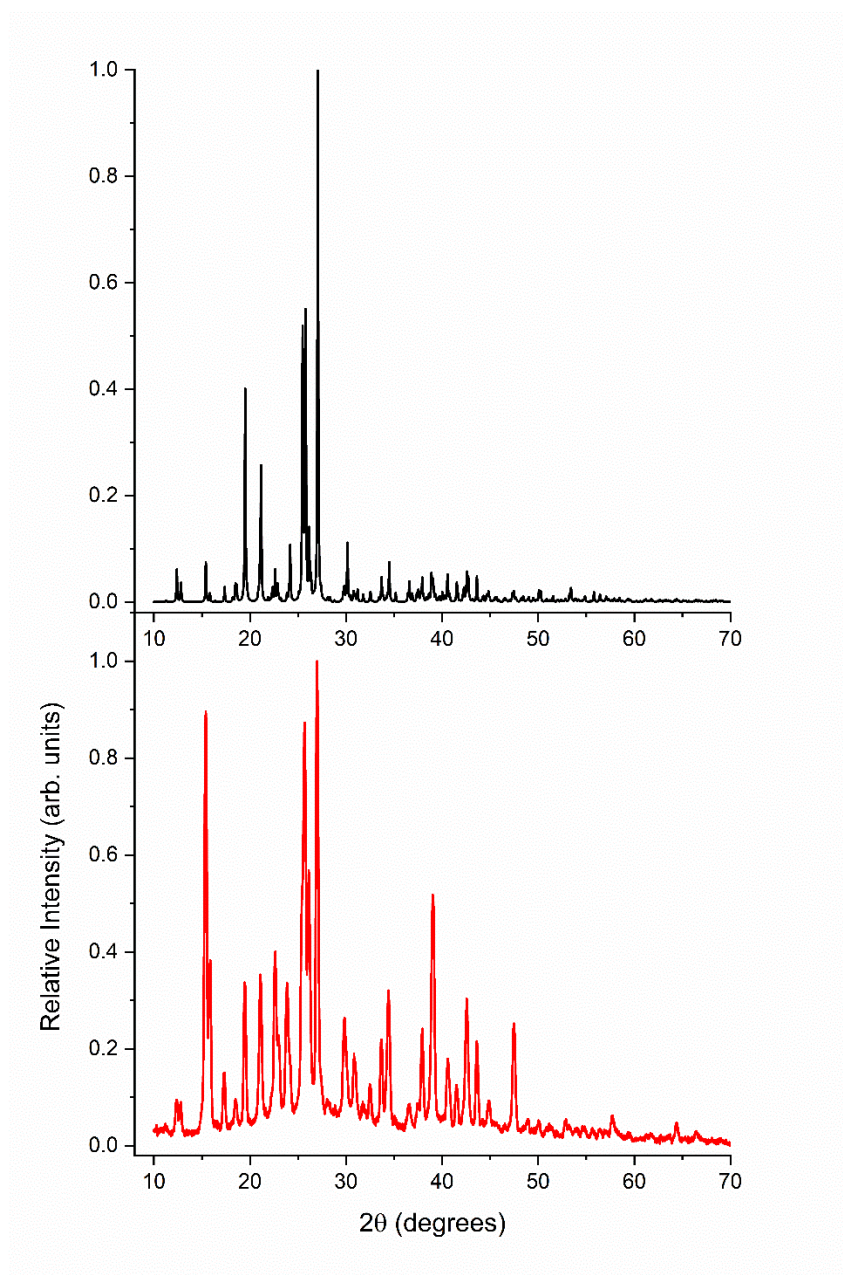
**Table of Contents:**

**Figure C-1.** Predicted powder X-ray diffraction pattern from room temperature SC-XRD β-triglycine structure (black, top) and experimental powder X-ray diffraction pattern (red, bottom).
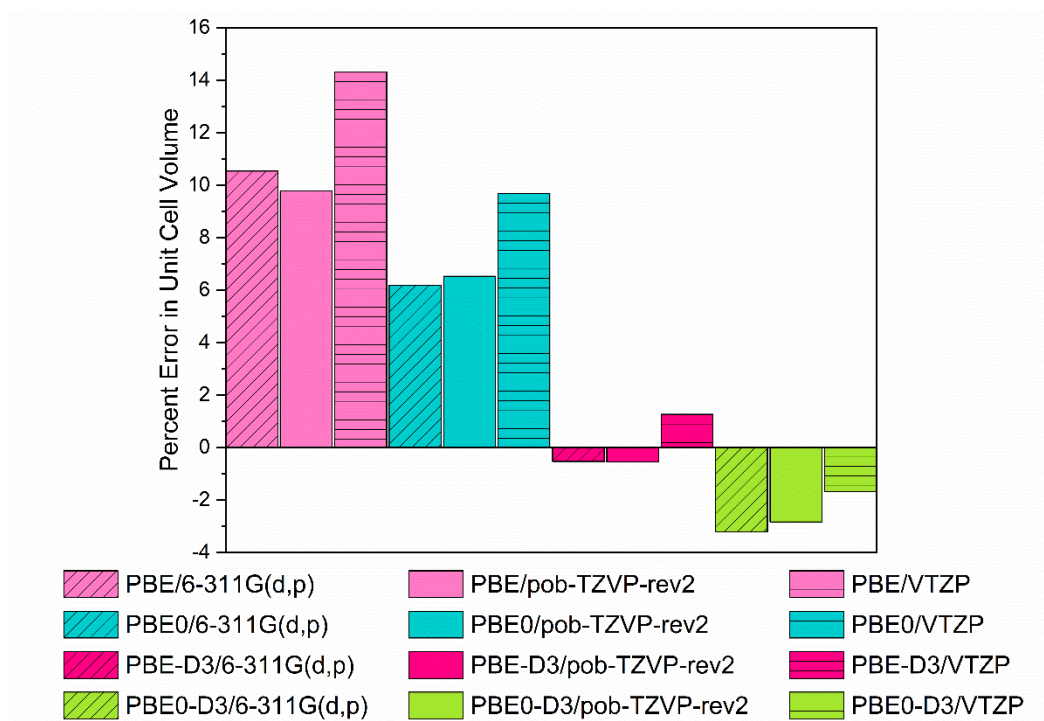
**Figure C-2.** Percent error in calculated unit cell volume with and without the dispersion correction compared to published SC-XRD measurements for crystalline β-triglycine.
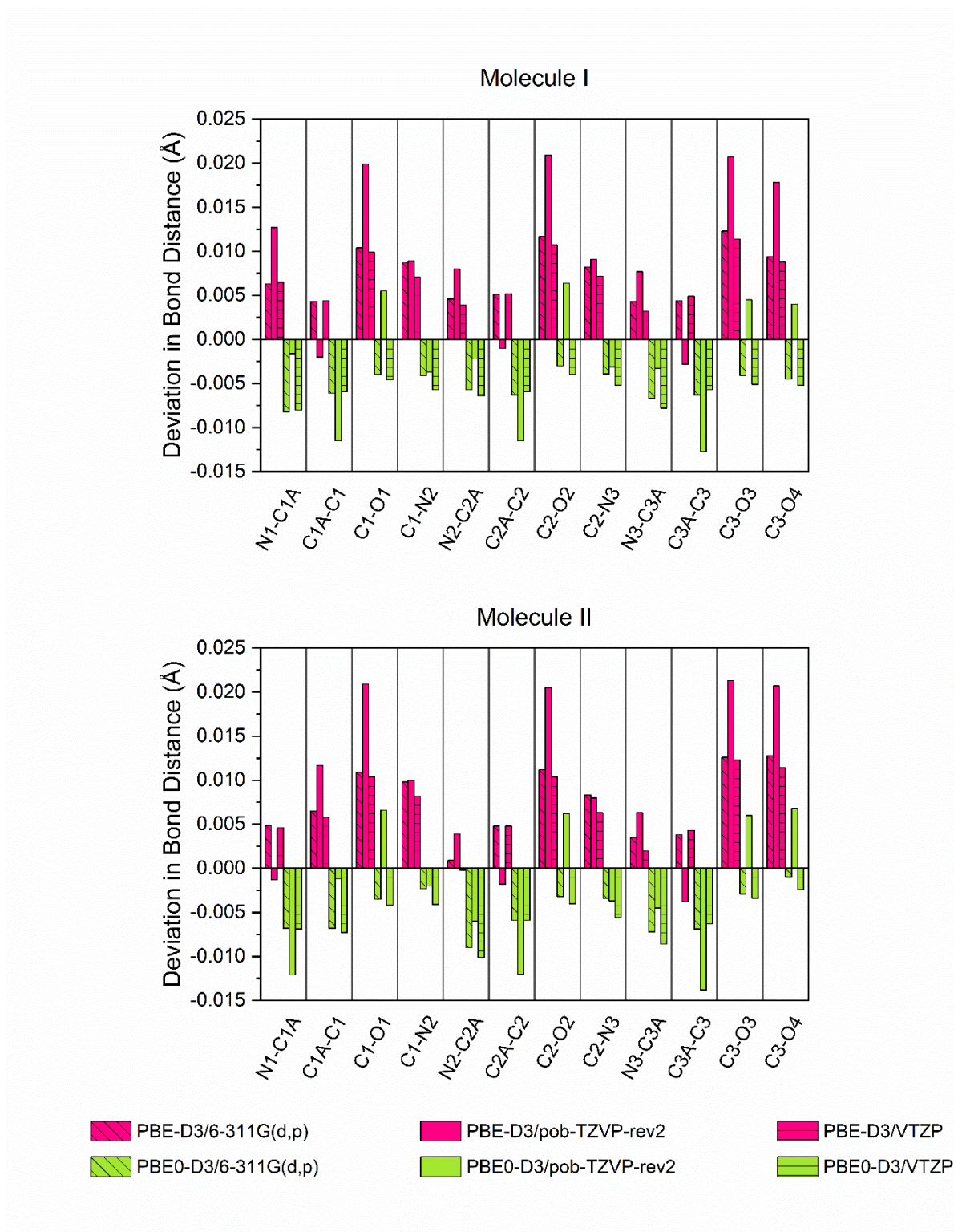
**Figure C-3.** Deviation in the calculated heavy atom bond distances compared to SC-XRD measurements for β-triglycine.
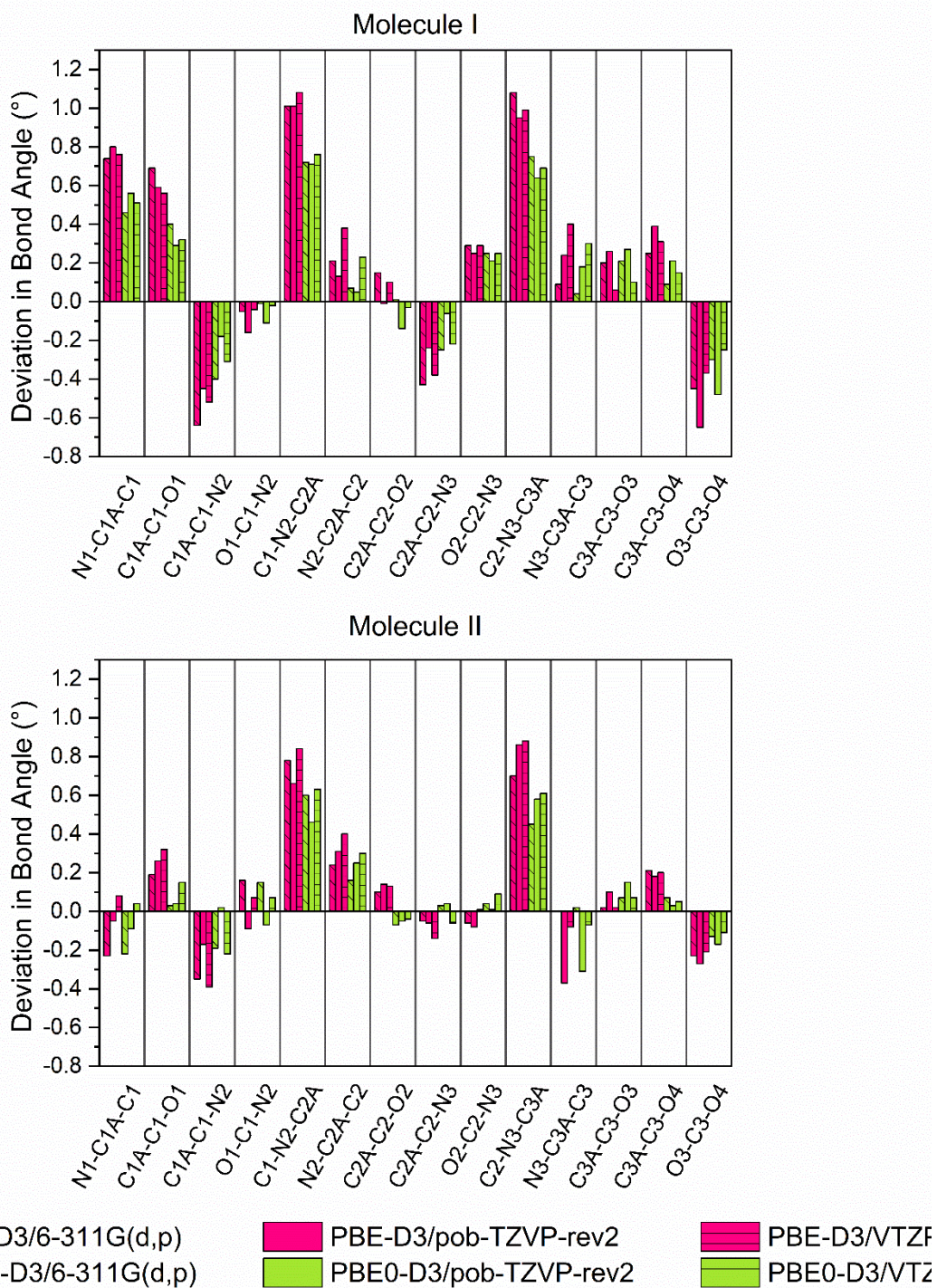
**Figure C-4.** Deviation in the calculated heavy atom bond angles compared to SC-XRD measurements for β-triglycine.
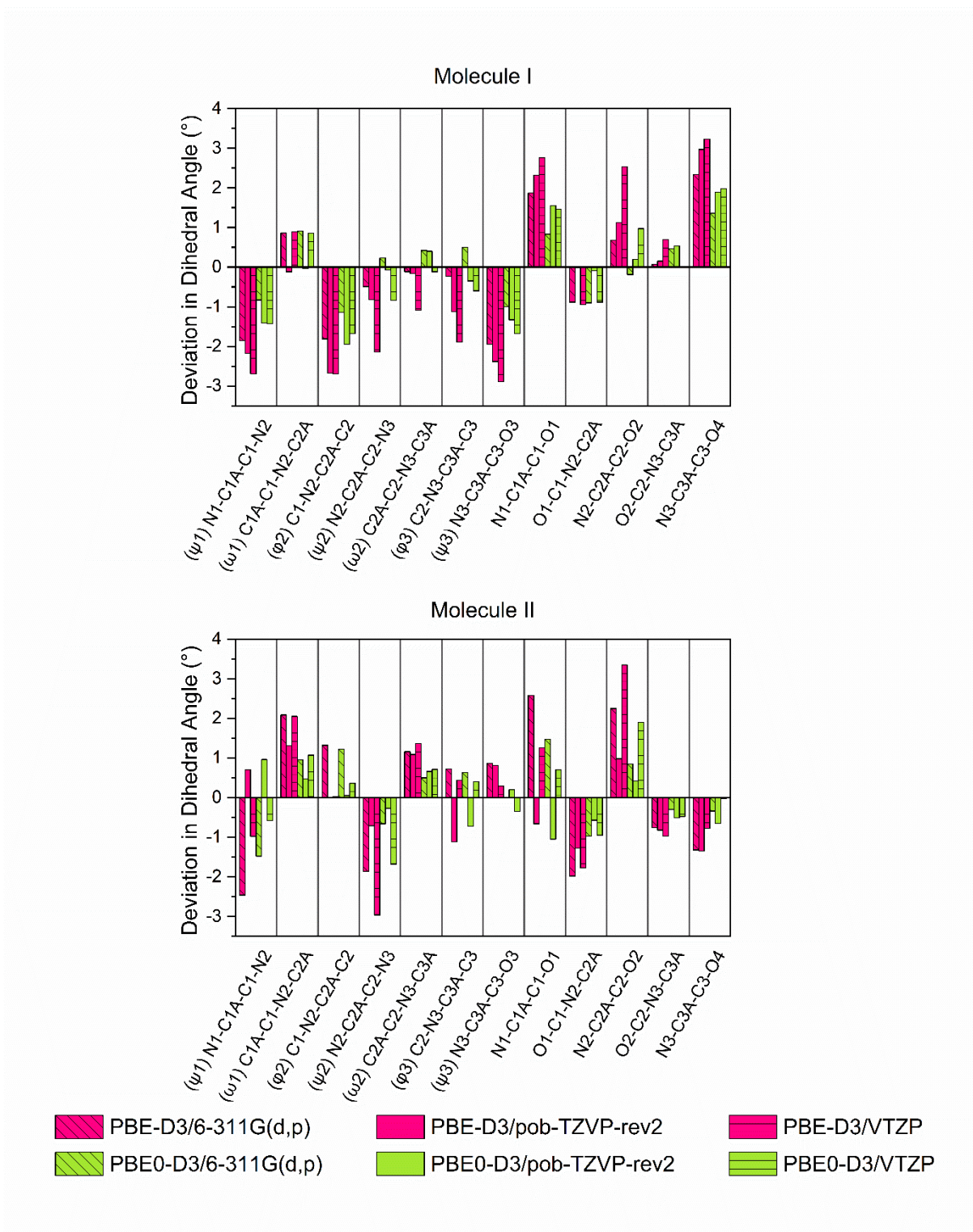
**Figure C-5.** Deviation in the calculated heavy atom dihedral angles compared to SC-XRD measurements for β-triglycine.
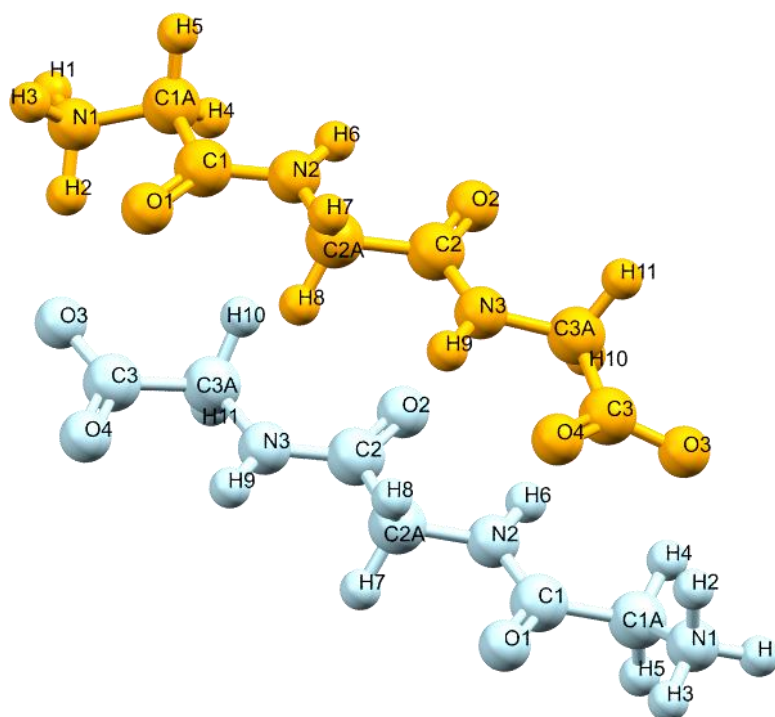
**Figure C-6.** Fully labelled asymmetric unit with molecule I in blue and molecule II in orange.
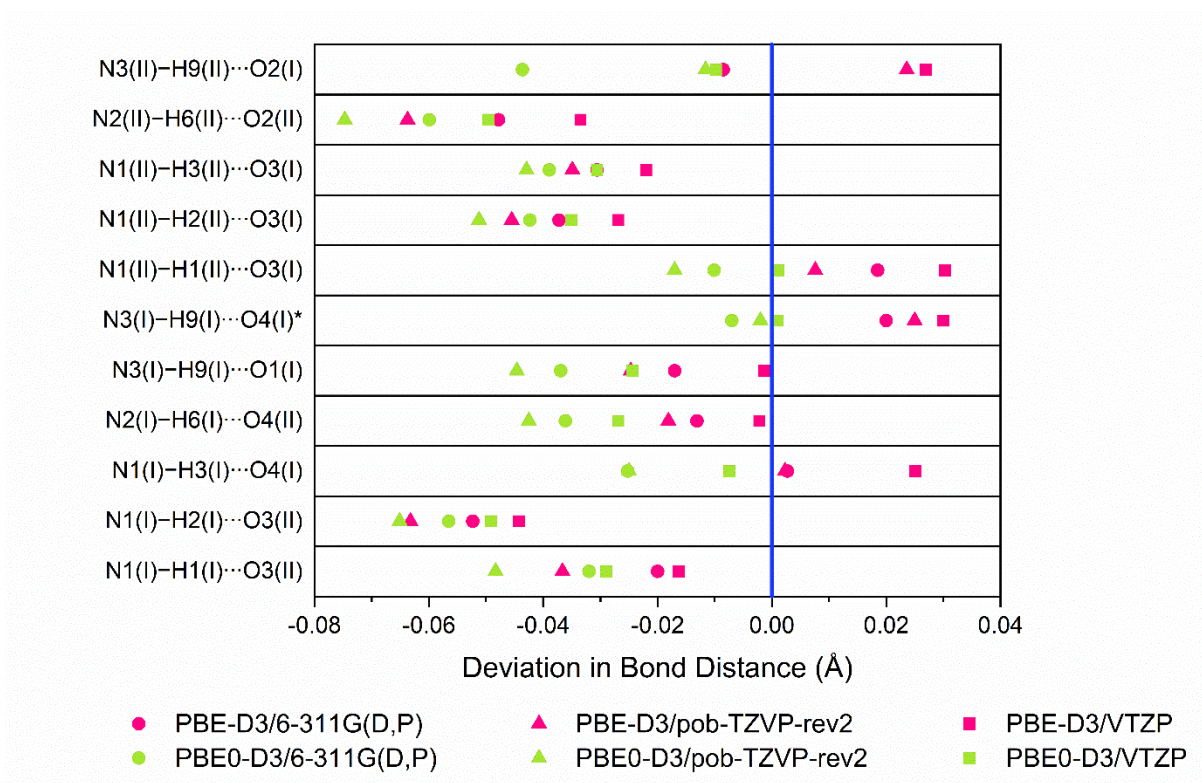
**Figure C-7.** Deviation in the calculated hydrogen bond distances compared to SC-XRD for β-triglycine with the * indicating the intramolecular hydrogen bond.

**Table C-1.** RMSD of calculated heavy atom bond distances, bond angles, and dihedral angles compared to SC-XRD measurements for β-triglycine.

|  | Bond distances | Bond Angles | Dihedral Angles |
|---|---|---|---|
| PBE-D3/6-311G(d,p) | 0.0082 | 0.45 | 1.55 |
| PBE-D3/POB-TZVP-rev2 | 0.0132 | 0.45 | 1.39 |
| PBE-D3/VTZP | 0.0075 | 0.47 | 1.96 |
| PBE0-D3/6-311G(d,p) | 0.0054 | 0.31 | 0.86 |
| PBE0-D3/POB-TZVP-rev2 | 0.0073 | 0.30 | 0.88 |
| PBE0-D3/VTZP | 0.0060 | 0.32 | 1.07 |

**Table C-2.** Deviation in predicted frequencies from experimental 78 K low-frequency Raman spectrum (cm$^{-1}$).

|  | Peak 1 | Peak 2 | Peak 3 | Peak 4 | Peak 5 | Peak 6 | RMSD |
|---|---|---|---|---|---|---|---|
| PBE-D3/6-311G(d,p) | -3.5 | -0.7 | 2.8 | 3.4 | 2.1 | 0.7 | 2.5 |
| PBE-D3/POB-TZVP-rev2 | -2.7 | -1.8 | 3.1 | 1.4 | 0.2 | -0.3 | 1.9 |
| PBE-D3/VTZP | -4.9 | -2.1 | 1.4 | 0.2 | 0.1 | -2.6 | 2.5 |
| PBE0-D3/6-311G(d,p) | 3.3 | 3.0 | 4.3 | 7.2 | 6.9 | 7.7 | 5.7 |
| PBE0-D3/POB-TZVP-rev2 | 1.0 | 1.2 | 5.1 | 4.2 | 4.2 | 5.3 | 3.9 |
| PBE0-D3/VTZP | -0.9 | 1.0 | 3.5 | 3.8 | 3.6 | 3.8 | 3.1 |
| FIXED LATTICE PBE0-D3/VTZP | -0.7 | 0.2 | 3.0 | 2.4 | 0.9 | 0.5 | 1.7 |

**Table C-3.** Deviation in predicted frequencies from experimental 25 K terahertz time-domain spectrum (cm$^{-1}$).

|  | Peak 1 | Peak 2 | Peak 3 | Peak 4 | Peak 5 | Peak 6 | Peak 7 | RMSD |
|---|---|---|---|---|---|---|---|---|
| PBE-D3/6-311G(d,p) | 2.2 | 0.5 | -0.9 | 0.4 | -0.9 | 3.7 | 0.3 | 1.7 |
| PBE-D3/POB-TZVP-rev2 | 2.2 | -1.5 | -2.3 | -1.3 | -2.4 | 1.7 | 3.6 | 2.3 |
| PBE-D3/VTZP | -1.2 | -3.3 | -0.8 | -1.8 | -2.7 | 0.4 | 0.6 | 1.9 |
| PBE0-D3/6-311G(d,p) | 4.7 | 5.6 | 4.2 | 4.6 | 1.6 | 6.9 | 6.0 | 5.0 |
| PBE0-D3/POB-TZVP-rev2 | 3.5 | 2.7 | 1.5 | 2.2 | -0.7 | 4.7 | 6.8 | 3.7 |
| PBE0-D3/VTZP | 0.5 | 1.0 | 1.4 | 1.6 | 0.3 | 4.1 | 4.1 | 2.4 |
| FIXED LATTICE PBE0-D3/VTZP | -0.8 | 1.2 | 3.0 | 1.9 | -1.8 | 1.4 | 2.5 | 1.9 |

# Curriculum Vitae

**Sara J. Dampf**

Department of Chemistry, Syracuse University, Syracuse, NY  13244-4100

Phone: +1 (315) 601-1738

Email: sjdampf@gmail.com

## EDUCATION

| | | |
|---|---|---|
| **PhD** | Chemistry - Syracuse University | Anticipated August 2021 |

Advisor: Dr. Timothy Korter

Thesis: <u>Computational Methodologies for the Simulation and Analysis of Low-Frequency Vibrations in Molecular Crystals</u>

| | | |
|---|---|---|
| **BS** | Chemistry - University of New Haven | 2015 |

Minor in Mathematics

Advisor: Dr. Howard Harris

Honors Thesis: <u>Recovery of Trace Evidence by Use of Peelable Films</u>

| | | |
|---|---|---|
| **BS** | Forensic Science – University of New Haven | 2015 |

## RESEARCH EXPERIENCE

Developed series of molecular standards for international testing and validation of terahertz time-domain spectroscopy, low-frequency Raman spectroscopy, and *ab initio* solid-state density functional theory simulations

Completed vibrational assignments and analyses of the low-frequency spectra of the neurotransmitter γ-aminobutyric acid (GABA), the related pharmaceuticals Phenibut and Baclofen, and their corresponding hydrochloride salts

Evaluated computational parameters necessary to model the weak intermolecular forces in complex molecular solids ranging from monomers to trimers

## TECHNICAL AND SPECIALIZED SKILLS

Experimental techniques: Terahertz (far-infrared) time-domain spectroscopy, low-frequency Raman spectroscopy, single-crystal X-ray diffraction, powder X-ray diffraction

Computational techniques*:* Extensive experience with CRYSTAL17 (*ab initio* solid-state density functional theory), experience with Gaussian and CP2K, familiar with python and SQL

Software: Origin, MS Office suite, Linux, APEX3, DIFFRAC.EVA, Cambridge Structural Database (Mercury, Conquest), ChemDraw, Endnote, SpectraGryph, WinSCP, PuTTY

## PUBLICATIONS

Davie, A.; Vandrevala, F.; **Dampf, S. J.**.; Deng, Y.; George, D.; Sylvester, E.; Korter, T.; Einarsson, E.; Benedict, J.; Markelz, A. Phonon Kinetics of Fructose at the Melting Transition. *J. Phys. Chem. C* **2021**, 125(22), 12269-12276.

Case, D.R.; Spear, A; Henwood A.F.; Nanao, M; **Dampf, S.J.**.; Korter, T.M.; Gunnlaugsson, T.; Zubieta, J.; Doyle, R.P. [Re(CO)$_3$(5-PAN)Cl], a Rhenium(i) Naphthalimide Complex for the Visible Light Photocatalytic Reduction of CO$_2$. *Dalton Trans.* **2021**, 50, 3479-3486.

Millimaci, A.M.; Meador, R.I.L.; **Dampf, S.J.**; Chisholm, J.D. Metal Free Amino-Oxidation of Electron Rich Alkenes Mediated by an Oxoammonium Salt. *Isr. J. Chem.* **2020**, 61, 322-326.

**Dampf, S. J**.; Korter, T. M. Crystalline Molecular Standards for Low-frequency Vibrational Spectroscopies. *J. Infrared, Millimeter, Terahertz Waves* **2020**, 41, 1284-1300.

**Dampf, S. J**.; Korter, T. M. Anomalous Temperature Dependence of the Lowest-Frequency Lattice Vibration in Crystalline γ-Aminobutyric Acid. *J. Phys. Chem. A* **2019**,123, 2058-2064.

Azzarelli, N.; Ponnala, S.; Aguirre, A.; **Dampf, S. J**.; Davis, M.P.; Ruggiero, M.; Lopez Diaz, V.; Babich, J.; Coogan, M.; Korter, T.M.; Doyle, R.P.; Zubieta, J. Defining the Origins of Multiple Emission/excitation in Rhenium-bisthiazole Complexes. *Inorg. Chim. Acta* **2019**, 489, 301-309.

## CONTRIBUTED TALKS

**Dampf, S.J.** ; Korter, T. M., Low-frequency Vibrational Spectroscopy Of γ-Aminobutyric Acid Derivatives: GABA Hydrochloride And β-Phenyl-GABA Hydrochloride, The International Society of Infrared, Millimeter, and Terahertz Waves, Buffalo, NY (Virtual). November 12, 2020.

**Dampf, S.J.**; Korter, T.M., Deriving Elastic Parameters from Lattice Vibrations In Copper (II) Acetylacetonate, The International Society of Infrared, Millimeter, and Terahertz Waves, Paris, France. September 5, 2019.

**Dampf, S.J.**; Korter, T.M., Computational Methodologies for the Accurate Simulation of Raman Intensities in the Low-frequency Vibrational Spectra of Molecular Crystals, 258th American Chemical Society National Meeting & Exposition, San Diego, CA. August 25, 2019.

**Dampf, S.J.**; Korter, T.M., Molecular Crystal Spectral Standards for Terahertz Spectroscopy, SciX 2018, Atlanta, GA. October 23, 2018.

**Dampf, S.J.**; Korter, T.M., Terahertz Spectroscopy of Vibrational Anharmonicity in Crystalline γ-Aminobutyric Acid, The International Society of Infrared, Millimeter, and Terahertz Waves, Cancun, Mexico. August 31, 2017.

**CONTRIBUTED POSTERS**

**Dampf, S.J.**; Korter, T.M., Molecular Crystal Standards for Low-frequency Spectroscopies, 8th International Conference on Optical Terahertz Science and Technology, Santa Fe, NM. March 12, 2019.

**Dampf, S.J.**; Korter, T.M., Crystalline Molecular Standards for Low-frequency Vibrational Spectroscopies, 256th American Chemical Society National Meeting & Exposition, Boston, MA. August 22, 2018.

**Dampf, S.J.**; Korter, T.M.., Comparison of Elastic Behavior in Copper (II) Acetylacetonate and Zinc (II) Acetylacetonate Crystals. CP2K Summer School, Warrington, UK. June 20, 2018.

**Dampf, S.J.**; Korter, T.M., Analysis of Anharmonicity in Crystalline γ-Aminobutyric Acid, The Minnesota Workshop on *ab initio* Modelling in Solid-State Chemistry with CRYSTAL, Minneapolis, MN. July 12, 2017.

**Dampf, S.J.**; Korter, T.M., Conformation and Cohesion Factors Stabilizing Crystalline GABA Polymorphs, 252nd ACS National Meeting & Exposition, Philadelphia, PA. August 24, 2016.

**HONORS AND AWARDS**

Summer Dissertation Fellowship, Syracuse University, Syracuse, NY. April 2021.

William D. Johnson Award for Outstanding Graduate Teaching Assistant, Syracuse University, Syracuse, NY. March 2020.

8th International Conference on Optical Terahertz Science and Technology Best Poster Award, Santa Fe, NM. March 2019.

Syracuse Chemistry Graduate Student Poster Competition Award, Syracuse University, Syracuse, NY. March 2018.

Wiley Outstanding Poster Award, Minnesota Workshop on ab Initio Modelling in Solid State Chemistry with CRYSTAL, Minneapolis, MN. July 2017.

Syracuse University Graduate Fellowship Recipient, 2015.

Inter-Chapter Relations Grant, American Chemical Society, January 2015.

Student Leadership Award, American Chemical Society, Spring 2014.

**PROFESSIONAL TRAININGS AND WORKSHOPS**

Advanced Chemical Crystallography Applications Training - Madison, WI. October 2018.

CP2K User Tutorial: Computational Spectroscopy - Paderborn, Germany. August 2018.

CP2K Summer School - Warrington, UK. June 2018.

IRMMW-THz Student Workshop - Cancun, Mexico. August 2017.

Bruker APEX II DUO Service Training - Syracuse University, Syracuse, NY. August 2017.

The Minnesota Workshop on ab Initio Modelling in Solid State Chemistry with CRYSTAL- Minneapolis, MN. July 2017.

Intro to Single Crystal X-ray Diffraction Applications Training - Madison, WI. October 2016.

*Ab initio* Modelling in Solid State Chemistry - Turin, Italy. September 2016.

Radiation Safety Training - Syracuse University, Syracuse, NY. Spring 2016.

American Chemical Society Leadership Institute - Dallas, TX. January 2014.

## TEACHING EXPERIENCE

X- ray Teaching Assistant - Syracuse University, Syracuse, NY                    2018-2020

> Maintained and scheduled service for a Bruker D2 Phaser and Bruker Kappa APEX Duo diffractometer.

> Trained new users on instrument use, safety, and analysis of data.

Teaching Assistant – Syracuse University, Syracuse, NY            2016-2018, 2020-2021

> General Chemistry I Lecture, General Chemistry II Lecture, General Chemistry I Laboratory, Forensic Science

> Developed and prepared online course material for transition to remote learning for General Chemistry I and II lecture and held weekly recitation and office hours for a total of 100 students.

> Provided pre-laboratory instruction, weekly office hours, and graded scientific reports for laboratory-based courses

## VOLUNTEER EXPERIENCE

Volunteer – Helping Hounds Dog Rescue, Syracuse, NY                    2016-Present

> Basic responsibilities include dog walking and shelter cleaning.

> Advanced responsibilities include hosting live stream of incoming transports, photographing adoptions, engaging in community events, assisting prospective adopters, and inputting medical records.

> Over 900 hours of recorded volunteer service.